Airfoil Drag with Uniform Blowing in Turbulent Boundary Layers

Zur Erlangung des akademischen Grades eines
Doktors der Ingenieurwissenschaften (Dr.-Ing.)
bei der KIT-Fakultät für Maschinenbau
des Karlsruher Instituts für Technologie (KIT)

angenommene

Dissertation

von

M.Sc. Georg Fahland

Tag der mündlichen Prüfung:	03.07.2024
Hauptreferentin:	Prof. Dr.-Ing. Bettina Frohnapfel
Korreferent:	Prof. Dr.-Ing. Rolf Radespiel

I declare that I have developed and written the enclosed thesis completely by myself, and have not used sources or means without declaration in the text. I used Grammarly (`https://www.grammarly.com/`) as an artificial intelligence spell and grammar checker.

Karlsruhe, 25.04.2024

.....

(**Georg Fahland**)

Abstract

The present work closes a gap in understanding the performance evaluation of the active flow control scheme of uniform blowing in turbulent boundary layers. Analytical investigations of the momentum and energy budgets reveal the nature of the theoretically necessary effort to operate the boundary layer control scheme and how this manifests in the wake of the body. By this, the term of the *inclusive drag* is introduced which resembles the actual drag force on the body — the *body drag* — plus the theoretically unavoidable effort to operate the control: the *boundary layer control penalty*. Numerical Reynolds-averaged Navier-Stokes equations are employed to explore the parameter field of airfoil flows with uniform blowing control to find general trends and dependencies. It is found that the control performance increases with a favorable pressure gradient and higher static pressure within the region where the control is applied. In terms of airfoil flows, this means that uniform blowing on the pressure side of the airfoil has a high performance which additionally benefits from medium to high lift coefficients and cambered, thin airfoils. Subsequently, this parameter set is also employed for experimental investigations which verify these trends. Furthermore, it is shown that the separation of inclusive drag and body drag resolves former contradictions in the agreement of numerical and experimental studies. Instead, it is found, that the physical implementation of uniform blowing — often called microblowing technique — performs close to the results of ideally uniform numerical simulations. Overall, uniform blowing can be employed successfully to achieve strong body drag reduction but fails in reducing the inclusive drag in the present study by a significant margin. Therefore, uniform blowing seems unsuitable for achieving a net drag reduction in the present implementation as a stand-alone boundary layer control scheme.

Kurzfassung

Die vorliegende Arbeit zeigt einen Weg zur vollständigen Widerstandbewertung der aktiven Strömungskontrolle des uniformen, wandnormalen Ausblasens in turbulenten Grenzschichten auf. Analytische Untersuchungen der Impuls- und Energiebilanz ergeben den theoretisch notwendigen Aufwand zum Betrieb der Grenzschichtkontrolle und wie diese Information im Nachlauffeld des Körpers enthalten ist. Dabei wird der Begriff des Gesamtwiderstands, *inclusive drag*, eingeführt. Dieser beschreibt die Summe aus der tatsächlichen Widerstandskraft am Körper, dem *body drag*, zuzüglich des theoretisch unvermeidbaren Aufwands für den Betrieb der Grenzschichtkontrolle, der *boundary layer control penalty*. Mit Hilfe numerischer Reynolds-averaged Navier-Stokes-Gleichungen werden die Parameterfelder von Tragflächenströmungen mit uniformen, wandnormalen Ausblasen untersucht, um allgemeine Trends und Abhängigkeiten zu ermitteln. Es zeigt sich, dass die Widerstandsreduktion mit einem negativen Druckgradienten und einem höheren statischen Druck innerhalb der Region, in der die Kontrolle angewendet wird, zunimmt. Bezogen auf Tragflügelströmungen bedeutet dies, dass Ausblasen auf der Druckseite des Profils besonders günstig ist, was zusätzlich von mittleren bis hohen Auftriebsbeiwerten gewölbter, dünner Profile profitiert. Anschließend werden experimentelle Untersuchungen durchgeführt, die v.a. diesen Parameterbereich untersuchen und die numerisch gefundenen Trends bestätigen. Weiterhin wird gezeigt, dass die Trennung von *inclusive drag* und *body drag* frühere Widersprüche in der Übereinstimmung von numerischen und experimentellen Studien auflöst. Stattdessen wird festgestellt, dass die physikalische Umsetzung des uniformen, wandnormalen Ausblasens — oft als *microblowing technique* bezeichnet — eine Leistung erbringt, die den Ergebnissen ideal gleichmäßiger Ausblasung numerischer Simulationen nahe kommt. Insgesamt kann uniformes, wandnormales Ausblasen eine starke Reduktion der Widerstandskraft am Körper bewirken. Der theoretische Gesamtwiderstand — *inclusive drag* — steigt jedoch bei allen numerischen und experimentellen Untersuchungen ausnahmslos an. Auf Basis der Ergebnisse der vorliegenden Arbeit erscheint es daher unwahrscheinlich, dass eine Reduzierung des Gesamtwiderstands mittels uniformen, wandnormalen Ausblasens in turbulenten Grenzschichten möglich ist, insofern die Grenzschichtkontrolle allein ohne Kombination mit anderen Grenzschichtkontrollen eingesetzt wird.

Acknowledgements

Multiple people contributed to the success of the present PhD thesis in many different ways which I am very grateful for. I want to thank Bettina Frohnapfel for her guidance in the scientific endeavor. More importantly, I want to sincerely thank her and Jochen Kriegseis for the trust they expressed over more than four years. This includes supporting the wind tunnel modernization with all the developments and additions as well as the design of an airfoil model. Both of which were neither cheap nor straightforward in terms of scientific success. Furthermore, I want to thank Davide Gatti and Alexander Stroh for their valuable time and advice about everything related to science, computers, blowing, and life. I want to extend a special thanks to Heiko Bendler, who took the project of wind tunnel modernization and manufacturing of measurement devices to an unexpected level. He and his workshop colleagues Michael Abramov, Marcel Stotz, Otto Vorreiter, Dominik Eikerling, and Daniel Kissenkötter brought all the ideas to life with great care and an open mind, always focused on the outcome, not the hurdles on the way.

I want to thank Rolf Radespiel for participating in the evaluation of this PhD thesis and for the help he and Peter Scholz provided by providing their HGR-01 airfoil model for validation purposes.

I am grateful for the deep discussions with Marco Atzori about flow control and numerical fluid mechanics. I enjoyed the happenings and talks with my direct colleagues at the laboratory: Lars, Sebastian, Robin, Jacopo, David, Saskia, Carola, Max, Marc, and Christian. They contributed to both my well-being at work and unexpected solutions in many ways. In that regard, I want to extend a special thanks to Jonathan Neuhauser, who helped me with a sincere LaTeX-typesetting issue of the final manuscript.

Finally, I want to express deep gratitude to my parents, who patiently supported me during my mechanical engineering studies. If it was not for some extra time during those years I could not have spent so much time at the Akaflieg workshop where I learned most of the skills I needed for my PhD studies. I want to apologize to the Akaflieg and KA-Racing members who voluntarily chose to work or write their theses with me at ISTM. I know that this time was very demanding and you could have made an easier cut. Thank you to Sabrina, who participated in this adventure even before it started. She kept asking questions about this niche topic and still expressed her love when I thought about so many other things. Without this, I could not have continued in the way I did.

Contents

Abstract . . . iii

Kurzfassung . . . v

Acknowledgements . . . vii

1 Introduction . . . 1
1.1 Motivation . . . 1
1.2 Research Objective and Outline of Study . . . 2

2 Fundamentals . . . 5
2.1 Governing Equations . . . 5
2.2 Turbulent Boundary Layers . . . 9
2.3 Airfoil Aerodynamics . . . 11
2.3.1 Lift . . . 12
2.3.2 Drag . . . 12
2.4 Numerical Techniques . . . 13
2.4.1 Potential Flow Solver . . . 14
2.4.2 Reynolds-Averaged Navier-Stokes (RANS) Simulations . . . 14
2.4.3 Large-Eddy Simulations (LES) . . . 15
2.5 Experimental Techniques . . . 15
2.5.1 Statistical Methods . . . 15
2.5.2 Uncertainty Treatment . . . 18
2.5.3 Point Measurement Techniques . . . 21
2.5.4 Field Measurement Techniques . . . 23
2.6 Skin Friction Drag Reduction by Flow Control . . . 26
2.6.1 Passive vs. Active Control Strategies . . . 26
2.6.2 Uniform Blowing in Turbulent Boundary Layers . . . 27

3 Analytical Investigation on Drag Quantities with Uniform Blowing . . . 29
3.1 Conservation Laws with Uniform Blowing . . . 29
3.1.1 Momentum Balance . . . 29
3.1.2 Energy Balance . . . 31
3.2 Local Drag Assessment with Control Penalty . . . 36
3.3 Conclusions of Analytical Results . . . 36

4 Numerical Investigation . . . 39
4.1 Methodology . . . 39
4.1.1 Simulation Setup . . . 39
4.1.2 Validation . . . 42
4.1.3 Parameter Variations . . . 45
4.2 Results . . . 47
4.2.1 Angle of Attack Dependency — Polar Sweep . . . 47
4.2.2 Reynolds Number Dependency . . . 50
4.2.3 Control Intensity Variation . . . 51

4.2.4 Geometry Variation — Camber and Thickness . . . 53
4.2.5 Pressure Level Effect . . . 55
4.3 Conclusions of Numerical Results . . . 57

5 Experimental Investigation . . . 59
5.1 Facility . . . 59
5.1.1 Characterization . . . 59
5.1.2 Wind-Tunnel Buffeting . . . 61
5.2 Setup . . . 62
5.2.1 Test Case Design . . . 62
5.2.2 General Test Rig Design Considerations . . . 63
5.2.3 Balance . . . 65
5.2.4 Pressure Taps . . . 68
5.2.5 Wake Rake . . . 70
5.2.6 Pressure Drop and Flow Meters . . . 73
5.2.7 Particle Image Velocimetry (PIV) . . . 74
5.2.8 Data Acquisition (DAQ) . . . 77
5.3 Application of Wind-Tunnel Corrections . . . 81
5.3.1 End-Plate Friction . . . 81
5.3.2 Horizontal Buoyancy . . . 82
5.3.3 Lift-Correction . . . 83
5.4 Data Reduction . . . 84
5.5 Results . . . 86
5.5.1 Result Scope and Data Quality . . . 86
5.5.2 General Boundary Layer Control Performance . . . 91
5.5.3 Influence of Static Pressure on Control Performance . . . 95
5.5.4 Flow through Control Surface . . . 100
5.5.5 Local Control Properties . . . 104
5.6 Conclusions of Experimental Results . . . 109

6 Conclusions and Outlook . . . 111

7 References . . . 115
Bibliography . . . 115
List of Conference Contributions . . . 126
List of Journal Publications . . . 126

Acronyms and symbols . . . 133

List of Figures . . . 139

List of Tables . . . 143

A Appendix: Facility Manuals . . . 145
A.1 G-Tunnel Manual . . . 145
A.2 Technische Dokumentation des Traversen Systems am Göttinger Windkanal am ISTM . . . 145
Reference to Manuals . . . 146

B Appendix: Student Contributions . . . 147
B.1 Investigation of requirements for a traverse system for the Göttinger wind tunnel of the ISTM and the resulting influence on flow measurements . . . 147
B.2 Development and commissioning of a scale model of the ISTM closed circuit wind tunnel . . . 147

B.3 Development and validation of a simulation of the flow in the scale model of the Göttinger wind tunnel . . . 147
B.4 Testing of optimisation measures on the scale model of the closed return wind tunnel at ISTM . . . 148
B.5 Testing of improvement measures at the nozzle outlet of the Göttinger wind tunnel at ISTM . . . 148
B.6 Investigation of collector improvement measures at the scale model of the Göttinger Wind Tunnel at ISTM . . . 148
B.7 Testing of two new collectors with breather gap to improve the flow at the closed-circuit wind tunnel at ISTM . . . 148
B.8 Development and Validation of a distributed Measurement System for a Modal Analysis of the Göttinger Windkanal . . . 149
B.9 Design and measurement of a Helmholtz resonator for the Göttingen wind tunnel at ISTM . . . 149
B.10 Aufbau und Verifikation von RANS-Simulationen für Flügelprofile mit turbulenter Grenzschichtkontrolle in kompressibler Strömung . . . 149
B.11 Effects of active flow controls on different airfoils with focus on laminar airfoils . . . 149
B.12 Numerical parametric analysis for flow separation on aerofoils induced by active flow control . . . 150
B.13 Numerical Research of Wind Tunnel Wall Corrections for Boundary Layer Control Experiments . . . 150
B.14 Measurement of Turbulent Boundary Layers via PIV . . . 150
Reference to Student Contributions . . . 150

C Appendix: Airfoil Specifications . . . 153

D Appendix: Airfoil Test Rig Properties . . . 173
Reference to Datasheets . . . 176

1 Introduction

1.1 Motivation

Flow control on airfoils has been a research topic from an early stage of aviation history and is becoming ever more important for further efficiency increase [65]. First thoughts on aircraft performance enhancement by active separation control date back to the 1920s and 1930s [121] whilst the idea of the corresponding boundary layer suction control originates from the first studies on boundary layer theory by Prandtl in 1904 [99].

Later it was understood that boundary layer suction could also delay the transition process from laminar to turbulent boundary layers. With this, a performance enhancement by skin friction reduction can be achieved. Although the first studies on this were conducted in the middle of the 20th century (e.g. [42]), it is still one of the most active fields of research on active flow control in aviation [8, 120]. Commercial adaption just started in recent years, e.g. by Boing on the tailplane of the B787 Dreamliner [60].

Despite the large drag reduction potential of laminar flow control, the transition to turbulent boundary layers cannot be or is not intended to be avoided indefinitely. This also includes aviation use cases. The corresponding skin friction of turbulent boundary layers is one of the major contributions of total aircraft drag [20]. Therefore, turbulent boundary layer skin friction drag reduction has been an active field of research for decades [144, 125]. It can be divided into passive and active methods. Passive control strategies are features set up before operations without any power or mass flux input upon operation, such as riblets [136]. On the other hand, active methods do require additional effort during operations such as additional energy, fluid, or both. Yet, the prospect of performance enhancement of many active control concepts is significantly larger than that of passive methods.

Wall parallel blowing achieves performance enhancement by local and temporal friction drag increase and subsequent separation control [135, 87, 112] which is linked to significant lift increase for aircraft. This allows for a reduction of wing area for a given mission profile which in turn reduces the overall friction drag of the aircraft. High-frequency wall normal blowing and suction can also act as a high-lift device [4, 146, 33, 149]. In contrast, wall-normal uniform blowing aims at reducing the friction drag directly. First studies investigated the idea in the 1950s [81, 55, 122]. However, back at the time the coinciding effect of heat transfer reduction gained more focus [83] as it enabled an increase in aircraft engine efficiency and rocketry. Numerical efforts on the friction drag reduction in turbulent boundary layers by uniform blowing were first conducted via Direct Numerical Simulations (DNS) in the 1990s [128, 92]. The focus was on turbulence properties and friction drag reduction. Also, the physics of decreased heat transfer due to blowing was investigated numerically [74]. In contrast to numerically feasible uniform blowing, experimental implementations require a porous surface which unavoidably leads to non-uniformities in the wall-normal velocity. Therefore, the term microblowing technique has been introduced [47]. In contrast to uniform blowing, microblowing has the finite character of a flow through a porous surface which results in a non-uniformity at small scales. Extensive experimental studies on canonical flows with

microblowing were done by Hwang [47] with a focus on drag reduction in compressible and incompressible flows for different surface properties. Further numerical studies explored the friction drag reduction potential [51, 52, 53, 127] and the underlying physics within the turbulent boundary layer subject to uniform blowing. Similarly, experimental studies on flat plates were conducted to obtain turbulence properties as well as an estimate of total drag reduction based on the measured friction drag reduction [58]. On a path to more realistic flow scenarios, newer studies aimed at increasing the Reynolds number both in numerical simulations [7] and experimental campaigns [35, 43]. Also, several studies started looking at airfoil flows in an attempt to close in on realistic flow scenarios and reported potential in terms of drag reduction [31, 59, 46, 57, 88, 82].

1.2 Research Objective and Outline of Study

In summary, many studies in the field addressed the working principle and the physics behind skin friction drag reduction, mostly in canonical flows. It was also tried to derive answers on the global or net drag reduction potential apart from the local skin friction drag reduction. Details on the current state of the art as well as the necessary fundamentals are summarized in chapter 2. However, no definite and general conclusions could be reached for various reasons. Yet, as Spalart & McLean [125] pointed out, this is a crucial step in advancing the understanding and adoption of a flow control scheme, which leads to the research question for the present thesis:

What drag reduction or net drag reduction can be achieved for a real-world flow scenario such as airfoil flows using uniform blowing?

To answer this question a reasonable metric for the net drag reduction will be defined which respects the main expenses during operation of uniform blowing or microblowing, respectively. This must be done in the most generalized way possible without actually introducing a specific support system implementation. Therefore, in chapter 3 both the momentum balance as well as the energy budget are investigated for a flow with mass injection perpendicular to the mean flow direction.

Airfoil flows pose a problem of a vast parameter space which has to be explored to avoid finding case-specific answers only. However, it is impossible to find a general conclusion with experiments only due to limited resources. Therefore, in chapter 4 numerical Reynolds-Averaged Navier-Stokes (RANS) simulations are employed to identify conditions and settings in which uniform blowing can reduce drag or increase the performance of airfoils.

Several uncertainties arise from the necessary assumptions made for the numerical simulations. Hence, in chapter 5 experimental investigations are employed to validate the results. The focus is laid on several subsequent research objectives: Is it possible to reproduce the trends predicted by RANS with a reasonable physical implementation? This is uncertain in two aspects. For one, RANS simulations are inherently inaccurate when it comes to adverse pressure gradient boundary layers [77, 76]. Yet, these flow regions dominate the performance an airfoil achieves. Additionally, the presence of wall-normal blowing violates the underlying assumptions of the applied turbulence models although there have been methods proposed to account for that [142, 45]. More uncertainty in this regard results from the fact that the physically possible representation of uniform blowing is the microblowing technique. It is of interest if there is a systematic performance difference that can be associated with the difference between uniform blowing and microblowing. In addition to that, the experiment can answer the question of the effort to inject mass flux through a surface which is one of the driving factors of aforementioned expenses to operate the control scheme. It therefore impacts the conclusions about the net drag reduction potential. Chapter 6 concludes

this thesis and provides an overview of the found insights in respect to the raised hypothesis and associated questions.

2 Fundamentals

This chapter comprises the relevant laws of physics in the context of the study's flow scenarios and analytical considerations (sections 2.1, 2.2 and 2.3) as well as the basics of numerical (section 2.4) and experimental (section 2.5) means to investigate such flow fields. Finally, literature on the current state of the art of flow control by wall-normal uniform blowing in turbulent boundary layers is given (section 2.6).

2.1 Governing Equations

Conservation of Mass The conservation of mass can be given in its differential form in *Eulerian Parametrization* [126, section 2.1]:

$$\underbrace{\frac{\partial \rho}{\partial t} + (\mathbf{u} \cdot \nabla)\, \rho}_{\frac{\mathrm{D}\rho}{\mathrm{D}t}} + \rho \nabla \cdot \mathbf{u} = 0 \tag{2.1}$$

The bold symbols with serifs mark all tensor quantities in symbol notation, such as tensors of first rank (vectors) and second rank. For the present study, the flow is assumed to be incompressible, which means that the material derivative of the density ρ vanishes ($\frac{\mathrm{D}\rho}{\mathrm{D}t} = 0$). This means that the divergence of the velocity $\mathbf{u}$ is zero:

$$\text{general formulation:} \quad \nabla \cdot \mathbf{u} = 0 \tag{2.2}$$

$$\text{cartesian coordinates:} \quad \frac{\partial u_i}{\partial x_i} = 0 \tag{2.3}$$

Note the use of *Einsteins Summation Convention* for the index notation variant of the formulas. The dot product of two vectors is defined as $\mathbf{a} \cdot \mathbf{b} = \mathbf{a}^T \mathbf{b} \rightarrow a_i b_i$ in an orthogonal base such as the aforementioned cartesian coordinates [1, section 2.4.1].

Conservation of Momentum The momentum balance (Newton's First Law) can be combined with the constitutive equation of a fluid. For the present (and common) case of a *Newtonian Fluid*, the internal shear stress tensor $\boldsymbol{\tau}$ is proportional to the symmetric portion of the velocity gradient $\nabla \mathbf{u}$. The material property that describes this proportionality is the dynamic viscosity μ which has no directional (common assumption of isotropic fluid), nor shear rate dependency [118, section 1.2]:

$$\text{general formulation:} \quad \boldsymbol{\tau} = \mu \left(\nabla \mathbf{u} + \nabla \mathbf{u}^T \right) = \nu \rho \left(\nabla \mathbf{u} + \nabla \mathbf{u}^T \right) \tag{2.4}$$

$$\text{cartesian coordinates:} \quad \tau_{ij} = \mu \left(\frac{\partial u_i}{\partial x_j} + \frac{\partial u_j}{\partial x_i} \right) = \nu \rho \left(\frac{\partial u_i}{\partial x_j} + \frac{\partial u_j}{\partial x_i} \right) \tag{2.5}$$

The kinematic viscosity $\nu = \mu / \rho$ can be obtained based on the aforementioned dynamic viscosity and density of the fluid ρ. Including this material law, the momentum budget of an incompressible

Newtonian fluid can be formulated and is then called the incompressible Navier-Stokes equations [126, section 2.1]:

$$\text{general formulation:} \quad \frac{\partial \mathbf{u}}{\partial t} + (\mathbf{u} \cdot \nabla)\,\mathbf{u} = \mathbf{g} - \frac{1}{\rho}\nabla p + \nu\,(\nabla \cdot \nabla)\,\mathbf{u} \tag{2.6}$$

$$\text{cartesian coordinates:} \quad \frac{\partial u_i}{\partial t} + u_j \frac{\partial u_i}{\partial x_j} = g_i - \frac{1}{\rho}\frac{\partial p}{\partial x_i} + \nu \frac{\partial^2 u_i}{\partial x_j \partial x_j} \tag{2.7}$$

$\mathbf{g}$ describes a force per mass vector such as the gravitational acceleration $g_{zg} \approx 9.81 \frac{\mathrm{m}}{\mathrm{s}^2}$. p denotes the static pressure.

Gauss's theorem is [1, section 2.3.3]:

$$\iiint \nabla \cdot (...)\ \mathrm{d}\mathcal{V} = \oiint \mathbf{n} \cdot (...)\ \mathrm{d}\mathcal{A} \tag{2.8}$$

The surface $\mathcal{A}$ encapsulates the volume $\mathcal{V}$ and the vector $\mathbf{n}$ is a unity vector normal on $\mathcal{A}$ and points to the outside of the volume. The circle in the integral sign clarifies that $\mathcal{A}$ is a closed surface.

Since the Navier-Stokes equations hold at any point within the flow field, the integral of the equations over any control volume also holds. Employing Gauss's Theorem, the integral form can be rearranged such that all of its terms which include a divergence can be expressed on the boundaries of a control volume (such as a physical measurement setup or a cell of a numerical mesh). The momentum budget for a steady state, incompressible flow without any external forces per mass or forces concentrated in one point can be given based on equation 2.6 and 2.8:

$$\rho \oiint (\mathbf{u} \cdot \mathbf{n}) \cdot \mathbf{u}\ \mathrm{d}\mathcal{A} = \oiint -p\mathbf{n}\ \mathrm{d}\mathcal{A} + \oiint \boldsymbol{\tau} \cdot \mathbf{n}\ \mathrm{d}\mathcal{A} \tag{2.9}$$

Note, that the dot product of a tensor of second rank with a vector is defined as $\mathbf{A} \cdot \mathbf{b} \rightarrow A_{ij} b_j$ and $\mathbf{b} \cdot \mathbf{A} \rightarrow b_i A_{ij}$ for tensors expressed in an orthogonal base [1, section 2.4.1]. The dot product of a scalar with a vector/tensor is identical to a product of scalar and non-scalar quantity ($a \cdot \mathbf{A} = a\mathbf{A} \rightarrow aA_{ij}$ and $a \cdot \mathbf{b} = a\mathbf{b} \rightarrow ab_i$). Therefore, $\nabla \cdot p \equiv \nabla p = \mathrm{grad}(p)$ whereas $\nabla \cdot \mathbf{u} = \mathrm{div}(\mathbf{u})$ for a first rank tensor $\mathbf{u}$ and $\nabla \cdot \boldsymbol{\tau} = \mathrm{div}(\boldsymbol{\tau})$ for a second rank tensor $\boldsymbol{\tau}$.

Energy Balance For the present thesis, the conservation of energy can be simplified to the mechanical energy balance because neither chemical, thermal, radiation, etc. processes are relevant for the considered flow.

The momentum balance (eq. 2.6) can be expressed for a steady-state case without any forces per mass for a general fluid (not necessarily a Newtonian Fluid, similar to the integral form in equation 2.9):

$$\rho\,(\mathbf{u} \cdot \nabla)\,\mathbf{u} = -\nabla p + \nabla \cdot \boldsymbol{\tau} \tag{2.10}$$

Drela [28] proposes a concept for the energy budget based on the idea of expressing the mechanical power (temporal derivative of the energy) by $P = \mathbf{F} \cdot \mathbf{u}$, with $\mathbf{F}$ being a force vector. This can be applied to equation 2.10:

$$\rho\,((\mathbf{u} \cdot \nabla)\,\mathbf{u}) \cdot \mathbf{u} = -\nabla p \cdot \mathbf{u} + (\nabla \cdot \boldsymbol{\tau}) \cdot \mathbf{u} \tag{2.11}$$

The following algebraic transformations can be used to rearrange this equation [62, Appendix A]:

$$(\mathbf{u}\cdot\nabla)\mathbf{u} = (\nabla\times\mathbf{u})\times\mathbf{u} + \frac{1}{2}\nabla(\mathbf{u}\cdot\mathbf{u}) \tag{2.12}$$

$$((...)\times\mathbf{u})\cdot\mathbf{u} = 0 \tag{2.13}$$

$$\nabla\cdot(\boldsymbol{\tau}\cdot\mathbf{u}) = (\nabla\cdot\boldsymbol{\tau})\cdot\mathbf{u} + (\boldsymbol{\tau}\cdot\nabla)\cdot\mathbf{u} \tag{2.14}$$

$$\nabla\cdot(p\mathbf{u}) = \nabla p\cdot\mathbf{u} + p\nabla\cdot\mathbf{u} \tag{2.15}$$

The rearranged mechanical power balance reads (equivalent to Drela [28, eq. 29]):

$$\underbrace{\rho\nabla\cdot\left(\mathbf{u}\frac{1}{2}|\mathbf{u}|^2\right)}_{①} - \underbrace{\frac{\rho}{2}(\mathbf{u}\cdot\mathbf{u})\,\nabla\cdot\mathbf{u}}_{②(=0)} = \underbrace{-\nabla\cdot(p\mathbf{u})}_{③} + \underbrace{p\nabla\cdot\mathbf{u}}_{④(=0)} + \underbrace{\nabla\cdot(\boldsymbol{\tau}\cdot\mathbf{u})}_{⑤} - \underbrace{(\boldsymbol{\tau}\cdot\nabla)\cdot\mathbf{u}}_{⑥} \tag{2.16}$$

$|\mathbf{u}| = \sqrt{\mathbf{u}\cdot\mathbf{u}}$ is the *Euclidean norm*. This equation can be transferred to an integral form. The divergence terms can be recast using the Theorem of Gauss again (eq. 2.8). By this, the energy balance is expressed as a budget of energy flux (≡ Power) over the control volume boundaries and the meaning of the individual terms becomes clearer.

The kinetic energy of the flow into and out of the control volume is associated to the ① term:

$$\iiint \rho\nabla\cdot\left(\mathbf{u}\frac{1}{2}(\mathbf{u}\cdot\mathbf{u})\right)\,\mathrm{d}\mathcal{V} = \rho\oiint\frac{1}{2}|\mathbf{u}|^2\mathbf{u}\cdot\mathbf{n}\,\mathrm{d}\mathcal{A} \tag{2.17}$$

The ② term relates to the kinetic energy of a mass flow originating or dissolving within the flow field which does not exist based on the conservation of mass (divergence-free flow field, eq. 2.2).

The ③ term relates to the energy that stems from the pressure acting on the control boundary surfaces through which a volume flux passes ($\mathbf{u}\cdot\mathbf{n} \neq 0$). Note, that this concerns the outer perimeter of a control volume as well as boundary surfaces inside the outer perimeter. A control volume boundary can always be defined as one closed surface, no matter how many individual entities lie within the outer perimeter. This also includes regions where the control volume boundaries do not enclose any volume. An example of such surfaces are those that model the pressure rise enacted by pumps or propulsors.

$$\iiint -\nabla\cdot(p\mathbf{u})\,\mathrm{d}\mathcal{V} = \oiint -p\mathbf{u}\cdot\mathbf{n}\,\mathrm{d}\mathcal{A} \tag{2.18}$$

The ④ term relates to the power of the mechanical work of expanding the working fluid. Here, the flow is assumed to be incompressible. Therefore, this term vanishes which can be seen as it comprises the divergence of the velocity field ($\nabla\cdot\mathbf{u} = 0$, eq. 2.2).

The ⑤ term relates to the power associated with the friction on the control volume boundaries. The vector $\mathbf{t} = \boldsymbol{\tau}\cdot\mathbf{n}$ describes the viscous stress vector on the boundary surface. This power results from the wall shear stress on a moving body within the flow or, in general, the viscous stresses on all control volume boundary locations at which $\mathbf{t}\cdot\mathbf{u} \neq 0$. For example in a *Couette Flow* [126, section 6.1.1], the wall moving in flow direction provides a positive friction power to the flow whereas the wall at rest provides no friction power because $|\mathbf{u}| = 0$.

$$\iiint \nabla\cdot(\boldsymbol{\tau}\cdot\mathbf{u})\,\mathrm{d}\mathcal{V} = \oiint(\boldsymbol{\tau}\cdot\mathbf{u})\cdot\mathbf{n}\,\mathrm{d}\mathcal{A} = \oiint\mathbf{t}\cdot\mathbf{u}\,\mathrm{d}\mathcal{A} = P_{\text{friction}} \tag{2.19}$$

Lastly, the ⑥ term relates to the viscous losses Ω within a control volume:

$$\iiint (\boldsymbol{\tau} \cdot \nabla) \cdot \mathbf{u} \, \mathrm{d}\mathcal{V} = \Omega \tag{2.20}$$

With this, the integral form of the mechanical energy balance can be given analog to Drela [28, eq. 30]:

$$\rho \oiint \frac{1}{2}|\mathbf{u}|^2 \mathbf{u} \cdot \mathbf{n} \, \mathrm{d}\mathcal{A} = \oiint -p\mathbf{u} \cdot \mathbf{n} \, \mathrm{d}\mathcal{A} + P_{\text{friction}} - \Omega \tag{2.21}$$

Considering a tube-like control volume along a streamline where all flow properties only depend on the streamwise position, equation 2.21 can be simplified with an inflow cross-section (A_0) and an outflow cross-section (A_1) of the control volume:

$$\frac{1}{2}\rho u_1^2(u_1 A_1) + p_1(u_1 A_1) - \left(\frac{1}{2}\rho u_0^2(u_0 A_0) + p_0(u_0 A_0)\right) = P_{\text{friction}} - \Omega \tag{2.22}$$

Mass conservation of an incompressible flow (constant volume flow rate: $\dot{V} = A_1 u_1 = A_0 u_0$) can be applied to this for any choice of a control volume along the tube around the streamline. Therefore, this power balance can be expressed at any point χ on this streamline. The *Law of Bernoulli* is obtained when the power balance is divided by the volume flow rate. If no power is transferred along the boundaries of the control volume ($P_{\text{friction}} = 0$) and no viscous losses are present within the control volume ($\Omega = 0$), the Law of Bernoulli reads:

$$\frac{\rho}{2}u(\chi)^2 + p(\chi) = p_t(\chi) = \text{constant} \tag{2.23}$$

In such loss-free form, the total pressure p_t is constant along the streamline.

If viscous losses are present that stem from shear within the flow domain, the viscous loss power Ω results in a total pressure loss from control volume inflow (χ_0) to control volume outflow (χ_1):

$$p_t(\chi_0) - p_t(\chi_1) = \frac{\Omega}{\dot{V}} = \Delta p_{\text{loss}} \tag{2.24}$$

Note that the total pressure loss obeys $\Delta p_{\text{loss}} \geq 0$ due to the *Second Law of Thermodynamics*. This relation is enforced by a proper modeling of the material properties in the constitutional equations. This *e.g.* means that the viscosity cannot be negative for the present example of a Newtonian Fluid.

If an external power source (*e.g.* pump) or sink (*e.g.* turbine) P_{ext} exists along the streamline within the control volume, the total pressure can be increased ($\Delta p_{\text{ext}} > 0$) or decreased ($\Delta p_{\text{ext}} < 0$):

$$p_t(\chi_1) - p_t(\chi_0) = \frac{P_{\text{ext}}}{\dot{V}} = \Delta p_{\text{ext}} \tag{2.25}$$

Helmholtz's First Vortex Theorem The first Helmholtz theorem states that the *circulation* Γ or *vortex strength* is constant along a vortex tube in an inviscid flow field, hence a vortex tube cannot end [126, section 4.2.3]. The infinitesimally thin vortex tube is called vortex filament for which the same statement holds. In other words, the circulation Γ that stems from a vortex filament is constant, no matter how or where the loop $\mathcal{C}$ is placed.

$$\oint \mathbf{u} \cdot \, \mathrm{d}\mathbf{x}_{\mathcal{C}} = \Gamma = \begin{cases} \text{constant}, & \text{for any loop } \mathcal{C} \text{ through which the vortex filament passes once} \\ 0, & \text{for any loop } \mathcal{C} \text{ through which the vortex filament does not pass} \end{cases} \tag{2.26}$$

Potential Flow For flow regions in which p_t is constant in any given direction the incompressible Navier-Stokes equations (eq. 2.6) as well as the conservation of mass (eq. 2.2) can be satisfied by a potential for the velocity [126, section 10]:

$$\text{general formulation:} \quad \mathbf{u} = \nabla\Phi \tag{2.27}$$

$$\text{cartesian coordinates:} \quad u_i = \frac{\partial\Phi}{\partial x_i} \tag{2.28}$$

Solutions of the velocity potential Φ fulfill the Laplace equation [126, section 10.3] which means multiple solutions of Φ can be super-positioned to form solutions of more complex problems. Elementary solutions for Φ relevant to the present study are summarized in table 2.1 similar to Zierep & Bühler [150, p. 88]. This means, that the challenge of solving a potential flow problem lies in finding a set of elementary solutions that — in superposition — satisfy all boundary conditions of a particular problem [150, p. 85] (discussed in sections 2.4.1, 5.3.3).

Elementary Flow Case	Potential that satisfies case	residual Force F_i
translational flow [126, eq. 10.60] – freestream velocity $U_{\infty,i}$	$\Phi = U_{\infty,i}x_i$	not applicable
point source at location $x_{0,i}$ [126, eq. 10.85] – strength $\dot{m}_s$ (source mass flux) – radius $r = \lvert x_i - x_{0,i}\rvert$	$\Phi = -\frac{\dot{m}_s}{4\pi}\ln r$	$F_i = 0$
point source in x_1-freestream [126, eq. 10.92] – freestream velocity U_∞ – radius r in (x_1, x_2)-plane	$\Phi = U_\infty x_1 - \frac{\dot{m}_s}{4\pi}\ln r$	$F_1 = -\dot{m}_s U_\infty$
potential vortex (x_1, x_2)-plane [126, eq. 10.195] – circulation $\Gamma = \oint u_i \, \mathrm{d}x_i$	$\Phi = \frac{\Gamma}{2\pi}\arctan\left(\frac{x_2}{x_1}\right)$	$F_i = 0$
potential vortex in x_1-freestream [126, adapted from eq. 10.255]	$\Phi = U_\infty x_1$ $+\frac{\Gamma}{2\pi}\arctan\left(\frac{x_2}{x_1}\right)$	$F_2 = -\rho U_\infty \Gamma$

Table 2.1: Elementary solutions for 2D potential flow cases within the x_1, x_2-plane

In case of discontinuities — such as a mass flow source — the solution is only valid for everywhere but the discontinuity location $x_{0,i}$. Furthermore, some elementary solutions in table 2.1 cause a residual force that has to be balanced by an external force to fulfill the momentum balance.

2.2 Turbulent Boundary Layers

Boundary layers mark the region within a flow field where viscous stresses due to shear exist such that the velocity changes from the shear-free freestream field to the boundary condition of zero velocity at the wall. The flow field within a boundary layer can either be laminar or turbulent. The latter shows random velocity fluctuations u_i' over time t [126, section 7.2]. The Reynolds

Decomposition (denoted by their first description by Reynolds [106]) can be used to separate these fluctuations from the time-averaged mean field:

$$\overline{x} = \frac{1}{t} \int x(t)\ \mathrm{d}t \tag{2.29}$$

$$u_i = \overline{u}_i + u_i' \tag{2.30}$$

With this, the Navier-Stokes equation (eq. 2.6) can be recast and time-averaged to obtain the *Reynolds-Averaged Navier-Stokes* (RANS) equation:

$$\rho \overline{u}_j \frac{\partial \overline{u}_i}{\partial x_j} = \rho \overline{g}_i + \frac{\partial}{\partial x_j} \left[-\overline{p}\delta_{ij} + \mu \left(\frac{\partial \overline{u}_i}{\partial x_j} + \frac{\partial \overline{u}_j}{\partial x_i} \right) - \underbrace{\rho \overline{u_i' u_j'}}_{\text{Reynolds Stress Tensor}} \right] \tag{2.31}$$

The *Kronecker delta* is defined as $\delta_{ij} = 1\ \forall i = j \cup 0\ \forall i \neq j$. The RANS equations describe the momentum transport due to time-averaged quantities and the effective (time-averaged) influence of the fluctuations. The fluctuations u_i' do not need to be calculated directly, though. Instead, they appear only as the so-called *Reynolds-Stress Tensor* $\rho\overline{u_i' u_j'}$. Overall, six unknowns $\overline{u_i' u_j'}$ ($\overline{u_i' u_j'} = \overline{u_j' u_i'}$) are introduced in comparison to the original Navier-Stokes Equations. The six Reynolds stresses reflect the mean momentum transport due to fluctuations. The momentum contribution of the Reynolds stress tensor is small on a global scale for most cases which justifies neglecting it for integral momentum balances performed throughout this study [131]. Yet, it has a sizable impact on the mean velocity fields of TBL. Its modeling will therefore be discussed in more detail in section 2.4.

From the mean velocity profiles, the thickness of the turbulent boundary layer (TBL) can be expressed in different forms, depending on their physical meaning. They can be defined based on the wall-coordinate system x, y with x being the wall parallel coordinate, the time-averaged wall-parallel velocity $\overline{u}$ as a function of wall distance y and the velocity outside the boundary layer U_e. The simplest way is to define the thickness of the boundary layer based on the wall-normal coordinate y at which the mean velocity reaches 99% velocity outside the boundary layer U_e:

$$\delta_{99} = y(\overline{u} = 0.99 U_e) \tag{2.32}$$

The displacement thickness $\delta^\star$ and the momentum loss thickness δ_θ are more important quantities for the present study. [118, section 2.2]:

$$\delta^\star = \int_{y=0}^{\infty} \left(1 - \frac{\overline{u}}{U_e} \right)\ \mathrm{d}y \tag{2.33}$$

$$\delta_\theta = \int_{y=0}^{\infty} \frac{\overline{u}}{U_e} \left(1 - \frac{\overline{u}}{U_e} \right)\ \mathrm{d}y \tag{2.34}$$

Note, that the integration cannot go towards infinity if $U_e \neq U_\infty$. In that case the integration has to be bound to $y(\overline{u} \approx \overline{U_e})$.

The Navier-Stokes equations (eq. 2.6) can be simplified for the boundary layer [117, p. 191] and expressed in terms of the following boundary layer parameters: displacement thickness, momentum

thickness, and velocity outside the boundary layer to determine the wall-friction τ_w. This results in the *von Karman equation* [41]:

$$2\frac{\tau_w}{\rho U_e^2} + 2\frac{\overline{v}|_{y=0}}{U_e} = 2\frac{\mathrm{d}\delta_\theta}{\mathrm{d}x} + 2\frac{2\delta_\theta + \delta^\star}{U_e}\frac{\mathrm{d}U_e}{\mathrm{d}x} \tag{2.35}$$

$\overline{v}$ denotes the time-averaged wall-normal velocity. Alternatively, the wall friction τ_w can be expressed via the constitutive equation of a Newtonian fluid evaluated directly at the wall:

$$\tau_w = \mu\frac{\partial u}{\partial y}\Big|_{y=0} \tag{2.36}$$

In contrast to internal flows such as channel and pipe flows, turbulent boundary layers do not converge to a state of *e.g.* a constant boundary layer thickness. Yet, they can reach a developed state, where solutions further downstream become self-similar. A necessary condition for a TBL in a equilibrium state is that outside conditions stay self-similar as well, which can be determined by the *equilibrium parameter* β [126, section 12.5], sometimes also denoted *Clauser parameter*:

$$\beta = \frac{\delta^\star}{\tau_w}\frac{\partial \overline{p}}{\delta x} \tag{2.37}$$

For a developed TBL, characteristic mean velocity profiles can be given to which similar TBL collapse [98]. Self-similar solutions can be expressed using dimensionless quantities. Relevant quantities are the velocity u^+ and the wall distance y^+ in *Inner Scaling* or *Viscous Units* which refers to the normalization that depends on the viscous velocity u_τ:

$$u_\tau = \sqrt{\frac{\tau_w}{\rho}} \tag{2.38}$$

$$u^+ = \overline{u}\sqrt{\frac{\rho}{\tau_w}} = \frac{\overline{u}}{u_\tau} \tag{2.39}$$

$$y^+ = y\frac{u_\tau}{\nu} \tag{2.40}$$

Several regions within a TBL can be defined based on viscous units [98, p. 303]:

- *Viscous Sublayer* $y^+ \lessapprox 5$ Within this region $u^+ = y^+$ is satisfied. Reynolds stresses do not contribute significantly to the momentum transport to the wall.
- *Loglayer* $y^+ \gtrapprox 30$ and $y/\delta_{99} \ll 1$ Within this region $u^+ \approx \frac{1}{\kappa}\log(y^+) + B$ can be given. $\kappa = 0.41$ and $B = 5.2$ are constants. Reynolds stresses play a dominant role in momentum transport to the wall and therefore strongly affect how the velocity profile is shaped.
- *Buffer Layer* This is a blending region between the former two. Both viscous stresses and Reynolds stresses contribute to momentum transport to the wall and therefore influence how the wall-parallel velocity profile is shaped.

2.3 Airfoil Aerodynamics

This chapter shall be focused on aerodynamic effects and their fundamentals which are directly affected by the flow control scheme investigated throughout this thesis. This limits the discussion mostly to drag quantities and fundamentals of lift generation. For a broader view on incompressible aerodynamics consider Flandro *et al.* [37] or Raymer [103] which were also the basis for this section.

To generalize flow patterns around airfoils, the following parameters are of importance: The angle of attack (AoA) α describes the angle between the incoming freestream flow and the airfoil chord line:

$$\alpha = \arccos\left(\frac{\mathbf{U}_\infty \cdot \mathbf{X}}{|\mathbf{U}_\infty| \cdot 1}\right) \tag{2.41}$$

The chord Reynolds number describes the ratio of inertial forces to viscous forces in the context of an airfoil in a freestream:

$$Re_c = \frac{U_\infty c}{\nu} \tag{2.42}$$

with the freestream velocity U_∞ and the airfoil chord length c.

2.3.1 Lift

The lift can be interpreted as the reaction force F_l to the deflection of a fluid stream. By definition, it acts perpendicular to the incoming freestream. For a general airfoil shape the inviscid flow around it can be expressed as the superposition of many (or infinite) elementary solutions described in table 2.1. The choice of elementary solutions has to be such that the stagnation point streamlines coincide with the boundary of the inviscid flow field. For an entirely inviscid modeling of the flow field (without boundary layer or $Re_c \to \infty$) this boundary of the inviscid flow field is represented by the surface of the airfoil. In case viscous effects lead to the formation of a boundary layer, the inviscid flow field is displaced. Therefore, the displacement thickness added to the airfoil shape represents the boundary of the inviscid flow field which consists of the outer part of the flow around the airfoil [26]. In particular, for a 2D airfoil flow, the lift force results from the summed-up circulation Γ of all elementary solutions, which is called the *Kutta-Joukowski Theorem* [126, section 10.4.4]:

$$c_l = \frac{F_l}{q_\infty s c} = \frac{2\Gamma}{U_\infty c} \tag{2.43}$$

c_l denotes the dimensionless lift coefficient which is formed from the lift force normalized with the freestream dynamic pressure q_∞, the spanwise dimension s, and the chord length of the airfoil c.

2.3.2 Drag

By definition, drag is the resulting force on a body F_d in the freestream direction:

$$c_d = \frac{F_d}{q_\infty s c} \tag{2.44}$$

The drag coefficient c_d is the dimensionless drag that is formed with the same reference quantities as the lift coefficient.

Based on lift c_l and drag c_d the efficiency E of an aircraft (or airfoil) can be given by:

$$E = \frac{c_l}{c_d} \tag{2.45}$$

Several phenomena contribute to the total drag.

Viscous Drag This portion is caused by viscous effects, *i.e.* the formation of a boundary layer on the surfaces of the body. It can be subdivided into its friction portion which is the integral

quantity derived from the wall friction (eq. 2.36), hence it is called *friction drag* $c_{d,f}$. Equally, the pressure on the airfoil surface can be integrated resulting in both lift (normal to freestream) and the *pressure drag* $c_{d,p}$ (in freestream direction). It is important to note, that the pressure drag would be zero in an inviscid 2D flow. This is called the Paradox of d'Alembert (*e.g.* described by Drela [26]). The pressure drag of the viscous flow case results from the displacement effect by the boundary layers, not from the deflection of the flow.

Induced Drag For a finite wing, the circulation cannot be constant over span due to Helmholtz's first vortex theorem (see eq. 2.26). This causes an additional drag component on a finite wing which depends on the strength and distribution of circulation and therefore lift. It is thereby called *lift-induced drag* or *induced drag*. Physically, it acts on a wing section or airfoil by an increased pressure drag portion which is caused by a change of direction of the incoming flow due to the trailing vortex filaments.

Further Drag Sources Effects of compressible flows such as shocks can cause additional drag called *wave drag* on a body which acts in the form of a pressure drag and friction drag [36]. Due to the incompressible nature of the considered flow in the present study, these are not of further importance.

The interaction of flows around multiple surfaces sometimes causes interference drag [10]. This includes drag caused by flow phenomena like corner roller vortices that are not present if two intersecting shapes are investigated separately. It can manifest in locally increased friction or pressure drag. This gains some importance for the experimental design (section 5.2.2).

Quasi-Drag from additional power requirements If an additional system is introduced to the aerodynamic analysis, the drag analysis becomes a problem that is not limited to the force balance on a body. This problem has been intensively discussed in laminar flow control research for which the power requirements of pump systems play a significant role in the overall system performance analysis [8]. It could be concluded, that the power of the freestream airflow $P_{\mathrm{jet},\infty}$ is the relevant quantity to express auxiliary power requirements P_{aux} in a dimensionless form equivalent to a drag force:

$$c_{d,\mathrm{aux}} = \frac{P_{\mathrm{aux}}}{P_{\mathrm{jet},\infty}} = \frac{P_{\mathrm{aux}}}{q_\infty U_\infty \underbrace{sc}_{A_{\mathrm{ref}}}} \tag{2.46}$$

with the reference area A_{ref}, the freestream dynamic pressure q_∞ and velocity U_∞.

2.4 Numerical Techniques

The present study uses numerical fluid mechanics as a tool for different purposes. Yet, no methodical development in numerical fluid mechanics of turbulent flows is carried out. Therefore, this chapter is focused on the fundamental advantages and limitations of the utilized methods in the presence of wall transpiration. An extensive introduction to computational fluid mechanics is provided *e.g.* by Piquet [97], Maliska [71] and Wilcox [143].

2.4.1 Potential Flow Solver

Potential flow solvers find a flow field description by a finite number of elementary potential flow solutions that — in superposition — fulfill the boundary conditions of the problem (see section 2.1). The boundary element method is a typical concept to discretize the domain in which the elementary solutions are located on the boundaries of the flow field. This leads to a limited number of degrees of freedom to describe the whole flow field which makes this method exceptionally fast in computation. This approach is particularly well suited for an airfoil in freestream because the whole flow field apart from the boundary layers on the airfoil itself fulfill the assumptions of a potential flow field. Furthermore, elementary solutions have to be placed only where the airfoil is as this is the only entity in the whole flow field (This becomes more complicated if multiple boundaries exist in the flow field as it is the case for a wind-tunnel flow domain, see section 5.3.3). Over the last decades multiple implementations have been proposed, *e.g.* by Eppler ("Eppler Code" [29]) and Drela ("XFOIL" [26, 27]). The codes have in common that a boundary layer solver is used to determine the displacement the boundary layer causes to the inviscid flow by leveraging the displacement thickness $\delta^\star$ (see eq. 2.33). Recently, extensions have been proposed to also solve for flow fields with suction boundary layer control ("XFOILSUC" demonstrated *e.g.* by Prasannakumar *et al.* [101]) as well as a blowing boundary layer control ("sfoglie" by Reder [104]). However, such implementation can only solve for flow effects that are already known, as the boundary layer properties development (such as transition, shape factor, etc.) are forecast by empirical models and not solved directly [26].

2.4.2 Reynolds-Averaged Navier-Stokes (RANS) Simulations

Physical Model RANS simulations are based on the Reynolds-decomposition (eq. 2.30) and subsequent application to the Navier-Stokes Equations (eq. 2.31). Several models exist to achieve closure, *i.e.* solving for the newly introduced Reynolds-Stresses. The so-called *Boussinesq Approximation* [98, p. 93, eq. 4.45] in which the *eddy viscosity* ν_t is introduced is used commonly. Such models are therefore called eddy viscosity models.

$$-\overline{u_i' u_j'} = \nu_t \left(\frac{\partial \overline{u}_i}{\partial x_j} + \frac{\partial \overline{u}_j}{\partial x_i} \right) - \frac{2}{3} k \delta_{ij} \tag{2.47}$$

The Reynolds-Stresses $-\overline{u_i' u_j'}$ are calculated from the apparent increase in momentum transport that the additional viscosity ν_t causes. The kinetic energy of these fluctuations — the *turbulent kinetic energy* (TKE) k — is represented by the trace of the Reynolds-Stress Tensor. This reduces the amount of unknown field values to those which are needed to determine the eddy viscosity. Multiple models exist that capture the turbulence properties differently for different flow scenarios [142, 124, 76]. These have in common that the concept of eddy viscosity is a simple and small effort in calculation yet it is limited in accuracy for many off-calibration flow scenarios, especially adverse pressure gradient boundary layer flows. This leads to inevitable inaccuracies in the prediction of adverse pressure gradient boundary layer flows. Even more uncertainty is introduced the more different the flow scenario is from the calibration test cases (test cases described by *e.g.* Savill [115]), for example, if wall normal flow is present. Some corrections have been described in the literature to mitigate this effect [142, 76, 21] for the group of $k\omega$-based eddy viscosity models. Yet, the difference to classical formulations is small [21] and the general problem persists that eddy viscosity models can cause significant errors in the prediction of turbulent boundary layers in adverse pressure gradient conditions [78].

2.4.3 Large-Eddy Simulations (LES)

Large-Eddy Simulations (LES) will be used in the present study as a means of validation of RANS simulations. In contrast to RANS, LES simulations resolve large turbulence structures directly both in time and space [95]. This is because such eddies and vortices are strongly affected by the specific conditions of a flow and contain most of the fluctuation energy. Smaller structures are still modeled but with simpler models which are deemed more general than RANS-models. These properties allow for a reliable simulation of difficult, off-calibration conditions like they are present for this study. The high resolution has the downside of high computational cost compared to RANS simulations. This limits the scales which can be spanned. Either (or both) the Reynolds number has to be limited and/or the macroscopic scale of the domain — the distance of an applicable far-field boundary — is quite limited.

2.5 Experimental Techniques

Similar to previous sections the focus shall be on the fundamentals of the necessary techniques for the present study. A more comprehensive introduction to the showcased techniques is provided by Nitsche & Brunn [86]. Tropea *et al.* [132] give a more complete description of available flow measurement techniques.

Generally speaking, the advantage of experimental investigations in comparison to numerical investigations lies in the ability to resolve complex flow scenarios such as high Reynolds Number TBL over many scales both in space and time. The disadvantage lies in the challenge to observe theses results accurately (section 2.5.3 and 2.5.4) and account for systematic and stochastic errors (sections 2.5.2.1, 2.5.2.2).

2.5.1 Statistical Methods

2.5.1.1 Low Order Moments

Multiple statistical moments can be defined to reduce the data from a large sample count (*e.g.* in space or in time) to a representative value of this set [107, section 4.2]:

- A simple unweighted average over all n samples of a time series (identical to the continuous time average in equation 2.29) is used to express the *mean* of a dataset x:

$$\overline{x} = \frac{1}{n}\sum_{i=1}^{n} x_i \tag{2.48}$$

- The *standard deviation* of a population is the root of the variance as given by Rice [107, section 4.2]:

$$\widetilde{x} = \sqrt{\mathrm{var}(x)} = \sqrt{\frac{1}{n}\sum_{i=1}^{n}(x_i - \overline{x})^2} \tag{2.49}$$

  Rice [107, section 6.3] also highlights the use $n-1$ as the denominator which results in the *sample variance* (and the *sample standard deviation*). The difference lies in the nature of the dataset which the variance is calculated from. If the dataset x describes the whole population of data of which the variance is to be calculated then the population variance as

given in equation 2.49 represents the desired quantity. If the dataset x is just a subset of the data population of which the variance is requested, then the sample variance of x gives an estimate of the variance of the whole data population. Note the ambiguous use of the word *sample* which in this context refers to a general subset of data (with n data points) whereas in data acquisition-related context (see section 5.2.8) it refers to a single data point of a measurement series (which is technically also a subset of a population but limited to a single probing event).

For a binomial (normal) data distribution, approximately 68.2% of all samples (in the data acquisition sense) fall within plus/minus the standard deviation from the mean. For the present thesis, the data cannot be expected to be exactly normal-distributed. Still, the standard deviation gives an impression of the spread.

- Skewness is a measure of how a variable distribution deviates from a symmetric distribution around the mean value.
$$\gamma_m = \frac{\frac{1}{n}\sum_{i=1}^{n}(x_i - \overline{x})^3}{\widetilde{x}^3} \tag{2.50}$$
Arnold & Groeneveld [5] provide an overview of alternative measures of skewness such as the non-parametric skew:
$$x^\star = \frac{\overline{x} - \mathrm{Median}(x)}{\widetilde{x}} \tag{2.51}$$
This measure of skewness is chosen for the present thesis as it indicates the location of the median of the dataset (see section 5.4).

2.5.1.2 Correlation Methods

Covariance is a measure of the joint variability of two variable sets and is defined like this [107, section 4.3]:
$$\mathrm{Cov}(x, y) = \mathrm{Exp}\left((x_i - \mathrm{Exp}(x))\,(y_i - \mathrm{Exp}(y))\right) \tag{2.52}$$
Exp() is the expectation operator which, for the present purpose, can be interpreted as the mean of a population (see eq. 2.48). With this, the covariance of two datasets x and y is:
$$\mathrm{Cov}(x, y) = \overline{(x_i - \overline{x})(y_i - \overline{y})} \tag{2.53}$$
Instead of expressing the covariance for the whole sequence (which is a scalar, note Einstein's summation rule in eq. 2.53), it is also possible to express the covariance of each x_i with each y_j. This spans two dimensions n_x, n_y which is why this is then called the *cross-covariance matrix* [107, section 14.4.1]:
$$\mathbf{C}_{xy} = \mathrm{Cov}(x_i, y_j) = \overline{(x_i - \overline{x})(y_j - \overline{y})} \in \mathbb{R}^{n_x \times n_y} \tag{2.54}$$
If x_i and y_i are scalars then the average of the trace of the cross-covariance matrix is the covariance from equation 2.53 again. If the cross-covariance matrix is formed from the set x with itself then the resulting matrix is called *auto-covariance matrix* or simply *covariance matrix* [107, section 14.4.1]:
$$\mathbf{C}_{xx} = \mathrm{Cov}(x_i, x_j) = \overline{(x_i - \overline{x})(x_j - \overline{x})} \in \mathbb{R}^{n_x \times n_x} \tag{2.55}$$

x_i can also be a set of scalars (*e.g.* a timeseries with m entries, hence the set x is actually a matrix $\mathbf{X} \in \mathbb{R}^{n_x \times m}$):

$$\mathbf{C}_{xx} = \overline{\left(X_{ik} - \underbrace{\frac{1}{m}\sum_{q=1}^{m} X_{iq}}_{\mathrm{Exp}(X_i)} \right)\left(X_{jk} - \underbrace{\frac{1}{m}\sum_{q=1}^{m} X_{jq}}_{\mathrm{Exp}(X_j)} \right)} = \underbrace{\frac{1}{m}\mathbf{X}\cdot\mathbf{X}^T}_{\mathrm{Exp}(\mathbf{X}\cdot\mathbf{X}^T)} - \underbrace{\underbrace{\overline{X_i}}_{\mathrm{Exp}(X_i)} \cdot \underbrace{\overline{X_j}^T}_{\mathrm{Exp}(X_j)}}_{=0 \forall \overline{X_i}=0} \in \mathbb{R}^{n_x \times n_x} \quad (2.56)$$

The covariance preserves the unit and scaling of the variable sets x and y. In many cases, it is more useful to have a normalized expression for the joint variability which is obtained with the so-called *correlation coefficient* [107, section 4.3]:

$$\mathrm{Corr}(x,y) = \frac{\mathrm{Cov}(x,y)}{\widetilde{x}\widetilde{y}} \quad (2.57)$$

The correlation coefficient becomes one, if all data points (x_i, y_i) lie on a monotonically increasing line, *e.g.* if $y \propto x$. Similarly, it becomes minus one if all data points (x_i, y_i) lie on a monotonically decreasing line. Data points that are only weakly correlated show a large spread to the best linear regression. In other words, x and y values show no systematic dependence on one another. The correlation can also be formed as a matrix similar to the cross-covariance matrix resulting in the *cross-correlation* of the datasets x and y.

The Proper Orthogonal Decomposition (POD) builds on the cross-correlation to find the main spatial patterns (eigenvectors $\mathbf{\Psi}_k$) that are strongly correlated within a time-resolved signal and the scalar functions $a_k(t)$ which describe how present each spatial pattern is throughout the investigated time-interval [139]. It does not matter how many spatial dimensions are investigated and how they are distributed geometrically. For POD, all spatial probe points are gathered in a list. The spatial index n then becomes one dimension of the snapshot matrix $\mathbf{K} \in \mathbb{R}^{m \times n}$ with m timesteps within the investigated interval. The covariance matrix $\mathbf{C}_{KK}$ of $\mathbf{K}$ can be formed in two ways. Since POD is interested in eigenvectors, it is ideal to build the covariance matrix such that it has the dimension of the smaller of the indices to reduce computational effort. For the present thesis, this is usually the timestep dimension m, therefore this POD variant is usually called snapshot POD [139].

$$\mathbf{C}_{KK} = \mathbf{K}\cdot\mathbf{K}^{\mathbf{T}} \in \mathbb{R}^{m \times m} \quad (2.58)$$

The spatial mode matrix $\mathbf{\Psi}$ is calculated from the eigenvectors of the covariance matrix $\mathbf{C}_{KK} \in \mathbb{R}^{m \times m}$ by:

$$\mathbf{\Psi} = \mathbf{K}^T \cdot \mathrm{eigVectors}\left(\mathbf{C}_{KK}\right) \in \mathbb{R}^{n \times k} \quad (2.59)$$

The spatial mode matrix $\mathbf{\Psi} \in \mathbb{R}^{n \times k}$ includes as many modes k as there are timesteps m and each of its k columns describes a spatial eigenvector with n entries. Each of the spatial eigenvectors in $\mathbf{\Psi} \in \mathbb{R}^{n \times k}$ can be normalized per mode $k \in [1, m]$ to obtain $\hat{\mathbf{\Psi}} \in \mathbb{R}^{n \times k}$. The time-coefficient function of the k-th mode $a_k(t)$ has m timesteps. Therefore, the set of all time-coefficient functions is a matrix $\mathbf{A} \in \mathbb{R}^{k \times m}$:

$$\mathbf{A} = \mathbf{K}\cdot\mathbf{\Psi} \in \mathbb{R}^{k \times m} \quad (2.60)$$

With this, each spatial mode k can be used to express its portion $\hat{\mathbf{K}}_k$ of the snapshot matrix $\mathbf{K}$ by:

$$\hat{\mathbf{K}}_k = \mathbf{A}_k \cdot \hat{\mathbf{\Psi}}_k^T \quad (2.61)$$

Naturally, the sum of all mode portions $\hat{\mathbf{K}}_k$ equals the original snapshot matrix $\mathbf{K}$ again:

$$\mathbf{K} = \sum_{k=1}^{m} \hat{\mathbf{K}}_k \tag{2.62}$$

2.5.2 Uncertainty Treatment

2.5.2.1 Systematic Errors

Systematic errors cause a persistent deviation of an experimental result from the true result. Therefore, they can also be categorized as *invariant error* [23, section 1-3.2]. Such persistent deviation can be caused by *e.g.* imperfections in the modeling of a numerical or physical experiment, such as model simplifications and physical restrictions or a persistent deviation of physical parameters from the intended/assumed ones. Systematic errors can be mitigated if their magnitude and sign can be determined. Calibration is a method to determine the systematic error of the acquisition hardware and analysis methods. However, even calibration is limited in accuracy due to the variance in the measurement of the calibrated system itself and the variance (and systematic) error of the calibration reference [23, section 1-3.5].

Apart from the calibration of hardware, systematic errors are largely driven by the test environment, *i.e.* the wind tunnel environment, which differs from the freestream environment by the existence of "not-so-far" far-field boundaries. A general and comprehensive overview of wind-tunnel corrections for a multitude of reference cases is given by Ewald [32].

The classical lift-correction deals with the problem that the boundary conditions at the edge of the wind-tunnel jet pose a different far field than the case with infinite far-field or the numeric representation of a far-field distance of *e.g.* $d_{FF} \approx 50c$ with the chord length c. Therefore, the streamlines at the wind-tunnel jet edge (wind tunnel walls in a closed test section, free shear layer in an open jet test section) have a different shape than in the freestream scenario [32]. Ewald [32, p. 2-14] gives a framework for applying lift correction between the wind-tunnel case and a 2D freestream but examples include closed test sections only. In the following, the correction between the wind tunnel case and a 2D freestream shall be derived based on the "approach of the images" as it is given by Ewald [32, p. 2-14]. The idea of defining the images is to find a set of potential elementary solutions which — in superposition — fulfill both the boundary conditions of the test section and the airfoil model. One can extract the change in the flow field which is induced by the

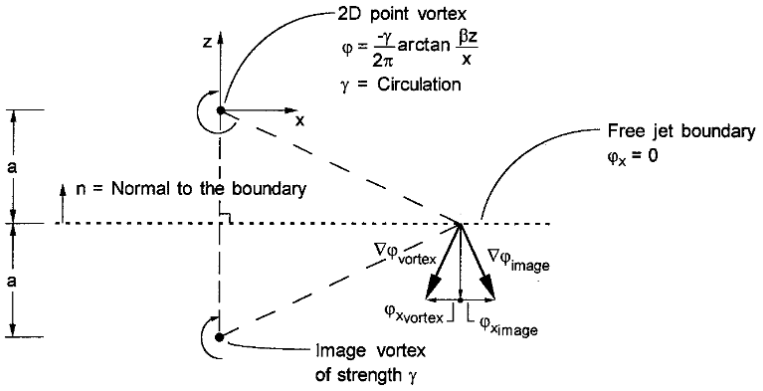

Figure 2.1: Principle of the images for closed and open 2D wind-tunnel sections [32, p. 2-11].

images excluding the influence of the model itself. This results in a function that describes how the

flow field seen by the model differs from that in free flight. This difference can be approximated as a different effective angle of attack α_{aero} which the airfoil would exhibit if it was not in a wind tunnel at the angle of attack α_{geom} but in free-flight with the same lift coefficient instead:

$$\alpha_{\text{aero}} = \alpha_{\text{geom}} + \arctan\Big(\frac{v_i(\overline{X}=0,\overline{Y}=0,\overline{Z}=0)}{U_\infty}\Big) \approx \alpha_{\text{geom}} + \frac{v_i(\overline{X}=0,\overline{Y}=0,\overline{Z}=0)}{U_\infty} \tag{2.63}$$

with v_i being the effective upwash created by the sum of the influence of all images i in the streamwise coordinate system images$\{\overline{\mathbf{X}},\overline{\mathbf{Y}},\overline{\mathbf{Z}}\}$. H describes the width of the jet which is identical to the distance of the images to one another.

	closed test section	open test section
Boundary	wall	shear layer
Interpretation	$u_{\perp\text{wall}} = 0$	$p_{\text{shear-layer}} = p_{\text{plenum}}$
potential theory	$\frac{\partial\phi}{\partial n} = 0$	$\frac{\partial\phi}{\partial\overline{X}} = 0$
neighboring image	$\Gamma_I = -\Gamma_M$	$\Gamma_I = \Gamma_M$

Table 2.2: Boundary conditions of closed jet and open jet and corresponding representations for the potential theory "approach of the images".

The general assumption for the 2D case is that the model induces a point vortex in the center of the test section (see figure 2.1). Similar to the model, any image of the model creates point vortices at their corresponding image position. The sign and strength of the image circulations are defined in such a way, that the boundary condition of the test section (table 2.2) is met. To counteract the influence of an image on the opposite wall/shear layer, an infinite series of potential images has to be defined. The main difference between the two test section types is that for the closed wall jet, an alternating image circulation pattern is present whereas for an open test section, the circulation of a single image Γ_I has the same sign as that of the neighboring image or the model itself (Γ_M). The strength of the circulation of a model (or a respective image) is given in equation 2.70:

$$\phi_m = -\frac{\Gamma}{2\pi}\arctan\Big(\frac{\beta_{Ma}\overline{Z}}{\overline{X}}\Big) \tag{2.64}$$

with: (2.65)

$$\Gamma = \frac{1}{2}U_\infty c_l c \quad | \quad \text{vortex strength} \tag{2.66}$$

$$\beta_{Ma} = \sqrt{1-Ma^2} \approx 1 \quad | \quad \text{compressibility parameter} \tag{2.67}$$

$$\xi = \frac{\overline{X}}{\beta_{Ma}H} \quad | \quad \text{dimensionless streamwise coordinate} \tag{2.68}$$

$$\zeta = \frac{\overline{Z}}{H} \quad | \quad \text{dimensionless out-of-plane coordinate} \tag{2.69}$$

$$\phi_m = -\frac{U_\infty c c_l}{4\pi}\arctan\Big(\frac{\zeta}{\xi}\Big) \tag{2.70}$$

The updraft v_i created by an image can be calculated from their potential:

$$v_i = \frac{\partial}{\partial z}\phi_I(\xi=0,\zeta=i|_{i=[-\infty,\infty],i\neq 0}) \tag{2.71}$$

For further processing, it is more meaningful to talk about the upwash parameter δ_0 which is a dimensionless form of the updraft v_i and its derivative which exclude the constants freestream velocity U_∞, chord length c and lift coefficient c_l:

$$\delta_0(\xi,\zeta) = \frac{v_i}{U_\infty}\frac{H}{c_l c} \tag{2.72}$$

$$\delta_1(\xi,\zeta) = \frac{\partial\phi_I(\xi,\zeta)}{\partial z}\frac{H}{c_l c U_\infty} = \frac{\partial\phi_I(\xi,\zeta)}{\partial\zeta H}\frac{H}{c_l c U_\infty} = \frac{\partial\phi_I(\xi,\zeta)}{\partial\zeta}\frac{1}{c_l c U_\infty} \tag{2.73}$$

	closed test section	open test section
upwash	$\delta_{0,\text{closed}}(\xi=0,\zeta=0)=0$	$\delta_{0,\text{open}}(\xi=0,\zeta=0)=0$
curvature	$\delta_{1,\text{closed}}(\xi=0,\zeta=0)=\frac{\pi}{24}$	$\delta_{1,\text{open}}(\xi=0,\zeta=0)=-\frac{\pi}{12}$
Lift curve	steeper than freestream	shallower than freestream
α_{aero}	$\alpha_{\text{aero}} > \alpha_{\text{geom}} \quad \vert \quad (c_l > 0)$	$\alpha_{\text{aero}} < \alpha_{\text{geom}} \quad \vert \quad (c_l > 0)$

Table 2.3: Upwash δ_0 and curvature parameter δ_1 of closed jet and open jet and corresponding representations for the potential theory "approach of the images".

As depicted in table 2.3 the upwash parameter δ_0 vanishes for both the open and the closed test section at the center of the circulation, hence where the model is. However, upstream and downstream the upwash is not zero, hence the streamwise gradient of the upwash parameter δ_0 can be formulated as streamwise curvature interference parameter δ_1 [32, p. 2-14]. This respects the fact that the actual model has a streamwise depth of chord length c which — due to the streamwise gradient of the upwash parameter — appears to be smaller for an open test section (larger for a closed test section). Consequently, the model experiences less lift (more lift for a closed test section) than in the corresponding freestream scenario. Hence, the corresponding freestream angle of attack α_{aero} for an open test section experiment appears to be smaller than the geometrical angle of attack α_{geom} (larger for a closed test section).

2.5.2.2 Random Errors

In contrast to their name, random errors are mostly not random but *variant* in a manner that is unpredictable to the experimentalist [23, section 1-3.2]. One origin of such error lies in the *standard uncertainties* $\mathcal{E}$ of all involved systems, such as sensors. This describes the uncertainty in a single measurement signal that includes all possible influences within the specified test conditions. Usually, measurement hardware manufacturers provide such information as well as a *combined standard uncertainty* as the general uncertainty information of their system (sensor, analog-digital converter, etc.). The influence of the uncertainty information of the subsystems can be combined in a combined standard uncertainty of the ultimate figure of merit of the experiment such as a drag quantity, *e.g.* through linear error propagation (section 2.5.2.3).

Apart from the accuracy limitation of the data acquisition (DAQ) hardware, there can also be random errors (or variant errors) associated with the physical domain of the experiment [23, section 1-3.2]. This involves *e.g.* uncertainties of material properties such as the working fluid air of the wind tunnel which may not be steady, especially over a long time such as days and weeks, despite changing so slowly that the experiment can still be considered steady-state in terms of flow physics. Synchronized measurement of such quantities (see section 5.1) can reduce their variant effect on the result as their influence becomes predictable to the experimentalist. Yet again, their variant effect on the result cannot be erased completely due to the standard uncertainty, that the

additional measurement hardware introduces. However, this additional uncertainty gets reduced if the measurement and processing chain stays *identical* throughout a measurement campaign as this reduces the source of uncertainty of changing hardware.

2.5.2.3 Linear Error Propagation

The standard uncertainty $\mathcal{E}_R$ (see section 2.5.2.2) of a result variable R depends on the values of all (n) influence quantities X_i (single sensors) and their respective uncertainty $\mathcal{E}_X$ [23, eq. 3.12]:

$$\mathcal{E}_R^2 = \sum_{i=1}^{n} \left(\frac{\partial R}{\partial X_i} \right)^2 \mathcal{E}_{X_i}^2 \tag{2.74}$$

Equation 2.74 implies that all single sensor readings are linearly independent or, in other words, their random errors (section 2.5.2.2) are uncorrelated. Therefore, the total uncertainty $\mathcal{E}_R$ can also be interpreted as the vector norm of n-dimensional orthogonal space in which each single error $\mathcal{E}_{X_i}$ is represented by an axis-parallel vector. It has to be noted that such correlation-free errors represent only an ideal case because, for the given measurement task of the present thesis, several sensor signals can show correlated uncertainties. One example is the cross-talk of multiple pressure reading channels [Els22] which are used to record the static pressure distribution around the airfoil (section 2.5.4). Therefore, linear error propagation can only give a rough estimate of how uncertainties propagate through the signal processing chain (section 5.5.1).

2.5.3 Point Measurement Techniques

The general concept of point measurements is that the quantity of interest or a derivative is measured as a scalar or vector quantity concentrated at one probe location. Thereby, it is assumed that the flow scenario provides this isolated value because this value is *e.g.* constant over the whole flow field or integrated over a certain region of the flow domain by a physical process. Also, higher order moments of time series, such as the deviation or the skewness of fluctuations u_i' (eq. 2.30) can be obtained from such signals.

Pressure Taps The concept of a pressure tap goes back to a basic assumption of boundary layers: The pressure at the wall equals the local static pressure of the flow field outside the boundary layer. Therefore, this pressure can be measured with a probe on the surface or through a hole small enough to not disturb the boundary layer flow. Nitsche & Brunn [86, p. 12] give correlations for accuracies based on the size of such pressure taps in viscous units (see eq. 2.38). Manufacturing limitations on one hand and the desire to be "as small as possible" on the other hand lead to a common diameter of such pressure taps of $0.3\text{mm} \lessapprox d_{\text{pTap}} \lessapprox 1\text{mm}$.

Prandtl Probe A very common probe to estimate the velocity is the Prandtl probe [86, p. 21]. It combines two pressure taps to retrieve the static pressure in a stagnation point and a point at which the outside velocity equals the velocity at infinity (infinity in this context means flow conditions identical to the flow conditions when the probe was not present). The difference of those pressures equals the dynamic pressure at the probe location as if there was no probe (see equation of Bernoulli, eq. 2.23).

Working Fluid Properties Usually, velocity measurements are even more important quantities than dynamic pressure. U_∞ can be calculated from q_∞ if the density ρ of the fluid is known. The density is constant for an incompressible flow over the whole flow domain and can therefore be calculated from point measurements at a random location within the flow. Several correlations are provided in literature to obtain density as well as the viscosity of air by measurement of temperature sensors, humidity sensors, and absolute pressure sensors [123, 129, 17] (see also methodology for the current study in figure 5.1).

Hotwire Velocimetry A high temporal resolution of velocity point measurements can be acquired with hotwires. A detailed description of a constant temperature hot-wire anemometer (CTA) is provided by Örlü & Vinuesa [151]. CTA allows for a frequency resolution well above 5kHz which enables the measurement of velocity fluctuations u_i' (compare eq. 2.30) in air flows. This allows for turbulence intensity and spectra measurements.

Force Sensors Force measurements are a classical example of how a structure within the flow is used to integrate the value of interest physically. Such integral value contains the resulting force of all pressures and stresses acting on the body of interest. Historically, the principle of balancing counterweights with the forces of interest was common, hence the name of force sensors applied in a wind tunnel: Balance. As such systems do not allow time-resolved measurements, they are considered outdated but their accuracy (roughly 1 in ten thousand of their full-scale [13, p. 36]) is high, also in nowadays standards. State-of-the-art sensor technology for wind-tunnel measurements consists of 4 general types [19]:

- **Resistive Strain gauge**. This is the industry standard for force sensors. Multiple foil-based strain gauges are connected as Wheatstone bridge to best amplify a deformation signal based on a change of the resistance of the strain gauge material which is directly attached to the deforming (strained) structure of the sensor. Such sensors have good long-term stability, including high-temperature stability (if used in a Wheatstone circuit layout). The downside is that the strain resolution is rather limited which means that the sensor structure has to be strained quite significantly which can be a problem both in terms of test rig stiffness as well as sensor fatigue, especially for applications with strong vibrations (which shall be measured).
- **Piezoelectric strain gauge** Such sensors are also very common, especially if high frequency and high stiffness measurements are required. As the measurement principle is to amplify a tiny charge which is generated by the deformation of the piezoelectric quartz the zero drift of such sensors is rather high due to leakage currents.
- **Surface Acoustic strain gauge** There is only limited availability of such sensors as the working principle is very much dependent on the test setup of which it measures the resonance frequency that depends on the strain. The advantage of a "wireless" measurement possibility is not of interest for the present measurement task
- **Fiber Optic strain gauges** This group of measurement principles is very common, especially the so-called Fiber Bragg-grating-based sensors. Their advantage lies in the possibility of including them in a test structure in such a way that the model itself becomes the sensor. It also allows for localized measurements in a single fiber. Calibration and temperature stability are challenging. Another handling challenge is associated with the limited bending radius which has to be kept for the whole fiber, not just the part within the structure.

2.5.4 Field Measurement Techniques

In contrast to point measurements, field measurements allow for a more comprehensive study of the flow field by means of capturing flow properties at multiple points within the domain simultaneously such that snapshot field information (1D, 2D, or 3D) becomes available.

2.5.4.1 Distributed Point Probes

Wake Rake Drag can be evaluated very accurately from the momentum deficit in the wake flow of a body for various scenarios (*e.g.* [94, 16, 67, 68]). For 2D airfoil flows simple methods were described by Betz [9] and (more commonly used) Jones [50]. Both methods give equal results if the measurement is taken at a moderate distance from the trailing edge of the airfoil [113, section 7.2.3]. One has to either traverse a Prandtl probe (point measurement) or use multiple probes (field measurement) in the wake plane which results in a so-called wake rake. The formula of Jones reads:

$$c_{d,W} = \frac{2}{c}\int_{-\infty}^{+\infty} \sqrt{\frac{p_{t,3}-p_3}{p_{t,\infty}-p_\infty}}\left(1-\sqrt{\frac{p_{t,3}-p_\infty}{p_{t,\infty}-p_\infty}}\right)\mathrm{d}\overline{Y} \tag{2.75}$$

c is the chord length. $\overline{Y}$ is the span-wise coordinate of the wake rake. In the wake rake plane (3), $p_{t,3}$ denotes the total pressure, and p_3 is the static pressure.

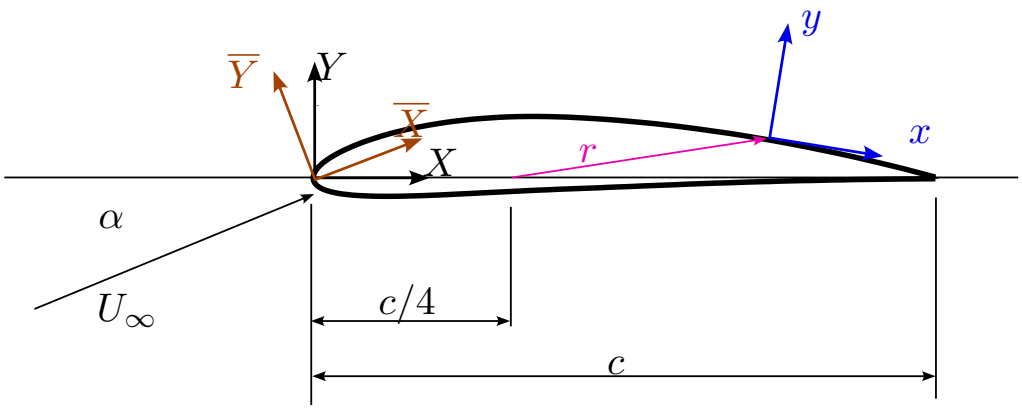

Figure 2.2: Relevant Vectors for Pressure Distribution Integration

Pressure Taps on Airfoils One major interest of an airfoil investigation lies in its pressure distribution, particularly localized phenomena such as separation. The integral quantities result from integrals around the whole circumference of the body. Note the three different relevant coordinate systems displayed in figure 2.2:

- $\{\overline{\mathbf{X}}, \overline{\mathbf{Y}}, \overline{\mathbf{Z}}\}$ This is the aerodynamic coordinate system. Its $\overline{\mathbf{X}}$-axis is parallel to the freestream velocity U_∞. Lift and Drag are axis-aligned to $\overline{\mathbf{Y}}$ and $\overline{\mathbf{X}}$ respectively.
- $\{\mathbf{X}, \mathbf{Y}, \mathbf{Z}\}$ This is the body-conform coordinate system. The airfoil chord line coincides with the $\mathbf{X}$-axis.
- $\{\mathbf{x}, \mathbf{y}, \mathbf{z}\}$ This is the wall coordinate system. The $\mathbf{x}$-axis corresponds to the tangent and the $\mathbf{y}$ axis to the normal direction of the wall at a respective position. The base point of the wall coordinate system is described by $[x_i, y_i, z_i]$.

The infinite formulation for the integral force $\mathbf{F_p}$ and torque vector $\mathbf{M_{p,c/4}}$ on the body can be given with:

$$\mathbf{F_p} = s \cdot \oint p\mathbf{y}\, \mathrm{d}\mathcal{C} \tag{2.76}$$

$$\mathbf{M_{p,c/4}} = s \cdot \oint p\mathbf{y} \times \mathbf{r}\, \mathrm{d}\mathcal{C} \tag{2.77}$$

with the spanwise dimension s, the airfoil perimeter $\mathcal{C}$ and the vector from the $c/4$ point to the location on the surface $\mathbf{r}$.

2.5.4.2 Particle Image Velocimetry

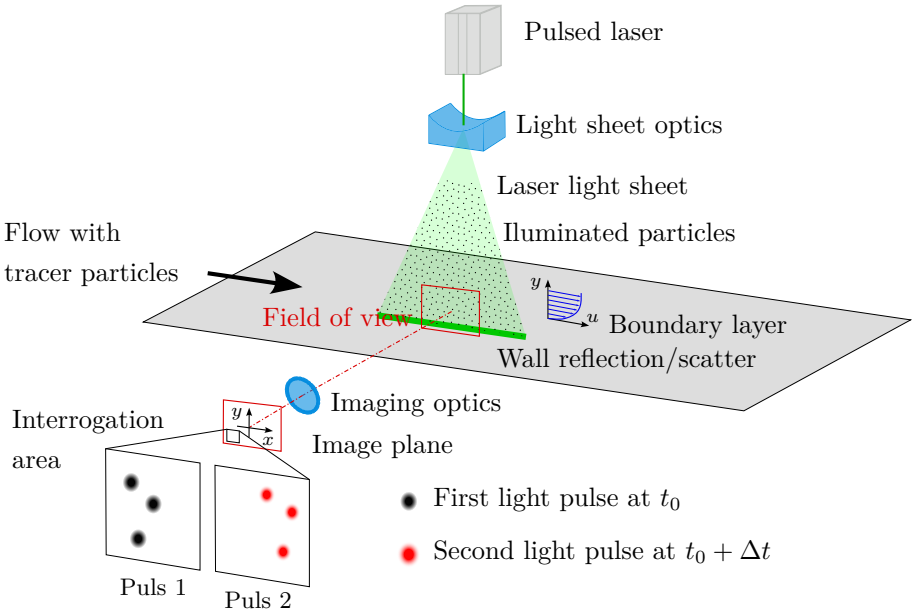

Figure 2.3: Experimental arrangement for planar 2C-2D PIV of a boundary layer flow. Inspired by [102, Fig. 1.9]

The main principle of Particle Image Velocimetry (PIV) is described according to Raffel *et al.* [102]. Figure 2.3 shows a schematic for the setup to measure 2 velocity components of a 2-dimensional field of view (2C-2D) of a boundary layer flow. Seeding particles are inserted into the flow for preparation. It is assumed that they follow the flow perfectly. This can be judged by the particle Stokes number Stk formed with the flow velocity u and a reference length l_c for which the boundary layer thickness and the local freestream velocity, *i.e.* the edge velocity U_e, are common quantities for turbulent boundary layer flow experiments [102, eq. 2.5]:

$$\mathrm{Stk} = \frac{t_p u}{l_c} \rightarrow \frac{t_p U_e}{\delta_{99}} \overset{!}{<} 0.1 \tag{2.78}$$

This Stokes number should be smaller than 0.1 for the particles to follow the flow acceptably [114]. t_p describes the response time of the particles which can be calculated from the density of the particle material ρ_p, the diameter of the particles d_p, and the dynamic viscosity of the working fluid, *e.g.* air, μ [102, eq. 2.4]:

$$t_p = \frac{\rho_p d_p^2}{18\mu} \tag{2.79}$$

A laser is used to illuminate the particles inside the Field of View (FOV) with two very short pulses. The short pulse ensures that no motion blur occurs. The time difference of the pulses Δt is used to express the displacement between the A-Frame (Puls 1) and the B-Frame (Puls 2) as velocity. The argument (shift in the x, y-plane) of the cross-correlation peak comparing the two frames of a given interrogation area (a subset of the image plane, *e.g.* 32x32 pixels) equals the aforementioned displacement. The displacement information is not limited to whole pixel steps but can be accurate to 1/10th of an integer pixel-shift if the particles illuminate more than one pixel with a Gaussian intensity distribution [102, section 5.3.5]. The principle of cross-correlation peak search means that the velocity field result contains one velocity vector per interrogation area. It is important to mention that this does not mean that the velocity vector of an interrogation area represents the average particle velocity within this region but only the argument of the cross-correlation peak. Such peak can also be caused by one very bright particle or, close to the wall, by bright light scattered from the wall. Furthermore, a velocity gradient within one interrogation area cannot be described by a simple cross-correlation peak search [63]. Instead, one random velocity (in other words: shift) will show the highest cross-correlation between frames. Velocity gradient flows therefore cause a large random error (see section 2.5.2.2) if the interrogation areas are large as well. Such problems can be treated with a so-called multigrid and multipass approach (figure

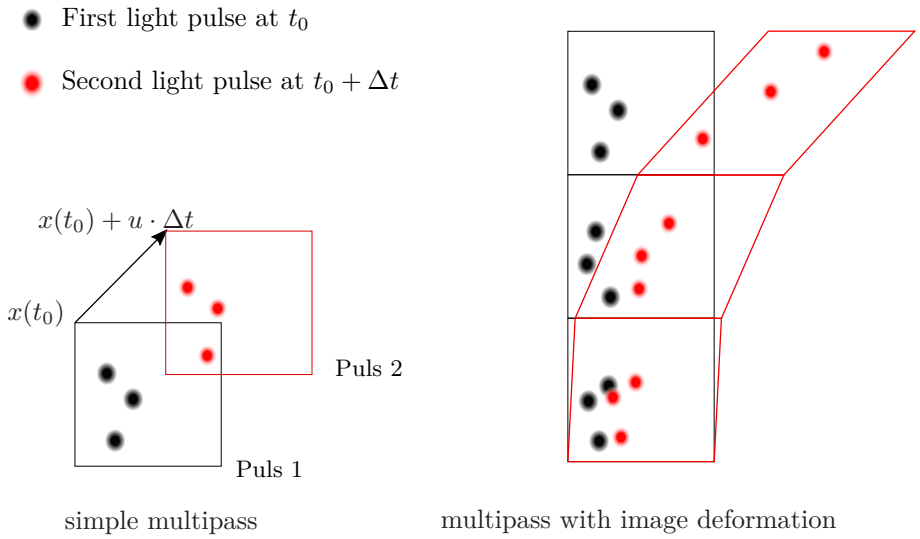

Figure 2.4: The shift and deformation of interrogation areas (squares) when using multipass and image deformation for multigrid algorithms. Inspired by [102, Fig. 5.22, 5.26]

2.4): The multipass procedure [102, section 5.3.4.1] uses predetermined velocity information (the source of this information becomes clearer further below) to shift the interrogation area to follow the flow when comparing A and B-frame (equivalent to the average material shift in between the two laser bursts of a frame pair). This keeps the particle patterns within this interrogation area roughly at the same location for the A and B-frame. Therefore, it is possible to find the correct displacement ($\equiv$ cross-correlation peak argument) even if the particles had displaced far beyond the size of the interrogation area. The multigrid procedure [102, section 5.3.4.1] improves the multipass method by starting the first evaluation with much larger interrogation areas. Thereby, it is possible to detect large shifts but the resolution of the velocity vector field is limited. In subsequent passes the interrogation areas are decreased until the desired final interrogation area size is reached. This results in a good resolution of the flow velocity vector field without losing the information of the large flow velocities (large shifts) thanks to the predetermined interrogation area shift. The multigrid/multipass procedure can be extended by not just including the average

shift of each interrogation area but also their deformation (equivalent to the material deformation in between the two laser bursts of a frame pair) [102, section 5.3.4.3]. This improves on finding the correlation peak of a flow with a strong velocity gradient, such as boundary layer flows. This would otherwise be difficult because in an interrogation area of a flow region with a velocity gradient, the particles experience different shifts which means there is not one but multiple correlation peaks resembling different particle velocities at different locations within one interrogation area. A deformation of the interrogation area allows the shear to be accounted for similar to the shift of the simple multipass procedure explained above. Again, the coarse grid evaluation results of earlier evaluation passes can be used as information about the deformation of the interrogation areas of subsequent steps with smaller interrogation area sizes.

In terms of the physical setup wall reflections have to be avoided. Otherwise, features of the wall appear like bright particles that do not move but shine so brightly that they also appear in interrogation areas that are above the wall. The correlation peak search will "lock" to such a strongly correlated pattern which results in zero displacement although there might be some fainter particles within the flow that do move. This means that reflective surfaces are less suitable for walls within the FOV and should be avoided if possible.

During postprocessing, the remaining static pixels/illumination can be reduced. One suitable method is to employ proper orthogonal decomposition (POD) [139] to remove temporally correlated illumination patterns [75]. This works for low-speed PIV because there is a "large" time interval (*e.g.* 1/10 of a second) in between subsequent frame pairs such that the flow has displaced far beyond the field of view. Therefore, the particle distribution of two subsequent frame pairs is completely uncorrelated whereas the location of light scattered from reflections is strongly correlated in between subsequent recordings because the wall has not moved except for deterministic body oscillation.

2.6 Skin Friction Drag Reduction by Flow Control

2.6.1 Passive vs. Active Control Strategies

Gad-el-Hak [38] collates flow control schemes to be either active or passive. Passive schemes are based on a predetermined set of features or properties of a flow boundary that do not require energy or mass input or any kind of feedback mechanism with a flow. Natural laminar flow airfoils [29, 133] fulfill this definition by designing the pressure gradient to delay transition. Riblets [136], vortex generators [14], or tripping devices [69] are examples of predetermined geometrical modifications that alter the state of the turbulent boundary layer or force transition in the first place.

In contrast, active flow control interacts with the flow either with (*reactive flow control*) or without (simply *active flow control*) knowledge of the current flow state [38]. One example of an active control is Laminar Flow Control (LFC) which employs suction to reduce growing instabilities which would lead to laminar-turbulent transition. The energy input required to operate the removal of the fluid via suction is significant and reduces the drag savings achieved by keeping the flow laminar [108]. For an aerodynamic flow, such additional power requirement can be expressed as an additional dimensionless drag quantity (see also eq. 2.46 and [8]). The reduction of the beneficial effects of the control due to the effort is a general property of active flow control schemes. The correct assessment of additional effort is not always straightforward, yet a crucial step to judge the *net drag reduction* potential for a complete system [125]. One way to reduce the parasitic impact of the effort is to leverage the combination of passive and active flow control strategies as it is done

e.g. for hybrid laminar flow control (HLFC) where the active control region is restricted to a small area and the remainder of the airfoil is shaped to enable natural laminar flow [148, 60, 120, 101]. Another strategy to reduce the parasitic impact of the control effort is to employ a temporal restriction of the control operation. This is done *e.g.* for synthetic jets which operate by alternating, wall-normal suction and blowing through a slit. This prevents flow separation in high-lift scenarios by creating strong vortex systems that increase momentum transport to the wall [33, 34, 54, 146, 4]. In contrast to LFC or HLFC, the temporal average of the control mass flux is zero, yet the energy effort is nonzero though limited to the time of near-stall flight situations. Periodic jets were also used to demonstrate a direct skin friction drag reduction when the slit orientation is in the streamwise direction [22].

2.6.2 Uniform Blowing in Turbulent Boundary Layers

Uniform blowing in turbulent boundary layers is an active scheme similar to synthetic jets in the sense that a wall-normal velocity is applied on the wall to change the properties of the turbulent boundary layer. In contrast to synthetic jets, the goal of uniform blowing is to reduce the momentum transport to the wall by introducing a continuous low-momentum wall-normal flux. In general, the effort of this scheme is the provision of the control mass flux. Depending on the local pressure level of the control additional energy may be required to operate the scheme.

Early investigations focused on the evolution of transfer coefficients (dimensionless quantities that describe a field quantity flux over the boundary, such as the wall shear stress or the heat transfer coefficient) for a flat plate laminar boundary layer subject to uniform blowing and suction. The general trend deduced from both theoretical [111] as well as experimental work [81] was that blowing reduces these transfer coefficients for both heat and momentum (friction drag c_f) transport. This could be extended also to turbulent boundary layers [11, 83, 122]. It was found that the reduction of heat transfer due to mass injection is mostly independent of the local pressure gradient whereas the wall shear within the control region strongly depends on the pressure gradient [110]. The evolution of the skin friction for different blowing ratios could be described and it could be confirmed that a significant reduction potential is present [55, 24]. Despite these local effects on the transfer coefficients, continuous uniform wall normal blowing was not adopted for drag reduction on industrial scope.

In the 1980s, the topic gained attention again through the theoretical optimization of a blowing and suction combination on a Joukowsky airfoil which was one of the first attempts to take the control scheme to more complex flow scenarios than flat plate boundary layers and channel flows [40].

With increasing computational power, numerical studies of the concept became popular, starting with LES simulations of channel flows subject to wall-normal blowing and suction [96]. DNS simulations of a similar setup confirmed the findings that the reduction of wall shear stress is in good accordance with the experimental data from literature [128]. The same could be found for turbulent boundary layer (flat plate) flow [92].

A new name — *micro blowing* or *micro blowing technique (MBT)* — was introduced by Hwang [47]. This was done to separate modern smooth injection surfaces from the rather rough surfaces from the experiments decades earlier. These smoother surfaces were achieved by laser drilling holes with a small diameter compared to the surface sheet thickness which enabled not only skin friction reduction compared to the uncontrolled case on the porous plate but also compared to an uncontrolled case on a non-porous surface. Hwang also identified the need to assess large-scale experiments to find answers to the penalty of operating the control scheme [47]. However,

subsequent experimental studies again focused on the boundary layer properties over permeable surfaces [58] again confirming large skin friction reduction potential. The cost of operating the scheme was regarded to be driven by pressure losses within the ducting system of the control device hence effort was focused on optimizing this internal flow. In a review of experimental studies by Kornilov [56], the general trends could again be confirmed: Local friction drag reduction can reach up to 90%, microblowing experiments and numerical studies mostly agree on the evolution of local wall friction despite the finite hole pattern in experiments and the uniform wall-normal velocity in simulations (apart from some small scale simulations of staggered hole patterns [66]) but there is no general answer on the effort to operate the supply system.

Meanwhile, more high-fidelity numerical simulations of spatially developing, turbulent boundary layers were carried out which identified the properties of the drag-reducing effects and the drag-increasing effects based on FIK identity [51]. Similar effects could be concluded for spatially intermittent blowing schemes [53] as well as the different streamwise sizes of blowing regions [52]. Importantly, it was also found that the friction drag-reducing effect persisted downstream of the blowing region [127] which favors total drag reduction as there is no additional effort for the drag reduction in the region downstream of the control.

In recent years research started to focus on applying uniform blowing on airfoils to obtain a more complex flow scenario as well as focusing on additional effects and penalties of the control scheme such as the still unsolved question of the supply effort. In a combined suction-blowing case, an increase in aerodynamic efficiency could be observed, yet the drag reduction was caused by the suction [59]. Also, an effort for the particular combined implementation could be formulated [57].

In a blowing-only control scheme on a ClarkY airfoil, the findings from canonical flows regarding local friction stress reduction could be confirmed [31]. However, the total drag of the airfoil determined by a wake survey increased which led to the conclusion, that an increase in pressure drag must have caused a total drag increase. This could be confirmed numerically, if blowing was applied on the upper side of an airfoil [AVF$^+$20]. Yet, for blowing on the lower side of an airfoil, a decrease in pressure drag as well as friction drag could be observed numerically.

The advantage of blowing on the lower airfoil side could also be shown in studies optimizing the control region location for aerodynamic efficiency E (eq. 2.45) [88, 89, 72]. Bayesian optimization for an optimal arrangement of blowing strength and location was also carried out for the simpler case of uniform blowing in a flat plate boundary layer which showed that an optimal control distribution could lead to drag savings including experimental power consumption data [70]. It could be shown that a passive blowing-suction scheme is feasible in practice [46] which eliminates the energy effort for the control system. Yet again, despite the confirmation of local friction drag reduction the total drag deduced from the wake increases.

Ultimately, all optimizations depend on a reliable, comparable quantity of effort to optimize for a true total drag reduction. Such *net drag reduction* is yet to be shown experimentally for an isolated blowing scheme despite numerous numerical studies showing strong aerodynamic drag reduction as well as experimental, theoretical, and numerical studies agreeing on local transfer coefficient reduction. It must also be noted though, that the term *net drag reduction* is used ambiguously in literature, despite all authors agreeing in the sense that they mean a drag reduction which could persist for a complete system implementation in practice.

3 Analytical Investigation on Drag Quantities with Uniform Blowing

3.1 Conservation Laws with Uniform Blowing

A complete analysis of the effort of BLC requires the analysis of all classical conservation laws. Hence, the subsections of this chapter consider the conservation of momentum and energy (section 2.1) in light of blowing BLC perpendicular to the main flow direction.

3.1.1 Momentum Balance

The momentum balance for an airfoil has been described by Fahland *et al.* [FAF+23]:

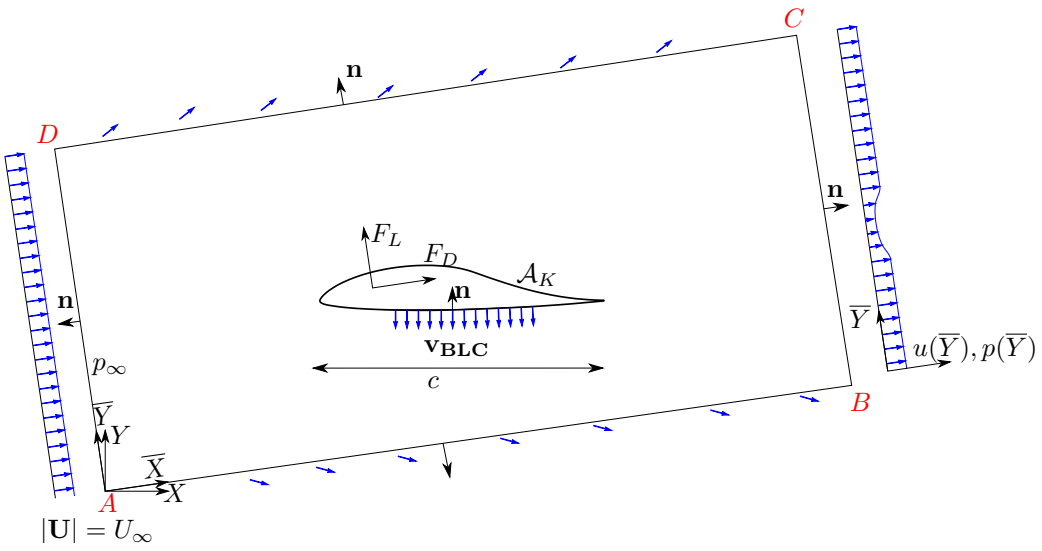

Figure 3.1: Control Volume (CV) for the airfoil momentum budget in which **n** is the normal vector pointing out of the CV. Adapted from [FAF+23]

From [FAF+23, section 2]: "We consider the integral momentum balance of a flow over a 2D airfoil with the control volume ABCD sketched in figure 3.1. As shown in the figure, the direction of the inflow and thus the direction of the drag force F_D coincides with $\overline{X}$. The corresponding normal direction and thus the direction of the lift force F_L is denoted by $\overline{Y}$. To allow for different angles of attack the orientation of the airfoil is described by a rotated coordinate system X, Y. Flow control due to wall-normal micro blowing on the pressure side of the airfoil is denoted by v_{BLC} and is assumed to be oriented in $\overline{Y}$-direction for small angles of attack. For the uncontrolled case $v_{\mathrm{BLC}} = 0$ applies. The control volume boundaries consist of the outer perimeter with the planes $\overline{AB}$ and $\overline{CD}$, aligned with the flow direction $\overline{X}$, and planes $\overline{BC}$ and $\overline{DA}$ which are parallel to $\overline{Y}$. At the wake survey plane $\overline{BC}$

we define a sampling coordinate s for pressure $p(\overline{Y})$ and velocity $u(\overline{Y})$. All other control volume boundaries are placed at a sufficiently large distance from the airfoil (e.g. $2/3c$ from the trailing edge [113, ch. 7.2.3]) such that the velocity component in $\overline{X}$-direction $u_{\overline{X}}$ and pressure p along these boundaries can be assumed to correspond to the inflow conditions at infinite distance upstream of the airfoil. The wetted surface of the airfoil is denoted by $\mathcal{A}_K$. Normal vectors $\mathbf{n}$ point out of the control volume.

The momentum budget for the flow in figure 3.1 without flow control ($v_{\mathrm{BLC}} = 0$) yields the well-known result that the force exerted from the fluid onto the airfoil in the mean flow direction ($\overline{X}$) can be recovered from the momentum deficit in the wake far downstream of the airfoil where the static pressure has recovered to its far upstream inflow value. The drag coefficient retrieved by integrating the stresses acting on the body (airfoil) is denoted with $c_{d,B}$ and defined as

$$c_{d,B} = \frac{2F_D}{\rho U_\infty^2 A_{\mathrm{ref}}}\,, \tag{3.1}$$

where A_{ref} is the product of chord length c and the span-wise airfoil dimension. Equivalently, the wake-survey also delivers the drag coefficient, which we denote with $c_{d,W}$, as follows:

$$c_{d,W} = \int_B^C \frac{2}{c}\frac{u(\overline{Y})}{U_\infty}\left(1 - \frac{u(\overline{Y})}{U_\infty}\right)\,\mathrm{d}\overline{Y}. \tag{3.2}$$

We refer to $c_{d,W}$ as *wake survey drag*. For an airfoil without blowing control, the *body drag* and *wake survey drag* are equivalent up to possible measurement uncertainties, i.e.

$$c_{d,B} = c_{d,W} \qquad \text{if } v_{\mathrm{BLC}} = 0. \tag{3.3}$$

The distinction between *body drag* $c_{d,B}$ and *wake survey drag* $c_{d,W}$ will become relevant for the controlled flow.

[...]

The additional momentum flux due to turbulent fluctuations were discussed for free shear layers [131, p. 93] but are rarely measured experimentally since their contribution to the drag coefficient is small even close to the airfoil trailing edge where high turbulence intensities are found [116, p. 703].

[...]

If the static pressure along the wake survey plane $\overline{BC}$ has not recovered to its far upstream value, equation 3.2 has to be extended to

$$c_{d,W} = \int_B^C \underbrace{\frac{2}{c}\frac{u(\overline{Y})}{U_\infty}\left(1 - \frac{u(\overline{Y})}{U_\infty}\right) + \frac{2}{c\rho U_\infty^2}\left(p_\infty - p(\overline{Y})\right)}_{\text{wake survey integrand } f_{\mathrm{WS}}}\,\mathrm{d}\overline{Y}. \tag{3.4}$$

Since the experimental determination of [both] $u(\overline{Y})$ [and] $p(\overline{Y})$ [simultaneously] can be challenging, alternative extensions to equation 3.2 are available in literature [9, 50]. For numerical data sets equation 3.4 can be applied directly. If any drag reducing flow control is realized on the airfoil without the addition or removal of mass inside the control volume, e.g. riblet-induced drag reduction, we expect a reduction of $c_{d,B}$ that can be deduced from the wake survey following equations 3.2 or 3.4 under the same assumptions as for the uncontrolled flow.

In the case of the active flow control scheme of micro blowing a source of mass is added into the airfoil which leaves the airfoil at speed v_{BLC} normal to the mean flow direction. Micro blowing on the pressure side of the airfoil is sketched in figure 3.1. Note that the injected control fluid does not carry any momentum in the streamwise direction (if we consider the flow in the airfoil reference system as indicated in figure 3.1). It is known that this particular type of micro blowing on the pressure side can reduce not only the skin friction drag but also the pressure drag along the airfoil [AVF$^+$20, FSF$^+$21]. The force F_D that the surrounding fluid exerts onto the airfoil, and thus $c_{d,B}$ (see equation 3.1), is reduced in this setting. However, due to the mass added inside the control volume, this change in force does not directly reflect in the wake flow. The fact that the injected mass flow for boundary layer control (BLC) has to be accelerated in streamwise direction causes an additional momentum deficit in the wake. This momentum deficit is given by the product of BLC mass flow rate and U_∞ which can be normalized in analogy to a drag coefficient (see equation 3.1) to obtain a dimensionsless number, c_{BLC}, that describes a BLC penalty. In the case of BLC control with (mass injecting) blowing the dimensionless momentum balance reads

$$c_{d,B} + \underbrace{2\frac{v_{\mathrm{BLC}}}{U_\infty}\frac{l_{\mathrm{BLC}}}{c}}_{c_{\mathrm{BLC}}} = c_{d,W}\,. \tag{3.5}$$

The BLC penalty thus describes the difference between *body drag* and *wake survey drag* in the blowing-controlled configuration. Large blowing rates can induce significant differences between the drag measured directly at the airfoil and the momentum deficit of the wake. Equation 3.5 indicates that $c_{d,B}$ may even assume negative values if $c_{\mathrm{BLC}} > c_{d,W}$ which is later shown in [section 4.2.3]. In the derivation of equation 3.5 the mass flow required for micro blowing flow control originates from an unknown source. It is simply assumed to be available on the controlled surface. In numerical simulations this is achieved through the definition of a suitable boundary condition. In experiments an external pressurized reservoir from which fluid is guided into the airfoil has to be made available.

More realistically, one may consider the collection of the required control fluid as a separate problem, where instead of a reservoir an air intake is utilised. The air intake redirects the collected fluid so that ultimately all its $\overline{X}$-momentum is transferred to the body. Even if viscous losses are neglected, this loss of $\overline{X}$-momentum causes an additional drag component at the intake which equals the term c_{BLC} albeit being of opposite sign. The difference of the wake-survey drag and the *body drag* of the airfoil-intake system still respects equation 3.5. In fact, the air-collection and the BLC only form a closed system in terms of mass continuity if considered simultaneously: in this case the equality of *body drag* and *wake survey drag* is restored. If the airfoil with BLC is considered without an air-intake, i.e. a mass source is present, the BLC penalty c_{BLC} has to be [added to the *body drag* in order to obtain the total drag of the system]." from [FAF$^+$23, section 2]

3.1.2 Energy Balance

The energy balance can provide information on the overall effort similar to the momentum balance. Drela [28] gave an approach for an integral energy budget of a complex aerodynamic flow. It builds on the idea that any deviation from the freestream flow state which is caused by the body/airfoil contains reversible and irreversible state changes. The irreversible changes and the reversible changes that carry energy and leave the control volume make up for the drag (in general: loss of

power) of a body/system. This procedure was adapted and simplified for the present study in the form of the *Bernoulli Equation* (section 2.1, eq. 2.23 – 2.25).

The effort has to be independent from the frame of reference which is why it will be derived for two general cases: First, for a moving body in resting fluid and second, a resting body in moving fluid. The energy balance provides additional information on the states of the BLC fluid and therefore extends the conclusions about feasible operations of uniform blowing BLC. In a first, step a finite

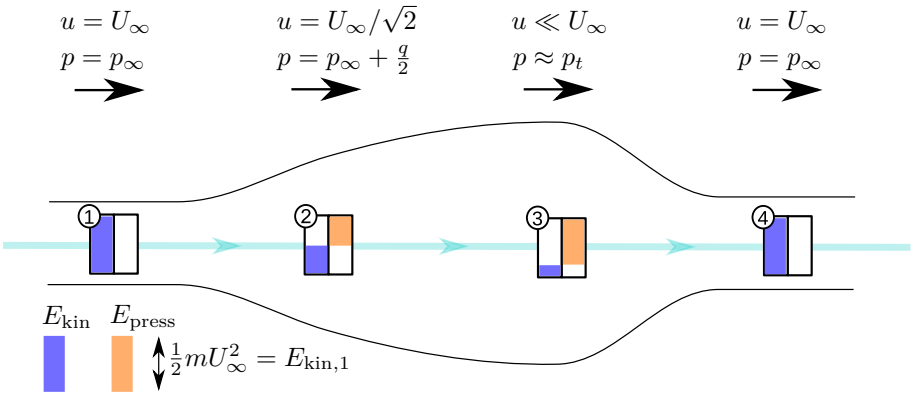

Figure 3.2: Law of Bernoulli for an isentropic flow at varying velocities.

air volume V_{batch} is considered traveling along its path line in figure 3.2. This is a visualization of the Law of Bernoulli as introduced in section 2.1 for steady-state conditions. The bars indicate what form of energy contains how much of the total mechanical energy at the respective state. This involves the two forms of energy from equation 2.23: Kinetic Energy E_{kin} and energy in the form of a compression E_{press} compared to the infinite pressure p_∞. In the case of an ideal — loss-free, isentropic — flow, the total energy has to be conserved, therefore both bars have to add up to the initial energy $E_1 = E_{\text{kin},1}$. As no losses exist, state ④ is equivalent to state ①, meaning no energy input has to be provided to achieve such a system.

Fluid at rest, Body in motion Based on the introduction to figure 3.2 a body with boundary layer control is investigated in figure 3.3 in terms of the path of the control fluid. Note, that the

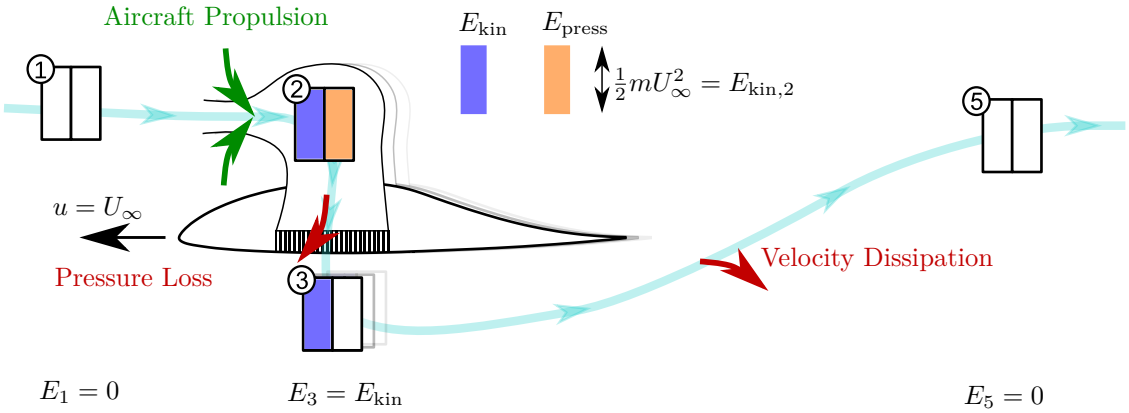

Figure 3.3: Energy Budget for a moving body in fluid at rest.

body moves in this case while the fluid is at rest. Therefore, the finite air volume V_{batch} has none of the two energy forms at the initial state ① (figure 3.3), with $p_1 = p_\infty$ and $u_1 = 0$. In a first step the finite air volume has to be accelerated to the speed of the intake diffusor of which it is collected in order to reach state ②. This energy is equivalent to:

$$E_{\text{kin},2} = \int\limits_{V_{\text{batch}}} \frac{1}{2}\rho U_\infty^2 \, \mathrm{d}\mathcal{V} = \frac{1}{2}\rho U_\infty^2 \cdot V_{\text{batch}} \tag{3.6}$$

Meanwhile, the observed acceleration is identical to a stagnation process in the moving frame of reference. Therefore, the stagnation quantities, such as the stagnation pressure p_t, depend on the speed of the moving object, hence

$$p_{t,2} = p_2 = p_\infty + \frac{1}{2}\rho U_\infty^2 \tag{3.7}$$

The compression energy can be expressed as

$$E_{\text{press},2} = \Delta p V_{\text{batch}} = (p_2 - p_1)V_{\text{batch}} = \frac{1}{2}\rho U_\infty^2 \cdot V_{\text{batch}} \tag{3.8}$$

Therefore, the total energy required to reach state ② can be computed to

$$E_{\text{ext}} = E_2 - E_1 = E_{\text{kin},2} + E_{\text{press},2} = \rho U_\infty^2 \cdot V_{\text{batch}} \tag{3.9}$$

This means, an external energy source E_{ext} (like the propulsive system of an aircraft) has to provide both energy portions.

The moment the finite air volume completes the transition from state ② to state ③ it reaches ambient pressure. For simplicity reasons this can be assumed to equal the static pressure at infinity, thus $p_3 = p_1 = p_\infty$. This simplification or rather the error associated with it correlates with the performance control and will be discussed later again (section 3.3 and section 4.2.5). It does not matter how the pressure of the finite air volume is reduced to ambient pressure. Yet, at least some part of the energy stored therein will inevitably be lost due to a non-ideal stagnation (from state ① to ②), internal flow resistance, and the flow through the (porous) surface. On the other hand, these losses — as long as they are smaller than the pressure difference from stagnation pressure p_t to ambient pressure p_3 — can be provided by this exact pressure difference without further energy input. Therefore, the pressure energy $E_{\text{press},2} - E_{\text{press},3}$ provides an energy "reservoir" which exists anyway and is available for BLC operations. In state ③ — right after passing through the control surface — the finite air volume still travels at the speed of the body and therefore preserves its kinetic energy $E_{\text{kin},3} = E_{\text{kin},2}$.

To complete the path line to state ⑤, which is equivalent to state ①, the kinetic energy of state ③ has to be erased. The kinetic energy is dissipated completely as this is a mixing process until eventually $u = 0$ is reached.

As suggested by the green and red arrows in figure 3.3 the finite air volume requires an external energy input E_{ext} of

$$E_{\text{ext}} = 2 \cdot E_{\text{kin},2} = \rho U_\infty^2 \cdot V_{\text{batch}} \tag{3.10}$$

to overcome all theoretical losses along the path.

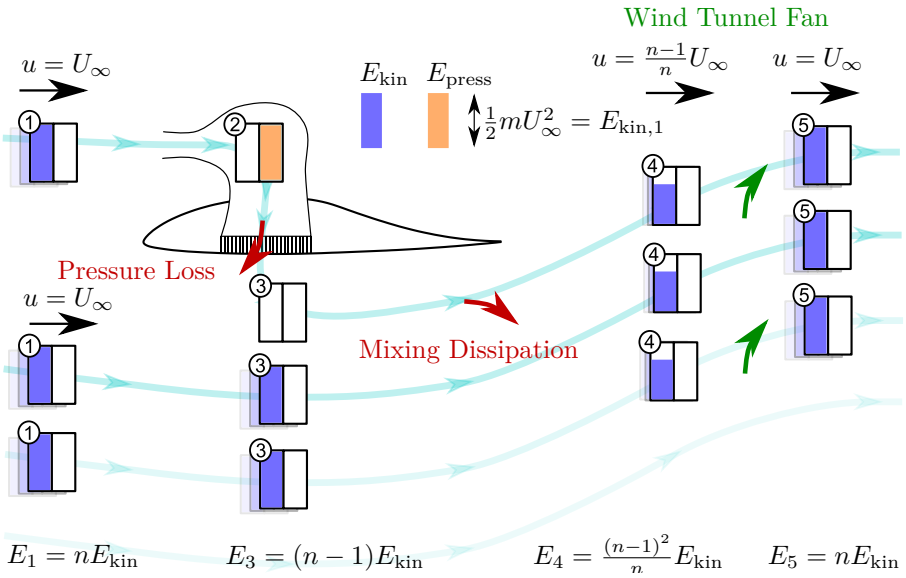

Figure 3.4: Energy Budget for a moving fluid and a body at rest.

Fluid in motion, Body at rest A more complex version of the energy balance is described in figure 3.4. In this case, the conversion from state ① to ② is equivalent to the transformation showcased in figure 3.2 in the sense that no energy has to be provided from an external source.

The step from state ② to state ③ is similar to the example earlier. The same is true for the "reservoir" effect discussed in the previous paragraph. The difference is, that at state ③ the finite air volume carries no energy.

If one were to compare state ③ with state ⑤ it looks as though only one "energy-bar" has to be provided to reach the initial state again. However, this ignores the process of how this state transition happens. Such a result would only be correct if the finite air volume was accelerated by an external power directly. Yet, this is not the case but mixing with the ambient moving fluid takes place upstream of external power input (This difference will be discussed again in section 3.3). During this mixing process the total momentum of the moving fluid has to be preserved from state ③ to state ④. This means for the velocity at state ④ u_4

$$0 \cdot \rho V_{\text{batch}} + \sum_{i=2}^{n} U_\infty \rho V_{\text{batch}} = \sum_{i=1}^{n} u_4 \rho V_{\text{batch}} \tag{3.11}$$

$$u_4 = \frac{n-1}{n} U_\infty \tag{3.12}$$

with n being the total number of finite air volumes including those, which do not pass through the BLC. For $n \to \infty$ the velocity at state ④ does go towards the freestream velocity $u_4 \to U_\infty$. The mean energy of a finite air volume at state ④ E_4 can be described with the expression of u_4:

$$E_4 = \frac{1}{2}\rho \left(\frac{n-1}{n} U_\infty \right)^2 \cdot V_{\text{batch}} n \tag{3.13}$$

This expression goes towards the energy level at state ⑤ E_5 for a large freestream with many n finite air volumes

$$E_5 = \frac{1}{2}\rho U_\infty^2 \cdot V_{\text{batch}} n \tag{3.14}$$

Yet, for the difference in the energy levels, the following can be said:

$$E_5 - E_4 = \frac{1}{2}\rho U_\infty^2 \cdot V_{\text{batch}} \underbrace{\left(n - n \left(\frac{n-1}{n} \right)^2 \right)}_{\text{required "energy-bars"}} \tag{3.15}$$

$$\text{for } n \to \infty \tag{3.16}$$

$$\lim_{n\to\infty} n - \frac{(n-1)^2}{n} = \lim_{n\to\infty} \frac{2n-1}{n} = 2 \tag{3.17}$$

$$E_{\text{ext}} = E_5 - E_4 = \rho U_\infty^2 \cdot V_{\text{batch}} \tag{3.18}$$

This energy difference requires an external source of energy E_{ext} to reach the initial state (⑤, respectively ①) again. As an example of fluid in motion and body at rest a wind tunnel fan has to provide this energy. Equation 3.18 has the same result as equation 3.10 which shows the independence of the frame of reference for the energy balance formulation. Also, it becomes apparent that the losses are generated in the same steps although in the case of the moving body (figure 3.3) the energy dissipation appears more intuitive than in the case of the moving fluid (figure 3.4).

Dimensionless Formulation The different frames of reference of the energy balance have been shown using finite volumes for clarity. However, the energy conservation balance has to take a dimensionless form without assuming volume batches and velocities in order to compare this with the result of the momentum balance and the force coefficients of the aerodynamic analysis.

For that purpose, the reference quantities have to be chosen equivalently to the reference quantities of the other analyses. A differential volume batch can be used to define a differential energy requirement. For this, one can consider the boundary layer control volume flux $\dot{V}_{\text{batch}}$:

$$\dot{V}_{\text{batch}} = v_{\text{BLC}} \underbrace{l_{\text{BLC}} s}_{\text{control area}} \tag{3.19}$$

$$= \frac{v_{\text{BLC}}}{U_\infty} \frac{l_{\text{BLC}}}{c} \cdot U_\infty \underbrace{cs}_{A_{\text{ref}}} \tag{3.20}$$

$$\tag{3.21}$$

This formulation already includes the reference area A_{ref} of the dimensionless form of aerodynamic coefficients based on span s and airfoil chord length c. Secondly, the dynamic pressure $q_\infty = 1/2\rho U_\infty^2$ at infinity is used as a reference for aerodynamic coefficients. It can also be applied here if the time-derivative of the required external energy — the required external power $\dot{E}_{\text{ext}}$ — is considered:

$$\dot{E}_{\text{ext}} = \rho U_\infty^2 \cdot \dot{V}_{\text{batch}} = \rho U_\infty^2 \cdot \frac{v_{\text{BLC}}}{U_\infty} \frac{l_{\text{BLC}}}{c} \cdot U_\infty A_{\text{ref}} \tag{3.22}$$

$$= 2\frac{v_{\text{BLC}}}{U_\infty} \frac{l_{\text{BLC}}}{c} \underbrace{q_\infty U_\infty A_{\text{ref}}}_{\text{freestream reference power } P_{\text{jet},\infty}} \tag{3.23}$$

$$e_{\text{BLC}} = 2\frac{v_{\text{BLC}}}{U_\infty} \frac{l_{\text{BLC}}}{c} = c_{\text{BLC}} \tag{3.24}$$

This results in a dimensionless form for the energy or power requirement of the BLC e_{BLC} which is identical to the result of the momentum balance c_{BLC} (section 3.1.1). The reference quantities that provide normalization are in accordance with what other authors derived to bring a subsystem

power requirement in a dimensionless form [8]. The free stream reference power (eq. 2.46) provides this set of reference quantities to make an external power requirement comparable to aerodynamic coefficients.

3.2 Local Drag Assessment with Control Penalty

From [FAF+23, section 3.2]: "The previously discussed difference between *body drag* and *wake survey drag* and the relevance of the latter in determining the air intake effort do not only concern airfoil flows or external geometries but hold true also for flow control on a flat plate. This is the scenario in which micro blowing has been intensively investigated in the last decades [55, 122, 92, 47, 51, 52, 127], mostly with a focus on the local skin friction drag reduction. In analogy to the discussion [in section 3.1.1], the wake of a finite size flat plate provides information about the corresponding inclusive drag. For the turbulent flow along the plate the momentum and displacement boundary layer thicknesses δ_θ and $\delta^\star$ carry the same information as the wake, as discussed in the following.

The von Karman equation describes the spatial evolution of the boundary layer and its corresponding friction drag. In general form [41] with additional wall-normal transpiration v_{BLC} the dimensionless friction drag is usually scaled with the wall-parallel freestream velocity at the edge of the boundary layer at the same streamwise coordinate U_e:

$$\underbrace{2\frac{\tau_w}{\rho U_e^2}}_{c_{f,l}} + 2\frac{v_{\mathrm{BLC}}}{U_e} = 2\frac{d\delta_\theta}{dx} + 2\frac{2\delta_\theta + \delta^\star}{U_e}\frac{dU_e}{dx}. \tag{3.25}$$

The term $2v_{\mathrm{BLC}}/U_e$ can be simply moved to the right-hand side if one is interested in the local friction drag $c_{f,l}$, which is usually the case when studying canonical flows such as flat plate boundary layers. However, similar to the case of the 2D airfoil one can show that this term carries the information on the momentum penalty the system experiences for collecting BLC fluid from the freestream. This motivates the interpretation of this term to be similar to the BLC penalty c_{BLC} described above. In order to have a more general view on the boundary layer of a flow around a body it is reasonable to rescale the equation with the velocity at infinity U_∞ which may differ from the velocity at edge of the boundary layer at the corresponding streamwise coordinate U_e in boundary layers with nonzero pressure gradients. Scaled with U_∞ the friction drag $c_{f,\infty}$ can be motivated alongside the local BLC-related penalty $c_{f,\mathrm{BLC}}$:

$$\underbrace{\underbrace{2\frac{\tau_w}{\rho U_\infty^2}}_{c_{f,\infty}} + \underbrace{2\frac{v_{\mathrm{BLC}}U_e}{U_\infty^2}}_{c_{f,\mathrm{BLC}}}}_{\text{inclusive drag } c_{f,\mathrm{inc}}} = \underbrace{2\frac{U_e^2}{U_\infty^2}\frac{d\delta_\theta}{d\bar{x}} + 2U_e\frac{2\delta_\theta + \delta^\star}{U_\infty^2}\frac{dU_e}{d\bar{x}}}_{\mathrm{RHS}} \tag{3.26}$$

Similar to the wake survey the contribution of the Reynolds stresses is negligible, except at the edges of the controlled area [127]. " from [FAF+23, section 3.2]

3.3 Conclusions of Analytical Results

In this chapter, a clear distinction of the drag quantity describing the resisting force on the body subject to uniform wall-normal blowing BLC — the *body drag* — and the total drag force of a

complete system including the provision of BLC fluid was made. In case of uniform blowing the latter can be obtained via a wake survey directly from the flow domain, hence it can be called *wake survey drag*. However, other boundary layer control schemes such as Laminar Flow Control (LFC) — or other suction flow control schemes — show different characteristics [8] which is why for a drag quantity *including* the theoretical provision effort of BLC a more universal name has to be conceived: the *inclusive drag* [FAF$^+$23]. In the case of uniform wall-normal blowing the *body drag* and *inclusive drag* (*wake survey drag* respectively) are separated by the BLC penalty (integral formulation in eq. 3.5, boundary layer formulation in eq. 3.26). The inclusive drag is the relevant quantity for a realistic estimate of the net drag reduction effect of the control. This means that both the body and wake-survey drag are legitimate measures of the drag force and carry a clear physical meaning [FAF$^+$23, section 4].

The "reservoir" effect denoted in the energy balance derivation (section 3.1.2) provides a pressure difference of which the energy effort is already accounted for by the BLC penalty c_{BLC}.

> From [FAF$^+$23, section 2]: "In this [...] case, there is at least some pressure difference available to overcome implementation-dependent losses (such as viscous losses of forcing the fluid through a porous surface) thus enabling a system of passive blowing as it has been described e.g. by Hirokawa *et al.* [46]. Theoretically, it may also be possible to harvest the pressure difference mentioned above, as explained e.g. by Fahland *et al.* [FSF$^+$21] who showed using energetic considerations that the BLC penalty drag coefficient c_{BLC} in this case would reduce to only half of what is obtained [as BLC penalty c_{BLC}]. [...] However, any attempt of energy recovery by expanding fluid through a recovery system is limited by viscous losses within the system itself, in addition to losses within the propulsive system exploiting the regained power to counteract the total drag of the aircraft. Therefore, any attempt of even marginally reducing the [...] BLC penalty c_{BLC} remains very inefficient and thus not viable due to inefficiencies in energy recovery as well as the additional mass of the recovery system. Therefore, the [...] BLC-penalty c_{BLC} derived here is a very reasonable measure of the unavoidable costs of the control scheme of uniform blowing. " from [FAF$^+$23, section 2]

Based on the conclusion that a power recovery from the pressure drop is unfeasible, the question arises if the pressure loss can be reduced by reducing the pressure drop. In section 3.1.2 it was assumed that the static pressure at the BLC surface equals the static pressure at infinity $p_3 = p_\infty$. Although common, it is not a necessary condition for applying BLC in external flows such as airfoil flows. Note, that the available "power reservoir" for internal losses decreases if the static pressure at the BLC location increases. As shown in section 3.1.2 the dissipation of energy during the mixing process of BLC fluid and ambient fluid is an inherent feature of the BLC scheme of uniform wall-normal blowing. The dimensionless drag which represents this dissipation of kinetic energy equals one of the showcased "energy bars", in other words, half the BLC penalty:

$$c_{\mathrm{dissipation},u} = \frac{1}{2} c_{\mathrm{BLC}} = \frac{v_{\mathrm{BLC}}}{U_\infty} \frac{l_{\mathrm{BLC}}}{c} \tag{3.27}$$

$$\text{if BLC is applied at ambient pressure } p = p_\infty \tag{3.28}$$

This loss is associated with the fundamental working principle of uniform blowing: The wall friction (or parts of it) are replaced by internal friction within the external flow. This loss gets smaller the higher the static pressure where uniform blowing is applied because the velocity difference to the

ambient flow and the associated mixing losses shrink. This effect is also directly reflected in the term for the boundary layer formulation of the BLC penalty $c_{f,\mathrm{BLC}}$ (section 3.2, eq. 3.26):

$$c_{f,\mathrm{BLC}} = 2\frac{v_{\mathrm{BLC}}U_e}{U_\infty^2} \tag{3.29}$$

The velocity at the edge of the boundary layer U_e gets smaller the higher the local static pressure, hence the magnitude of the BLC penalty shrinks. This supports the hypothesis raised above and agrees with the conclusions from Drela that losses scale with the boundary layer edge velocity of where they occur [28]. Yet, lower edge velocity usually also correlates with lower friction drag, hence less potential for reducing this friction drag via BLC. As these trade-offs correlate negatively an additional hypothesis can be formulated which will be discussed in section 4.2.5 and 5.5.3.

Hypothesis: For a given control intensity, uniform blowing BLC causes more body drag reduction the higher the static pressure where it is applied relative to the stagnation pressure. The hypothesis can also be reformulated, such that it states: **BLC performance of uniform blowing with a certain intensity yields less body drag reduction or even body drag increase the lower the static pressure at BLC location relative to stagnation pressure.**

This hypothesis will be investigated both numerically and experimentally in the following chapters. Uniform blowing boundary layer control will be activated in different flow scenarios (varying angle of attack and airfoil geometry) and for different size and location of the controlled region. This enables performance comparison for different static pressures within the controlled region.

4 Numerical Investigation

Simulations shown in this chapter are based on the RANS equations (eq. 2.31) and validated with LES simulations performed by Atzori [7] and Atzori *et al.* [AVF+20]. The presented content was in part published previously by Fahland *et al.* [FSF+21, FAF+23] (sections 4.1 & 4.2.1 - 4.2.4).

4.1 Methodology

4.1.1 Simulation Setup

4.1.1.1 Solver and Models

> From [FSF+21, section 2]: "The calculations are performed with the open-source computational-fluid-dynamics (CFD)-toolbox OpenFOAM [140]. In particular, the steady state, incompressible solver simpleFoam is used. The k-ω-SST model is employed as turbulence model [76]." from [FSF+21, section 2]
>
> From [FSF+21, section 2.B]: "The convergence criterion for the parameter study is then set to reach $r \leq 10^{-6}$. The chosen discretization schemes are Gauss linear for gradients, Gauss linear upwind for divergence schemes and Gauss upwind for the convective schemes. All calculations are set to be steady state." from [FSF+21, section 2.B]

Excluding some details on alternative turbulence modeling for the flow control regions, the turbulence properties are treated this way:

> From [FSF+21, section 2.A]: "Within the airfoil boundary layer, laminar flow upstream of the transition location is ensured by enforcing $k = 10^{-16}[\frac{\mathrm{m}^2}{\mathrm{s}^2}]$ up to shortly upstream ($\Delta X = -1\%c$) of the intended tripping position, at which a source term is added to the TKE equation. The source term $S_{\mathrm{k,a}}$ is treated as a semi-implicit scalar source, albeit we only use the explicit part, as described in [93]. [...] The source term ensures an immediate transition at all considered Reynolds numbers. This setup is used to provide a realistic smooth transition from the laminar to the turbulent state, which also ensures a physical distribution of the wall-shear stress avoiding unrealistic overshooting or spatial delay. Similar transition behaviour is observed in the T3 test cases [115]. This setup is similar to the transition handling in regular transitional models like SSTγ or γ-Re_θ by Menter *et al.* [78, 79] except for the prediction of the transition location. [...] The marginal differences achieved through specific ω treatments combined with their additional complexity, slower convergence and model uncertainty motivate our choice to consider in the following only the standard SST formulation for ω. " from [FSF+21, section 2.A]

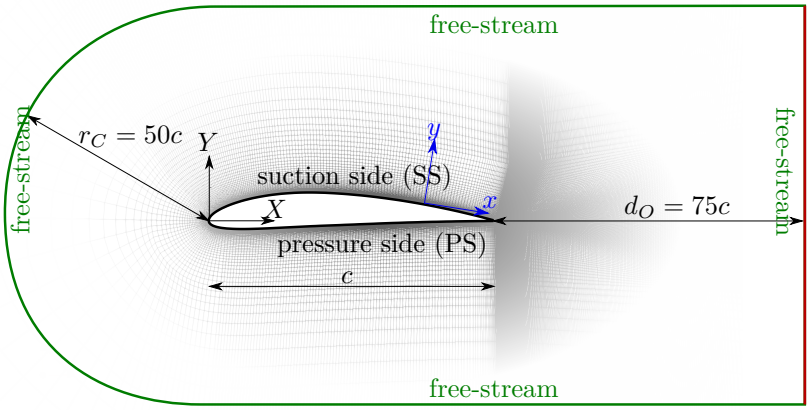

Figure 4.1: Computational domain with definition of boundaries and coordinate axes: the global rigid body coordinate system $\{X, Y, Z\}$ and the local wall coordinate system $\{x, y, z\}$. Adapted from [FSF+21, figure 1]

4.1.1.2 Mesh generation

From [FSF+21, section 2]: "The numerical grid shown in Fig. 4.1 utilizes hexahedral cells in a 2D C-shaped block pattern with a C-radius of $r_C = 50c$, where c is the chord length and a trailing-edge to outlet distance of $d_O = 75c$. Meshes are generated separately for each airfoil and Reynolds number with an automated script leveraging the meshing tool blockMesh. A precursor XFOIL-calculation [26] is executed to determine the distribution of the wall shear stress τ_w along the perimeter $\mathcal{C}$ of the airfoil, which determines the wall-normal mesh resolution $y_{\min}$ required for application of the turbulence model without wall functions, according to the criterion $y^+_{\text{wall}} \leq 1$. The requirement $y^+_{\text{wall}} \leq 1$ can be recast in terms of the chord length c, the speed of the incoming flow U_∞ and the local skin-friction coefficient $c_{f,\infty} = 2\tau_w/\rho U^2_\infty$ as:

$$y_{\min} = \beta_{y^+} \min_{\mathcal{C}} \left(\frac{\sqrt{2}c}{Re_c \sqrt{c_{f,\infty}}} \right) , \tag{4.1}$$

where $Re_c = cU_\infty/\nu$ is the chord-based Reynolds number, $\beta_{y^+} = 1.5$ is a coefficient to include a margin for varying angles of attack and control schemes as well as y^+_{wall} being determined in the center of the first cell whereas $y_{\min}$ describes the wall-normal height of the first cell-layer. The fullfillment of the mesh requirements for the control cases has been verified a posteriori based on the output of the RANS calculations. For the validation case (uncontrolled, NACA 4412, $Re_c = 4 \cdot 10^5$, $\alpha = 5°$), the maximum and average values of y^+_{wall} are 0.72 and 0.27 respectively, accommodating a margin to allow simulations of different angles of attack and controlled configurations with the same mesh. A comprehensive grid convergence study was carried out focusing on a specific case (NACA 4412, $Re_c = 4 \cdot 10^5$, $\alpha = 6°$) as well as some operating points with other airfoils (blunt instead of sharp trailing edge variants), AoA ($\alpha = 0°$) and different Reynolds number ($Re_c = 4{\cdot}10^6$). The resulting mesh parameterization was suitable for various airfoil geometries without violating skewness, non-orthogonality and aspect rations criteria and able to reproduce validation data. The approximate total cell count of a typical airfoil mesh resulting from this was $n_{\text{cell}} \approx 110.000$ for $Re_c = 4 \cdot 10^5$ and $n_{\text{cell}} \approx 210.000$ for $Re_c = 4 \cdot 10^6$. After reaching this we evenly refined the resulting meshes for 4 different cases of the baseline airfoil NACA 4412: $Re_c = \{4 \cdot 10^5, 4 \cdot 10^6\}$, $\alpha = \{0°, 6°\}$. The finest meshes for $Re_c = 4 \cdot 10^5$ had a cell count of $n_{\text{cell}} \approx 430.000$ ($Re_c = 4 \cdot 10^5$) and

$n_{\text{cell}} \approx 830.000$ ($Re_c = 4 \cdot 10^6$). Taking the results of the finest meshes as comparison the chosen parameterization stayed within an error margin of 0.6% for the airfoil efficiency E. Larger errors have been considered elsewhere as acceptable for a parameter study, *e.g.* by Kim *et al.* [54]." from [FSF+21, section 2]

4.1.1.3 Boundary Conditions

variable	freestream	airfoil surface	airfoil surface
p	*freestreamPressure* ($p_{\text{ref}} = U_\infty^2$)	*zeroGradient*	*zeroGradient*
U	*freestreamVelocity* $U_\infty = \begin{pmatrix} cos\alpha & sin\alpha & 0 \end{pmatrix}^T_{\{X,Y,Z\}}$	*fixedValue* $(0,0,0)^T$	*fixedValue* $v_{\text{BLC}}\|\|y$
k	*inletOutlet* $k = 10^{-16}U_\infty^2$	*fixedValue* $k = 10^{-16}U_\infty^2$	*fixedValue* $k = 10^{-16}U_\infty^2$
ω	*inletOutlet* $\omega_{\text{in}} = 0.068\frac{U_\infty}{c}$	*omegaWallFunction*	*omegaWallFunction*

Table 4.1: OpenFOAM boundary conditions in their incompressible form including applicable Dirichlet values. All values are given relative to the freestream velocity U_∞ and chord length c. Adapted from [FSF+21, Table 1], note that all quantities are given as kinematic quantities (meaning *e.g.* pressure quantities are expressed as pressure divided by the density).

From [FSF+21, section 2.A]: "Table 4.1 shows the applied boundary conditions along with their OpenFOAM acronyms as well as the field values, if applicable. A homogeneous Neumann condition is imposed for the pressure p on the airfoil surface. The far-field boundary conditions for all quantities are set to be Dirichlet conditions at the inlet and Neumann conditions of vanishing gradient at the outlet. In this context, inlet and outlet are determined by the prescribed flow direction. This is important, since the change in AoA is realized by changing the inflow direction and thus also the faces where fluid actually enters the domain. On the airfoil surface the velocity **u** is set to zero except for the regions of boundary layer control where a uniform, wall-normal velocity component v_{BLC} is introduced. [...] At the wall, the turbulent kinetic energy (TKE) k is set to practically zero ($k = 10^{-16}$ as this is numerically more stable) as well." from [FSF+21, section 2.A]

4.1.1.4 Control Scheme

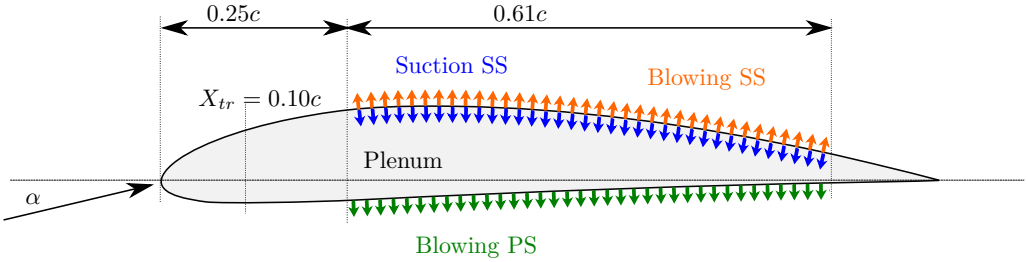

Figure 4.2: Control schemes and their location. Modified from [FSF+21, figure 2].

From [FSF+21, section 3]: "The BLC considered in the present study is wall transpiration, realised as spatially homogeneous wall-normal blowing or suction. This idealisation is convenient for addressing the global effect of the control — the main goal of the present study

— while avoiding to focus on the details of the large variety of possible implementations. Nevertheless, homogeneous blowing and suction do not reflect realistic implementations of the control, which necessarily involve distributed transpiration through discretely perforated plates or porous media. Since the lengthscale of e.g. a perforation is well below the resolution of the presented RANS, it cannot be directly addressed within the scope of the present modelling. However, experimental studies by Hwang [47], at the Fukagata-Lab [46, 30] and by Kornilov *et al.* [59, 57] showed that experimental implementations agree fairly well with the ideally uniform transpiration imposed numerically as far as boundary layer velocity distributions are concerned. Similar observations have been made for Laminar Flow Control through perforated plates, for which the effect of non-uniformity directly affects transition. Sizeable effort was put in minimising local disturbances, by considering different hole patterns (*e.g.* [148, 120]), as well as in providing a suitable streamwise distribution of wall-normal velocity, e.g. by tailoring the pressure drop along the fluid supply lines for flow control [119, 120].

The region of BLC is located between $x/c = 25\%$ and $x/c = 86\%$. The general idea was to realize large but yet reasonable BLC regions regarding basic engineering hurdles: we chose the start location of $x/c = 25\%$ in order to account for an undisturbed laminar region ($x_{tr}/c = 10\%$) augmented with some downstream distance to allow for the TBL to fully develop in any operating point. The aft end of BLC was set to $x/c = 86\%$ to account for trailing edge components such as flaps, ailerons or other parts to still be implemented and furthermore ensure enough space for BLC implementation without interfering with the opposite airfoil surface. Uniform blowing is applied separately on the suction (orange plot lines) and on the pressure side (green plot lines), while uniform suction is investigated only on the suction side of the airfoil (blue plot lines), since suction on the pressure side is not expected to yield turbulent drag reduction." from [FSF+21, section 3]

4.1.2 Validation

For the description of the LES simulation consider Atzori *et al.* [AVF+20, 7], as well as Fahland *et al.* [FSF+21, FAF+23]. These simulations were not carried out as part of the present thesis but results were reevaluated for validation purposes only.

From [FSF+21, section 4]: "In order to validate the present simulation approach the obtained results are compared against well-resolved LES data for $Re_c = 4 \cdot 10^5$ [134] and $Re_c = 2 \cdot 10^5$ [AVF+20]. In the reference database the AoA is $\alpha = 5°$ and the airfoil geometry is NACA4412 with a sharp trailing edge." from [FSF+21, section 4]

From [FSF+21, section 4A]: "The integral lift c_l and drag coefficients c_d are compared for all cases in Fig. 4.3(a). Figures 4.3(b-d) show the relative change in aerodynamic coefficients induced by the BLC with respect to the uncontrolled case for both RANS and LES simulations. Even though RANS consistently underestimates both lift ($\sim 2\%$) and drag ($\sim 9\%$) coefficients for all cases including the uncontrolled one, all trends regarding the effect of BLC are confirmed and agree reasonably well with the LES data throughout the controlled cases. A possible explanation for the differences in drag predictions is related to figure 4.4. As can be seen in sub-figure c) RANS predicts a smaller displacement thickness $\delta^\star$ as well as friction velocity u_τ. Note that figure 4.4 shows cases at $Re_c = 4 \cdot 10^5$ yet the effect is similar at $Re_c = 2 \cdot 10^5$. A smaller displacement thickness correlates with less momentum deficit in the wake and therefore smaller drag in the uncontrolled case [...]. The smaller friction velocity indicates reduced friction drag in the RANS compared to the LES, which

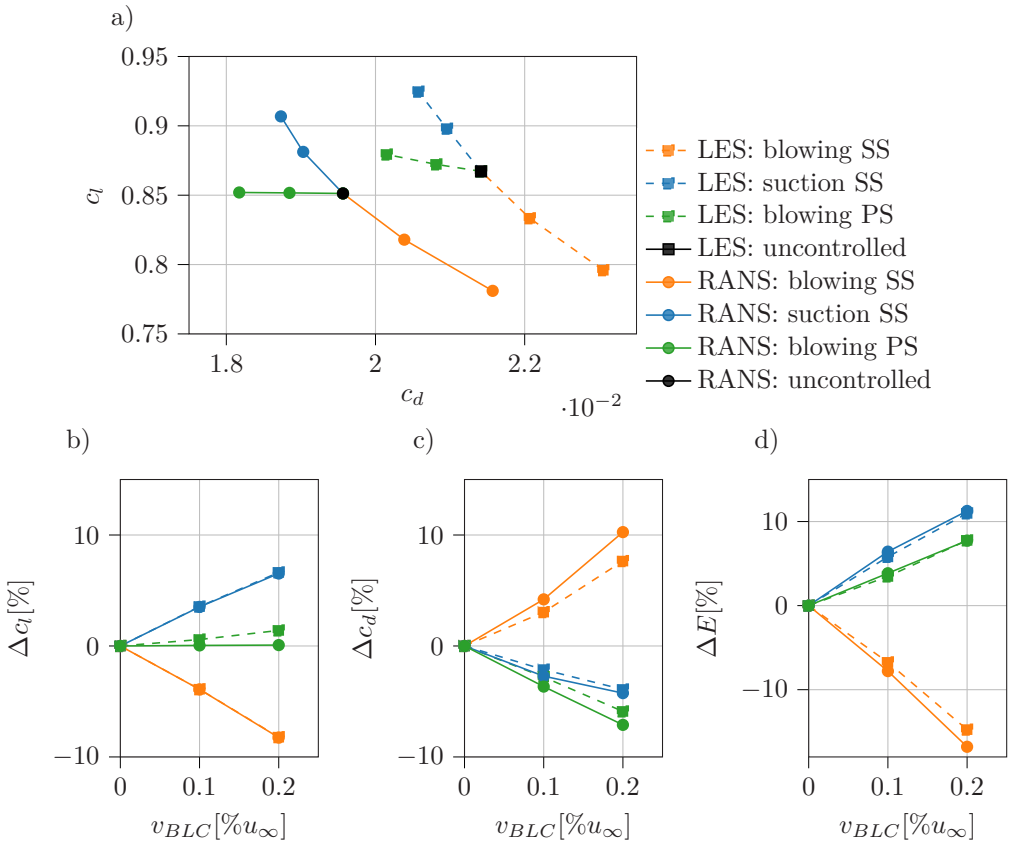

Figure 4.3: Comparison of LES (dashed) and RANS (solid) predictions of the BLC effect on aerodynamic coefficients at $Re_c = 2 \cdot 10^5$ and $\alpha = 5°$. Adapted from [FSF+21, figure 5]

is confirmed by the accumulated friction drag values for RANS ($c_{\mathrm{d,f}} = 0.011292$) and LES ($c_{\mathrm{d,f}} = 0.012764$). There are plenty of different reasons which could lead to the described effect: First of all the applied turbulence model of the RANS does not account for curvature effects [44] which results in an error of the transport of TKE and the corresponding shear stress. It is also known that viscosity based turbulence models show problems predicting the separation points correctly [112], which in turn alters the circulation around the airfoil which feeds back on the boundary layer development. Since the circulation directly affects lift, small deviations equally affect the corresponding lift coefficient. In addition it is also possible that the different far-field domains of the presented LES and RANS are responsible for the small deviation in lift. The same is true for the tripping at $x_{tr} = 10\%$ which is realized through a source term for TKE in the RANS simulations and by a volume force term in the LES. Figure 4.4 a) shows that the LES produce a more sudden change in friction velocity than the RANS simulations.

There is excellent agreement in the control effects on lift (Δc_l) when the control is applied on the suction side. However, the LES results show a small lift increase when blowing is applied over the pressure side, which does not appear in RANS. Confinement effects due to the more restricted domain in the LES may be a possible explanation for this discrepancy, similar to what is observed in wind-tunnels [32], but a detailed analysis will be required to clearly identify the cause for this specific behavior. Concluding, the trends of RANS and LES align quite well for the compared cases. Since the absolute values differ, some uncertainties might remain, especially when using the RANS to extrapolate to different airfoils and Reynolds numbers. In order to rule out a systematic error regarding the general airfoil flow, comparison to various uncontrolled cases of different airfoils and Reynolds numbers was

performed [in addition to the validation with LES simulations shown here]." from [FSF+21, section 4A]

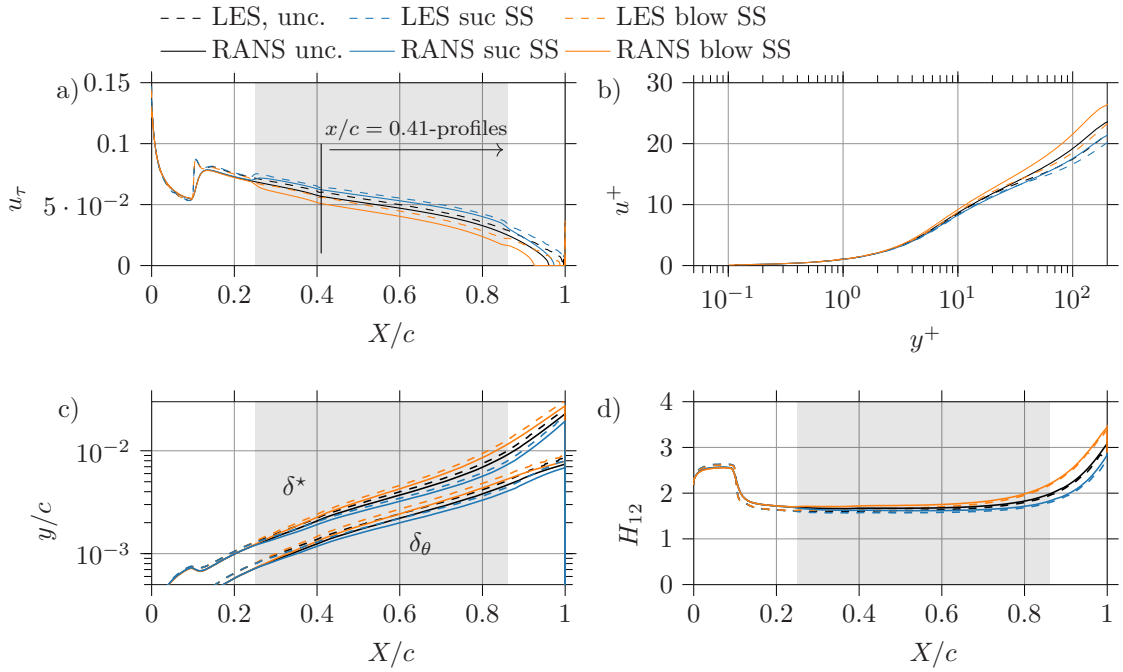

Figure 4.4: Comparison of boundary-layer properties of LES and RANS. The shaded area indicates the region where BLC is active. $Re_c = 4 \cdot 10^5$, $\alpha = 5°$. Adapted from [FSF+21, figure 6]

From [FSF+21, section 4B]: "Figure 4.4(a) shows u_τ along the suction side for the validation case of $Re_c = 4 \cdot 10^5$, $\alpha = 5°$. The RANS simulations seem to predict consistently lower u_τ values than the corresponding LES. However, the changes induced by BLC agree surprisingly well between LES and RANS. This is true except for the flow separation predicted by RANS, which is indicated by u_τ dropping to zero whilst LES predicts no separation also with BLC in action. Interestingly, the shape factor $H_{12} = \frac{\delta^\star}{\delta_\theta}$ does not show a significant difference between LES and RANS results, despite the latter showing flow separation. RANS simulations exhibit a smaller increase of displacement $\delta^\star$ and momentum δ_θ thickness then LES once the pressure recovery reaches its steepest and constant slope (at around $x/c \approx 0.4$). This confirms previously reported findings [77, 147] that boundary layer development predictions in adverse pressure gradients have limited accuracy in eddy-viscosity based turbulence models. In this context it is important to note, that this lack in accuracy does not invalidate the predictions for flow control cases: the deviation keeps the same trends and magnitude for all three cases compared in Fig. 4.4." from [FSF+21, section 4B]

From [FSF+21, section 4B]: "Figure 4.5 shows the comparison of LES and RANS regarding the distribution of the pressure coefficient c_p along the SS and PS of the airfoil for the validation cases. At the position $x/c \approx 2\%$ the largest deviation between pressure coefficients can be observed ($\Delta c_p \approx 0.1$ on the SS). The agreement of both setups is especially good within the BLC region which is crucial since the local changes of c_p by the BLC are only slight but still result in significant overall changes *e.g.* in lift as seen above." from [FSF+21, section 4B]

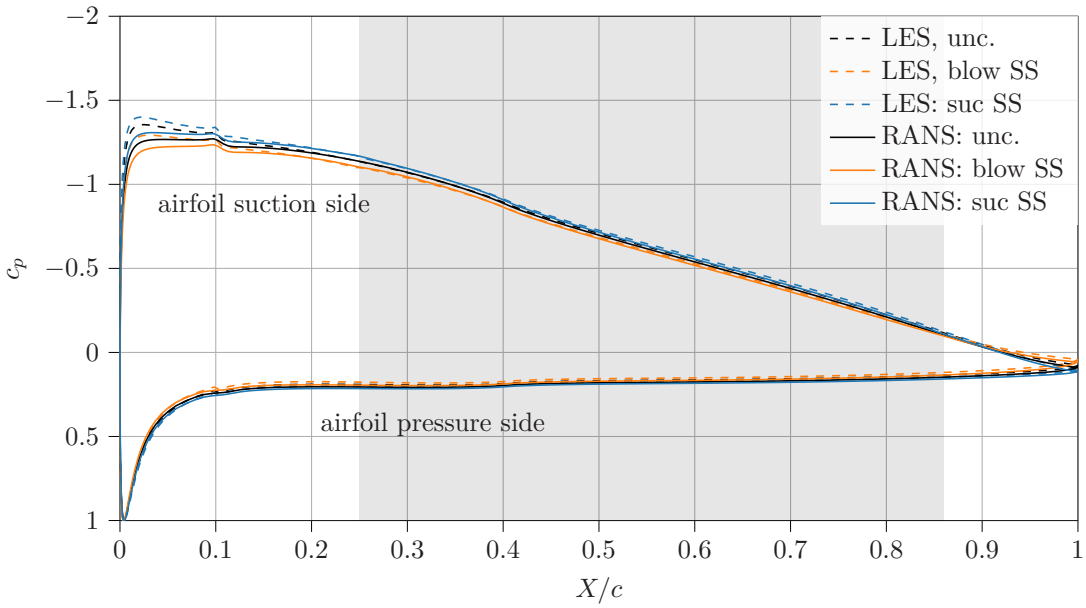

Figure 4.5: Pressure coefficent c_p for $Re_c = 4 \cdot 10^5$, NACA 4412, $\alpha = 5°$,$v_{\mathrm{BLC}} = 0.1\% U_\infty$. Adapted from [FSF+21, figure 7]

4.1.3 Parameter Variations

Table 4.2 summarizes the parameter variations throughout the whole study. This includes several sub-studies of which some results were published already. Additionally, comparison simulations were carried out in preparation for the experimental campaign data analysis. Note, that table 4.2 only summarizes parameter variations of which results are actually presented in the present manuscript.

first publication	airfoil name/group	camber f	thickness t_a	AoA α	Reynolds Number Re_c	BLC Blowing Rate $c_q = \frac{v_{\mathrm{BLC}}}{U_\infty}$	Regions X_{BLC}/c
Fahland *et al.* [FSF+21]	NACAx4xx	$\{0, 2, 4, 6\}\%$	$\{6, 9, 12, 15\}\%$	$[-3°, 15°]$	1e5 2e5 ... 4e6	0.05% 0.1% 0.2% 0.5%	$[0.25, 0.86]$ (figure 4.2)
Fahland *et al.* [FAF+23]	NACA4412	4%	12%	$[-3°, 15°]$	4e5	0.1% 0.2% ... 5%	$[0.25, 0.86]$ (figure 4.2)
Dissertation	GFAPG006	3.9%	13.4%	1°	1e6	0.1% 0.2% 0.5% 1%	$[0.2, 0.3)$ ... $[0.8, 0.9)$ (figure 4.16)
	GFMPG002	2.6%	17.8%	7°	1e6	0.1% 0.2% 0.5% 1%	$\{[0.25, 0.35), [0.85, 0.95)\}$ $\{[0.23, 0.45), [0.75, 0.85)\}$ $\{[0.45, 0.55), [0.65, 0.75)\}$ (figure 4.17)
	VACA4412s019	4.0%	12.0%	$[-9°, 15°]$	6.5e5 1e6 1.5e6	$[0.1, 1.1]\%$	$[0.36, 0.82\overline{6}]$ (figure C.3)

Table 4.2: Parameter variations for numerical investigations

4.2 Results

In this section previously published results from [FSF+21] are combined with the methodology published by [FAF+23] and new conclusions are drawn from this (sections 4.2.1 to 4.2.4). Additionally, results are discussed focusing on the effect of pressure level within the BLC region on the drag reduction (section 4.2.5).

4.2.1 Angle of Attack Dependency — Polar Sweep

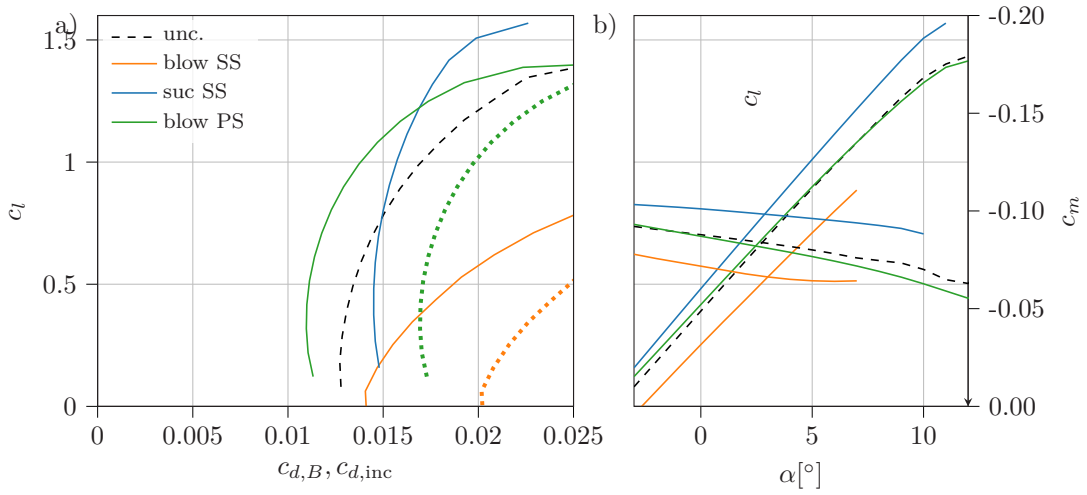

Figure 4.6: Polar plot of three example cases ($Re_c = 4 \cdot 10^5$) with a blowing rate of $v_{\mathrm{BLC}} = 0.5\%U_\infty$. Straight lines show the polar of the body drag coefficient $c_{d,B}$. The dotted lines show the polar of the inclusive drag coefficient $c_{d,\mathrm{inc}}$. Updated from [FSF+21, figure 8] to show inclusive drag

From [FSF+21, section 5A]: "In this section we report the results of the parametric study with Reynolds number $Re_c = 4 \cdot 10^5$ and blowing intensity of $v_{\mathrm{BLC}} = 0.5\%U_\infty$ for varying values of AoA. The results are mainly analysed in terms of the polar plot presented *e.g.* in figure 4.6, which reports both the [body and inclusive] aerodynamic coefficients [...]. First, we discuss the effect of suction on the SS, which was already identified by Prandtl to be beneficial in high-lift configuration by preventing separation in strong adverse pressure gradient (APG) environment [100]. The effectiveness of suction on SS to enhance lift has also been demonstrated in flight by Schrenk in the 1920s [121]. The polar for suction on SS clearly shows the enhancement of c_l, which is particularly significant at larger AoA. This is also true for the increase of section moment c_m over AoA (figure 4.6(b)). The additional lift is accompanied by a reduction in drag, at least for high-lift scenarios (Fig. 4.6(a)). Suction increases the wall shear stress, as discussed previously [127, AVF+20]. Thus, the drag reduction through suction on the SS is only due to the reduction of pressure drag. For small and negative AoA, *i.e.* for small enough lift coefficients, the decrease in pressure drag is entirely consumed by the increase in friction drag. As a result, suction on SS does not improve performance for low-c_l conditions, unless suction-induced relaminarisation occurs. This scenario is not considered in the present work.

With respect to blowing on SS, the aerodynamic effects are opposite to those of suction, mostly yielding an unfavorable configuration. Blowing on SS amplifies the effect of the strong APG and significantly thickens the boundary layer with respect to the uncontrolled case (see figure 4.4(c)). The resulting decrease in friction drag does not compensate for the large increase in pressure drag, as can be observed in the polar plot in figure 4.6(a).

Therefore, drag is overall increased. The detrimental effect of blowing on SS is severer for stronger APG and thus for high-lift scenarios. In these situations the separation is moved upstream by BLC which can also be seen in the wall shear stress curve crossing zero at lower X-values than in the uncontrolled case (figure 4.7). In summary, BLC on the SS results in a rotation of the polar: anticlockwise (beneficial) for suction and clockwise (detrimental) for blowing." from [FSF+21, section 5A]

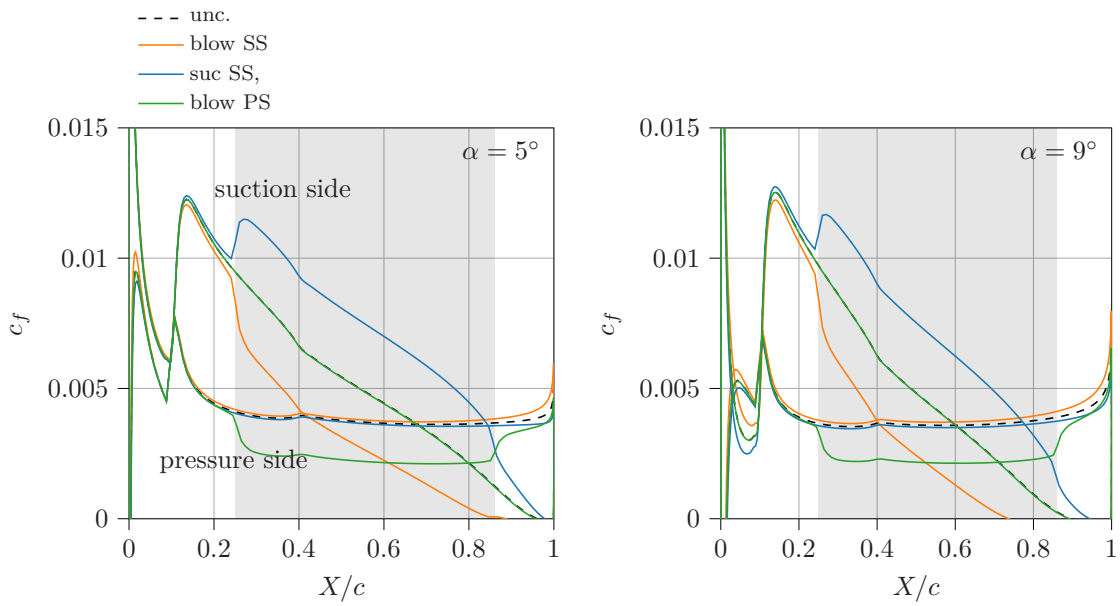

Figure 4.7: Skin-friction coefficient c_f at $\alpha = 5°$ (left) and $\alpha = 9°$ (right). The shaded area represents the BLC location. Adapted from [FSF+21, figure 9]

From [FSF+21, section 5A]: "BLC on PS behaves differently due to the mild pressure gradient (*e.g.* figure 4.5). Without the interaction with a strong APG, blowing on the PS successfully reduces friction without significantly increasing the boundary layer thickness. In fact, the overall pressure drag is reduced by blowing on the PS (NACA 4412, $\alpha = 5°$, $Re_c = 4 \cdot 10^5$, $v_{\mathrm{BLC}} = 2\%U_\infty$: $\Delta c_{d,p} = -6.1\%$) thanks to the thrust produced by the deflection of the additional mass flux introduced by BLC towards the streamwise direction. " from [FSF+21, section 5A]

This effect is directly linked to the potential flow solution of a source in a flow field and corresponds to the body drag reduction effect which can be attributed to the BLC-penalty discussed in section 3.1.1.

From [FSF+21, section 5A]: "This drag-reducing effect is always present for blowing, regardless of whether it is applied on PS or SS. However, on the SS it is exceeded by the pressure drag increase owing to the streamwise momentum deficit associated with the significant thickening of the boundary layer. Lift is essentially unaffected by blowing on the PS. [...]." from [FSF+21, section 5A]

The difference in the effect in strong APG boundary layers is also observable in the wake.

From [FAF+23, section 3.1]: "Comparing the mean flow contributions to the momentum deficit in the wake for the two different control scenarios (blue curves in figure 4.8) reveals significant differences. Blowing on the suction side deflects the wake upwards which is related to a substantial thickening of the boundary layer due to blowing in a region of adverse pressure gradient [AVF+20] thereby reducing circulation/lift. The boundary layer

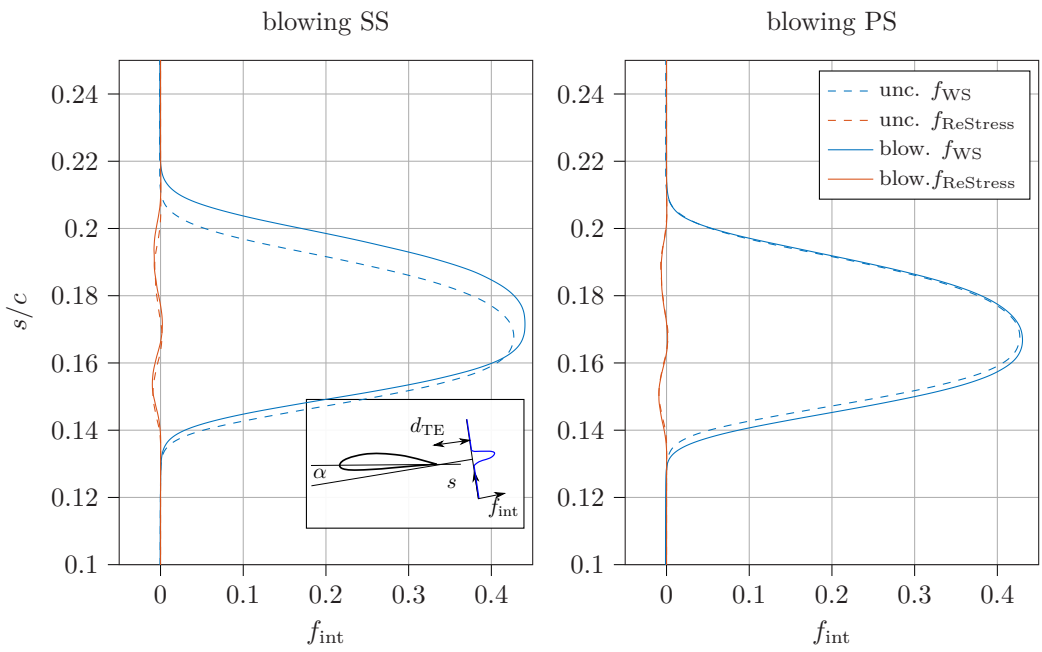

Figure 4.8: Wake profile f_{WS} (eq. 3.4) and Re-Stresses f_{ReStress} ([FAF+23, eq. 4]) for blowing on the SS and blowing on the PS at $d_{\mathrm{TE}}/c = 0.2$ behind the trailing edge. NACA 4412, angle of attack $\alpha = 5°$, $Re = 4 \cdot 10^5$, $v_{\mathrm{BLC}} = 0.1\%U_\infty$. Adapted from [FAF+23, figure 2]

on the pressure side of the airfoil is similar to a ZPG boundary layer resulting in a smaller growth of the boundary layer thickness due to the applied blowing compared to the suction side. Therefore, the corresponding downward deflection of the wake is less pronounced. ” from [FAF+23, section 3.1]

Moreover, in figure 4.8 the position of the wake flow for blowing on PS suggests that the flow on the upper (uncontrolled) side of the airfoil (SS) is barely affected and the wake keeps its position from the uncontrolled case.

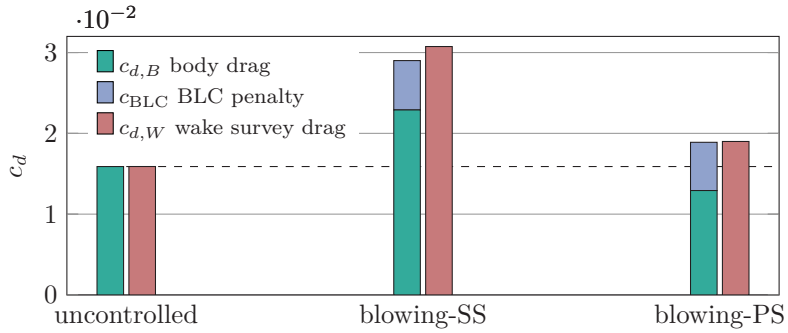

Figure 4.9: Comparison of *wake survey* drag, *body drag* and *BLC penalty*. NACA 4412, $Re = 4 \cdot 10^5$, $v_{\mathrm{BLC}} = 0.5\%U_\infty$, $d_{\mathrm{TE}}/c = 0.8$, $h/c = 1.1$, $\alpha = 5°$. $\Delta c_d = c_{d,\mathrm{controlled}} - c_{d,\mathrm{uncontrolled}}$. Modified from [FAF+23, figure 3]

It must be noted, that the conclusion about the beneficial effects of the blowing on PS is only true in the context of body drag. Figure 4.8 clearly shows that the wake survey drag (integral under the blue curves) increases also for the blowing on PS case (section 3.3). In other words, blowing on PS does not improve to outperform the uncontrolled polar in figure 4.6 in terms of inclusive drag. Figure 4.9 demonstrates this effect for an AoA of $\alpha = 5°$. The BLC penalty surpasses the body drag (reduction) significantly. This indicates that a reduction of inclusive drag (in case of

blowing equivalent to wake survey drag) and therefore a true *net drag reduction effect* cannot easily be achieved even for a case where a strong viscous drag (friction + pressure drag = body drag) reduction is present.

4.2.2 Reynolds Number Dependency

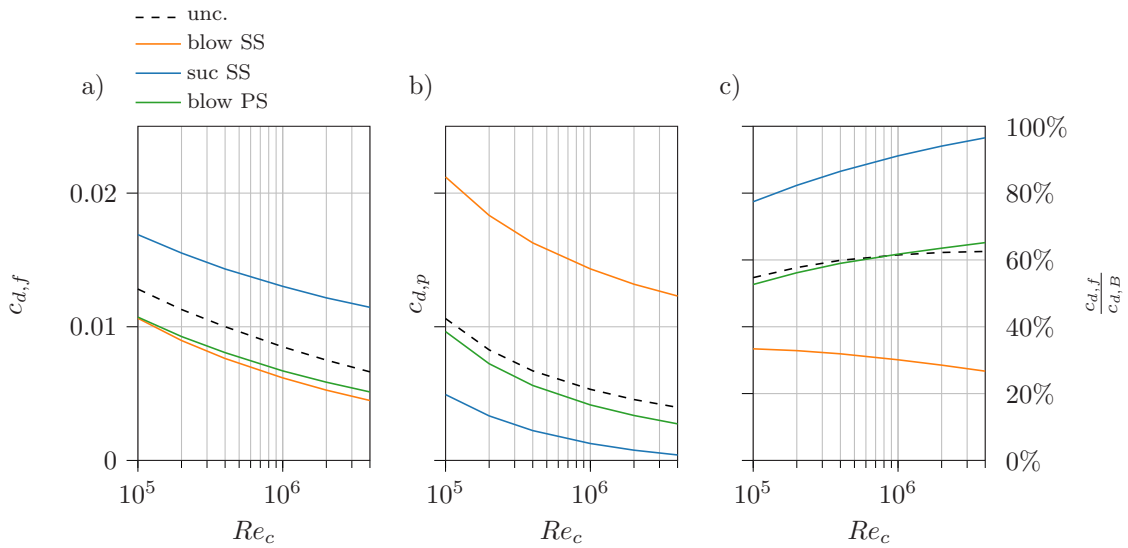

Figure 4.10: Development of drag components with Reynolds number. $\alpha = 5°$, $v_{\mathrm{BLC}} = 0.5\%u_\infty$. Friction drag $c_{d,f}$ (a), pressure drag $c_{d,p}$ (b), and ratio of friction drag to total body drag $c_{d,f}/c_{d,B}$ (c). Modified from [FSF+21, figure 10]

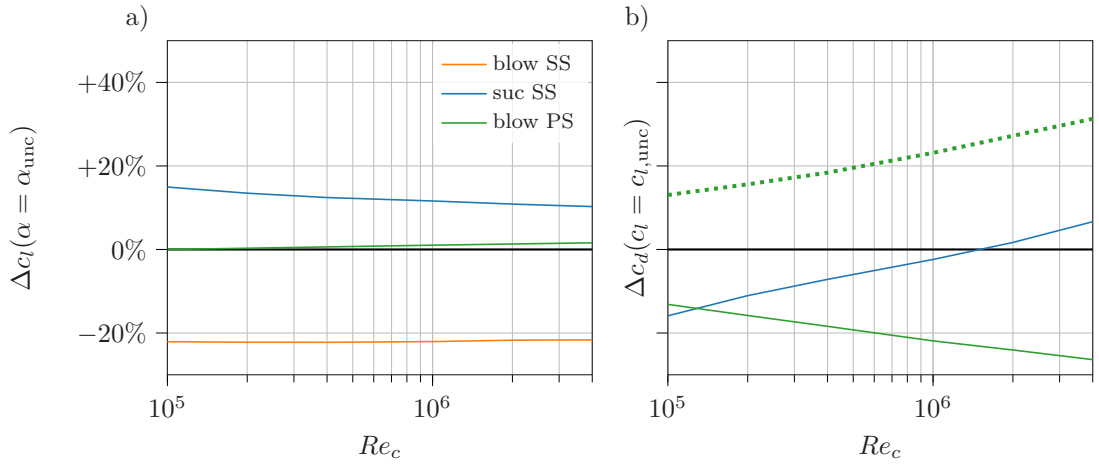

Figure 4.11: Development of aerodynamic coefficients and efficiency improvement relative to the uncontrolled polar. Operating point: NACA4412, $\alpha = 5°$, $v_{\mathrm{BLC}} = 0.5\%U_\infty$. Modified from [FSF+21, figure 11] to add inclusive drag evolution (dotted)

From [FSF+21, section 5B]: "In this section, the effect of the Reynolds number on the control performance is assessed by considering the configuration with AoA of $\alpha = 5°$ and the control intensity of $v_{\mathrm{BLC}} = 0.5\%u_\infty$ as baseline. Overall, as the Reynolds number increases, the lift coefficient c_l rises and the drag coefficient c_d drops. In particular, both drag contributions $c_{d,p}$ and $c_{d,f}$ decrease with Re_c, as it is shown in figure 4.10(a-c). Considering the BLC cases, the most interesting observation is that uniform blowing does not necessarily increase pressure drag despite boundary layer growth, as already discussed in the previous section.

Blowing yields similar friction drag reduction on both PS and SS, while only the former yields a reduction of pressure drag at all values of Re_c considered here. As a result, blowing on PS exhibits a ratio of friction-to-total drag of around 60%, which is similar to the uncontrolled case. Different results are observed for suction on SS which delivers negligible pressure drag towards $Re_c \to 10^7$. This means that the boundary layer is almost completely removed leaving no pressure drag at all but a solution close to the inviscid solution regarding pressure drag. The opposite is true for blowing on SS, since boundary layer growth and thus pressure drag are amplified resulting in a friction-to-total drag ratio below 40% and exhibiting a negative slope with Re also beyond $Re_c = 4 \cdot 10^6$. [...] The performance enhancement is evaluated either as drag reduction for equal c_l (figure 4.11(b)) [...]. The control intensity is chosen as $v_{\mathrm{BLC}} = 0.5\% u_\infty$.

Since uniform suction reduces boundary layer thickness in a similar way as an increase of Re_c would do, the performance improvements relative to the uncontrolled case drop with higher Re_c for suction on SS. [...]

Since uniform blowing locally increases the boundary layer thickness, the achieved variations compared to the uncontrolled case rise with increasing Re_c and thus overall shrinking boundary layer thickness. Blowing on SS confirms to be detrimental to performance at all considered values of Re_c. Although flow separation following uniform blowing is reduced for higher Re, the adverse pressure gradient on SS remains large and results in high pressure drag if blowing is applied there. Despite the rather negative effect of blowing on the SS, regarding both development with Re and AoA (previous section), the configuration may still offer possibilities related to indirect drag savings. Since the effects reported for this scheme are almost exactly opposite to the effects of suction on SS this scenario might be beneficial for roll control with the advantage of not producing a negative but positive roll-yaw moment. The combination of blowing and suction on SS could therefore replace classical ailerons similar to a solution recently adopted by BAE-Systems [138]. In principle this would lead to a possible reduction of vertical stabilizer size and its corresponding drag. The local pressure in the BLC region (figure 4.5) would also allow for passive convection thus enabling actuation via valves only.

Again, blowing on PS is the only scheme among the considered ones to consistently improve performance over the investigated parameter range. It should be noted, however, that it might be unrealistic to assume large turbulent boundary layer areas at $Re = 10^5$ on PS, as we do in the present study. However, this way the trend for the turbulent case becomes apparent and thus it is important to note that even for the highest Reynolds number investigated in this study the slope of improvement is still positive [...]." from [FSF+21, section 5B]

Similar to the previous section, the findings by Fahland *et al.* [FSF+21] hold for the body drag only. Considering the inclusive drag, a relative drag increase can be observed for rising Reynolds number even for the scheme with significant body drag reduction: blowing on PS. This stems from the — in the dimensionless form — constant BLC penalty (eq. 3.5) of which the relative impact rises if the viscous drag (compare figure 4.10) falls as it does for increasing Reynolds number.

4.2.3 Control Intensity Variation

From [FAF+23, section 3.1]: "The effect of increased blowing intensity $v_{\mathrm{BLC}}/U_\infty$ on the global drag coefficients is shown in figure 4.12. The left part of the figure corresponds to blowing on the suction side of the airfoil for which the *body drag* increases in general. The contributions of friction and pressure drag to the *body drag* $c_{d,B}$ are marked in color. It

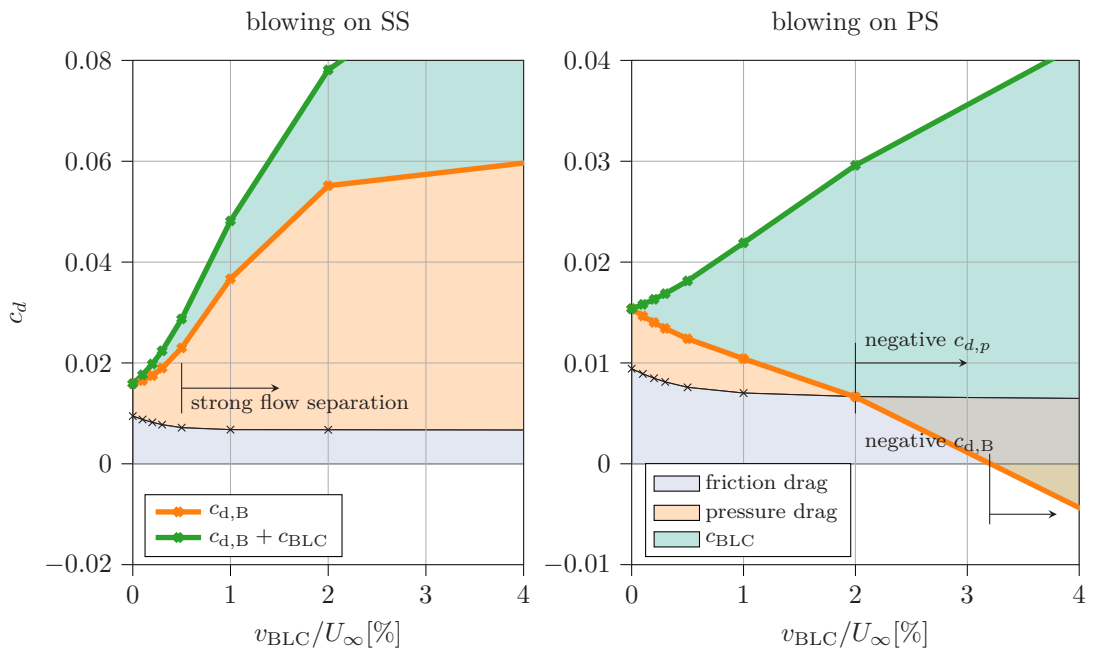

Figure 4.12: Drag portion development for increasing intensity of uniform blowing on SS (left) and PS (right) for NACA 4412, $Re = 4 \cdot 10^5$, $\alpha = 5°$. Adapted from [FAF+23, figure 4]

can be seen that the pressure drag strongly increases with increasing blowing intensity. The skin friction drag is reduced by blowing as expected and converges to a constant value for $v_{BLC}/U_\infty > 1\%$ (for the present configuration) which stems from the friction contribution of the uncontrolled parts of the surface. Since blowing is applied in an adverse pressure gradient boundary layer, the controlled flow region becomes susceptible to separation and strong flow separation is observed for $v_{BLC}/U_\infty > 0.5\%$. The boundary layer control penalty c_{BLC} increases linearly with v_{BLC}/U_∞ and needs to be considered on top of $c_{d,B}$ as discussed above.

The case of blowing on the pressure side of the airfoil is shown in the right part of figure 4.12. Note that the vertical axis is scaled differently than in the left part of the figure. The friction drag contribution develops very similar to the case of blowing on the suction side. However, the pressure drag contribution exhibits a distinctly different behavior. As previously discussed by Fahland *et al.* [FSF+21], it continuously decreases with increasing blowing intensity. For $v_{BLC}/U_\infty > 2\%$ the pressure drag switches signs indicating a negative contribution to the *body drag* which leads to negative $c_{d,B}$ for $v_{BLC}/U_\infty > 3.2\%$. In this flow control regime, the airfoil itself thus experiences a negative drag, or in other words a thrust in upstream direction. This counter-intuitive phenomenon comes at a cost translated into c_{BLC}. The sum of $c_{d,B}$ and c_{BLC} constantly increases with v_{BLC}/U_∞ indicating that the total force required to move the airfoil with BLC at U_∞ does never fall below the uncontrolled reference case. As discussed above this total force requirement is reflected in the momentum deficit in the wake which increases with increasing blowing rate since the added control mass flow rate has to be accelerated to U_∞. " from [FAF+23, section 3.1]

4.2.4 Geometry Variation — Camber and Thickness

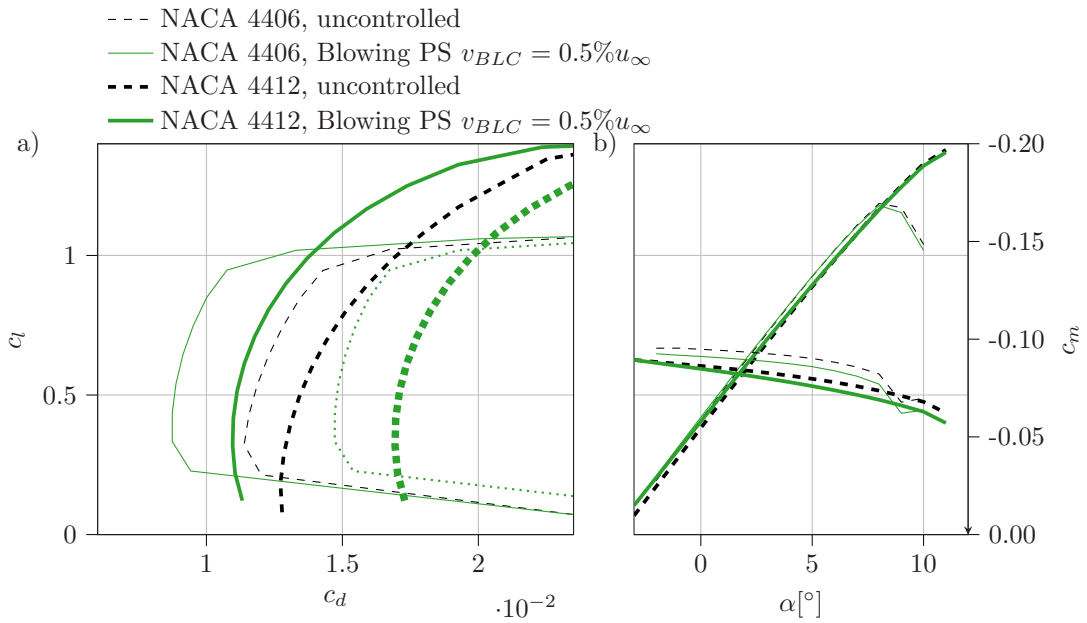

Figure 4.13: Polar plot for varying thickness in case of blowing on PS with $v_{\mathrm{BLC}} = 0.5\%$,$Re_c = 4 \cdot 10^5$. Dashed lines are uncontrolled cases. Modified from [FSF+21, figure 12] to show inclusive drag (dotted)

> From [FSF+21, section 5D]: "As known since the studies by Jackobs *et al.* [49], thicker airfoils are more capable of producing lift than thinner airfoils while allowing for higher structural strength of the wing. This comes at the cost of higher drag at low-lift cruise conditions, as nicely illustrated in figure 4.13, which also shows the polar plots for the most promising configuration of blowing on PS ($v_{\mathrm{BLC}} = 0.5\%u_\infty$, $Re = 4 \cdot 10^5$) at various thicknesses.
>
> The drag reduction at low c_l is larger for thinner airfoils, while the BLC effects on c_m and c_l *vs.* AoA are minor. For the thinnest airfoil considered here (thickness $t = 6\%c$), the aerodynamic drag savings at lift coefficient $c_l \approx 0.5$ (cruise conditions, $\alpha = 2°$, $v_{\mathrm{BLC}} = 0.5\%u_\infty$) accumulate at $\frac{\Delta c_d}{c_d} = 33\%$ for Reynolds number $Re = 4 \cdot 10^6$ and $\frac{\Delta c_d}{c_d} = 24\%$ for $Re = 4 \cdot 10^5$." from [FSF+21, section 5D]

Yet again, the inclusive drag polars (dotted lines in figure 4.13) show higher drag for all cases considered.

> From [FSF+21, section 5D]: "Figure 4.14 shows the combined effects of simultaneously varying blowing intensity v_{BLC}, Re as well as thickness t_a at $Re = 4 \cdot 10^5$ at AoA of $\alpha = 5°$. Beside confirming that the BLC is more effective for thinner airfoils, it shows that the dependencies with t_a, Re_c and v_{BLC} are almost linear in the three parameters when the BLC system drag is not included into the computation. This observation might not hold for more extreme parameter variations but the scope of the study covers the most feasible variations for aviation application in incompressible flows. " from [FSF+21, section 5D]

It is observable again that the decrease in body drag does not convert to inclusive drag reduction. On the contrary, the control penalty drag is only proportional to the strength of the blowing velocity v_{BLC} (figure 4.14 left). The apparent increase of inclusive drag with Reynolds number Re_c is an effect of decreased uncontrolled drag: The respective uncontrolled case experiences less

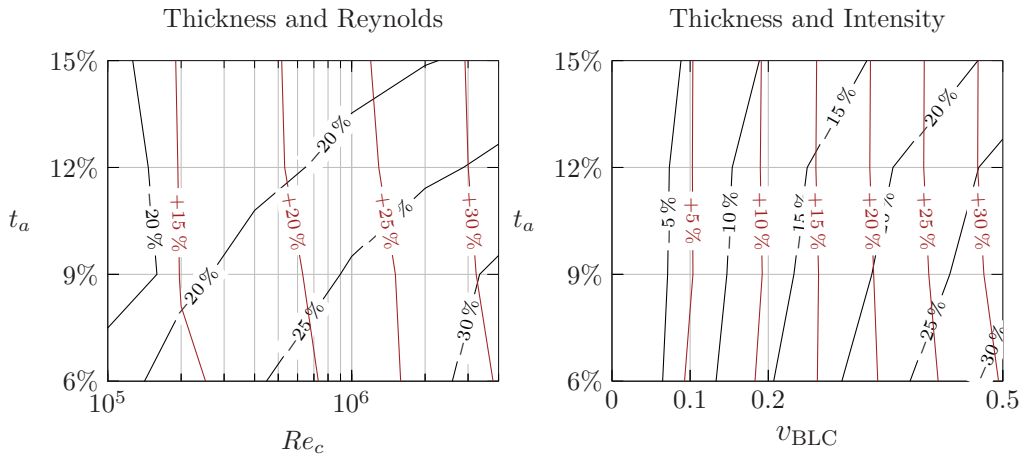

Figure 4.14: Drag reduction ($\Delta c_d < 0$: drag reduction; $\Delta c_d > 0$: drag increase) as function of airfoil thickness t_a and Reynolds number Re_c (a) respectively blowing intensity v_{BLC} (b). Plain aerodynamic comparison $\Delta c_{d,B}$ is plotted in black, and inclusive drag difference $\Delta c_{d,\mathrm{inc}}$ is plotted in red. $\alpha = 5°$ Modified from [FSF+21, figure 13] to show inclusive drag.

drag at higher Re_c. Therefore, a constant inclusive drag increase by uniform blowing will reach a higher percentage for lower uncontrolled drag. In figure 4.14 this is demonstrated for varying airfoil thickness and therefore pressure gradient and pressure level within the blowing region. However, the effect that inclusive drag is increased proportionally to the blowing rate persists for all cases investigated.

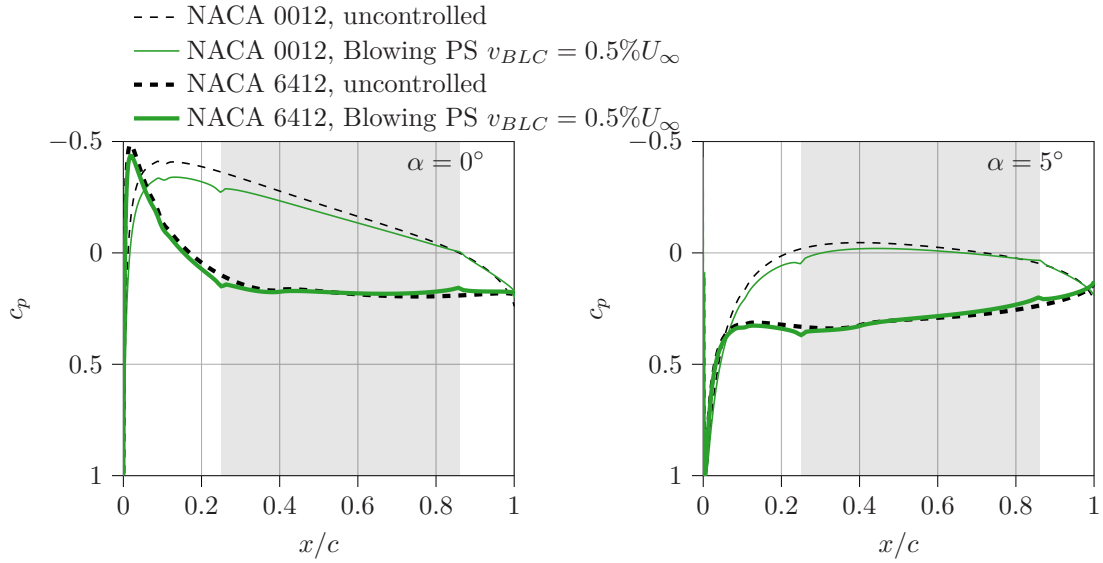

Figure 4.15: Pressure coefficient c_p on PS for $\alpha = 0°$ (left) and $\alpha = 5°$ (right). $Re = 4 \cdot 10^6$. The shaded area represents the BLC location.

From [FSF+21, section 5D]: "As long as the suction peak at the leading edge on the PS does not become too strong (see Fig. 4.15 for pressure distribution), substantial relative improvements can be reached for cambered airfoils at low AoAs. In principle, symmetric airfoils are more suited to be used in a low-c_l configuration, yet this is not the case including BLC: the plain aerodynamic drag at $\alpha = 0°$ is basically constant over Re and does not follow the improvement of cambered airfoils which is approximately logarithmic in Re. [...] This can be explained by considering Fig. 4.15, where the pressure coefficient on the PS of differently cambered airfoils is shown for two different AoA. Smaller camber implies a more

adverse pressure gradient on the PS within the BLC region for a given AoA, a condition which intensifies at lower at AoA approaching $\alpha = 0°$. Therefore, even for high values of Re, blowing on PS acts on a turbulent boundary layer with limited capability of reducing friction drag without excessively amplifying boundary layer growth. The performance of BLC on symmetric airfoils improves for larger AoA or c_l respectively as the pressure distribution on the PS gets more favourable within the control region. Meanwhile cambered airfoils show a significant improvement [of body drag] over the full range of AoA investigated here." from [FSF+21, section 5D]

4.2.5 Pressure Level Effect

So far, the present study could confirm a finding of Atzori [7] for uniform blowing in TBL: The correlation of body drag reduction and favorable pressure gradient and vice versa the correlation of body drag increase and adverse pressure gradient (see section 2.6 and sections 4.2.1, 4.2.4).

However, the presented results also correlate with the static pressure level at the control location: The higher the local pressure, the better the BLC performance. Two test cases are developed to separate the effects of pressure gradient and pressure level. This aims at evaluation of the hypothesis raised in section 3.3 and therefore answer the question: Does the BLC performance of uniform blowing depend on the local pressure level at the control position?

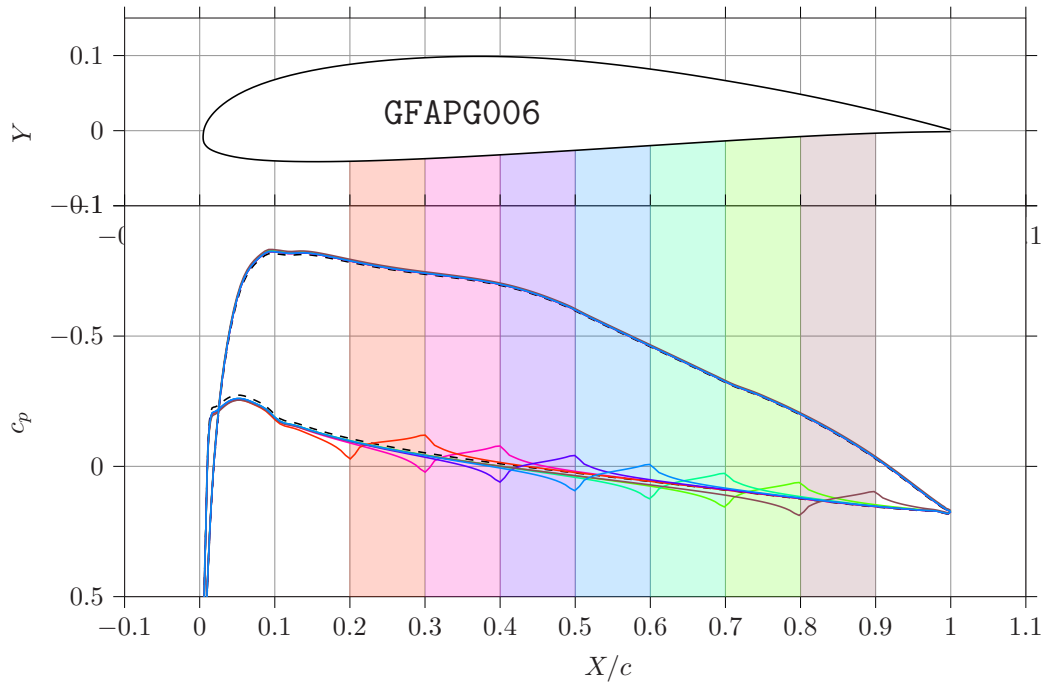

Figure 4.16: Airfoil GFAPG006 with 7 different blowing regions on airfoil PS at approximately similar pressure gradient but different mean pressure level. AoA $\alpha = 1°$, $Re_c = 1$Mio, $c_q = 1\%U_\infty$. Airfoil coordinates in table C.1

The first test case "GFAPG006" shows an airfoil conceived exclusively for this test. It yields an adverse pressure gradient (APG) on the pressure side (PS) of the airfoil (figure 4.16). This is an atypical case because common test cases of uniform blowing BLC in the current study and literature studies usually show favorable pressure gradient (FPG) on the PS, at least for positive lift $c_l > 0$. The blowing is applied in 7 individual regions with increasing static pressure c_p to the aft of the airfoil. The pressure distributions of the controlled cases (curve color identical to control

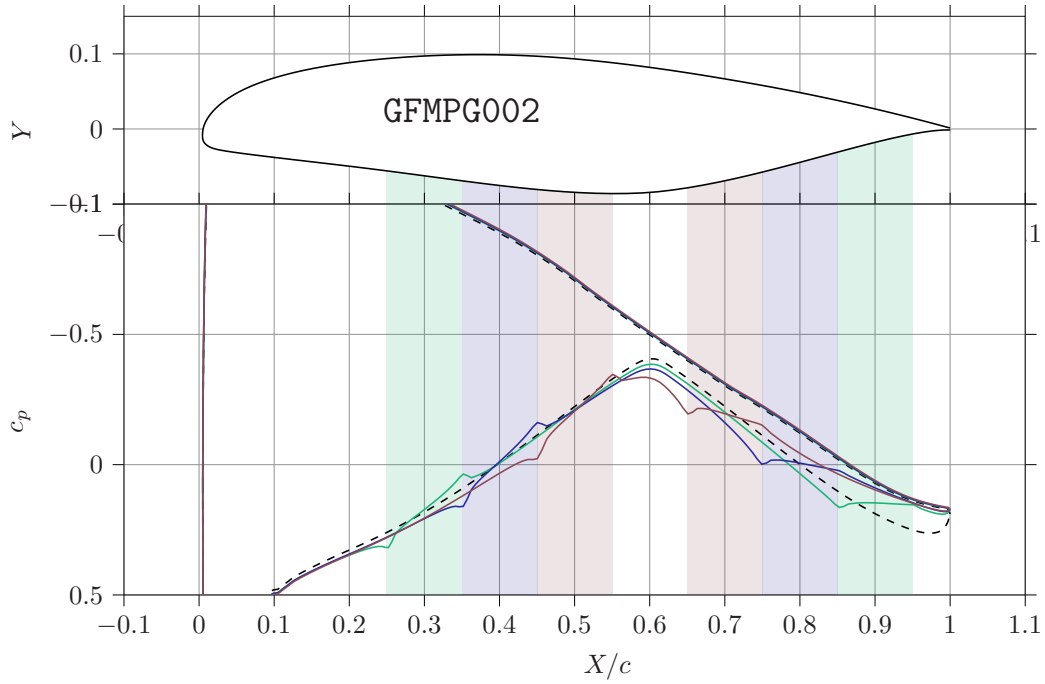

Figure 4.17: Airfoil MPG with 3 different blowing regions on airfoil PS at similar adverse and favorable pressure gradients but three different mean pressure levels. AoA $\alpha = 7°$, $Re_c = 1\text{Mio}$,$c_q = 1\%U_\infty$. Airfoil coordinates in table C.1

region color) show a distinct slope of a slight stagnation at the beginning and an acceleration at the downstream end of each control region. This effect is consistent with the literature (*e.g.* [70]). To the trailing edge, all cases collapse with the uncontrolled case (dashed black line).

The second test case is carried out on another individually designed airfoil "GFMPG002" (figure 4.17). The design goal was to remove a pressure gradient bias by applying the control at both adverse and favorable pressure gradients simultaneously and testing this setup for different pressure levels. The BLC region again is located on the pressure side of the airfoil and the control configuration consists of two regions at similar pressure level c_p but opposite pressure gradient $\partial c_p/\partial x$. Again, the distinct stagnation-acceleration pressure distribution is observable for the different control cases at the start respectively end of each control region.

Figure 4.18 shows the drag development for identical blowing ratios applied to regions with different static pressure relative to stagnation pressure. Clearly, the friction drag reduction is less ($c_{d,f}$ is higher) if the blowing is applied to a region of higher c_p. This is expected as higher c_p means lower velocity at the edge of the boundary layer U_e. Lower velocity correlates with less wall friction τ_w in most cases hence less reduction potential for flow control. Vice versa, at higher local velocity the shear is stronger. Therefore the wall friction is larger which means that also the reduction potential is larger. Despite this favorable condition regarding friction drag reduction for blowing applied at lower static pressure, the overall drag is increased in this scenario. This stems from the strong pressure drag increase if blowing is applied at lower c_p. The better performance of pressure drag for BLC applied to higher c_p is also reasonable considering the energy budget (section 3.1.2). If one approaches the maximum of $c_p = 1$ the total energy (corresponding to total pressure) of the injected BLC fluid equals the total pressure of the freestream, therefore causing no subsequent mixing losses. Both test cases show that, at least for stronger blowing rates, this decrease in pressure drag for higher c_p in the blowing region surpasses the reduced effectiveness of friction drag reduction clearly.

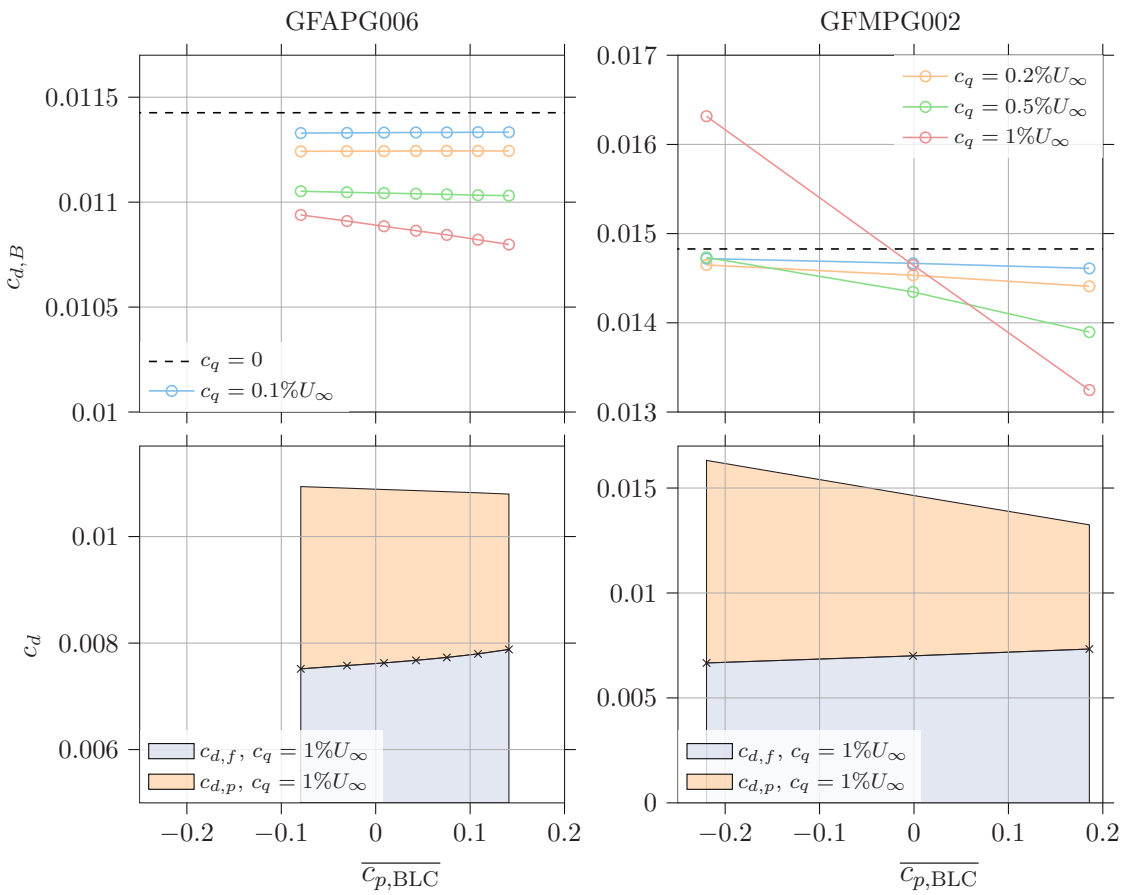

Figure 4.18: Comparison of drag reduction due to uniform blowing for different pressure levels in application region. Left: Adverse Pressure Gradient test case; right: mixed pressure gradient test case. Re_c = 1Mio, $c_q = 1\%U_\infty$

The results for both test cases show a clear correlation despite different pressure gradient situations on boundary layer development: The higher the local static pressure c_p within the control region, the lower the drag or, in other words, the higher the drag reduction. It must be noted, that this is merely a correlation, and no definite conclusion can be drawn. Yet, both test cases very strongly support the hypothesis raised in section 3.3: The evidence shown here and in the analytical section 3.1.2 clearly indicates a dependency on the control performance from the local pressure relative to stagnation pressure.

4.3 Conclusions of Numerical Results

The numerical investigations of the present study could confirm the findings of previous studies: Uniform blowing in turbulent boundary layers is suitable for reducing the skin friction drag substantially. In fact, the skin friction within the control region tends towards zero for increasing blowing strength. The local skin friction drag reduction due to blowing persists downstream of the control region in accordance with findings from literature (*e.g.* [127, 70]). In consequence, the integral friction drag of the airfoil with control tends towards a limit for increased blowing. This limit depends on the ratio of the controlled to the uncontrolled surface area.

Uniform blowing was not found to necessarily increase pressure drag which is a common suspicion in conference discussions when it comes to the penalty of friction drag reduction. This argument relies on the increase in boundary layer thickness which is then generalized to result in pressure

drag increase [31]. However, this is only true for most cases of uniform blowing on the suction side of an airfoil. Instead, blowing on the pressure side of an airfoil is favorable in terms of pressure drag reduction despite a boundary layer thickness increase. The present study explains this seeming contradiction by the potential solution of a flow with a source of fluid which reduces drag. The favorable pressure gradient on the pressure side of the airfoil ensures that separation and excessive boundary layer growth are avoided. Thereby, the force resulting from the source flow acts against the pressure drag of the body. This source flow force is much smaller than the increase in pressure drag due to boundary layer separation or excessive boundary layer growth in case of blowing in adverse pressure gradient on the suction side.

Drag reduction gets stronger the more favorable the pressure gradient on the PS. Therefore, an increase in camber and a decrease in thickness leads to a stronger drag reduction for blowing applied on the airfoil PS because the pressure gradient becomes more favorable within the blowing region.

In addition to this, the present numerical investigations confirm the hypothesis from the analytical investigations (section 3.3): Drag reduction (or increase) also correlates with the local static pressure level: The higher the local pressure within the BLC location, the lower the drag with active blowing control. This is true for all cases investigated for the NACA airfoil series. Furthermore, the present numerical investigations could show that the drag reduction trends persist if pressure level and pressure gradient are investigated in a case that separates their common coincidence. All numerical evidence strongly suggests that uniform blowing performance is indeed coupled to the pressure level within the controlled region although this may not be regarded as a final conclusion due to the complexity of the flow scenario around airfoils.

Despite the strong friction drag reduction potential as well as the cases in which a pressure drag reduction is observable, no cases could be found where the inclusive drag — the drag quantity that respects the theoretical effort to supply the control fluid — is decreased by uniform blowing on airfoils.

Even if uniform blowing in turbulent boundary layers may not be able to yield net drag reduction (inclusive drag reduction) the numerical results of the present study showed good performance as a boundary layer control scheme in terms of controlling local lift and drag quantities similar to geometrical changes of the airfoil or control surfaces. Therefore, aircraft control by uniform blowing BLC may be possible. An augmented control for aircraft maneuver enhancement was *e.g.* investigated by Bonfert [Bon21] numerically.

5 Experimental Investigation

This chapter covers the design and operation of a test stand (section 5.1, 5.2.2 – 5.2.7) as well as the test case model (section 5.2.1) created to measure multiple performance quantities (lift, drag, wake and boundary layer uniformity) affected by uniform blowing in turbulent boundary layers on an airfoil.

5.1 Facility

The Göttingen-Type Windtunnel at the Institute of Fluid Mechanics was commissioned in 1957 [73, p. 17-30]. It features a closed return circuit and an open jet test section layout. Due to this layout, it is prone to low-frequency pressure fluctuations [141, 105, 18, 137, 12], often called wind-tunnel buffeting. For this particular facility, such fluctuations were also reported to influence experimental campaigns (*e.g.* [64] although no direct connection is drawn to the phenomenon of wind-tunnel buffeting). The prospect of improving the flow quality sparked an interest in a thorough refurbishment which started in 2017.

At the start of the present PhD studies the engine, settling chamber, and nozzle were already modernized. The measurement systems, tunnel control, test section housing, traverse system, flow quality improvement as well as synchronized data recording were developed alongside the present work to meet the scientific requirements. The present manuscript is focused on the wing test rig and the airfoil model. The remainder of the information about the facility can be found in the facility manuals (Appendix A) which were created alongside this manuscript.

5.1.1 Characterization

The nozzle cross-section of the wind tunnel is width x height: 1.8m $\times$ 1.4m. The core length can be described at the extension from the nozzle exit plane where a laminar block profile core jet still exists. It reaches a length of about three to four meters depending on the exact test case of the wind tunnel. The velocity of the wind tunnel can be controlled within a range of $U_\infty \in [2, 50]\frac{\mathrm{m}}{\mathrm{s}}$. Further details on the properties of the wind tunnel and test section can be found in [Fah24b].

Thermodynamic quantities of the working fluid (air) determine the current setpoint of reference quantities such as velocity or Reynolds number of an operating point. Therefore, even dimensionless values are not independent of the chosen tunnel operating point which in turn requires the tunnel control to acquire all necessary thermodynamic quantities in real time. This is done according to figure 5.1 and results are stored alongside acquired test object measurement data for consistency in data processing. This is necessary to achieve *e.g.* identical Reynolds number settings in different weather situations, such as winter and summer (see measurement campaign list in table 5.6).

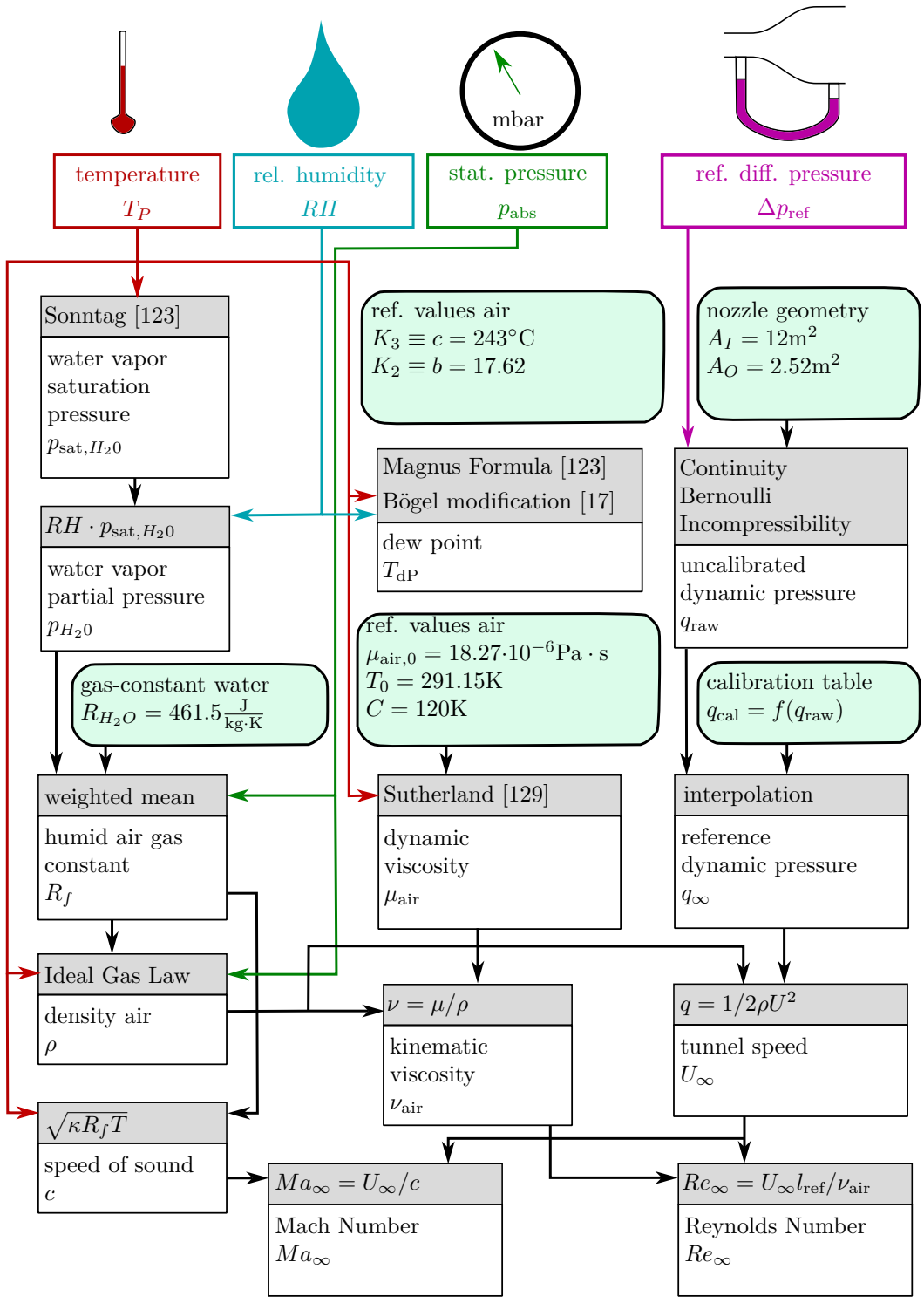

Figure 5.1: Calculation of Wind-Tunnel reference quantities

5.1.2 Wind-Tunnel Buffeting

The aforementioned low-frequency wind-tunnel fluctuations were one of the main targets for flow quality improvement of the facility. The research was carried out in parallel to the present PhD study and was driven mostly by student contributions in the form of Bachelor's and Master's theses. See Appendix B for detailed acknowledgment of each contribution. This led to a joint conference contribution regarding the analysis and improvement measures for the Göttinger Windtunnel at ISTM [FEW+23].

> From [FEW+23, Abstract]: "Low-frequency wind-tunnel fluctuations occur especially in open-jet closed-return circuit wind-tunnels. The present work addresses identification of modes within the frequency and spatial domain of these fluctuations. Experimental data is collected in a full scale tunnel and its scale model by the means of distributed, synchronized pressure measurements. Application of spectral proper orthogonal decomposition revealed the existence of multiple acoustic and convective modes. This in part confirms previous findings which were based on frequency analysis only, such as the existence of the edge-tone feedback mechanism for low speed wind-tunnels. For other idealizations, such as the wind-tunnel acting as Helmholtz resonator, no proof could be found. With this understanding improvement measures were developed, tested and improved. During this process modal decomposition led the way to fluctuation reductions of over 6dB, i.e. 50%." from [FEW+23, Abstract]

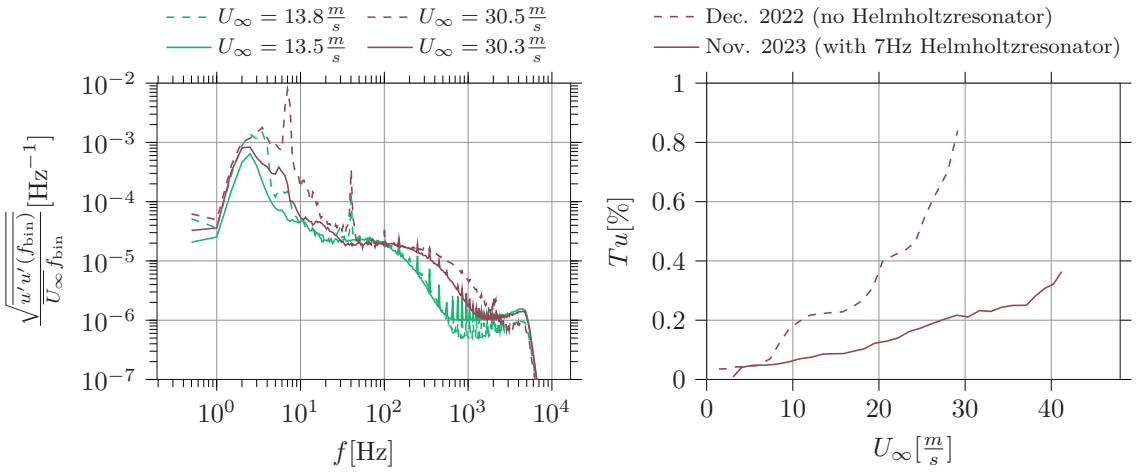

Figure 5.2: Turbulence Spectra prior and after the measurement campaign of VACA4412s019, bandpass filtered $[2, 5000]$Hz (left), bin size $f_{\mathrm{bin}} = 0.5$Hz, integral turbulence intensity over wind-tunnel velocity (right)

At this point, the most effective improvement measure so far shall be mentioned, because it also affected the measurements of the present thesis. The addition of the Helmholtz Resonator reduced the integral turbulence level by a factor of 2 to 3. This becomes visible by comparing the turbulent spectra of the wind tunnel (figure 5.2) before the measurement campaign (before the installation of the Helmholtz Resonator) and afterward. As the Helmholtz Resonator was installed quite early into the campaign, most of the presented results were obtained with the superior turbulence conditions (installation between March 25 and April 10, 2023. See table 5.6 for detailed information on which measurements were conducted in which environment). All PIV measurements were conducted with the Helmholtz Resonator installed.

5.2 Setup

5.2.1 Test Case Design

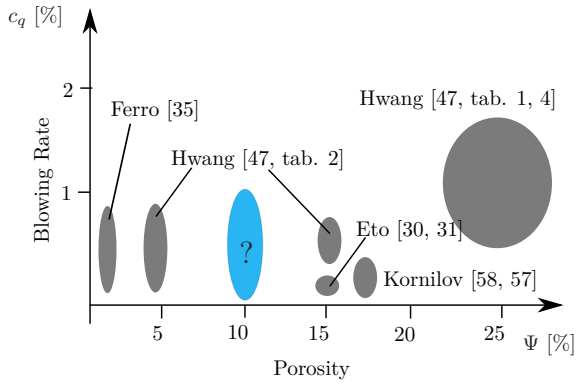

Figure 5.3: Porosity with circular and conical holes of experimental studies from literature on uniform blowing in turbulent boundary layers

On one hand, the questions to the experimental study focus on validating the trends derived from the numerical studies which were based on RANS simulations mostly and therefore do not necessarily capture the physics of the control acting in TBL accurately. Furhermore, the implementation of a porous surface instead instead of a uniform wall is not modelled in RANS (or higher fidelity simulations such as well-resolved LES and DNS simulations in this field [7]). The data available from experiments in the literature is rather sparse for porous plates of which the porosity is based on laser-drilled hole patterns (figure 5.3). There is a lack of porosity $\Psi = A_{\text{hole}}/A_{\text{BLC}} \approx 10\%$ with the area of open surface (holes) A_{hole} and the total area of the BLC surface A_{BLC}. Hwang suspected this to be a suitable porosity level in terms of maximizing skin friction drag reduction and minimizing manufacturing effort [47, p. 13] but had no experimental test case with this parameter combination himself. This is why $A_{\text{hole}}/A_{\text{BLC}} = 10\%$ is chosen for the present experimental investigations.

The airfoil model shall accommodate cases that showed a strong change in integral quantities in order to provide a significant and accurate measurement result. This means, that blowing on PS is the most suitable scheme to investigate as pressure drag reduction and friction drag reduction coincide such that they do not erase each other in integral quantities. Furthermore, the experiment shall be suitable for comparisons with other experiments in the field. The numerical studies showed that the performance of blowing on the pressure side thrives with increased airfoil camber f and decreased thickness t_a (section 4.3). This makes a thin and cambered airfoil most interesting to investigate. Yet, the boundary layer control has to be implemented within the available model volume and the structural integrity of the model has to be ensured. A strong camber leads to strongly curved surfaces, also on the airfoil pressure side. This can become problematic regarding the precise assembly of the BLC surface. In consequence, NACA4412 is chosen as an airfoil shape. For one, it is rather thin and still cambered. Furthermore, it is a common choice for experimental and numerical studies as well as for small-sized aircraft (general aviation). In particular, NACA4412 [72] or similar airfoils like ClarkY [31, 46] are also common for studies of uniform blowing on airfoils. Choosing such an airfoil for the present study provides better comparability than choosing a more exotic airfoil. In addition, NACA4412 comprises a very flat surface on the pressure side which can be used to achieve both mildly positive and negative pressure gradients depending on the angle of attack. This makes the model also suitable for boundary layer flow investigations, not just integral quantity investigations.

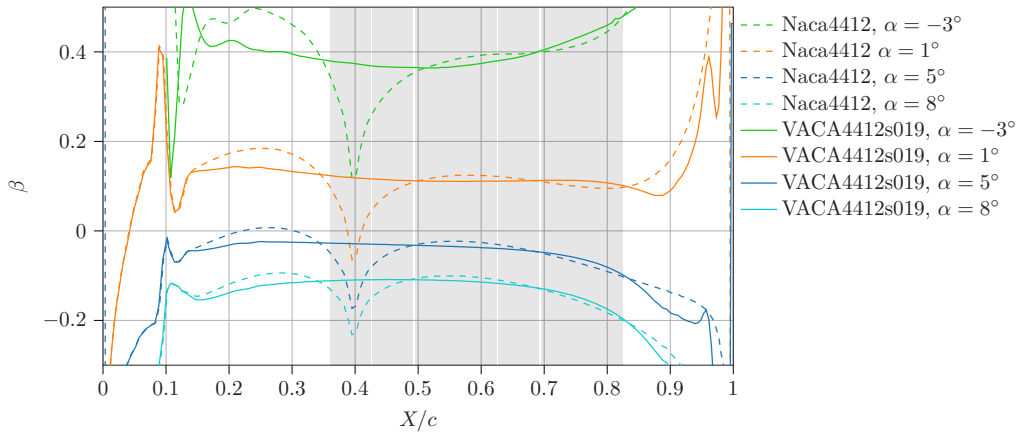

Figure 5.4: RANS data: Boundary layer equilibrium parameter / Clauser Parameter β for different freestream AoA, $Re_c = 10^6$, NACA4412 and VACA4412s019. The final location of the control area is given in grey.

Yet, NACA4412's shape definition is based on multiple polynomials that have a non-steady curvature at their intersection at $x/c = 40\%$ (slightly visible in pressure distribution figure 4.5). Moreover, the Clauser-Parameter β (eq. 2.37) has a distinct dent on the airfoil pressure side at the aforementioned $X/c = 40\%$. This indicates that the boundary layer strongly deviates from equilibrium. Therefore, this feature is removed using XFOIL inverse design method [26]. The resulting airfoil VACA4412s019 (table C.2, figure 5.8) shows identical macroscopic properties in integral quantities as NACA4412. As figure 5.4 shows, the boundary layer equilibrium parameter (Clauser Parameter) is far more steady for VACA4412s019 than for NACA4412.

The boundary layer control is integrated such that the control surface is maximized in streamwise ($\equiv$ chord) direction. Some trade-offs have to be made between maximizing control surface size and minimizing model size. Larger model size coincides with more blockage (section 5.2.2) and more severe wind-tunnel correction (section 5.3.3). The model chord length is chosen as $c = 750$mm, which favors control surface area over the maximum reasonable angle of attack (discussion about the wind-tunnel correction effects and their accuracy for the present choice of model size in section 5.5.1). The support structure of the control sheet has to fit inside the model and is further limited by not intersecting the main model spar at quarter chord length. By this, the maximum control surface is achieved for $X_{\mathrm{BLC}}/c = [0.360, 0.825]$ (table C.3, and grey area in figure 5.4).

The subsequent engineering details for the VACA4412s019 airfoil model are summarized in appendix C

5.2.2 General Test Rig Design Considerations

Requirements Preparation of the test rig started before completing numerical and analytical results (sections 3, 4). Also, it was unclear what measurement technique would be most suitable to complement numerical and analytical results which were unavailable at that time. Therefore, it was decided to head for a multitude of measurement options for each integral quantity. This means that lift could be measured by a balance (section 5.2.3) and pressure taps (section 5.2.4), drag by a wake survey (section 5.2.5) and the balance, the pitching moment by the balance and the pressure taps and the pressure drag by the pressure taps. Furthermore, optical measurements should be possible to implement easily and flexibly in order to investigate details in the controlled boundary layer depending on the later course of the study.

Design choices The second Helmholtz-Theorem requires an infinite span of the wing section or a phase boundary (see section 2.1) to allow for 2D flow conditions. As the former is infeasible, the test section includes **endplates for the airfoil**. The endplates are separated into **turntables**

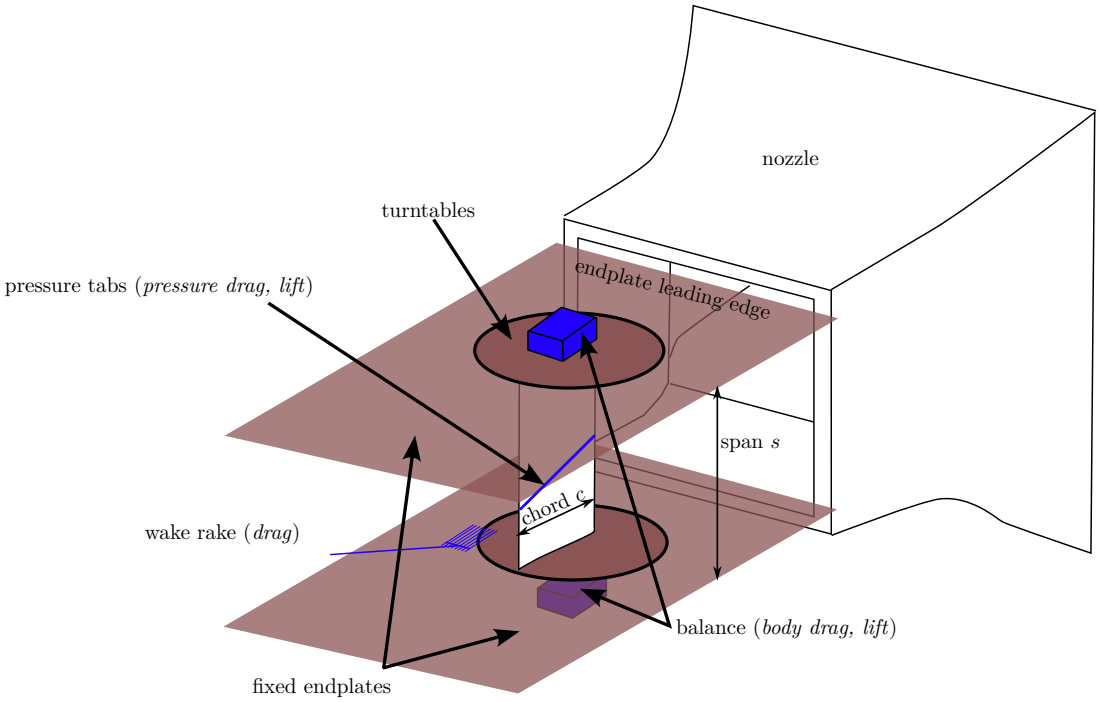

Figure 5.5: General test rig schematic and part nomenclature. Final test rig design in figure D.1

which are connected to the model and the balance and **fixed endplates** which make up for the largest portion (see figure 5.5). This way, the influence of that wall friction on the balance result is limited. Still, wall-shear stress on the turntables has to be quantified (see section 5.3.1) which is done most easily if the boundary layer state is known. This can be realized if a new (turbulent) boundary layer develops at the start of the test section while the boundary layer exiting the wind tunnel nozzle is removed. This means that the span of the model has to be smaller than the nozzle dimension in the respective direction (see figure 5.5). The span-to-nozzle-dimension difference has to be at least twice the nozzle boundary layer thickness to completely remove it at both endplates. The leading edges of the endplates are **elliptical leading edges** thus large separation upon small stagnation point errors is avoided.

Assuming a 2D flow can be ensured, the flow pattern gradients extend only streamwise and perpendicular to the plane of the airfoil (airfoil plane ≡ span direction times chord direction). In comparison to freestream, the wind tunnel restricts the far-field significantly which acts back on the flow in proximity. The **airfoil has to be oriented vertically** so the largest nozzle dimension (horizontal: 1.8m) is oriented perpendicular to the plane of the airfoil. These choices put the test section to comparable aspect ratios (*e.g.* [3, p. 2], [84]) and model orientation (*e.g.* [3, p. 2]) of other wind tunnels.

The decision of vertical orientation has further advantages:

- The parasitic effects of the model weight on the balance measurements are minimal if the model is oriented vertically (see section 5.2.3).

- Maximum forces on the whole rig will be smaller if the span of the airfoil covers the smaller dimension of the nozzle. Even then, the drag measurements remain unaltered, at least those of wake rake and pressure taps (compare section 2.5.4).
- The total blockage $B = A_f/A_t$ of the test section is given by the frontal area of the airfoil A_f and the total nozzle cross-section area $A_t = 1.3\text{m} * 1.8\text{m} = 2.52\text{m}^2$

	Re_c			Blockage A_f/A_t[%]		
c	$U = 20$m/s	$U = 33$m/s	$U = 45$m/s	$\alpha = 0°$	$\alpha = 5°$	$\alpha = 10°$
0.4	5.73e05	9.46e05	1.29e06	2.7	4.6	6.5
0.7	1.00e06	1.65e06	2.26e06	4.7	8.0	11.3
0.75	1.07e06	1.77e06	2.42e06	5.0	8.6	12.2
0.8	1.15e06	1.89e06	2.58e06	5.3	9.2	13.0
0.9	1.29e06	2.13e06	2.90e06	6.0	10.3	14.6
1	1.43e06	2.36e06	3.22e06	6.7	11.5	16.2

Table 5.1: Re_c and blockage ratio for different combinations of angle of attack α and chord length c. Brown entries mark the operating point of the HGR-01 validation campaign. Blue entries mark possible operating points of the VACA4412s019 campaign.

$$A_f = s \cdot (t_a \cos \alpha_{\text{geom}} + c \sin \alpha_{\text{geom}}) \tag{5.1}$$

with airfoil thickness t_a, chord c and the geometric angle of attack α_{geom}. It becomes clear that using the smaller test section dimension as the span dimension is beneficial in terms of maximum blockage. Meanwhile, the chord length also influences the achievable chord Reynolds number Re_c which is limited also by $U_\infty = [2, 50]$m/s. The kinematic viscosity ν is that of the ambient air and cannot be changed for the present wind tunnel infrastructure. This means blockage on one hand and, on the other hand, maximizing Re_c have to be weighted as seen in table 5.1. In that sense increasing blockage also means stronger lift-correction as circulation Γ scales with chord length c, too (sections 5.3.3, 2.1).

Apart from the endplates, it is decided to keep the remaining two open jet boundaries to achieve a semi-open jet. This has the advantage of avoiding wake blockage [32], ensuring good optical access to the test section as well as less effort in mounting and modifying the rig. The downside of this decision is that the wind tunnel lift correction becomes larger and less accurate compared to a closed test section (see section 5.3.3).

5.2.3 Balance

Implementation Resistive strain gauges are best suited for the present measurement task as long-term stability, low zero drift, and commercial availability are the most important properties (compare sensor properties in section 2.5.3). Frequency resolution is not as important since the high model weight has the effect that high-frequency fluctuations are barely passed on to the sensors. Furthermore, high-frequency signals of local effects are already blurred in integral signals due to the large integration area for the force that reaches the sensor.

Two general concepts of force sensor layout based on resistive strain gauges can be considered:

- **Mechanically separated degrees of freedom with single axes sensors** The different degrees of freedom (DOF) are separated from one another using levers and bearings in such

a way that each component can then be measured separately. Historically, this approach was used with all wind-tunnel balances [13] using wires and levers to connect the model to the balances. A large advantage is that the sensors (balances) can be chosen independently for each degree of freedom depending on the order of magnitude of the expected signal. The disadvantage lies in the mechanical complexity and associated cross-talk, especially for 6 DOF balance systems and if large weight taras are to be expected [91].

- **Integral force sensors** These are the most common sensors for multi-axes measurements nowadays which can be concluded from review articles that discuss such sensor types [19] and the huge variety of commercially available models. Their advantage lies in the simple mechanical design (one geometry with many strain gauges which measure the complex deformation of this geometry and determine the single components by calibrated interaction matrices). The downside of such sensors lies in the dependencies of the measurement signal magnitudes of one another. For one sensor geometry, the possible loads and associated strains are given for all DOFs. Commercially available sensors tend to be small which favors force measurement magnitude over bearable torque magnitude.

The present measurement task requires large torque bearing capabilities because large torque variations occur due to the shift in the resulting pressure point which depends on the angle of attack (in general [2] and in particular figure 4.6 right). In addition, the ratio of forces of the DOF is large. Therefore, a balance system similar to the "historic" is most suitable, cheap, and accurate also for the use of different airfoil models and different load scenarios.

It is possible to find five linearly independent vectors in two planes given by the two attachment points and the line connecting them as normal vectors of these planes. A sixth linear independent vector can be found in the direction of the connection axis (figure 5.5). Within each attachment point plane, only two, respectively three, linearly independent vectors have to be represented by a one-axis force sensor to fix the model in place. This means that all forces acting on the model can be measured directly by the attachment apart from the one acting in the direction of the connection axis.

Figure 5.6 shows the reduction of the 5 sensor readings to the 3 relevant figures of merit ($F_{\overline{X}}$,$F_{\overline{Y}}$,$M_{\overline{Z}}$)

$$\text{horizontal, out-of-plane DOF: } F_{\overline{Y}} = F_{\overline{Y}1,U} + F_{\overline{Y}2,U} + F_{\overline{Y},L} + F_{R,L} \tag{5.2}$$

$$\text{horizontal, in-plane DOF: } F_{\overline{X}} = F_{\overline{X},U} + F_{\overline{X},L} \tag{5.3}$$

$$\text{vertical, rotational DOF: } M_{\overline{Z}} = F_{\overline{Y}2,U} \cdot l_{\overline{Y}2,U} + F_{R,L} \cdot l_{R,L} \tag{5.4}$$

The vertical DOF is restricted by an air bearing (EZ4000 [183]) which carries the weight of the model whilst creating no in-plane friction. Such a design concept is also used in other load measurement tasks where high model weights have to be carried [90].

Random Errors and quasi-random Errors Thanks to the air bearing, cross-talk in between the DOF is only due to the stiffness of the single-axis force sensors and the bearings with which they are connected. S-shaped single-axis force sensors with spherical-plain-bearings-rod-ends provide the best properties in that regard — meaning they have high stiffness and a response only in their designated load direction and have almost no stiffness and response to off-axis loads thanks to the spherical-plain-bearings-rod-ends. A calibration test showed that the associated error does not follow a systematic pattern and was reduced to the sensor error level if a TARA was applied to the sensor readings after setting a new AoA. This procedure was therefore used for the whole campaign with boundary layer control (see timeline in table 5.6). Even without this procedure, the error

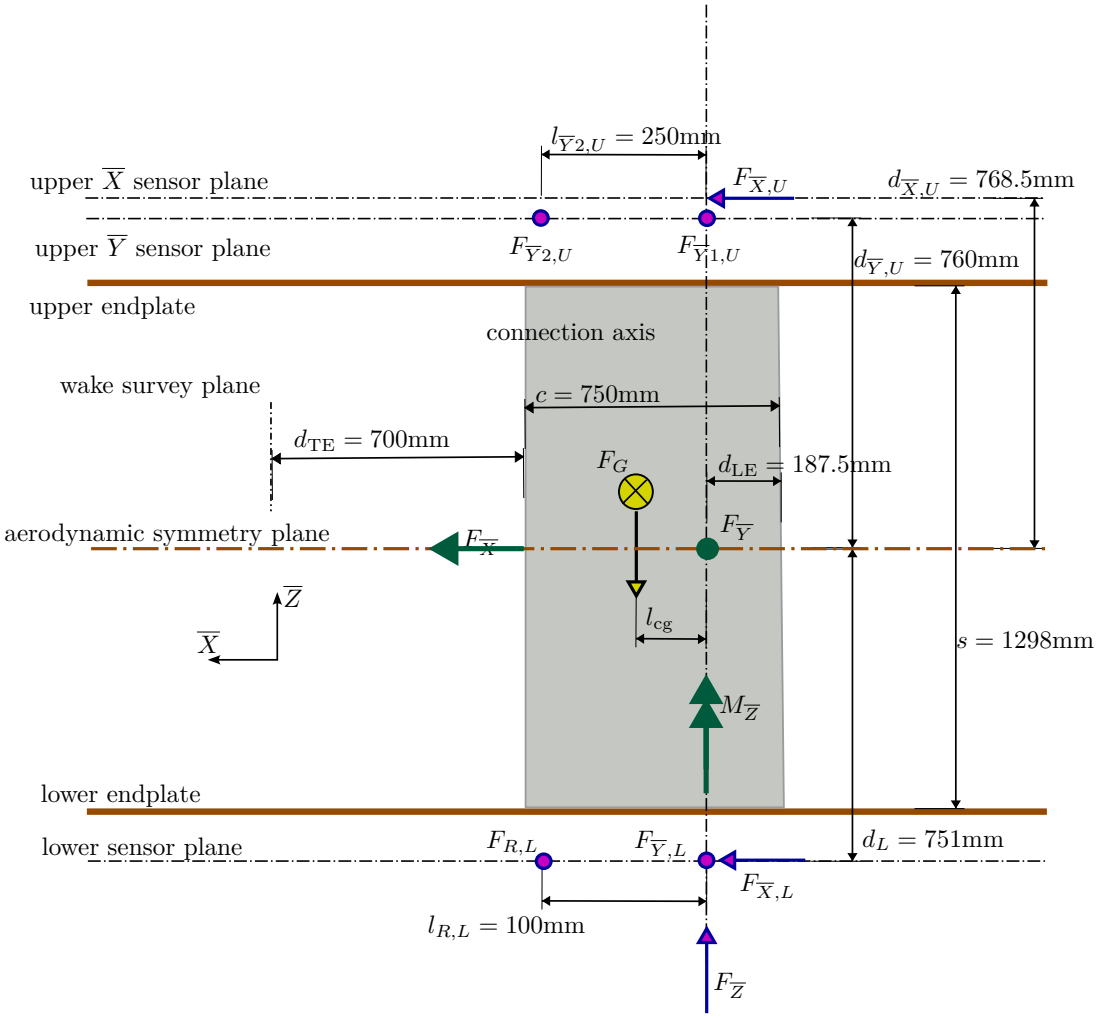

Figure 5.6: DOF decoupling for the balance for the installation with the VACA4412s019 airfoil model. The forces measured by the balance directly do not represent the actual lift and drag forces but have to be corrected by the angle of attack error (see section 5.3)

was below distinguishable for lift and almost negligible for drag readings given the fact that the absolute drag measurement of the balance is subject to significant wind tunnel corrections anyway (section 5.3).

Figure 5.7 shows the accuracy and range properties based on linear error propagation (section 2.5.2.2) for the KDs40 sensor family and the given sensor assignment (table 5.2). Engineering details about the balance system are provided in [Fah24b].

Sensor station	Sensor Type	$\mathcal{E}_{r,s}$	$\epsilon_{r,s,\mathrm{FS}}$
$F_{\overline{X},U}$	KDs40 50N	0.05N	0.1%
$F_{\overline{Y}1,U}$	KDs40 200N	0.2N	0.1%
$F_{\overline{Y}2,U}$	KDs40 100N	0.1N	0.1%
$F_{\overline{X},L}$	KDs40 50N	0.05N	0.1%
$F_{\overline{Y},L}$	KDs40 500N	0.5N	0.1%
$F_{R,L}$	KDs40 10N	0.01N	0.1%

Table 5.2: Absolute random sensor error ($\mathcal{E}_{r,s}$) and random sensor error relative to the respective sensor range ($\epsilon_{r,s,\mathrm{FS}}$) for the assignment of KDs40 sensors as it was used for the VACA4412s019 campaign

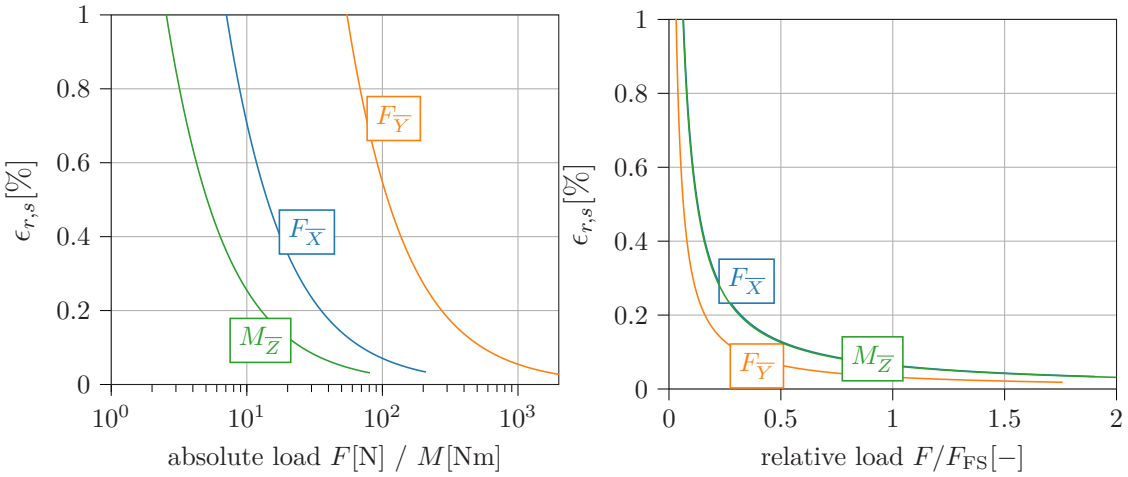

Figure 5.7: Errors of the balance readings based on sensor error (table 5.2) and linear error propagation through the coupling equations 5.2 - 5.4.

5.2.4 Pressure Taps

Implementation The integral values of pressure forces are defined according to equation 2.76 and 2.77. In practice, the finite number of pressure taps needs to be treated. Therefore, the integral becomes a weighted sum, following a trapezoidal integration rule. The wall-normal vector for each section $\mathbf{y_{S,i}}$ is calculated with forward differences which results in a trapezoidal rule due to the way the segments are defined. This gives the forces in the body conform coordinate system ($\{X, Y, Z\}$, see figure 2.2):

$$\begin{bmatrix} F_X \\ F_Y \\ F_Z \end{bmatrix} = s \cdot \sum_{i=1}^{n|i=n,i+1=1} w_i \frac{p_{i+1} + p_i}{2} \mathbf{y_{S,i}} \tag{5.5}$$

$$\begin{bmatrix} M_X \\ M_Y \\ M_Z \end{bmatrix} = s \cdot \sum_{i=1}^{n|i=n,i+1=1} w_i \frac{p_{i+1} + p_i}{2} \left(\frac{\mathbf{r_{i+1}} + \mathbf{r_i}}{2} \times \mathbf{y_{S,i}} \right) \tag{5.6}$$

$$w_i = \sqrt{(x_{i+1} - x_i)^2 + (y_{i+1} - y_i)^2} \quad | \text{ weight} \tag{5.7}$$

The resulting vectors have to be rotated to get the forces aligned with the infinite wind direction. For the pitching moment M_z this has no effect. For the forces the following equation can be applied

based on the geometric angle of attack α_{geom} (which is identical to the AoA $\alpha = \alpha_{\text{aero}}$ only in freestream domain, see lift-correction section 5.3.3):

$$\begin{bmatrix} F_{\overline{X}} \\ F_{\overline{Y}} \\ F_{\overline{Z}} \end{bmatrix} = \begin{bmatrix} \cos\alpha_{\text{geom}} & \sin\alpha_{\text{geom}} & 0 \\ -\sin\alpha_{\text{geom}} & \cos\alpha_{\text{geom}} & 0 \\ 0 & 0 & 1 \end{bmatrix} \begin{bmatrix} F_X \\ F_Y \\ F_Z \end{bmatrix} \tag{5.8}$$

Sensor station	Sensor Type	$\mathcal{E}_{r,s}$ (abs.)	$\epsilon_{r,s,\text{FS}}$
SS, $x = 0..0.46$	MPS 4264 1psid ($\pm$6894.76Pa)	4.14Pa	0.06%
SS, $x = 0.50..1$	MPS 4264 8inH_2O ($\pm$1992.72Pa)	2.39Pa	0.12%
PS, $x = 0..0.02$	MPS 4264 1psid ($\pm$6894.76Pa)	4.14Pa	0.06%
PS, $x = 0.03..1$	MPS 4264 8inH_2O ($\pm$1992.72Pa)	2.39Pa	0.12%
BLC chambers	MPS 4264 8inH_2O ($\pm$1992.72Pa)	2.39Pa	0.12%

Table 5.3: Sensor Accuracy of pressure taps as applied on the VACA4412s019 model for the present measurement campaign using the MPS 4264 Sensors from Scanicalve [201]

Random Errors Table 5.3 gives the accuracies for the applied multi-channel pressure sensors [201]. Uncorrelated linear error propagation can be applied to pressure force integration (eq. 5.5) and M_z (eq. 5.6) assuming uncorrelated random sensor channel error (which is not entirely true for the MPS sensors as found by Elsner [Els22, p. 45] due to cross-talk).

$$\begin{bmatrix} \mathcal{E}_X \\ \mathcal{E}_Y \\ \mathcal{E}_Z \end{bmatrix} = s \cdot \sqrt{\sum_{i=1}^{n|i=n,i+1=1} \left(\sum_{j=i-1}^{i} w_j \frac{1}{2} \mathbf{Y_{W,i}} \right)^2 \mathcal{E}_i^2} \tag{5.9}$$

$$\begin{bmatrix} \mathcal{E}_{M_X} \\ \mathcal{E}_{M_Y} \\ \mathcal{E}_{M_Z} \end{bmatrix} = s \cdot \sqrt{\sum_{i=1}^{n|i=n,i+1=1} \left(\sum_{j=i-1}^{i} w_j \frac{1}{2} \left(\frac{\mathbf{r_{j+1}} + \mathbf{r_j}}{2} \times \mathbf{Y_{W,j}} \right) \right)^2 \mathcal{E}_i^2} \tag{5.10}$$

$$w_i = \sqrt{(x_{i+1} - x_i)^2 + (y_{i+1} - y_i)^2} \qquad | \text{ weight} \tag{5.11}$$

The errors can then be rotated similarly to the forces to fit the frame of reference of the wind tunnel downstream axis (eq. 5.8).

Systematic Errors Additionally, there are systematic errors in the pressure tap system which can lead to systematic deviation of resulting force coefficients.

- **Inaccuracy of the pressure taps** This error depends on the exact shape of the error taps. Nitsche & Brunn [86, p. 13] give the estimates for this error depending on various influences most of which have a dependency on the outer flow dynamic pressure. Therefore, the error due to the pressure tap inaccuracy is always the same relative to the sensor reading. This also means though, that it cannot be calibrated with feasible effort. In consequence, although it is a systematic error, its influence of the tap shape inaccuracy has to be quantified similarly to the random errors in equation 5.9 and 5.10 with

$$\mathcal{E}_i = 1\% \cdot |p_i| \tag{5.12}$$

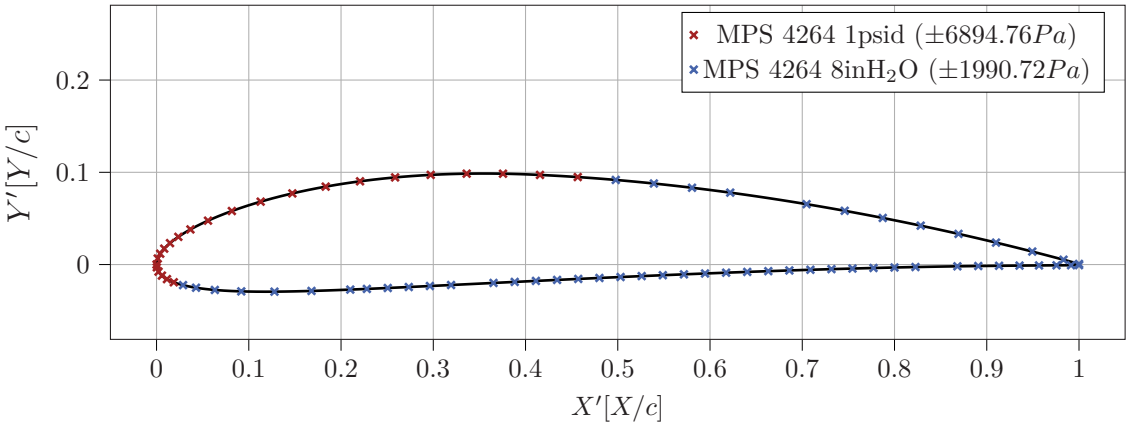

Figure 5.8: Distribution of pressure taps of the VACA4412s019 airfoil model (development of the model described in section 5.2.1)

- **Inaccuracy of the surface normals** This error arises if the surface normal upon calculation does not represent the true effective surface normal of the area represented by the pressure tap. It can be limited by setting the distance of pressure taps inverse proportional to surface curvature (compare figure 5.8 and table C.2).
- **Changes in streamwise static pressure** Despite the correction of the mean horizontal buoyancy (see section 5.3.2) there is the possibility that the pressure distribution within the test section is changed differently due to the presence of the airfoil than it would be in freestream. This error cannot be quantified easily but will be noticeable in the drag polar curve of the pressure drag coefficient $c_{d,p}$ (see figure 5.14).

Engineering details about pressure tap distribution and model design are listed in appendix C.

5.2.5 Wake Rake

Implementation A wake rake is designed to scan the field information of the total pressure $p_{t,3}$ as well as the static pressure p_3 behind the body (wake survey plane is denoted with index ③) based on the principle of measuring the wake deficit (sections 2.5.4, 3.1.1).

The formula of Jones (eq. 2.75) cannot be used directly as a wake rake does not provide the absolute quantities but differential pressures only. Therefore, the formula of Jones has to be interpreted for the given rake tubing (see figure D.3). The freestream dynamic pressure of the wind-tunnel q_∞ can be used to express the terms in the denominator of equation 2.75:

$$p_{t,\infty} - p_\infty = q_\infty \tag{5.13}$$

The physical reference pressure of the sensor is connected to the pitot tubes which are always to be placed outside the wake ($\overline{Y} = \pm 150$mm) of which the stagnation pressure will be called $p_{t,\mathrm{wk},\infty}$. The same is done with the static pressure probes. Hence, in a freestream the sensor readings of the total pressure rake $p_{t,\mathrm{SR}}(\overline{Y}) = 0$Pa will read zero, whilst the readings of the static pressure

rake will be at minus the dynamic freestream pressure $p_{s,\mathrm{SR}}(\overline{Y}) = -q_\infty$. The following can be said about the first numerator term of equation 2.75 and the pressure p_3 in the wake rake plane ③:

$$p_{t,3}(\overline{Y}) - p_3(\overline{Y}) = \underbrace{p_{t,3}(\overline{Y}) - p_{t,\mathrm{wk},\infty}}_{\text{sensor reading Stagnation Rake}} - \underbrace{(p_3(\overline{Y}) - p_{t,\mathrm{wk},\infty})}_{\text{sensor reading Static Rake}} \tag{5.14}$$

$$p_{t,3}(\overline{Y}) - p_3(\overline{Y}) = \overbrace{p_{t,\mathrm{SR}}(\overline{Y})}^{\text{sensor reading Stagnation Rake}} - \overbrace{p_{s,\mathrm{SR}}(\overline{Y})}^{\text{sensor reading Static Rake}} \tag{5.15}$$

The second numerator term of equation 2.75 is a bit more complex to resolve and requires a static reference pressure at a position within the tunnel which is unaffected by the presence of the airfoil model. Kaiser found in numerical simulations [Kai22] that the pressure ports at the nozzle exit are most suitable for that purpose for the present test rig design. With this, the differential pressure can be described which identifies the pressure loss from infinity static pressure p_∞ to the wake survey plane static pressure $p_3(\overline{Y} = 0)$. A detailed derivation is given in [Fah24b].

$$p_{t,3}(\overline{Y}) - p_\infty = p_{t,\mathrm{SR}}(\overline{Y}) + \Delta p_{\mathrm{loss1},3(\overline{Y}=0)} - p_{s,\mathrm{SR}}(\overline{Y} = 0) \tag{5.16}$$

Ultimately, the formula of Jones (eq. 2.75) can be expressed based on actual sensor reading (index SR):

$$\begin{aligned} c_{d,W} = \frac{2}{c} \int_{-y_w}^{+y_w} & \sqrt{\frac{p_{t,\mathrm{SR}}(\overline{Y}) - p_{s,\mathrm{SR}}(\overline{Y})}{q_\infty}} \cdot \\ & \cdot \left(1 - \sqrt{\frac{p_{t,\mathrm{SR}}(\overline{Y}) + \Delta p_{\mathrm{loss1},3(\overline{Y}=0)} - p_{s,\mathrm{SR}}(\overline{Y} = 0)}{q_\infty}} \right) \mathrm{d}\overline{Y} \end{aligned} \tag{5.17}$$

Random Error Slight variations in the exact span-wise (in terms of the tube row) tube location are observable (see figure D.4) despite the very good manufacturing accuracy. This blurs the information of the span-wise location of a measurement, which is not important in absolute values but relative to the neighboring tubes. Yet, it is difficult to correctly measure the associated error as a dislocated tube does not only carry the wrong location label but also some slight signal change due to the closer proximity to the neighboring tube. Furthermore, the position is very likely to slightly change due to wind forces or simply wear and tear during the campaign. The subsequent error can be reduced by sampling the wake multiple times with slightly different rake positions. This way certain wake features are captured by different pitot tubes for the same operating point. This method is inspired by pixel shift technology for noise reduction and resolution enhancement of digital cameras (short description in *e.g.* [130, p. 39]).

As written above, it is necessary to measure at a location some distance from the airfoil itself. Therefore, the flow has already reached a state, where the shape of the wake follows a Gaussian bell curve. This allows to reduce the effect of single channel sensor errors at the cost of introducing an assumption about the shape of the resulting curve:

$$G(y) = a_{\mathrm{wk}} \exp\left(- \frac{(y - b_{\mathrm{wk}})^2}{2c_{\mathrm{wk}}^2} \right) \tag{5.18}$$

Such a curve can be fitted with only three parameters: height a_{wk}, shift b_{wk} and variance c_{wk}^2, although it must be noted that the shift is irrelevant for the resulting integral quantity. The advantage of such a fit function lies in its values going toward zero outside the bell shape which is important because the wake rake has a limited span.

The error of the of the wake survey drag $c_{d,W}$ can now be estimated in two ways:

- **Error of the fit** The uncertainty parameters of the fit give an error for each fit parameter, which can be propagated through equation 5.17. This error also includes how ill-posed the assumed fit function is.
- **Propagation of the sensor error** The sensor error given by the manufacturer is propagated through equation 5.17 based on how many channels contribute to the function of the total pressure reading $p_{t,\mathrm{SR}}(\overline{Y})$. Therefore, its error $\mathcal{E}_{t,r,s}$ — if all of the physical channels contribute similarly to the fit of $p_{t,\mathrm{SR}}(\overline{Y})$ — reads:

$$\mathcal{E}_{t,r,s} = \sqrt{\sum_{i=0}^{n=57} \left(\frac{\partial f}{\partial p_i}\right)^2 \mathcal{E}_i^2} = \sqrt{57}\Big(\underbrace{\frac{\partial f}{\partial p_i}}_{\frac{1}{n}=\frac{1}{57}} \Big)\mathcal{E}_{r,s} \quad | \quad i = \text{channel index} \tag{5.19}$$

  It has to be noted though, that this procedure is mathematically wrong because the assumption that all channels contribute to the overall error equally is wrong. Nevertheless, equation 5.19 shows the effect, that a high number of physical channels contributing to the same integral quantity leads to less random sensor error than that of a single sensor reading.

At this point, it can be disclosed that both methods give almost identical results as long as a fit can be found (despite the wrong concept of equation 5.19). From this, the conclusion can be drawn, that the sensor error given by the manufacturer (MPS 4264 4inH_2O ($\pm$996.36Pa) $\epsilon = 0.20\%\mathrm{FS} \equiv \mathcal{E}_{r,s} = 1.99\mathrm{Pa}$ [201]) is well suited to calculate the combined standard uncertainty of the wake rake fairly well.

Systematic Error Traditionally, it is believed that the wake survey gives very accurate drag measurements, e.g. errors $\leq 2\%$ of the measured value [113, chapter 7.2.3]. However, this is hard to judge solely based on experiments due to the lack of a more accurate measurement method. Indeed, there is a systematic error that is not covered in the explanation by Russo [113] which relates to the properties of such a wake in reality. Both the methods of Jones and Betz rely on forming an integral that vanishes outside the wake. This allows a finite integration length, which is crucial for measurements but also inherent to the approach in general. However, if one considers a measurement to be taken very close to the trailing edge of the airfoil the wake consists only of the two boundary layers which developed over the surface of the body. But it is important to note that the boundary layers displaced some of the mean flow which is now outside the wake therefore outside the effective integration length. Both Jones and Betz avoided this problem by stating that the measurement is taken far enough away so the velocity overshoot due to the displacement of the mean flow vanished. Yet this does not solve the problem completely: The displaced flow leaves the control volume of the momentum budget calculation (see figure 3.1). Since the measurement can only take place in the designated wake plane, an assumption has to be made about the velocity and therefore the momentum of the displaced flow. Assuming this flow to leave the control volume with freestream velocity leads to the momentum budget similar to the form of Jones or the complete version (eq. 3.4). However, this assumption does not hold in reality due to the potential flow field around the body. In consequence, the drag estimated from the wake integral is systematically wrong. One approach to quantify this error is to use numeric simulations to calculate the difference between the wake survey drag and the true body drag (integral forces on the body and control volume perimeter momentum flux have to balance as long as no BLC is considered, as shown in section 3.1.1) Although quite accurate, a considerable systematic error exists which is within the order of magnitude of $\epsilon \approx 10\%$, definitely larger than $\epsilon \leq 2\%$ if one compares the wake survey

results for different sampling plane distances d_{TE} [Kai22, p. 87,88]. Therefore, a sampling position is chosen at which the error becomes minimal which is in the region of $d_{\mathrm{TE}}/c \approx 0.9$ based on airfoil chord length c.

Engineering details as well as detailed derivations for the wake rake design shown here are provided in [Fah24b].

5.2.6 Pressure Drop and Flow Meters

Implementation The flow meters enable two measurement quantities. For one, the BLC penalty (eq. 3.5) depends on the integral control mass flow rate $\dot{V}_{\mathrm{BLC}}\rho$ and the correct setting of the control rate $c_q = v_{\mathrm{BLC}}/U_\infty$ requires the BLC mass flow for correct labeling. Secondly, the dimensionless flow resistance of the BLC surface ζ_{BLC} depends on the volume flow rate as well.

$$\zeta_{\mathrm{BLC}} = \frac{\Delta p_{\mathrm{BLC}}}{\frac{\rho}{2} v_{\mathrm{BLC}}^2} = \frac{2\Delta p_{\mathrm{BLC}} A_{\mathrm{BLC}}^2}{\rho \dot{V}_{\mathrm{BLC}}^2} \tag{5.20}$$

Δp_{BLC} is the pressure loss over the control surface plate. Its measurement requires the pressure taps on the outer airfoil surface at the BLC location (section 5.2.4) as well as inside the model in the control flux distribution chambers (see figure C.1). This means the pressure loss of each control section is computed based on four physical pressure readings:

$$\Delta p_{\mathrm{BLC}} = \frac{1}{3} \sum_{i=1}^{3} p_{\mathrm{outer},i} - p_{\mathrm{inner}} \tag{5.21}$$

The mass flow rate is acquired with calorimetric mass flow meters (testo 6451 [204]). The measurement principle is based on combined pressure and temperature measurements during the heating of a known working fluid (air).

Random Errors The mass flow meters are calibrated for different operating conditions to an error of $\mathcal{E}_{r,s} = 2\% \cdot \dot{V}_{\mathrm{SR}} + 0.5\% \cdot \dot{V}_{\mathrm{FS}}$. This means both the current sensor reading ($\dot{V}_{\mathrm{SR}}$) as well as the full range ($\dot{V}_{\mathrm{FS}}$) of the sensor impact the error. The sensor error of the pressure drop is given by the combined error of multiple MPS 4264 channels, as three channels contribute to the mean outer pressure and one channel contributes to the inner chamber pressure (eq. 5.21, table C.3 & table C.2).

Systematic Errors A systematic error of the mass flow and pressure drop measurement is given by the non-uniformity of the flow through the BLC surface. In that regard this is not about the finite character of the flow through the holes, but the macroscopic non-uniformity due to different flow resistance of the flow inside the model and the variations in flow resistance through the porous plate. The latter is also driven by clogging due to dirt deposited by the BLC air. To reduce this effect as much as possible, a filter system is introduced upstream of the flow meters which catches dirt particles (see figure D.1). The BLC air is drawn from outside of the wind tunnel for most of the PIV experiments. Hence, it does not contain tracer particles. Finally, the variations between the results of the individual BLC chambers provide an impression of the systematic variations of the BLC properties (section 5.5.4).

5.2.7 Particle Image Velocimetry (PIV)

Implementation Wöllstein investigated multiple parameters on how to ideally perform turbulent boundary layer PIV for the given test-stand [Wö23]. Figure 5.10 provides the processing algorithm which builds on the best practices from [Wö23]. The procedure consists of two main processing systems: A custom code for image preprocessing and velocity data postprocessing, and a commercial program that calculates the velocity fields from the grey value image pairs.

Task	Device	Specifications	
Seeding	PIVLIGHT PIVlight30	water-based	
		particle diameter $d_p = 1.2\mu$m [198]	
		response time $t_p \approx 4.4\mu$s (eq. 2.79)	
Illumination	Evergreen	Wave length	532nm
		Power	200mJ
Magnification	Nikon f/4D IF-ED Nikkor	Focal length	200mm
	Teleplus HD 2.0X DGX		x2
Recording	PCO Edge	Sensor	sCMOS
		Resolution	2560 x 2160
Calibration	2D-Target	Figure 5.9	107.4 $\frac{\text{Pixel}}{\text{mm}}$
Post-Processing	Figure 5.10		

Table 5.4: Devices for 2D-2C PIV measurements in wall-normal plane of the turbulent boundary layer at the wing profile

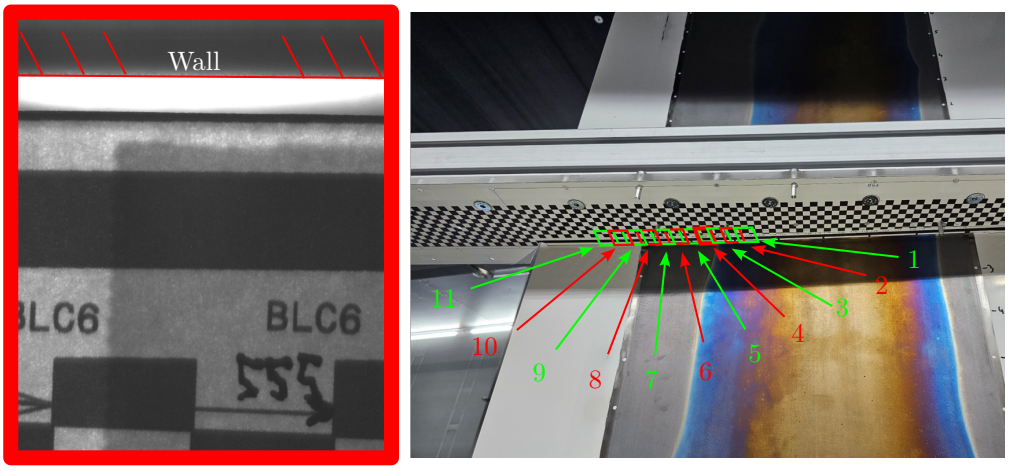

Figure 5.9: PIV calibration target and positions of Field of Views (FOV). The quad-pattern has an edge length of 1% airfoil chord length ($c/100 = 7.5$mm)

Specifications of the final setup of the boundary layer velocity profile measurements are given in table 5.4. The camera was mounted outside the flow and its view was directed in the spanwise direction with about 700mm working distance from the lens to the light sheet and crossing the lower endplate (camera position is depicted in figure D.1). It traversed 11 different FOV to capture the boundary layer in the interval $X/c = [66, 89]\%$ (figure 5.9) The investigated operating points are listed in table 5.6. For each operating point, an image series consists of 450 images of which the first 40 images are excluded in postprocessing to avoid changes in particle lightning that stem from the laser ramp-up that lasts about two seconds after the laser was triggered the first time. The pulse distance for the results shown in this thesis ($Re_c = 1.5$Mio, wall-normal light sheet) was

$\Delta t = 6\mu$s. The Reynolds number $Re_c = 1.5$Mio is achieved for a flow velocity of $U_\infty \approx 32$m/s with a boundary layer thickness within the FOV of $\delta_{99} \approx 10$mm which results in a particle Stokes number (eq. 2.78) of Stk $\lessapprox 0.014$ which satisfies Stk $\overset{!}{<} 0.1$ as described in section 2.5.4.

Figure 5.10 displays the final data processing chain which builds on the lessons learned from Wöllstein [Wö23]. The raw images of both A and B frames are used to determine the location of

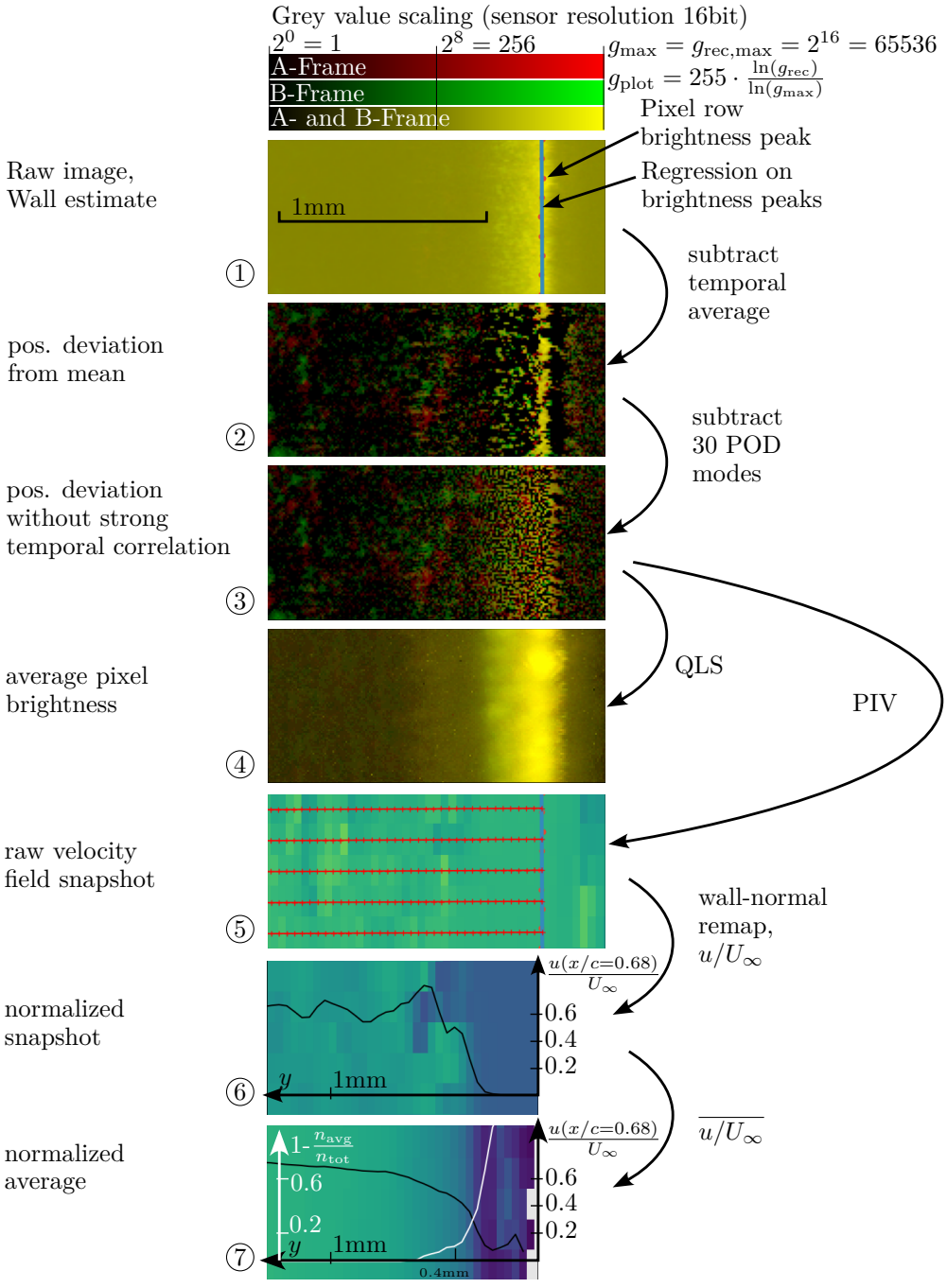

Figure 5.10: Data processing chain for 2D-2C PIV measurements at the wing test stand

the wall (Figure 5.10 ①). This is done separately both for A and B as well as for each snapshot to account for a movement of the wall due to vibrations. The estimation is a two-step process: First,

a skewed Gaussian bell curve is fitted onto the intensity peak of each pixel row and its maximum marks the most likely position of the wall in this pixel row. Secondly, a 3rd-order polynomial is fitted onto the row estimates to get a smooth regression of the wall throughout the FOV. The third-order polynomial is to account for the macroscopic curvature of the airfoil within the region.

In the next step, the average intensity of each pixel of all snapshots (A and B separately) is subtracted from the corresponding pixel of each frame (Figure 5.10 ②). Therefore, the background noise level of the camera and the bright reflection of the wall are removed. A (red) and B (green) frames can now be told apart clearly because the particles moved in between the frames. Yet, the wall is still visible and its yellow color indicates that it is strongly correlated in between a single A and B snapshot. This is problematic because such a strong correlation will inevitably lead to PIV evaluation "locking" onto the static, highly correlated parts of the frames, which reduces the likelihood of correlating particle displacement close to the wall. Furthermore, a clear dark line can be observed right next to the bright yellow line which indicates that the average of all frames was brighter at a location a couple of pixels to the right of the brightest line of the presented frame pair.

This motivates the third step in image processing (Figure 5.10 ③). Therein, the most prominent spatial patterns are subtracted from each frame according to their respective intensity within this timestep. These spatial patterns and their time-coefficient function which allows to scale them for each snapshot are determined by spectral proper orthogonal decomposition (see section 2.5.1.2 and [139]). In contrast to the test case of Mendez [75], the wall reflection of the present study is made up of scatter on a "rough" surface as light is reflected from the edges of the tiny holes of the boundary layer control surface. Therefore, there is a large quasi-random portion of the wall reflection which cannot be removed by this approach. However, the comparison of figure 5.10 ③ vs. ② shows that the amount of yellow pixel clusters is strongly removed and instead red and green pixel noise indicates quite uncorrelated light scattering in A and B frames. This serves the goal of reducing the "locking-on" to static pixels during PIV evaluation and therefore enhances the likelihood of finding an actual particle displacement as the correlation peak close to the wall.

Figure 5.10 ④ shows the brightness of each pixel as an average over time. This is also called Quantitative Light Sheet (QLS) [109]. It can be used to determine the origin of the fluid at a certain location if there are two sources with different tracer particle concentrations. In the present study, the free flow was seeded whereas the control mass flux was unseeded to avoid clogging of the porous material.

Figure 5.10 ⑤ shows the magnitude of velocity in vertical image direction together with the wall-normal sampling points which can be calculated from the wall estimate in 5.10 ①. The images from step ③ are processed with the software *PIVview2C* [199]. The parametrization goal was to achieve results as close to the wall as possible. The presented results are all obtained with the following settings: A multigrid/multipass approach with grid refinement is used. The initial interrogation area size is 128px × 128px from which the subsequent three calculation passes reduce the interrogation area size and deform the mesh to fit the material deformation calculated from the velocity fields of the former calculation step as described by Raffel *et al.* [102, Fig. 5.26]. The final interrogation area size is 8px × 32px (wall-normal × wall-parallel) with a 50% overlap in both directions. This results in a datapoint step size of 4px × 16px ≡ 0.037mm × 0.149mm. Subpixel shift is calculated based on a Gaussian fit. Outliers are detected by a normalized median test with a threshold of 3, a minimum correlation coefficient of 0.2, and a minimum signal-to-noise ratio of 5. The same validity check is performed on second-order cross-correlation peaks which are used to replace outliers. Interpolated results from neighboring interrogation areas replace results where neither the result of first-order nor second-order cross-correlation peak passed the validation.

The velocity is resampled along the wall-normals (red lines) to get a flattened 2D, wall-parallel velocity field for all individual FOVs (FOVs in figure 5.9).

Figure 5.10 ⑥ shows the remapped velocity field of a single snapshot which is normalized to the wind-tunnel velocity to avoid freestream velocity fluctuations to be interpreted as boundary layer flow fluctuations. The correct temporal association of wind-tunnel velocity U_∞ and PIV velocity u is done by cross-correlating both time series.

Figure 5.10 ⑦ shows the temporal average of the wall-parallel velocity which is the basis for further processing and the showcased data in section 5.5.5. The temporal average is formed over all snapshots but excludes sampling points below the threshold of $u/U_\infty = 3\%$. This is done to exclude snapshots in which static pixels were mistakenly identified as particle shifts. This procedure is justified as no backflow events are expected within this environment. The portion of excluded snapshots in the average $1 - \frac{n_{\mathrm{avg}}}{n_{\mathrm{tot}}}$ does not contain exact uncertainty information but serves as a qualitative indicator of the robustness of the result. The portion of excluded snapshots is given by the white line in figure 5.10 ⑦. It shows that the results become unreliable for $y \lessapprox 0.4$mm above the wall when the portion of excluded snapshots in the average surpasses 20%.

Systematic Error Wöllstein investigated the influence of multiple processing steps and how they influence result quality [Wö23]. The most prominent problem for the present test case is the light scattered from the wall. It leads to the aforementioned "locking" as static pixels show the strongest correlation of an A and B frame. The more snapshots show such an effect close to the wall, the more the average will underestimate the true velocity at the affected interrogation area systematically. In the previous paragraph, a method was introduced to remove this bias. Yet, the velocity threshold which defines what snapshots to exclude in the average of an interrogation area leads to another bias: The result will most likely overestimate the true average velocity of an interrogation area if all statics and very low displacements are removed.

Random Error Random error in an average velocity vector of one interrogation area stems from the uncertainty of pixel displacement evaluation of individual snapshots significantly. This is not to confuse with the general physical fluctuation of the velocity signal of an interrogation area which requires a sufficient amount of single snapshots to acquire a converged temporal average. Each average field is generated from 410 single snapshots. The procedure of the velocity threshold reduces the number of used snapshots for the average. This means that both the error of the propagated uncertainty as well as the uncertainty of non-converged average fields rise for interrogation areas closer to the wall.

5.2.8 Data Acquisition (DAQ)

Hardware The data acquisition (DAQ) hardware was chosen and assembled for the present study but is in broader use, especially in the Göttinger Windtunnel at ISTM now. Table 5.5 contains the settings for the present measurement campaign. In general, there are 4 main measurement systems:

- The QuantumX [186] is the main DAQ system. It is used to operate and sample various single-channel sensors, such as force sensors, flow sensors, and precision pressure sensors. It also serves as the master clock for synchronization. Its data is used to monitor the thermodynamic properties of the wind tunnel and control its speed. In addition, all of its data is sampled

for post-processing, which leverages the 2-signal-per-channel option to not interfere with controlling the wind tunnel.

- Three different range MPS 4264 [201] are operated to conduct simultaneous multi-channel pressure measurements.
- A MKS Baratron [193] with range 100Torr is used as a pressure normal to calibrate the slopes of all differential pressure sensors. It is not used during active measurements.
- The PIV system is operated completely independent of other systems but its camera trigger pulse is recorded in order to synchronize PIV data with remaining data. During PIV post-processing it was found that cross-correlation (eq. 2.54) of PIV velocity with wind-tunnel velocity also provides synchronization of signals to an accuracy below the PIV sampling frequency of $f_s = 15\text{Hz}$.

Sampling and Filter The main sample frequency of the present study is $f_s = 200\text{Hz}$ with a resolution of 24 bit. The measurement interval has a duration of $t = 30\text{s}$ per set. At least four sets are recorded per operating point (see table 5.6). All data recorded by the QuantumX is low-pass filtered with an infinite impulse response (IIR) filter of Bessel type at the Nyquist frequency (lower frequency for thermodynamic properties and PIV). The MPS4264 does not provide such a hardware filter option, but the tubing provides a somewhat physical low-pass filter to avoid aliasing [48]. The function values of the wake rake momentum budget (eq. 5.17) are low-pass filtered at a filter rate of $f_f = 10\text{Hz}$ with a finite impulse response (FIR) filter of type central moving average before fitting (eq. 5.18). For postprocessing, intersecting time intervals of all DAQ hardware are extracted based on sampling timestamps from hardware internal clocks. Hardware internal clocks are synchronized via precision time protocol (PTPv2, IEEE-1588).

Further information about hardware, synchronization, implementation, and measurement functionality is provided in the Wind-Tunnel Manual [Fah24b].

Physical Domain			DAQ-Hardware			Digital Domain	
Group	Quantity	Sensor Typ	Sampling	Filter	Hardware internal Sync.	ext. Sync.	Code/ Computer
Wind-Tunnel Properties (fig 5.1)	Temperature	PT100 [181]	$f_s = 20$Hz	IIR Bessel $f_f = 0.2$Hz	QuantumX FireWire	PTPv2	Wind-Tunnel Control Code/ Wind-Tunnel Control Computer
	abs. pressure	Model 278 [203]					
	rel. humidity	HM1500LF [196]					
	nozzle diff. pressure	ASL 500Pa [202]		IIR Bessel $f_f = 1$Hz			
		ASL 2500Pa [202]					
Wind-Tunnel Fluctuations	static pressure along tunnel	ABP2 5inH_2O [192] sync via CAN [Web22]	$f_s = 150$Hz	none	QuantumX FireWire		Measurement Code/ Measurement Computer
Balance	forces	KDs40 Family [188]	$f_s = 200$Hz	IIR Bessel $f_f = 100$Hz	QuantumX FireWire		
Pressure Taps	static pressure airfoil surface	MPS 4264 1 psid[201]	$f_s = 200$Hz	none	MPS 4264 sampling		
		MPS 4264 8inH_2O [201]	$f_s = 200$Hz	none	MPS 4264 sampling		
BLC	static pressure BLC chambers						
	flow Rate	Testo 6451 [204]	$f_s = 200$Hz	IIR Bessel $f_f = 100$Hz	QuantumX FireWire		
Wake Rake	total pressure	MPS 4264 4inH_2O [201]	$f_s = 200$Hz	none	MPS 4264 sampling		
	static pressure						
	pressure loss	ASL 0.5inH_2O [202]	$f_s = 200$Hz	IIR Bessel $f_f = 100$Hz	QuantumX FireWire		
PIV	camera pulse	none	$f_s = 200$Hz	none	QuantumX FireWire		
	images pairs	PCO Edge [197]	$f_s = 15$Hz	none	camera pulse	camera pulse	PIV Computer

Table 5.5: Data Acquisition (DAQ) properties of all recorded quantities

Experiment Group (Date)	airfoil VACA4412s019 tripping	Date	Case Count per Set	Case Count total	AoA α_{geom}	AoA α_{aero}	Reynolds Number Re_c	BLC Rate c_q	chambers (X_{BLC}/c)
B001 (Feb. 2023)	$X_{\text{tr,SS}}/c = 1$ $X_{\text{tr,PS}}/c = 1$	Feb. 2023	10	120	$[-4°, 12°]$	$[-3.67°, 5.68°]$	1.5e6	0%	n.a.
C002 (Feb. 28 - Oct 25, 2023)	$X_{\text{tr,SS}}/c = 0.1$ $X_{\text{tr,PS}}/c = 0.1$	Feb. 28/ Mar. 01	8	100	$[0°, 5°]$	$[-1.07°, 1.63°]$	1.5e6	$\{0, 0.5\}$%	ch. $[1, 7]$ $(X/c = [0.36, 0.83])$
		Mar. 23/ Mar. 24	8	116	4°	1.09°	6.5e5	$[0, 0.9]$%	ch. $[1, 7]$
		Apr. 11/ Apr. 12	4	142	$[-9°, 4°]$	$[-6.56°, 1.09°]$	1.5e6	$\{0, 0.5\}$%	ch. $[1, 7]$
		June 1	4	60	$[4°, 12°]$	$[1.09°, 5.67°]$	1.5e6	$\{0, 0.5\}$%	ch. $[1, 7]$
		Oct 13 - Oct 25	14	470	$-9°, -3°$	$-6.56°, -2.92°$	1.5e6	$\{0, 0.5\}$%	ch. {1}, {2}, ... ,{7}
PIV-1 (May 23 - July 13)	$X_{\text{tr,SS}}/c = 0.1$ $X_{\text{tr,PS}}/c = 0.1$	May 23- June 1	13	104	4°	1.09°	1.5e6	$\{0, 0.5\}$%	ch. $[1, 7]$ ch. $[6, 7]$
		June 16	15	15	4°	1.09°	6.5e5	0%	n.a.
		June 19/ June 20	13	72	4°	1.09°	1e6	$\{0, 0.5\}$%	ch. $[1, 7]$ ch. $[6, 7]$
		June 20/ July 14	11	35	10°	4.48°	1.5e6	$\{0, 0.5\}$%	ch. $[1, 7]$ ch. $[6, 7]$
		June 29/ July 13	11	35	10°	4.48°	6.5e5	$\{0, 0.5\}$%	ch. $[1, 7]$ ch. $[6, 7]$
PIV-2 (July 31 - August 08)	$X_{\text{tr,SS}}/c = 0.1$ $X_{\text{tr,PS}}/c = 0.1$	July 31 - Aug 04		174	4°	1.09°	6.5e5	$\{0, 0.5, 1\}$%	ch. $[6, 7]$ $(X/c = [0.69, 0.83])$
		Aug 7/ Aug 8	23	46	4°	1.09°	1e6	$\{0, 0.5\}$%	ch. $[1, 7]$
		Aug 8	13	27	4°	1.09°	1.5e6	$\{0, 0.5\}$%	ch. $[1, 7]$

Table 5.6: Parameter variations for experimental investigations

5.3 Application of Wind-Tunnel Corrections

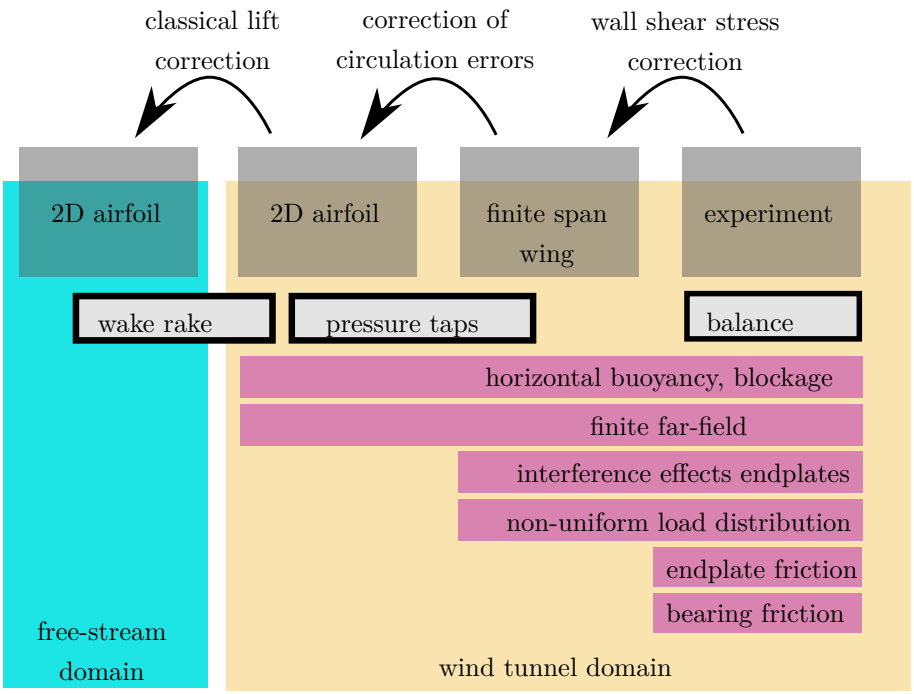

Figure 5.11: Overview of the wind-tunnel corrections to mitigate the errors (violet boxes) and the location of measurement methods (wake rake, balance, pressure taps) in terms of necessary corrections steps

Figure 5.11 gives an overview of some of the influences a test rig for a 2D airfoil flow within a wind-tunnel domain causes to the measurement in comparison to a true freestream domain. This means, that only those flow domain features are considered which cause most of the systematic deviation that can be expected from an experiment inside the wind-tunnel domain. This includes the finite span of a test model, the interaction with the phase boundary at the spanwise end, and the limited size of the wind tunnel jet perpendicular to the spanwise and streamwise directions.

5.3.1 End-Plate Friction

The friction of the turbulent boundary layer on the endplates also affects the turntables and therefore the drag measurement of the balance. Kaiser [Kai22, p. 57] showed that the assumption of a streamwise developing boundary layer in the empty wind tunnel gives a relatively good approximation of the friction drag originating from the turntables. This holds despite the presence of the airfoil which partially covers the turntables and partially accelerates the flow. The integral wall friction on the turntables can therefore be computed from the following equation based on Schlichting & Gersten [118, p. 31]

$$c_{f,\mathrm{EP}}(x) = \left(2\log_{10}(\mathrm{Re}_x) - 0.65\right)^{-2.3} = \left(2\log_{10}\frac{U_\infty x}{\nu} - 0.65\right)^{-2.3} \tag{5.22}$$

$$c_{d,\mathrm{EP}} = \underbrace{2}_{2\text{ endplates}} \frac{1}{cs}\int_{x=-R}^{x=+R} c_{f,\mathrm{EP}}(x) \underbrace{\int_{y=-y(x)}^{y=+y(x)} \mathrm{d}y}_{\text{turntable width}}\,\mathrm{d}x \tag{5.23}$$

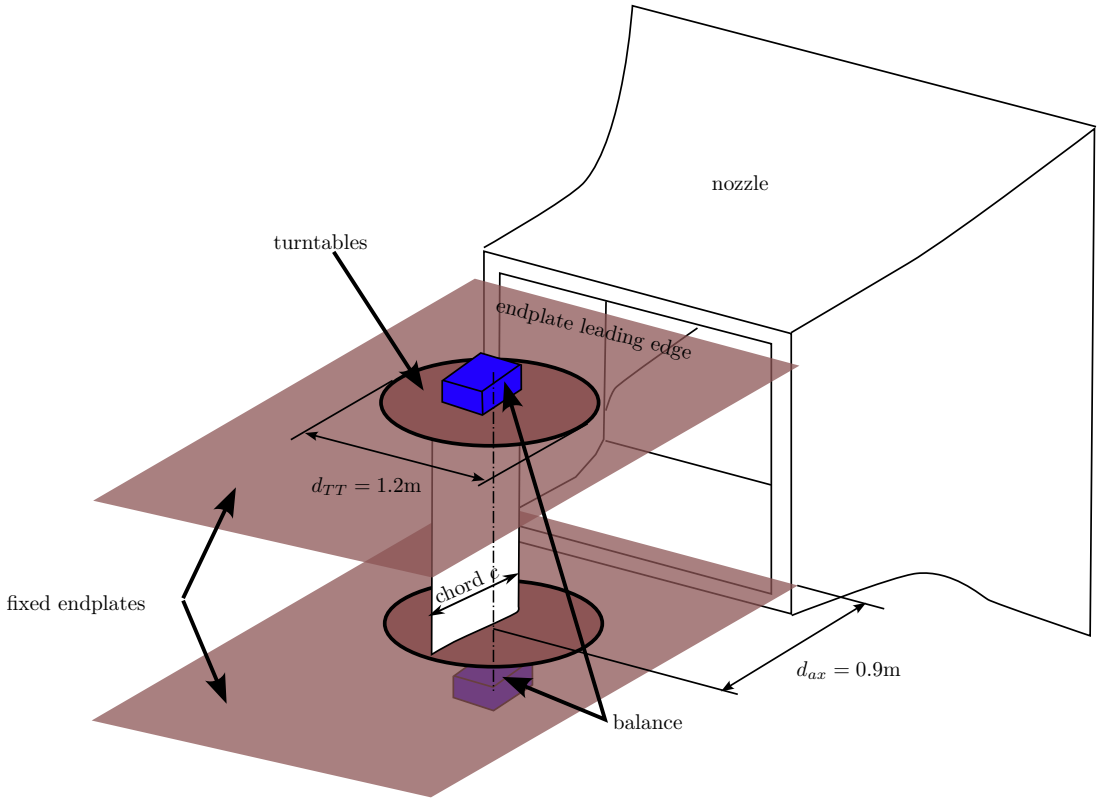

Figure 5.12: Geometric properties of the turntables contributing to the balance drag measurement due to turbulent boundary layer friction drag

5.3.2 Horizontal Buoyancy

Open jet wind tunnels tend to have a non-uniform static pressure along the streamwise axis [80]. Assuming a linear slope, hence a constant pressure gradient, the following simplifications for the

horizontal buoyancy can be made. A constant pressure gradient causes a constant volumetric force, therefore the Archimedes principle can be employed:

$$F_d = ma = \rho V a \quad | \quad \text{Mass } \rho V, \text{ acceleration } a \tag{5.24}$$

$$| \quad \partial p = \rho a \partial h \quad | \quad \text{Archimedes' principle, pressure gradient over height } \frac{\partial p}{\partial h} \tag{5.25}$$

$$| \quad | \quad \partial h == \partial x \quad | \quad \text{"horizontal" buoyancy} \tag{5.26}$$

$$| \quad \frac{\partial p}{\partial x} = -\rho a \tag{5.27}$$

$$F_d = -\rho V \frac{\partial p}{\partial x} / \rho = -V \frac{\partial p}{\partial x} \tag{5.28}$$

$$| \quad V = A_{\text{airfoil}} s \quad | \quad \text{Model Volume } V, \text{ Cross-section } A_{\text{airfoil}}, \text{ span } s \tag{5.29}$$

$$c_d = \frac{F_d}{q_\infty S_{\text{ref}}} = -\frac{A_{\text{airfoil}} s \frac{\partial p}{\partial x}}{q_\infty S_{\text{ref}}} \tag{5.30}$$

$$| \quad S_{\text{ref}} = cs \tag{5.31}$$

$$c_d = -\frac{A_{\text{airfoil}} \frac{\partial p}{\partial x}}{q_\infty c} \tag{5.32}$$

$$| \quad \frac{\partial p}{\partial x} = \frac{\partial C_p}{\partial x} q_\infty \tag{5.33}$$

$$c_d = \underbrace{\frac{A_{\text{airfoil}}}{c^2}}_{\text{dimensionless airfoil cross-section}} \cdot \underbrace{-\frac{\partial C_p}{\partial x}}_{\text{streamwise pressure gradient}} \cdot \underbrace{c}_{\text{airfoil chord}} \tag{5.34}$$

The cross-section of the airfoil for the VACA4412s019 airfoil model is $A_{\text{airfoil}} = 459\text{cm}^2$. The gradient of the static pressure coefficient within the empty wind-tunnel is $\frac{\partial C_p}{\partial x} \approx -0.009 \frac{1}{\text{m}}$ [Fah24b].

5.3.3 Lift-Correction

Method of Vandrey The Method of Vandrey improves the method of the images (section 2.5.2.1) such that the nozzle and the collector of the free jet test section setup are taken into account. By this, a mixed-boundary problem is created which respects the fact that nozzle and collector have solid walls [39, p. 51]:

$$\Delta\alpha = -\frac{c_l c}{4H} \left(G_0 + \frac{\pi c}{\beta_{Ma} H} \left(\frac{1}{4} + \frac{c_m}{c_l} \right) G_1 \right) \tag{5.35}$$

$$\Delta c_m = -\frac{\pi^2 G_1}{32} \left(\frac{c}{\beta_{Ma} H} \right)^2 c_l \tag{5.36}$$

Two parameters G_0 and G_1 exist which depend on the exact test section geometry. In that context, the length of the open part of the test section is given as $l = 6.66m$. The distance of the model from the nozzle is given in figure 5.12 as $d_{ax} = 0.9m$. This way, the model is deemed to be at the approximate circulation center, hence the $c/4$-point. Note though, that [39, eq. 2.73, p.51] has a

typo in the lower part of the fraction: The whole lower part has to be raised to the power of 2, not just the first bracket!

$$G_0 = \frac{\left(\exp\left(\frac{2\pi l}{\beta_{Ma}H}\right) - 1\right)\exp\left(\frac{2\pi x_0}{\beta_{Ma}H}\right)}{\left(1+\exp\left(\frac{2\pi x_0}{\beta_{Ma}H}\right)\right)\left(\exp\left(\frac{2\pi l}{\beta_{Ma}H}\right)+\exp\left(\frac{2\pi x_0}{\beta_{Ma}H}\right)\right)} = 0.8904 \tag{5.37}$$

$$G_1 = -\frac{1}{6} + \frac{\left(\exp\left(\frac{2\pi l}{\beta_{Ma}H}\right) - 1\right)\exp\left(\frac{2\pi x_0}{\beta_{Ma}H}\right)}{\left(1+\exp\left(\frac{2\pi x_0}{\beta_{Ma}H}\right)\right)^2\left(\exp\left(\frac{2\pi l}{\beta_{Ma}H}\right)+\exp\left(\frac{2\pi x_0}{\beta_{Ma}H}\right)\right)^2}\times$$
$$\times\left(\exp\left(\frac{2\pi l}{\beta_{Ma}H}\right)\left(1+\frac{1}{2}\exp\left(\frac{2\pi x_0}{\beta_{Ma}H}\right)\right) - \exp\left(\frac{2\pi x_0}{\beta_{Ma}H}\right)\left(\frac{1}{2}+\exp\left(\frac{2\pi x_0}{\beta_{Ma}H}\right)\right)\right) \tag{5.38}$$

$$= 0.3373 \tag{5.39}$$

The Method of Vandrey allows for the most accurate representation of the test section geometry of the Göttinger-Windtunnel at ISTM and will therefore be employed during post-processing.

5.4 Data Reduction

The data is acquired in time series (acquisition settings in table 5.5, parameter settings in table 5.6).

The statistical moments defined in section 2.5.1.1 are used to assess different measurement properties as depicted in figure 5.13. Note, that the error bars are centralized over the median instead

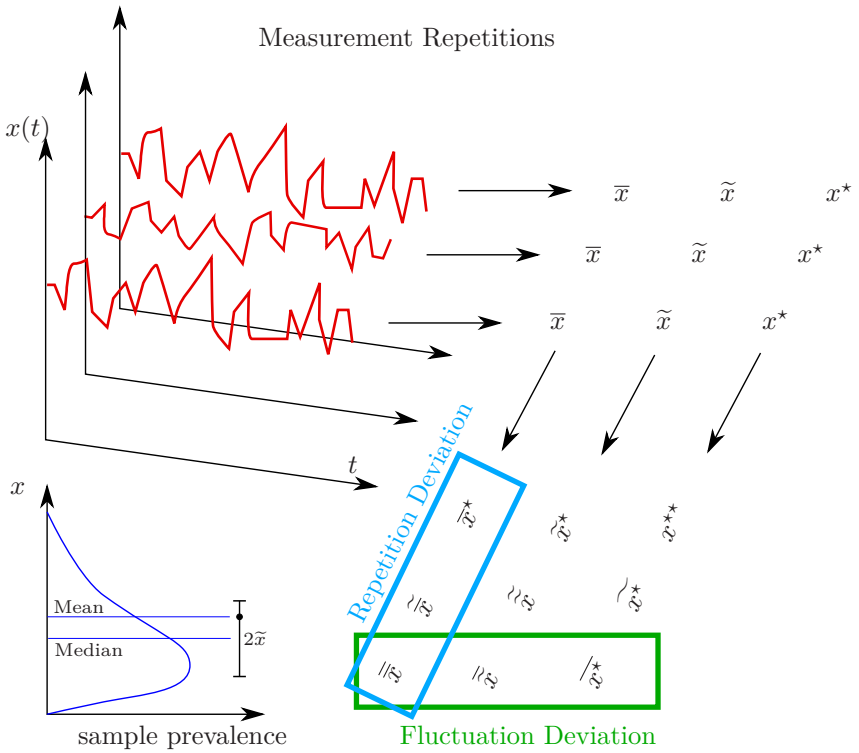

Figure 5.13: Repetition and Fluctuation Deviation Definition and Error Bar Representation.

of the mean value. For an arbitrary data distribution, this means that the error bar span does not cover a well-defined percentage of the samples. Instead, it gives a rather qualitative impression where the bulk of the data lies relative to the mean. Strong skew can be used as an indicator if there is a small amount of samples, which drags the mean away from the majority of data points. This allows an interpretation similar to the concept of so-called box plots [61, p. 54]. However, it keeps plots readable also at locations of data point concentration which is not the case for box plots.

Fluctuation Deviation This concept describes the fluctuations within a time series. Such fluctuations consist of measurement noise (sensor signal noise) as well as physical fluctuations of the measurement quantity. Signal fluctuations can be caused by processes that are an inherent feature of the measurement quantity, such as the velocity fluctuation of a hotwire measurement — and therefore of interest. Similarly, such fluctuations can also stem *e.g.* from test stand vibrations resulting from wind-tunnel fluctuations. The statistical moments of all individual time series with identical parameters are averaged for plotting. Technically, the sample standard deviation has to be used for the fluctuation deviation because it describes the spread of data of the physical process for which the acquired data points only mark a subset of all conceivable data points. However, the difference between sample standard deviation and population standard deviation is negligible in this case. This is because a dataset from which the fluctuation deviation is calculated consists of at least four repetitions of $t = 30$s measurement intervals with $f_s = 200$Hz which accumulates to $n_s \geq 24000$ datapoints which is why the population variance as described in equation 2.49 is used anyway.

Repetition Deviation / Repetition Error Naturally, individual time series of the same parameter combination will not lead to identical mean values (see uncertainty definition in section 2.5.2.1 & 2.5.2.2). Instead, mean values will vary over the repetitions of a measurement. The repetition error therefore expresses a measure of the reliability and significance of a certain mean value. In this context, the available dataset is the whole population of which the spread is to be determined, hence the population standard deviation is required.

Ideally, the repetition sample distribution should be unskewed or marginally skewed if all remaining parameters are kept identical. Yet, this cannot be guaranteed — especially over multiple months of the measurement campaign. Additionally, the large and complex test rig leaves room for human error during data acquisition such as inaccuracies in reinstating a certain parameter combination. Such replication error results in an increased repetition error [23, chapter 1-3.7]. For the present study, a strong skew of the repetition error indicates strong outliers, *e.g.* caused by replication errors.

Sensor manufacturers usually provide a sensor uncertainty that covers multiple error sources. Zero drift — the largest error source of most of the used sensors — can be significantly reduced in practice by employing zero measurements/tara. Therefore, the repetition deviation should be well within the uncertainty estimated by linear error propagation of the sensor uncertainties. Otherwise, significant unidentified error sources exist.

5.5 Results

5.5.1 Result Scope and Data Quality

This section displays results from experiments without flow control ("uncontrolled") both with and without tripping. This serves as a validation process to determine the reliability of the measurement system and analyze the properties of the test case.

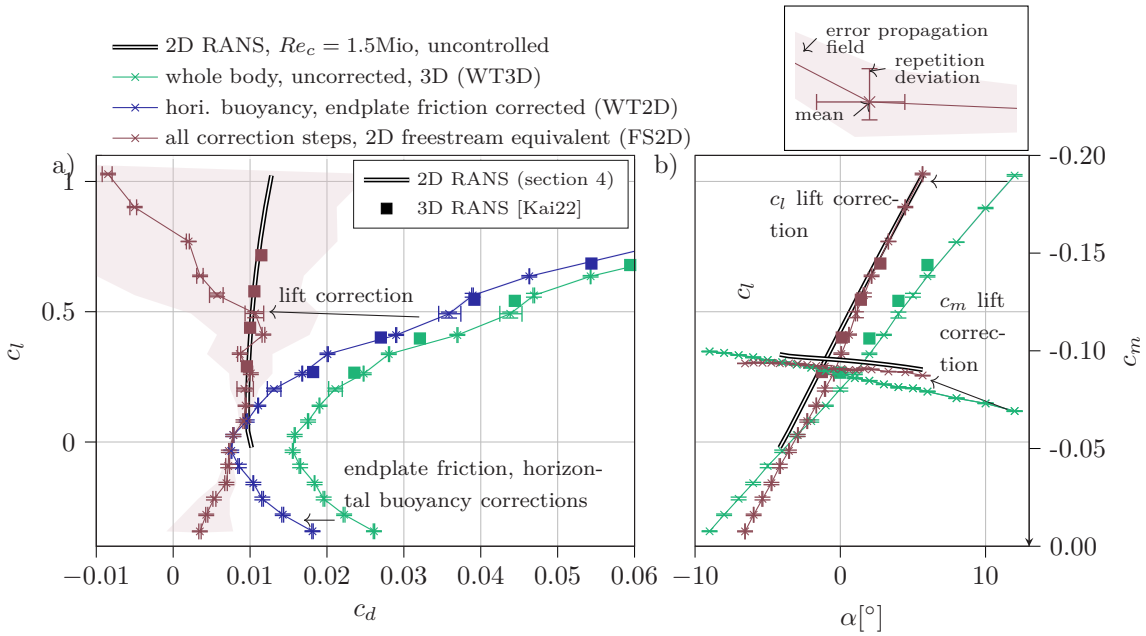

Figure 5.14: Wind tunnel correction steps applied to the balance measurement results including the linear error propagation fields and the repetition error. Uncontrolled cases, tripping at $X_{tr}/c = 10\%$, Re_c = 1.5Mio, VACA4412s019 airfoil model.

In the first step, the applied wind tunnel corrections (section 5.3) shall be examined on their effectiveness and how they affect result uncertainty. Figure 5.14 shows the results of the balance in the context of a polar plot with different levels of correction applied. The raw measurement is given by the green curves and represents the integral quantities of the three-dimensional airfoil model in the wind-tunnel domain and its streamwise coordinate system (WT3D). Clearly, the drag is overestimated significantly in the lift-over-drag polar. However, the result is well in line with the respective uncorrected results from the digital twin [Kai22], which is represented by the squared markers. In the next step, the drag measurement can be corrected by the approximate friction of the endplates (section 5.3.1) and the horizontal buoyancy of the airfoil model due to the static pressure gradient of the test section (section 5.3.2). With these two correction steps applied, the drag polar is shifted to the left, and the blue curve is obtained. Again, good agreement with the data from the digital twin can be observed. This data now represents the drag of a 2D airfoil section in the wind-tunnel domain streamwise coordinate system (WT2D). In the last step, the lift correction by Vandrey is applied (see section 5.3.3). This correction works by identifying the equivalent aerodynamic angle of attack α_{aero}. Therefore, the lift-over-AoA-curve is scaled in AoA-direction. As derived in section 2.5.2.1, the equivalent aerodynamic angle of attack is smaller than the geometrical AOA in the wind-tunnel domain. The lift curve (brown line) quite accurately resembles the lift curve obtained by RANS results of a 2D airfoil flow simulation (double line). The change in the angle of attack affects the coordinate system in which lift and drag are expressed. Therefore, some of what was measured as drag instead represents lift within the

corrected coordinate system. This effect can be seen when looking at the brown curve in the lift-over-drag polar plot of figure 5.14, to which all wind tunnel correction steps have been applied. The brown curve represents the experimental data in its 2D-freestream-equivalent form (FS2D). This last correction step — the lift-correction — most severely affects the result. The experimental results match the 2D airfoil RANS and the digital twin results within the lift range of $c_l \in [0, 0.5]$. Yet, below and above this range, a strong deviation of the experimental data from the numerical data can be observed. As this was not the case for the previous correction steps, it is quite clear, that the lift correction is responsible for overestimating the drag correction.

The strong effect of the lift correction on the results can also be observed regarding the uncertainty fields (transparent fields in similar color behind a plot) which stem from linear error propagation. Lift and drag forces span more than 2 orders of magnitude in figure 5.14. Within this macroscopic view of the data, the uncertainty fields from the raw data and the first correction step can hardly be seen behind the markers and interpolation lines. However, for the lift-corrected results of the drag, linear error propagation suggests a large uncertainty of the balance drag measurement result.

In section 5.4 it was expressed that the repetition error (thin error bars, figure 5.14) should be well within the uncertainty field if all relevant random error sources were identified correctly when analyzing the measurement methods. Clearly, this is the case for the presented data. Even for the data with all correction steps applied (FS2D), the repetition error bars are much smaller than the uncertainty field. This confirms that the sensor error given by the manufacturer is most likely dominated by the zero drift which is erased by daily zero offset corrections in the current measurement campaign. As a result, the true sensor repetition error is much smaller than the uncertainty estimated by the manufacturer's error estimate. This leads to an overall smaller repetition error than what is projected by the uncertainty fields estimated from linear error propagation.

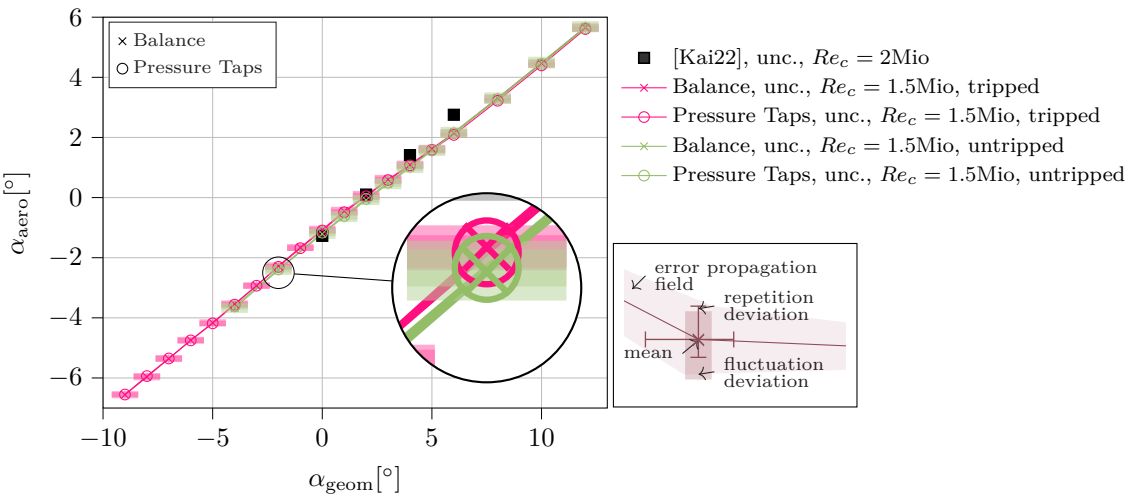

Figure 5.15: Comparison of digital twin results [Kai22] for lift-correction consequences in terms of effective AoA (α_{aero}) vs. geometrical AoA during experiments (α_{geom}) for pressure taps and balance. Uncontrolled Cases, $Re_c = 1.5$Mio, tripped cases: $X_{\text{tr}}/c = 10\%$, VACA4412s019 airfoil model.

The small repetition error compared to the uncertainty fields in the balance drag measurement leads to the conclusion that the overcompensation of the lift correction is a systematic error and not just a random artifact. Figure 5.15 shows the relevant relation, that the lift-correction establishes: The equivalent angle of attack of the case in freestream α_{aero} as a function of the geometrical angle of attack α_{geom}. The results of both balance and pressure tap measurements are displayed for two different airfoil model configurations. As lift-correction methods depend on circulation

and therefore lift, it is not surprising that the pressure taps and the balance agree well on the correction function because lift force is largely passed by pressure forces. Meanwhile, friction forces — which are not captured by the pressure taps measurement — hardly contribute to lift. Yet, the agreement is even better than expected as the curves for balance (x-markers) and pressure taps (o-markers) can hardly be told apart. This means, that the flow around the airfoil is closer to two-dimensional as expected and no significant interference of the endplates exists. Otherwise, the balance result would deviate stronger from that of the pressure taps which only acquire data in proximity to the symmetry plane of the airfoil model whereas the balance result is averaged over the whole surface. In consequence, both results follow the same slope which has a little dent in between $\alpha_{\text{geom}} \approx [3° - 6°]$. At this point, the experimental results clearly deviate from the results of the digital twin. Interestingly, these observations also hold for two different airfoil model configurations almost identically: The case, where no tripping is applied vs. the main experiment case with tripping at $X_{\text{tr}}/c = 10\%$. The latter configuration was also used for the digital twin [Kai22].

The fluctuation (for definition see section 5.4) of the lift-correction with time is almost identically small for both measurement techniques. This part is important because it means, that the bound vortex at the airfoil is quite steady in time which is crucial to apply the potential flow methods the lift-correction relies on.

The good agreement of balance and pressure taps, yet the non-ideal agreement with the digital twin, back the claim, that the Method by Vandrey results in a systematic error outside the range of $c_l \in [0, 0.5]$ for the present airfoil model. Most likely, this effect is responsible for the overcompensated drag correction by the lift-correction method of Vandrey. It has to be noted, that a similar analysis was conducted for alternative correction methods denoted in Ewald [32] as well as the one investigated by Kaiser [Kai22]. Yet, the Vandrey method gave the best agreement both in terms of correct lift slope as well as its effects on the drag measurements. This could also be expected since the method of Vandrey relies on the most accurate theoretical modeling of the present test section (compare section 5.3.3). However, the effect of the lift correction is almost independent of the configuration: The correction of the case with tripping is almost identical to the case without tripping. This means, that the lift correction has little effect on the drag changes for a given angle of attack. This is important because it implies, that a change in drag can be captured quite well despite the lack of accuracy of absolute values.

Figure 5.16 displays the measurement results of all measurement techniques for the main investigation configuration of the campaign: $X_{\text{tr}}/c = 10\%$ at a Reynolds number of $Re_c = 1.5$Mio. The conclusion of the systematic error in the lift correction can be confirmed again, as the pattern of the pressure drag curve in the lift-over-drag polar is almost identical to the already discussed pattern of the balance drag measurement. If the wind-tunnel correction is the main source of error here, this is to be expected as the same lift-correction method is applied to get from the 2D wind-tunnel domain results (WT2D) to the 2D freestream results (FS2D). Naturally, the pressure drag is always smaller than the total drag on the body, as the pressure taps do not capture the friction drag. The repetition error and the uncertainty field of pressure taps and balance are in the same order of magnitude, again confirming similar sources of errors.

A last strong argument on the topic of lift correction can be given considering the results of the validation campaign with the rented HGR-01 airfoil model of TU-Braunschweig [145] (figure D.5). This model has much less chord length ($c = 400$mm instead of VACA4412s019 $c = 750$mm). Clearly, the balance drag results are well in line with the wake rake measurements and do not show the overcompensation although the post-processing of the data is completely identical to the BLC campaign with VACA4412s019 airfoil. Reiterating on the statement of section 5.2.1: The model

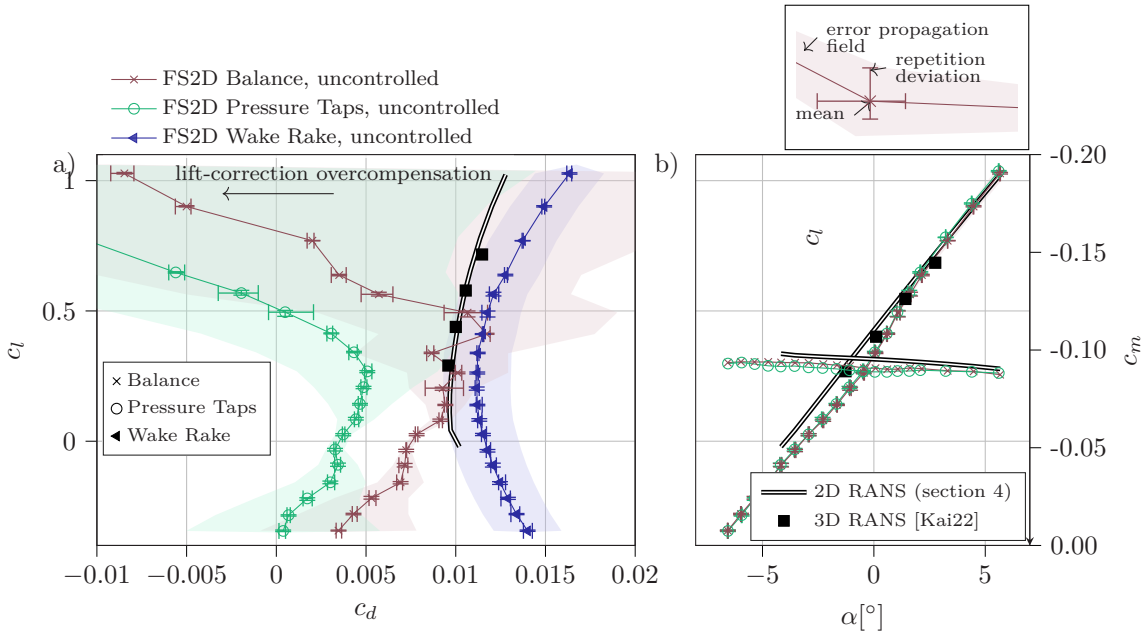

Figure 5.16: Comparison polar plot of measurement techniques balance, pressure taps, and wake rake. All wind-tunnel corrections applied (FS2D). Uncontrolled cases, tripping at $X_{tr}/c = 10\%$, $Re_c = 1.5$Mio, VACA4412s019 airfoil model.

size of the VACA4412s019 model with $c = 750$mm is indeed too large for the present wind-tunnel test section (section 5.1) if the goal is to investigate high-lift scenarios and measure lift and drag accurately. Meanwhile, the wake rake gives a very monotonic and smooth drag-polar with an extremely small repetition error and a lift-independent error propagation field. Note, that the lift information for the wake rake drag polar is taken from the balance results.

Considering the lift-over-AoA of figure 5.16, the implication of figure 5.15 can be confirmed: Balance and pressure taps give identical lift results with very high accuracy. The same is true for the pitching torque c_m which is also quite similar for balance and pressure taps. This can also be expected from the fact that the turbulent wall friction is about similar on both airfoil sides because the turbulent boundary layer has identical extensions due to the tripping at $X_{tr}/c = 10\%$.

In the next step, the significantly larger drag result of the wake rake compared to numerical data shall be discussed. This could be due to a systematic measurement error, *e.g.* triggered by a wrong estimate of the static pressure loss along the tunnel axis because the wake rake result strongly depends on this (see section 5.2.5). However, this seems to be unlikely considering the results without the tripping device both in figure 5.17 as well as figure D.5. Instead, it can be observed, that the XFOIL results of the untripped configurations match the experimental data very well. Meanwhile, the XFOIL results of the tripped configuration match well with the RANS results. This leads to the conclusion, that the tripping device at $X_{tr}/c = 10\%$ causes a significant form drag on its own which is not simulated in either numerical method.

The significant local impact of the tripping device on the local pressure field can also be seen in figure 5.18. The tripping location is at a very low c_p-value, hence a very high local velocity and within an accelerated flow (c_p still dropping at the tripping location). This means that the tripping device, which has a thickness of 1mm most likely sticks out significantly from the boundary layer and therefore experiences high velocity, and subsequently high drag. For the untripped case, the natural transition is caused by a laminar separation bubble which has a distinct yet small footprint on the airfoil suction side pressure distribution. The wake survey result in figure 5.18 right shows the strong effect of the tripping device on the suction side wake portion which is significantly

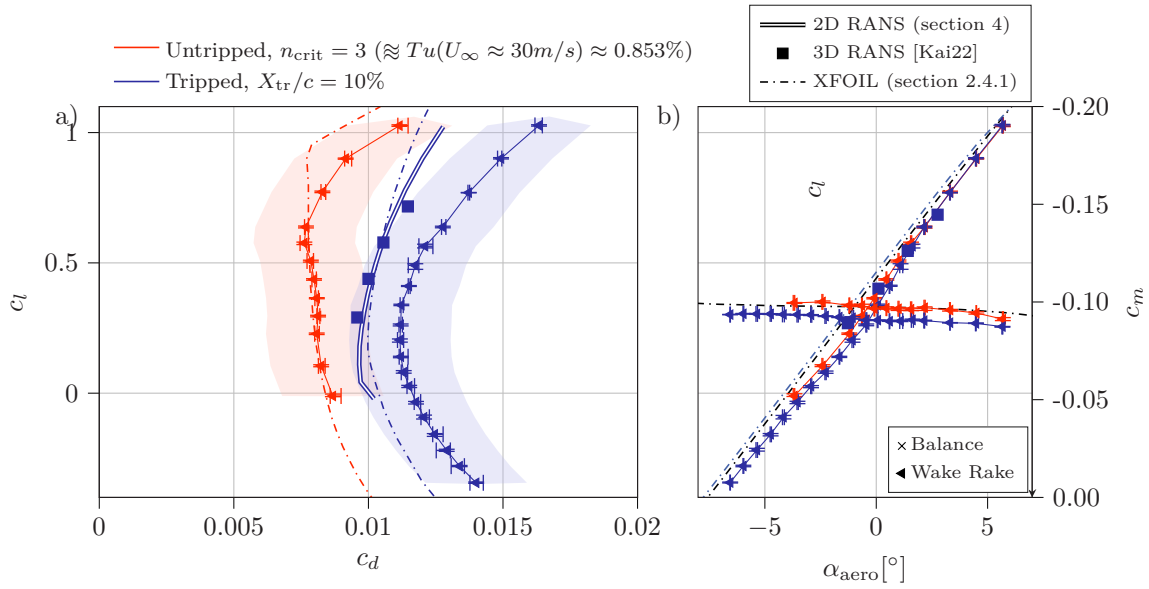

Figure 5.17: Comparison of tripped and untripped polar plots. Uncontrolled cases, $Re_c = 1.5$Mio, VACA4412s019 airfoil model.

enlarged compared to the untripped case. Although this can be expected by the presence of a larger development length of the turbulent boundary layer in the tripped case, the significant drag increase can also be attributed to the drag of the tripping device itself.

In terms of errors, the local pressure distribution c_p is very repeatable. This cannot be said about the local wake survey shape, which shows a significant repeatability error. As noted above, the integrated wake survey drag shows a much smaller repeatability error compared to the pressure tap result. This seeming contradiction can be resolved by the fact of how the wake survey measurement is acquired. For that purpose, the wake rake is moved by a traversing system both in spanwise and perpendicular ($\overline{Y}$) direction to average out manufacturing errors in the total pressure probes. However, this movement is only repeatable to about 2mm in the perpendicular direction. Yet, as a position label the required position is used. Therefore, the true $\overline{Y}/c$ coordinate of a wake survey measurement differs from its nominal (labeled) value up to about 2mm. This results in the wake survey curves being shifted to one another whilst keeping their integral value much more accurately than their $\overline{Y}$ position.

With this, the validation process of the test rig, the measurement techniques, and the test case (VACA4412s019 model) design can be concluded. The following statements can be made for the analysis of the boundary layer control experiments:

- Lift and drag can be measured to very good agreement by balance and pressure tap measurements.
- Within a range of $c_l \in [0, 0.5]$ absolute values of drag measured by balance and pressure taps seem reasonable, yet noisy. Outside this range, the absolute drag values lose their validity. However, drag differences of different configurations can still be obtained at quite a high repeatability.
- The wake survey measurements deliver accurate and repeatable drag measurements for a large range of AoA. However, the test case design shows a strong drag penalty due to the large tripping device, which has a pronounced effect within the low drag region of the airfoil ($c_l \in [0, 0.5]$). Yet, this can be deemed a somewhat constant drag offset, which is unaltered as long as the tripping device remains unchanged, which is the case for subsequent analysis.

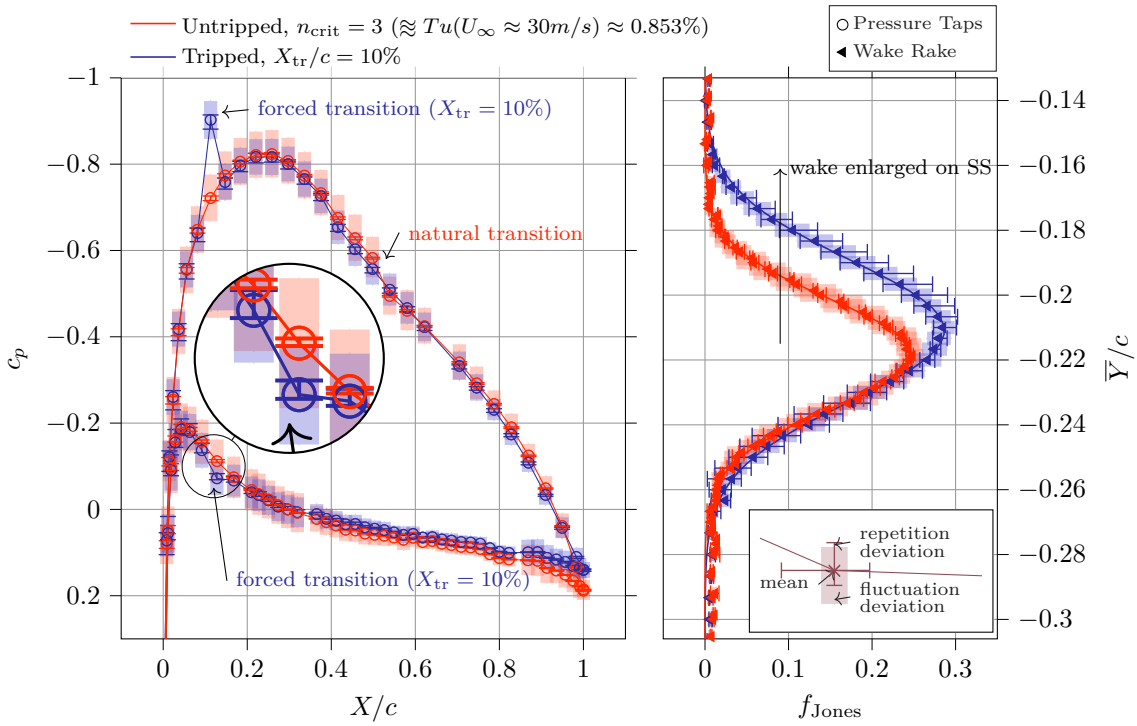

Figure 5.18: Comparison of tripped and non-tripped: Pressure Distribution (left) and wake survey (right). Uncontrolled cases, $Re_c = 1.5$Mio, AoA $\alpha_{geom} = 4°$, VACA4412s019 airfoil model.

- The wake survey is a very sensitive indicator of changes in circulation and therefore lift. However, it is not used to calculate changes in lift for the present study in a quantitative manner. Such methods have been described to identify lift and also different drag components [16] and could therefore be interesting for future use in the wind tunnel at ISTM.

5.5.2 General Boundary Layer Control Performance

In this section, the focus shall be put on general BLC properties both in terms of integral as well as localized quantities.

Figure 5.19 shows the pressure distribution on the airfoil pressure side as well as the corresponding wake survey for different angles of attack. The pressure distribution plots show that the test case allows for the BLC (location: grey areas) to be operated in very different pressure gradient environments. For all of them, it can be observed that the controlled case shifts the pressure to slightly higher pressure $c_{p,\text{controlled}} > c_{p,\text{uncontrolled}}$. This eventually reverses at the aft end of the control region where the controlled case shows a lower or equal pressure level compared to the uncontrolled case. A notable difference to the numeric results is the already mentioned (section 5.5.1) effect of the tripping device which leaves a significant footprint in the local pressure distribution. As expected that does not seem to influence the comparison of controlled and uncontrolled cases much, as the effect of the tripping device is similar for controlled and uncontrolled cases no matter which AoA is investigated. However, it can be observed that the footprint of the tripping device in the pressure curve becomes less pronounced for progressively more favorable pressure gradients (FPG) up to a point that it is hardly visible (at $\alpha_{geom} = 12°$). Because FPG stabilizes the boundary layer, the tripping device has to introduce enough turbulent kinetic energy to keep the turbulent boundary layer present throughout the FPG region without relaminarizing. This was one reason for the choice of the rather intrusive size of the tripping device. It seems though,

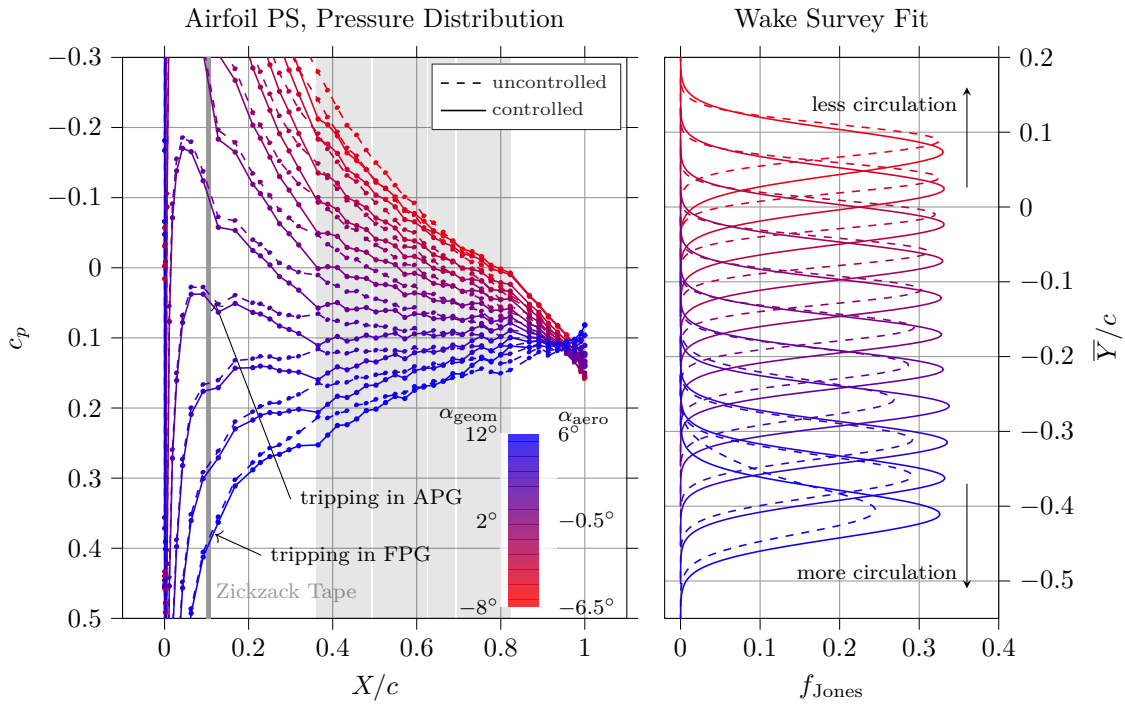

Figure 5.19: Pressure Distribution (left) and fitted wake survey results (right) for controlled (solid lines) and uncontrolled cases (dashed). $Re_c = 1.5$Mio, control rate $c_q = 0.5\%$ chambers 1 through 7, VACA4412s019 airfoil model. Grey areas show the X location of the BLC chambers.

that for the most favorable pressure gradient case $\alpha_{geom} = 12°$ the tripping device still fails to ensure a turbulent boundary layer along the entire airfoil PS surface for the uncontrolled cases. This can be deduced from the wake survey, for which the largest case shows a different wake shape for the uncontrolled case with a much smaller deficit. Blowing BLC destabilizes the relaminarizing boundary layer which leads to a wake shape similar to the neighboring angle of attack. In this context though, the BLC does not act as it is supposed to because it acts on a (at least partially) laminar boundary layer, possibly increasing viscous drag. This has to be kept in mind for analyzing integral quantity changes due to boundary layer control. Apart from that, the wake survey shapes of the controlled cases relate equally to their uncontrolled counterpart for the remaining AoA: The controlled cases always show a larger wake which is pushed towards the airfoil pressure side. This is also an indicator of slightly increased circulation and therefore lift of the controlled cases. This is well in line with numerical results (figure 4.8).

In terms of integral quantities, the relevant quantity for comparing BLC cases is the drag change compared to the corresponding uncontrolled case. As known from numeric results such drag change can be expected to fall within the order of $\left|\frac{\Delta c_d}{c_d}\right| = 0\%..30\%$ for the present configuration. Therefore, it is yet again one order of magnitude smaller than the already small drag values. Naturally, the error propagation fields in figure 5.20 appear much larger than in the polar plots displayed above. Similarly, the repetition error appears larger such that the error bars become visible behind their markers. Still, the repetition error is well within the error propagation field which is important as explained in section 5.4. Also, the skew of most repetition error bars is rather small, indicating that the single measurements fall randomly around their mean and do not show large outliers.

The trend of the mean values with the size of the repetition errors is still such that it can be called significant: Overall, a drag reduction with increasing lift can be seen both in terms of body drag as well as inclusive drag. The trends of both measurement techniques — balance and wake rake —

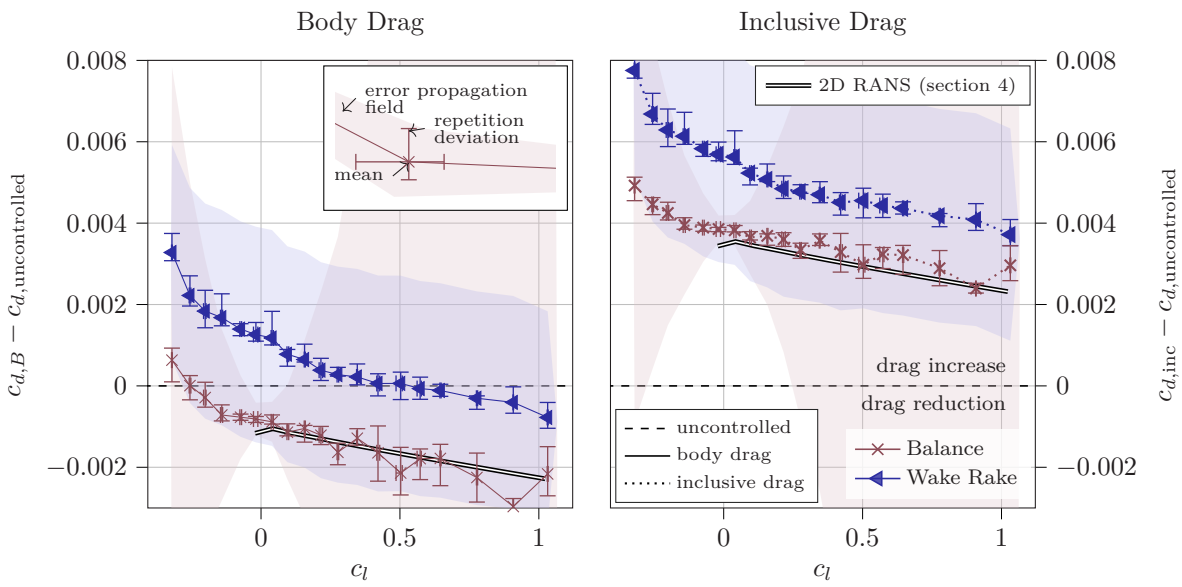

Figure 5.20: Drag change $\Delta c_d = c_{d,\text{controlled}} - c_{d,\text{uncontrolled}}$ for body drag (left) and inclusive drag (right) over airfoil lift. $Re_c = 1.5$Mio, tripping at $X_{\text{tr}}/c = 10\%$, $c_q = 0.5\%$, AoA $\alpha_{\text{geom}} = [-9°, 12°]$

are identical but offset to one another. This offset can have several reasons. As it is constant over varying AoA (*i.e.* lift) though, it is due to an effect that exists systematically at equal blowing magnitude throughout the variation of AoA. One possibility is that the tubing that delivers the control fluid has a residual force acting on the model. This would be constant as it depends on the inside pressure of the tubing. As such, it influences the balance measurement result. However, the balance result very accurately resembles the results that are calculated by RANS. This means, that the systematic deviation of balance and wake rake result is more likely to be due to a systematic error in the wake rake measurement. The current means of investigation make it difficult to find a ground truth here other than the excellent agreement of balance and RANS results. Nevertheless, the similar trends of balance and wake rake results agree well despite the offset between the curves.

As the balance result of drag reduction over the polar is deemed more accurate in terms of systematic errors, a body drag reduction is achieved for almost the complete AoA sweep. Figure 5.20 also suggests that the experimental control performance is comparable to the numeric results. This is interesting because it could be expected that experimental microblowing tends to be at least partially less efficient. Such expectation is based on the finite character of the micro-blowing which introduces additional turbulent kinetic energy compared to truly uniform blowing as it is implemented in the numerical studies. The fact that the associated penalty seems to be negligible (as far as the balance result is concerned) indicates that truly uniform blowing was achieved from a macroscopic point of view. Local boundary layer properties within the controlled region are treated in more detail in sections 5.5.4 and 5.5.5. For integral quantities, it can stated that body drag reduction by uniform blowing turbulent boundary layers is possible by employing the microblowing technique and the chosen perforation properties. Meanwhile, inclusive drag reduction is not possible within the investigated parameter range. The small repeatability error and the agreement of both measurement techniques are good enough that such a statement can be made with very high certainty. Additionally, this finding agrees very well with numerical results.

In the numerical section (4.2.3) it was found that the effects of uniform blowing scale about linearly with control intensity. On one hand, this can be expected if the control performance is largely driven by the potential flow properties of the source in freestream (section 3.1.1). However, it can also be expected that the exact properties of the turbulent boundary layer play a role

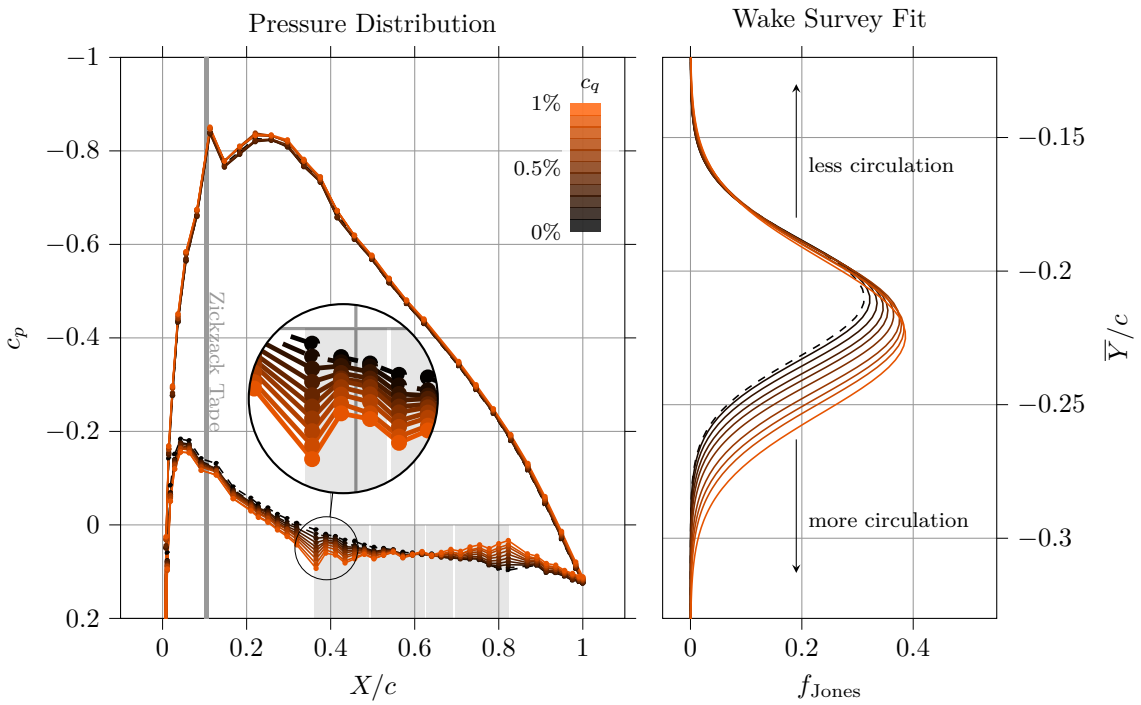

Figure 5.21: Pressure Distribution (left) and wake survey fit (right) for increasing control intensity $c_q = [0, 0.9]\%$. $Re_c = 650000$, tripping at $X_{\text{tr}}/c = 10\%$, $\alpha_{\text{geom}} = 4° \equiv \alpha_{\text{aero}} \approx 1.1°$

which was also found in literature (*e.g.* [7, 51]). As such, the RANS method used for the present numerical investigations may not be suitable when it comes to analyzing the control performance with increasing control intensity. Figure 5.21 shows the local effects on the pressure distribution and the wake flow for an airfoil chord Reynolds number of $Re_c = 650000$ for control intensities in the interval of $c_q \in [0, 0.9]\%$. The experimental results show a linear scaling with the control intensity. This is true both for the pressure distribution as well as the wake survey. Figure 5.21 shows a similar pressure increase at the start of the control region as figure 4.16. Meanwhile, the opposite airfoil side is hardly affected by the control on the airfoil pressure side (similar to numeric results in figure 4.5). The wake survey also hints at the linear correlation of control intensity and inclusive drag increase by steadily increasing wake size towards the airfoil pressure side with increasing control intensity. This already explains the development of integral drag quantities which can be seen in figure 5.22. The agreement of balance results and 2D freestream RANS is again much better than the result of the wake rake. For the lower Reynolds number $Re_c = 650000$, the balance shows some systematic difference to the RANS result yet it nicely resembles the slightly curved character of the curve which stems from a saturation in friction drag reduction whereas the pressure drag reduction follows a linear curve. Such a trend in integral quantities is very similar to the numeric results in figure 4.12. Also, it can be observed, that the results are Reynolds-independent as far as the result accuracy allows such a statement. Reynolds independency is a strong indicator for the conclusion that the performance of uniform blowing is mostly driven by potential flow effects, which are independent of the Reynolds number whereas turbulent boundary layer properties have a weaker impact on the control performance.

The results of the pressure taps show an interesting effect, which concerns the uncertainty about the uniformity of microblowing in experimental investigations: The pressure drag for very low blowing ratios is constant at first whereas the balance results indicate body drag decreases. This means that the friction drag is reduced. The ratio of controlled area $l_{\text{BLC}}/c = 0.466$ to total airfoil circumference $l_{\text{foil}}/c = 2.05$ is only $l_{\text{BLC}}/l_{\text{foil}} \approx 22.7\%$. Even if the whole wall friction within the

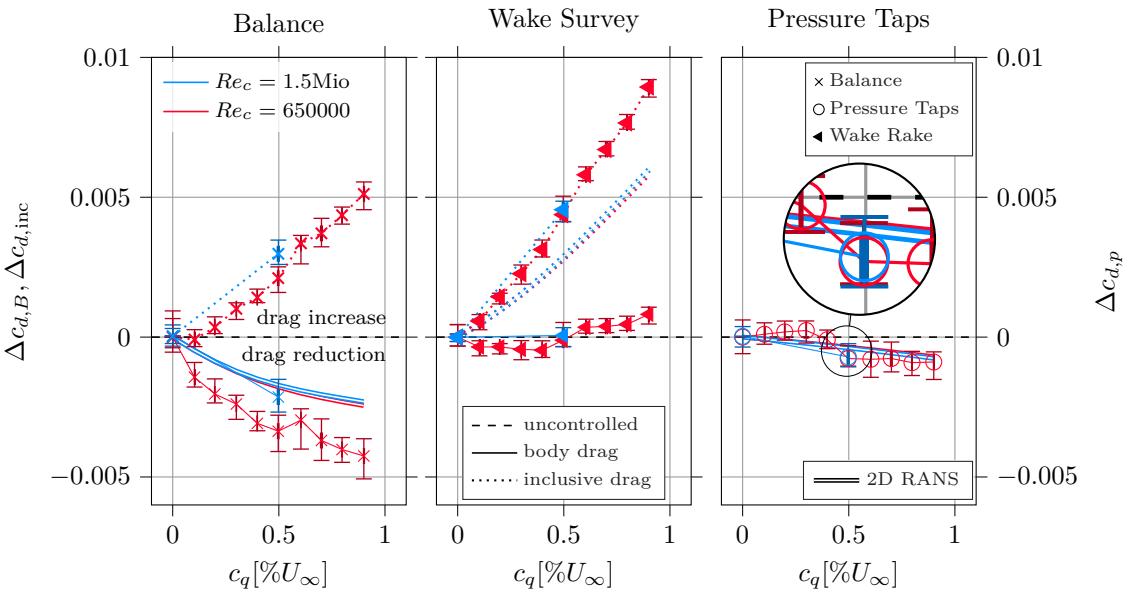

Figure 5.22: Comparison of drag change $\Delta c_d = c_{d,\mathrm{controlled}} - c_{d,\mathrm{uncontrolled}}$ for different airfoil chord Reynolds numbers Re_c and increasing control intensity. Tripping at $X_{\mathrm{tr}}/c = 10\%$, AoA $\alpha_{\mathrm{geom}} = 4°$

controlled area was erased by the control, the total friction drag would only be reduced about the portion that stems from the control area. Even substantial local wall friction reduction of 50% would only lead to roughly 8% of total friction drag reduction. This explains, that such friction drag reduction is hard to detect and — given the repetition error in the pressure taps and balance result — could be a wrong conclusion of the results in figure 5.22. For higher blowing ratios it can be expected that blowing acts less uniform and instead more closely resembles the physics of synthetic jet flow control. Eventually, such an effect could lead to friction increase [33, 149] or at least a saturation of local friction drag reduction. For the results at $Re_c = 650000$, this effect and/or saturation of friction drag reduction can indeed be observed regarding the slope of the body drag curves of both wake rake and balance which is bent upward for higher blowing ratios. This means that the drag reduction becomes less for higher blowing rates. It has to be stressed again though, that the repetition error of the pressure taps does not allow a definite statement here. Therefore, the results can only be seen as an indicator of friction drag reduction. Friction drag reduction will be investigated in section 5.5.5 again.

5.5.3 Influence of Static Pressure on Control Performance

The findings about the possible influence of static pressure within the control region on the control performance (section 3.3) were made after designing the experimental test case. Fortunately, figure 5.19 gives a hint on how to operate the existing airfoil model such that the control performance of uniform blowing in turbulent boundary layers can be studied for different static pressure and otherwise unchanged parameter settings: Choosing an appropriate angle of attack, a pressure distribution comparable to figure 4.16 can be obtained: There is a slightly adverse pressure gradient along the controllable portion of the model. This allows for different static pressures within the active, controlled region if only one control chamber is operated at a time. The strength of the adverse pressure gradient depends on the angle of attack. AoA $\alpha_{\mathrm{geom}} = -9°$ and $\alpha_{\mathrm{geom}} = -3°$ (about zero lift) are chosen for this particular study. The downside of the $\alpha_{\mathrm{geom}} = -3°$ is, that the adverse pressure gradient is smaller which directly affects the range of different static pressures at which the BLC is operated for different active control chambers.

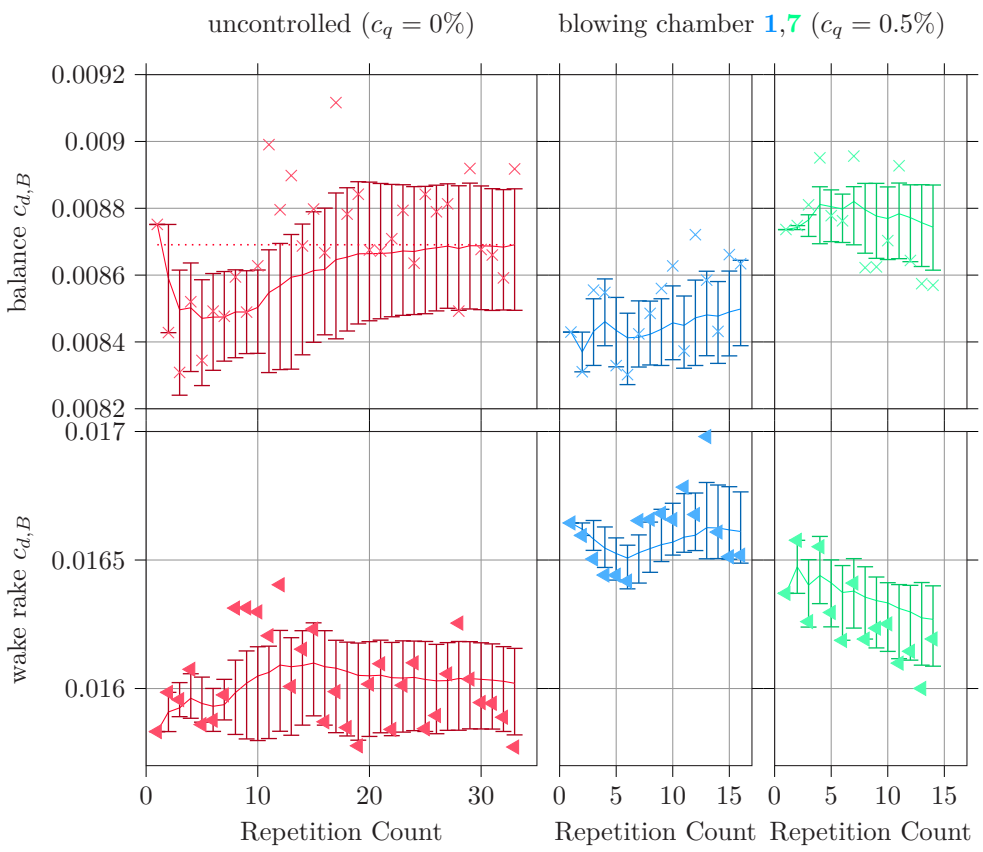

Figure 5.23: Convergence Plot AoA -3 oder -9, balance and wake rake results for uncontrolled cases and cases with different individual control chambers (1 and 7) turned on separately. $Re_c = 1.5$Mio, tripping at $X_{tr}/c = 10\%$, $c_q = 0.5\%$, AoA $\alpha_{geom} = -9°$.

The downside of using only one control chamber at a time instead of seven simultaneously is that the control effect is reduced by a factor of roughly 1/7 yet again compared to figure 5.20. This increases the demands on measurement accuracy and error propagation even more. Therefore, figure 5.23 is used to showcase how the repetition error defined in section 5.4 is obtained for the present experimental campaign. As an example, the operating points of an uncontrolled case are compared to two cases that have only one active control chamber. The number of repetitions is increased compared to the results shown in the previous sections (see also table 5.6) to improve the repetition error convergence. Figure 5.23 displays how the mean body drag develops with increasing measurement repetition count and how this affects the calculation of the repetition error bars. It becomes very clear that the investigation of the static pressure level influence by operating only single BLC chambers takes the measurement techniques to the limit of acquiring significant drag difference results. Fortunately, the number of seven different control chambers adds certainty again by achieving results for multiple different static pressure levels and not just the two displayed in figure 5.23.

Figure 5.24 shows the results of the change of drag compared to the uncontrolled case $\Delta c_d = c_{d,\text{controlled}} - c_{d,\text{uncontrolled}}$ for two different angles of attack. The range of static pressure levels at the individual control chamber positions is different for the two AoAs due to the different pressure gradients of these two cases. The balance results show a vague trend with differences of means about as large as the respective repetition error. Meanwhile for the wake rake and the pressure taps the results are a little bit more consistent for varying pressure levels although the repetition error of single chamber results is not significantly smaller than that of the balance. Still, the large number of different cases due to the two different angles of attack and the seven individual

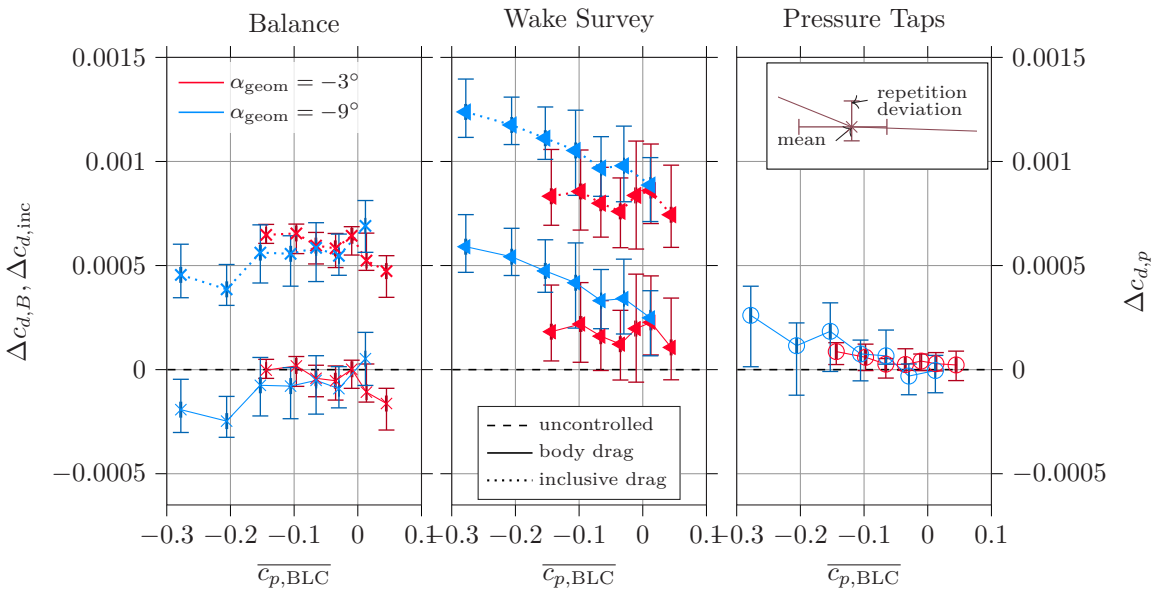

Figure 5.24: Comparison of drag change $\Delta c_d = c_{d,\text{controlled}} - c_{d,\text{uncontrolled}}$ for changing of which control area of the model is operated. This involves operating the same control schemes in different static pressures $\overline{c_{p,\text{BLC}}}$. Red curve for zero overall lift ($\alpha_{\text{geom}} = -3° \equiv c_l \approx 0$), blue curve for negative lift ($\alpha_{\text{geom}} = -9° \equiv c_l < 0$). $Re_c = 1.5$Mio, tripping at $X_{\text{tr}}/c = 10\%$, $c_q = 0.5\%$

control chambers allows the statement that the drag is reduced more or increased less the higher the average static pressure within the control region $\overline{c_{p,\text{BLC}}}$. It has to be noted again that this is a mere correlation because — due to the nature of airfoil flows — it is impossible to change **only** the pressure level whilst keeping every other parameter such as pressure gradient, boundary layer development length, etc. constant. Yet, the trend is similar to the numerical cases in section 4.2.5 although various parameters such as airfoil, control region size, control region position, and Reynolds number are different. Observing similar behavior despite different conditions supports the hypothesis from the analytical section (3.3).

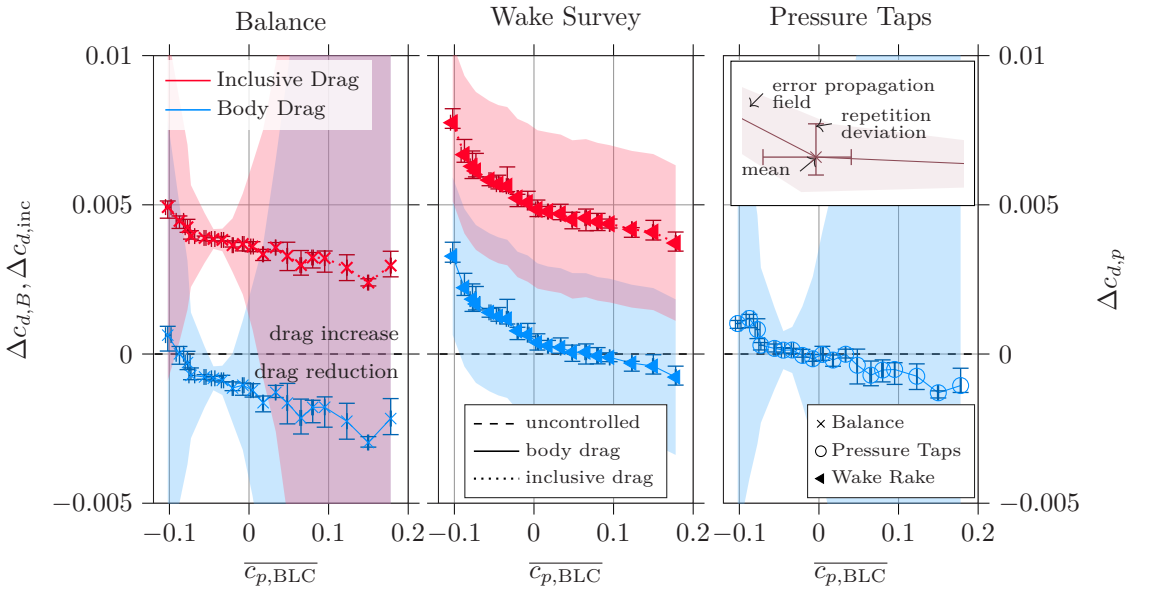

Figure 5.25: Drag change $\Delta c_d = c_{d,\text{controlled}} - c_{d,\text{uncontrolled}}$ for body drag and inclusive drag (right) over the average static pressure $\overline{c_{p,\text{BLC}}}$ within the active control region (chamber 1 through 7). Individual datapoints are created by varying AoA $\alpha_{\text{geom}} = [-9°, 12°]$. $Re_c = 1.5$Mio, tripping at $X_{\text{tr}}/c = 10\%$, $c_q = 0.5\%$.

The search for more cases to investigate the hypothesis about the influence of pressure level on uniform blowing performance leads to figure 5.19 again. Changing AoA also leads to different mean static pressures within the control region, not just different pressure gradients. Therefore, figure 5.20 can also be plotted over the mean static pressure of all control chambers. This leads to figure 5.25. The significance of the results is higher compared to operating just single BLC chambers like in figure 5.24. As mentioned above, this comes at the cost of not only varying the mean static pressure but also the pressure gradient. Nevertheless, the correlation of improving control performance (reducing drag) with increasing static pressure within the control region is similar despite the fact, that a different parameter was varied compared to the example from figure 5.24. The fact, that body drag decreases similar to the pressure drag backs the hypothesis that the drag reduction is caused by a potential flow effect and less by a viscous effect. Therefore, figure 5.25 is another indicator that backs the hypothesis that uniform blowing improves drag reduction (or reduces drag increase) for higher static pressure levels within the control region.

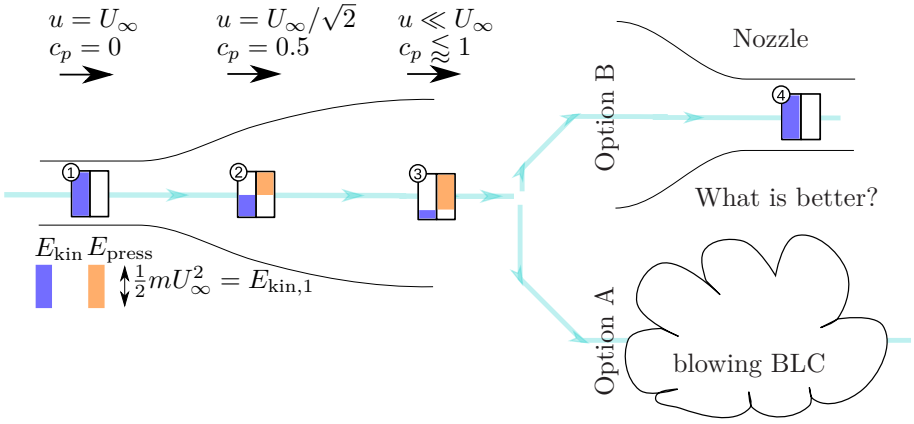

Figure 5.26: Hypothetical comparison of exhausting the BLC fluid at collection pressure ($c_p = 1$) through a nozzle (identity, momentum, and energy balance remain unaltered to the uncontrolled case: Option B) vs. using the BLC fluid to operate blowing control (Option A).

The hypothesis about the influence of static pressure within the BLC region on BLC performance can be specified based on the results so far: If uniform blowing only scales with pressure level, then the following thought experiment can be made: Does the inclusive drag of the controlled case equal the body drag of the uncontrolled case if the static pressure in the control region is increased until total freestream pressure is reached ($c_{p,\text{BLC}} = 1$)? Such comparison is depicted in figure 5.26 which is an adaption of figure 3.2. Expelling the collected fluid through a nozzle causes no residual force. Therefore, adding this to an uncontrolled body is an identity operation such as multiplying a quantity by 1. Indefinitely many of such ideal (loss-free) collector-nozzle combinations may be added, but the total drag of the system will not change. The question is: Is this the same for applying uniform blowing on the body at $c_p = 1$? In other words: Is blowing at $c_p = 1$ equivalent to expelling the same fluid through a nozzle in the streamwise direction?

1. If a body with uniform blowing is equivalent to expelling the control fluid through a nozzle then uniform blowing performance scales only with pressure level and is, in fact, an identity operation in an external flow.

2. If a body with uniform blowing is superior to expelling the control fluid through a nozzle then uniform blowing can be — at the right conditions — act as a turbulent boundary layer control scheme that allows actual net drag reduction (≡ inclusive drag reduction).

3. If a body with uniform blowing is less efficient than expelling the control fluid through a nozzle it means uniform blowing cannot act as a net drag reduction boundary layer control scheme — not even theoretically.

So far, all results acquired in the present numerical and experimental campaigns fell into category 3: No inclusive drag reduction could be observed, therefore it would have been better to just expel the control fluid in a nozzle or not collect it in the first place and stick with the uncontrolled airfoil. However, all presented cases acted at static pressures within the control region very far from $c_p = 1$, therefore causing large losses both in internal flow and mixing losses within the external flow. Yet, all cases presented within the current section also showed that their performance increases with increasing static pressure within the control region. This raises the question of what happens if the investigated uniform blowing configuration could be operated at higher static pressure than that possible within the current study.

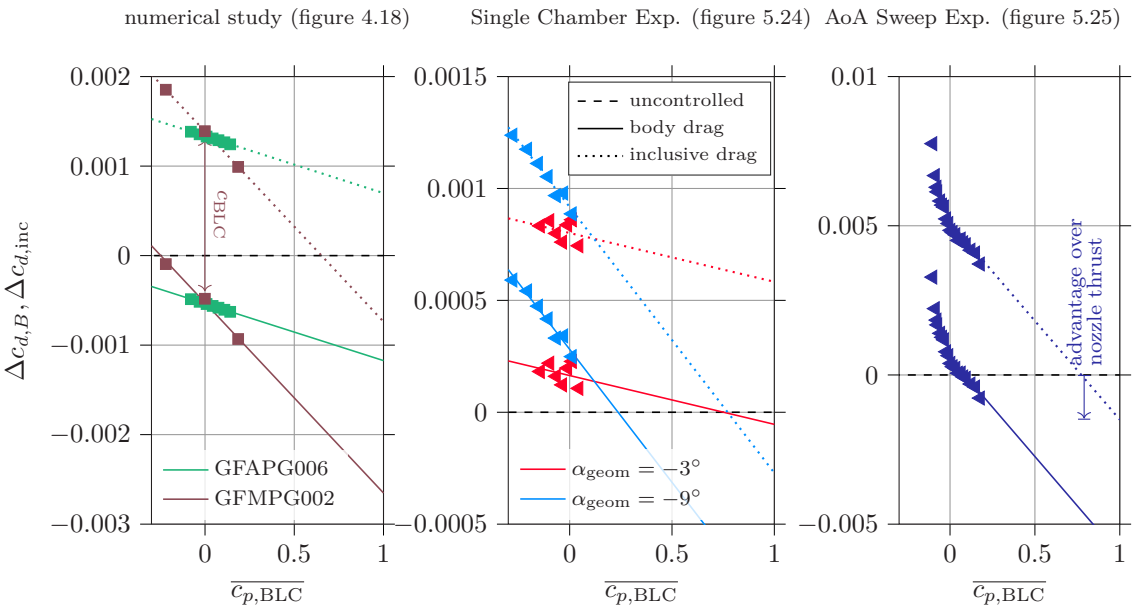

Figure 5.27: Drag change $\Delta c_d = c_{d,\mathrm{controlled}} - c_{d,\mathrm{uncontrolled}}$ for body drag (solid lines) and inclusive drag (dotted lines). Trendlines extrapolated for $\overline{c_{p,\mathrm{BLC}}} \to 1$. Data from previous figures is indicated in the respective title. $c_q = 0.5\%$

Figure 5.27 uses the data from numerical and physical experiments of the present studies to extrapolate the expected control performance to higher static pressures. Both body drag and inclusive drag are plotted. For the judgment of the net drag reduction potential only inclusive drag is relevant though.

One statement can be made with very high certainty: The different slopes of the cases compared in figure 5.27 are a clear sign that uniform blowing is not an identity operation so category 1 of the aforementioned possibilities can be ruled out with very high certainty: Uniform blowing does not only scale with the static pressure level within the control region.

No certain statement can be made if uniform blowing can be a net drag reduction scheme due to the strong extrapolation. It looks as though some of the cases intersect the inclusive drag reduction barrier even if operated at static pressure levels $c_{p,\mathrm{BLC}} < 1$. This means, that at the right parameter combination and suitable pressure level, such a scheme could be superior to expelling the control fluid via a nozzle and therefore be a net drag reduction boundary layer control scheme. Other cases have a slope of drag change that does not intersect the drag reduction barrier before reaching a static pressure within the control region equal to stagnation pressure ($c_p = 1$) which means they

would be less effective than expelling the control fluid via a nozzle, even if operated at hypothetical $c_p = 1$. As mentioned above, these statements suffer from the strong extrapolation character, and due to the influence of viscous effects it is also unlikely that the drag change always follows a linear slope. Deviations from the linear slope are also observable in the data of figure 5.27. Therefore, it remains unclear if a net drag reduction with uniform blowing is possible. Still, it can be stated, that all of the presented configurations are quite far from inclusive drag reduction for the pressure levels at which they were operated.

5.5.4 Flow through Control Surface

The previous section and the numerical results (section 4.2) only discussed the resulting external flow field with uniform blowing flow control and subsequent changes to integral lift and drag quantities. This was done both in terms of the immediate effect on the body where the control is applied (body drag) as well as the overall drag including the collection of the required control fluid (inclusive drag). In this section, the analysis will focus on the effort of getting the control mass flux from its point of collection to the point where it reenters the external flow domain at the blowing location. Most importantly and most generally this regards the viscous losses that stem from the flow through the porous surface.

This may seem like a pure question of implementation, which is why the research question shall be specified more precisely to extract the general conclusions that can be drawn:

1. What is the pressure loss of the flow through a surface with an open area of $A_{\text{hole}}/A_{\text{BLC}} = 10\%$ and how does that compare to the literature results of other open areas (figure 5.3). In other words: Is the chosen open area a good compromise in terms of pressure loss and blowing uniformity as it was suspected, *e.g.* by Hwang [47]?

2. Given the available supply pressure of freestream total pressure — which is the consequence of how fluid can be collected from freestream and which led to the conclusion that the inclusive drag is the relevant drag quantity to judge net drag reduction potential, see section 3.3 — can uniform blowing be supplied without additional pump effort and regulated by valves only?

    - If **yes**, this means that the inclusive drag is a universal drag quantity that covers every effort to operate uniform blowing and is therefore the only relevant drag quantity for assessing net drag reduction potential. If the control goal is not net drag reduction but simply localized force control then inclusive drag is also the relevant quantity to assess the control operating effort. This means, there is an **implementation-independent** quantity, which makes it much more easy to judge the control effectiveness for an application. Such judgment was identified to be an important step in advancing a boundary layer control scheme [125].

    - If **not**, additional effort in terms of pump operating power has to be considered to estimate the overall effort to operate uniform blowing.

The pressure loss is a function of the control velocity, *i.e.* the control mass flux. Both quantities have been measured throughout the whole measurement campaign (methodology in section 5.2.6) and independently for each control area of the airfoil model (see appendix C). The results are presented in the dimensionless form ζ_{BLC} as it is given in equation 5.20. Several references can be formulated to provide context to this quantity:

- **Lower Bound** The experimental pressure loss in the subsonic regime consists of two loss-portions: The viscous loss originates from the wall friction inside the porous surface and the Carnot loss is a total dissipation of kinetic energy. The latter only depends on the velocity the BLC fluid reaches inside the porous material. Its mean quantity can be calculated based on the mean control velocity v_{BLC} and the ratio of the open area of the control surface:

$$\Delta p_{\mathrm{Carnot,BLC}} = \frac{\rho}{2}\left(\frac{A_{\mathrm{BLC}}}{A_{\mathrm{hole}}} v_{\mathrm{BLC}}\right)^2 \tag{5.40}$$

  Based on the normalization with the mean BLC velocity (same normalization as with ζ_{BLC}) the dimensionless Carnot loss can be expressed:

$$\zeta_{\mathrm{BLC,Carnot}} = \left(\frac{A_{\mathrm{BLC}}}{A_{\mathrm{hole}}}\right)^2 = 100 \tag{5.41}$$

  This is the minimum possible dimensionless pressure loss even if no viscous losses were present in the flow through the porous surface.

- **Realistic Lower Bound** It is not reasonable to expect a flow resistance for the flow through the porous surface less than the minimum friction of pipe flows. For this, the Darcy-Weisbach Equation [15] can be employed to retrieve a lower bound reference.

$$\frac{\Delta p}{\rho g} = 64\nu \frac{L}{D^2}\frac{U}{2g} \tag{5.42}$$

  In the case of the flow through the perforated sheet metal, the pressure difference Δp is given by the difference of chamber pressure to local pressure at the airfoil surface. The length L of the pipes is given by the thickness of the sheet metal which is $L = D_{\mathrm{BLC}} = 1\mathrm{mm}$ whilst the diameter is given by the hole diameter $D = d_{\mathrm{hole}} = 68\mu\mathrm{m}$ (see manufacturing report in appendix C). The bulk velocity of the flow through the holes is given by the control velocity v_{BLC} and the portion of open surface A_{hole} to total surface A_{BLC}, resulting in $U = \frac{A_{\mathrm{BLC}}}{A_{\mathrm{hole}}} v_{\mathrm{BLC}}$.

$$\text{dimensional: } \Delta p = \frac{\rho}{2} v_{\mathrm{BLC}}^2 \left(\frac{A_{\mathrm{BLC}}}{A_{\mathrm{hole}}}\right)^2 \frac{64\nu}{v_{\mathrm{BLC}}\frac{A_{\mathrm{BLC}}}{A_{\mathrm{hole}}} d_{\mathrm{hole}}} \frac{D_{\mathrm{BLC}}}{d_{\mathrm{hole}}} \tag{5.43}$$

$$\text{normalized: } \zeta_{\mathrm{lam,BLC}} = \frac{A_{\mathrm{BLC}}}{A_{\mathrm{hole}}} \frac{64}{Re_{\mathrm{hole}}} \frac{D_{\mathrm{BLC}}}{d_{\mathrm{hole}}} \tag{5.44}$$

  It cannot be expected to reach a fully developed laminar flow profile inside the holes despite suitable pipe flow Reynolds numbers $Re_{\mathrm{hole}} \ll 2300$ due to the short development length.

$$Re_{\mathrm{hole}} = \frac{d_{\mathrm{hole}} v_{\mathrm{BLC}} \frac{A_{\mathrm{BLC}}}{A_{\mathrm{hole}}}}{\nu} \approx [0.1, 10] \ll 2300 \tag{5.45}$$

  Therefore, additional losses atop laminar pipe flow pressure loss can be expected from imperfect inflow, the rough surfaces of the laser-drilled holes (it is rather a laser shooting than a drilling process in which the material is ripped out by one strong laser pulse), and the short development length.

- **Upper Bound** The upper bound is given by the available pressure difference from the supply pressure to the static pressure within the BLC region. As pointed out in section 5.5.3 this is not a fixed quantity. Instead, the available pressure difference depends on the pressure level at the control surface $c_{p,\mathrm{BLC}}$. The source pressure is approximately given by the freestream

dynamic pressure q_∞ which gets converted to static pressure upon stagnation. Therefore, the upper bound of the dimensionless pressure difference is given by:

$$\zeta_{\text{avail}} = \frac{q_\infty - c_{p,\text{BLC}} q_\infty}{\rho/2 v_{\text{BLC}}^2} = \frac{U_\infty^2 (1 - c_{p,\text{BLC}})}{v_{\text{BLC}}^2} = \frac{1 - c_{p,\text{BLC}}}{c_q^2} \tag{5.46}$$

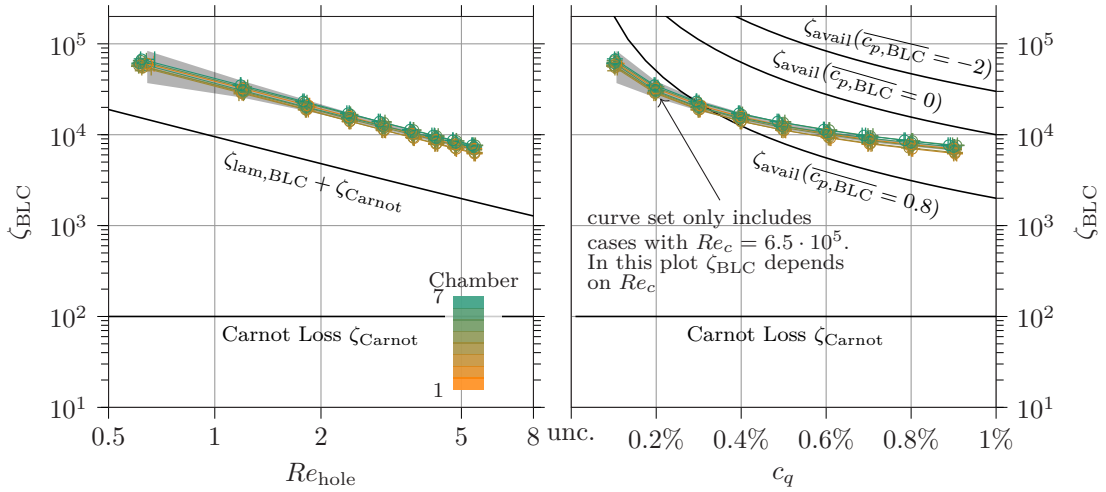

Figure 5.28: Dimensionless pressure loss plotted over the Reynolds number formed with the hole bulk velocity (left) and over the dimensionless blowing ratio (right). Based on data with $Re_c = 6.5 \cdot 10^5$, AoA $\alpha_{\text{geom}} = 4°$.

Figure 5.28 shows the results in two scalings: On the left side the scaling with the hole Reynolds number allows a case-insensitive plot: This means no matter what the airfoil Reynolds number Re_c, all measurements collapse to one dimensionless function $\zeta_{\text{BLC}}(Re_{\text{hole}})$ for each control chamber. Despite the large number of measurements and the seven individual control chambers, all measurements collapse to one function with a high repeatability. This plot is therefore suitable to judge the control surface properties. As expected, the flow resistance is higher than an ideal laminar pipe flow resistance, by roughly a factor of 4. Despite this significant penalty in comparison to laminar pipe flow, it is clear, that the regime can be characterized as a fully laminar flow given its resemblance to the linear character in the double logarithmic plot.

The variance of literature results for the flow resistance is high despite the small amount of available data. This is not surprising because the result scales exponentially with hole-Reynolds number, whereas it scales *e.g.* linearly with sheet thickness. To the author's knowledge there is one study with a comparable hole-Reynolds number by Kornilov & Boiko [58] with $Re_{\text{hole}} \approx 6$ and a reported pressure drop of $\Delta p = 94.5\text{Pa}$. This is similar to the present result which has an average pressure loss of about

$$\Delta p = \zeta_{\text{BLC}} \rho/2 v_{\text{BLC}} (Re_{\text{hole}} \approx 6)^2 \tag{5.47}$$

$$= \underbrace{\zeta_{\text{BLC}}}_{\approx 6000\text{ , fig. 5.28}} \rho/2 \underbrace{\left(\frac{Re_{\text{hole}}}{d_{\text{hole}}} \nu \frac{A_{\text{BLC}}}{A_{\text{hole}}} \right)^2}_{\approx v_{\text{BLC}} \approx 0.15 \frac{\text{m}}{\text{s}}} \approx 80\text{Pa} \tag{5.48}$$

despite the differences in hole diameter, sheet thickness, blowing intensity, open area ratio, etc.

The context of external flow is given in figure 5.28 on the right. The external flow provides the available pressure difference from the collection at freestream total pressure to control area static pressure $c_{p,\text{BLC}}$. This is the available pressure difference for uniform blowing provided by

freestream and it can be used to overcome remaining duct flow resistance and regulation losses, *e.g.* by valves as well as the pressure losses through the porous surface. As visible in figure 5.28 right, the pressure losses through the porous surface stay well below the available pressure difference if blowing is applied in a region with local control surface pressure equal to static pressure at infinity ($c_{p,\mathrm{BLC}} \approx 0$). This means passive convection without additional pump effort is possible similar to passive convection schemes demonstrated by Eto *et al.* [31]. Furthermore, in this case, **the inclusive drag is the only relevant drag quantity** to judge net drag reduction potential or control effort in general for uniform blowing provided by freestream airflow. Yet, it would be better to apply uniform blowing in higher static pressure because it was shown in the previous section (5.5.3) that control performance increases with static pressure within the control region ($c_{p,\mathrm{BLC}} \to 1$). The margin for additional pressure losses atop the viscous pressure losses of the flow through the surface shrinks for higher control region static pressure. For the given airfoil Reynolds number ($Re_c = 6.5 \cdot 10^5$) and the measured control surface properties (figure 5.28 left) the available margin becomes negative at $c_{p,\mathrm{BLC}} \approx 0.8$ depending on blowing intensity c_q and airfoil chord Reynolds number Re_c. In other words, the porous surface requires approximately 10-30% of the freestream dynamic pressure to operate in the investigated range of $c_q \in [0.1, 0.9]\%$ Obviously, the margin is always negative if uniform blowing is applied at $c_{p,\mathrm{BLC}} = 1$ for which case the available pressure difference is $\zeta_{\mathrm{avail}}(c_{p,\mathrm{BLC}} = 1) = 0$. Hence, the more favorable the drag reduction potential the smaller and eventually negative the margin to operate the control scheme passively. If the required pressure ζ_{BLC} surpasses the available pressure difference ζ_{avail} **the inclusive drag does not cover all efforts** of the control scheme operation because additional pumps are required to achieve the desired blowing velocity.

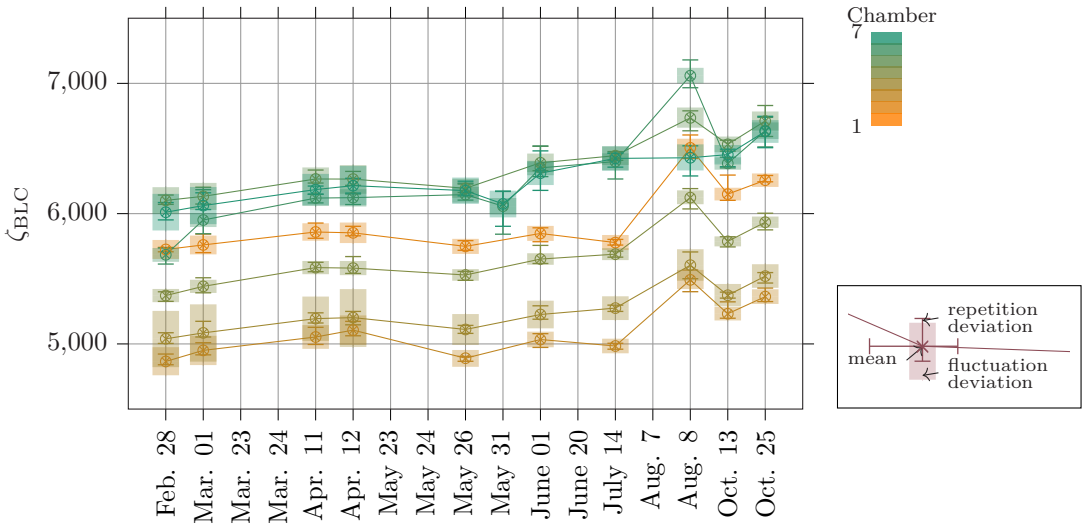

Figure 5.29: Development of flow resistance over measurement campaign for $Re_{\mathrm{hole}} \in [6, 7]$ which is equivalent to the most common investigated blowing rate $c_q = 0.5\%$ at $Re_c = 1.5\mathrm{Mio}$.

In the last step, the reliability of the control surface shall be examined. Figure 5.29 provides information about how the flow resistance differs between the chambers and how it develops over 8 months of the measurement campaign. The differences between the chambers are much larger than the repeatability error of single-chamber results. However, a significant drift to higher pressure loss can be observed. This can easily be explained by clogging due to dust and/or seeding particles and was also expected. It has to be noted though, that the results of figure 5.29 include hole Reynolds numbers between $Re_{\mathrm{hole}} \in [6, 7]$. As visible from figure 5.28 this allows for quite some systematic changes of ζ due to changing Re_{hole}.

The increase in pressure loss throughout a total operating time of about 24 hours with active BLC is in an order of magnitude of about 10% of the measured value. This is consistent for all control chambers. Meanwhile, the differences in individual control areas (control chambers) vary by up to 20% of the measured value and remain at this variance consistently.

5.5.5 Local Control Properties

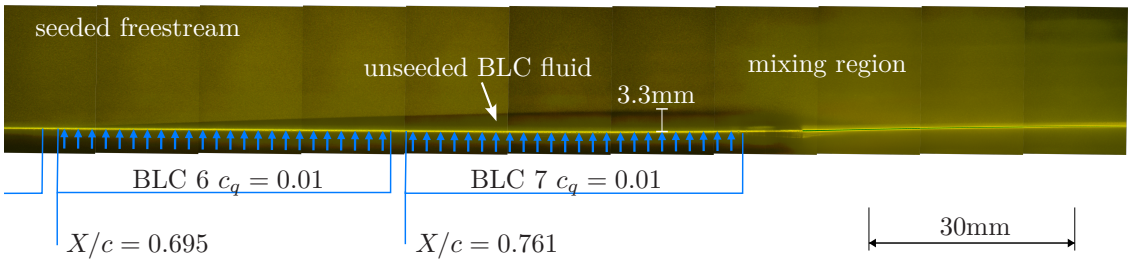

Figure 5.30: Quantitative Light Sheet (QLS) result (410 A-Frames in red, 410 B-Frames in green) with unseeded blowing. Logarithmic brightness scaling: plotted brightness is calculated $g_{\text{plot}} = 255 \cdot \ln(g_{\text{rec}}) / \ln(g_{\max})$ with recorded grey value g_{rec} and a maximum displayed grey value of $g_{\max} = 600$. AoA $\alpha_{\text{geom}} = 10°$, $\alpha_{\text{aero}} = 4.7°$, pressure gradient within the controlled region $\frac{\partial c_p}{\partial x} \approx -0.15 \frac{1}{\text{m}}$, $Re_c = 650000$, $c_q = 1\%$ (chamber 6 and 7 only), absolute wall-normal blowing velocity $v_{\text{BLC}} = 13.8 \frac{\text{cm}}{\text{s}}$, wind tunnel speed $U_\infty = 13.8 \frac{\text{m}}{\text{s}}$

First, the focus shall be put on the question of uniformity of the microblowing implementation. There are multiple strategies to answer this question, *e.g.* comparing turbulent statistics of high-fidelity simulations with experiments. Yet, such a strategy usually suffers from the difficulties of reproducing exact conditions as well as the limited measurement accuracy and resolution close to the wall for high Reynolds number turbulent boundary layers. Figure 5.30 shows a rather qualitative approach to judging the implementation used for the present studies. It shows a Quantitative Light Sheet (QLS) which is a time-average of grey values for all 11 FOV of the present study. A certain grey-value average can be associated with a certain tracer particle density. The freestream is seeded with tracer particles, yet the control fluid that comes out of the last two control chambers is unseeded. If the two flows were to mix quickly, the grey value within the external flow would be altered but without sharp phase separation to the control fluid. Yet, a clear phase separation of seeded and unseeded flow is observable which means that the two flows do not mix. Observing this separation in a time average of 11 completely different time intervals (the 11 FOV are recorded one after the other) is only possible though if the phase boundary is laminar and steady. Otherwise, the phase boundary would blur as it does downstream of the 7th chamber which is denoted as the mixing region in figure 5.30. This means, that the blowing does not cause the laminar sublayer to retransition for over 100mm development length and up to a thickness of over 3mm. It has to be noted, that the pressure gradient for the displayed case is favorable, which significantly stabilizes the boundary layer. Still, if the blowing was too non-uniform and introduced significant turbulence, such an effect would be unlikely to be observed due to the immediate bypass transition. Overall, figure 5.30 provides a qualitative result about the uniformity of the implemented microblowing of the present study: It is uniform enough to not immediately trigger the transition of the new lower part of the boundary layer that is generated from the blown fluid.

Figure 5.31 provides quantitative information about the scales of the measured quantities over all FOV. The total streamwise length of the investigated area is $l_{\text{PIV}} \approx 170\text{mm} \equiv \Delta X/c = 22.5\%$. This covers the last two control chambers in the streamwise direction: BLC 6 and BLC 7 as well as some distance downstream of the end of the control region. In the wall-normal direction, the flow field can be observed up to $y \approx 20\text{mm}$. Figure 5.31 shows the wall-normal velocity profiles at 4

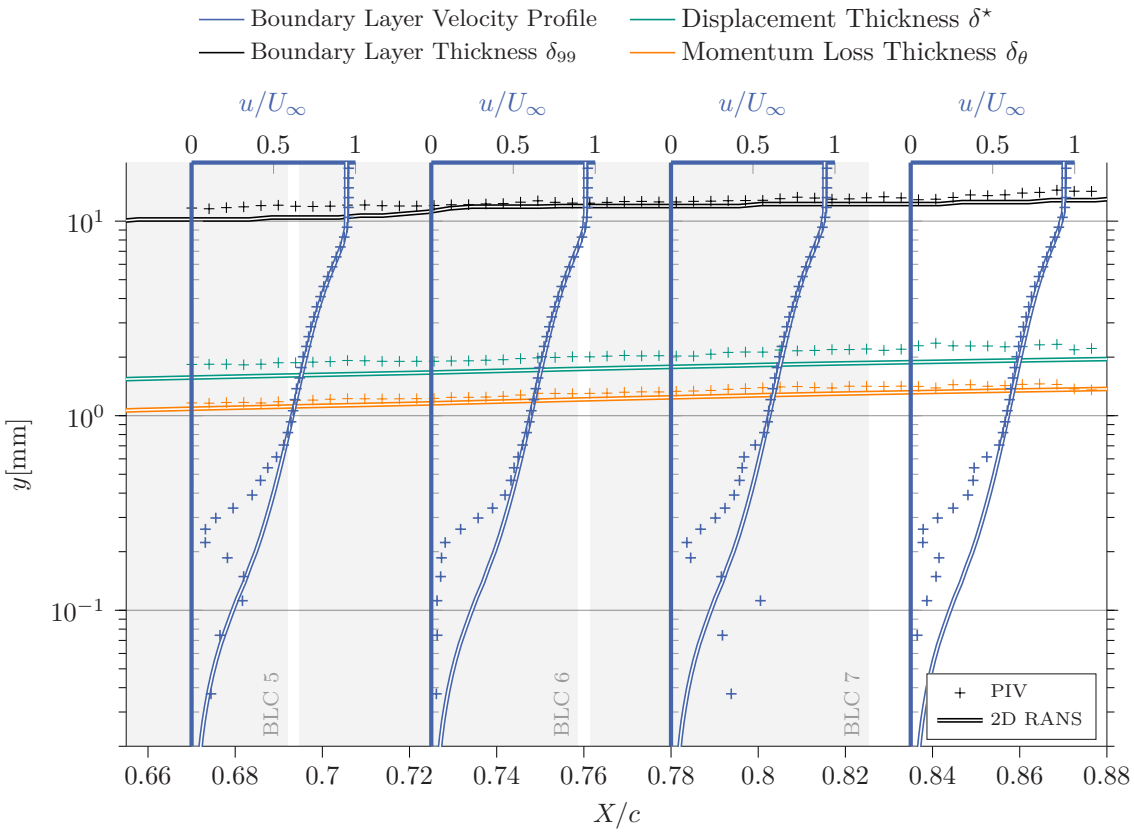

Figure 5.31: Boundary layer velocity profile and boundary layer layer thickness development of an uncontrolled boundary layer flow. AoA $\alpha_{\text{geom}} = 4°$, $\alpha_{\text{aero}} = 1.09°$, $Re_c = 1.5$Mio, wind tunnel speed $U_\infty = 31.8\frac{\text{m}}{\text{s}}$

positions and the boundary layer thicknesses δ_{99}, $\delta^\star$, and δ_θ for scale. It becomes clear that RANS simulations and PIV results agree fairly well for the boundary layer thickness δ_{99} which measures about $\delta_{99} \approx [10, 12]$mm for the investigated uncontrolled case of $Re_c = 1.5$Mio, $\alpha_{\text{geom}} = 4°$. It is also observable, that the displacement thickness and the momentum loss thickness are estimated slightly larger in PIV. The reason for this can also be observed in figure 5.31: The wall parallel velocity u matches RANS simulations accurately for $y \gtrapprox 0.6$mm above the wall. Below $y \approx 0.6$mm the velocity signal in PIV becomes more scattered and deviates from the RANS results. Although the RANS results may also be wrong, it is very clear, that the PIV results are less accurate still and tend to underestimate the true velocity. This underestimation of the wall-parallel velocity close to the wall directly leads to a larger displacement thickness and momentum loss thickness result.

Figure 5.32 provides the wall-normal velocity profiles at the same locations as figure 5.31 but in the typical orientation which allows separating the different regions of the turbulent boundary layer. Clearly, the wall distance at which the PIV results start to deviate from the RANS results is within the loglayer, substantially above the viscous sublayer. The opaque fields in figure 5.32 provide information on how many snapshots were used to form the time average of the wall-parallel velocity u. This shows, that the portion of snapshots used for the average n_{avg} relative to the total number of snapshots n_{tot} helps in judging the reliability of the measurements. Below the aforementioned $y \approx 0.6$mm most of the snapshots seem to lock into static pixels of the wall reflection. Therefore, their result is excluded and the number of snapshots available for averaging is reduced, which increases the uncertainty of the result. This increase in uncertainty stems from both the reduced sample count included for averaging as well as the increased uncertainty about the correctness of the remaining samples. After all, it is unclear from this procedure if a sample is truly

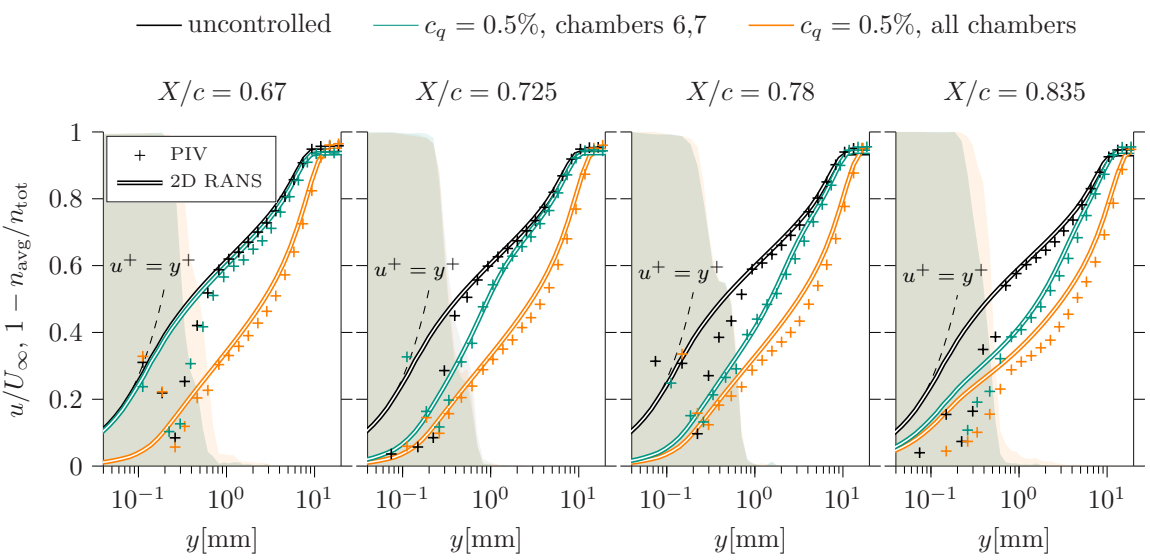

Figure 5.32: Time-averaged wall-parallel velocity u normalized by wind tunnel velocity U_∞ displayed by lines and markers. Opaque fields show the uncertainty indicator $1 - n_{\text{avg.}}/n_{\text{tot}}$ of the average as a function of wall distance as described in section 5.2.7. The colors of the opaque fields correspond to the case colors. The greyish areas are made up of overlapping opaque fields. AoA $\alpha_{\text{geom}} = 4°$, $\alpha_{\text{aero}} = 1.09°$, $Re_c = 1.5$Mio, absolute wall-normal blowing velocity $v_{\text{BLC}} = 15.9\frac{\text{cm}}{\text{s}}$, wind tunnel speed $U_\infty = 31.8\frac{\text{m}}{\text{s}}$

valid just because it passed the arbitrarily set threshold of $u/U_e = 3\%$. There is another reason that points towards wall reflections as the limiting factor of getting closer to the wall: The uncertainty measure as well as the obvious deviation of RANS and PIV results seem largely unaffected by the strength of the blowing and the corresponding reduction in particle concentration close to the wall. (Note, that the case of figures 5.32 and 5.31 is different from the case displayed in figure 5.30 such that no phase separation is present.) This means, that it is not a lack of particles that causes the reduction in measurement accuracy of the velocity close to the wall. Therefore, the opaque uncertainty fields in figure 5.32 provide a good cut-off where to mistrust the PIV measurement results.

Overall, a very good agreement of the boundary layer log-law region can be observed by comparing experiments and RANS simulations. This is true for uncontrolled cases at which it should be expected as this is a close-to-zero pressure gradient turbulent boundary layer for which RANS models are calibrated. However, it is also true for the controlled cases. The only consistent difference is, that the PIV velocity profiles show a bit more of a belly toward the aft end of the airfoil, especially in the case of blowing with all 7 control chambers. Other than that, the RANS simulations seem to capture the main features of the boundary layer velocity profiles well. This is also true for the case where blowing is active only in chambers 6 and 7. The green curve in figure 5.32 clearly shows the transition from an uncontrolled boundary layer velocity profile at $X/c = 67\%$ towards a developed boundary layer velocity profile at $X/c = 78\%$. Interestingly, RANS and PIV results also agree well for $X/c = 72.5\%$ which is directly after the start of the blowing. Downstream of the controlled region ($X/c = 83.5\%$) the controlled boundary layer velocity profiles have a similar shape to one another which again is captured well by RANS simulations. Overall, the RANS simulations of the present study seem to represent the outer regions of the turbulent boundary layer well. No statement can be made about the RANS simulation validity in the buffer region and the viscous sublayer, as the PIV results are not valid there. However, within the viscous sublayer, the methodical drawbacks of RANS simulations are not as dominant as the flow is steady and laminar which renders the modeling limitations unimportant. Therefore, it can be concluded

that the RANS simulations of the present setup give reasonable results of the turbulent boundary layer flow subject to uniform blowing or microblowing respectively.

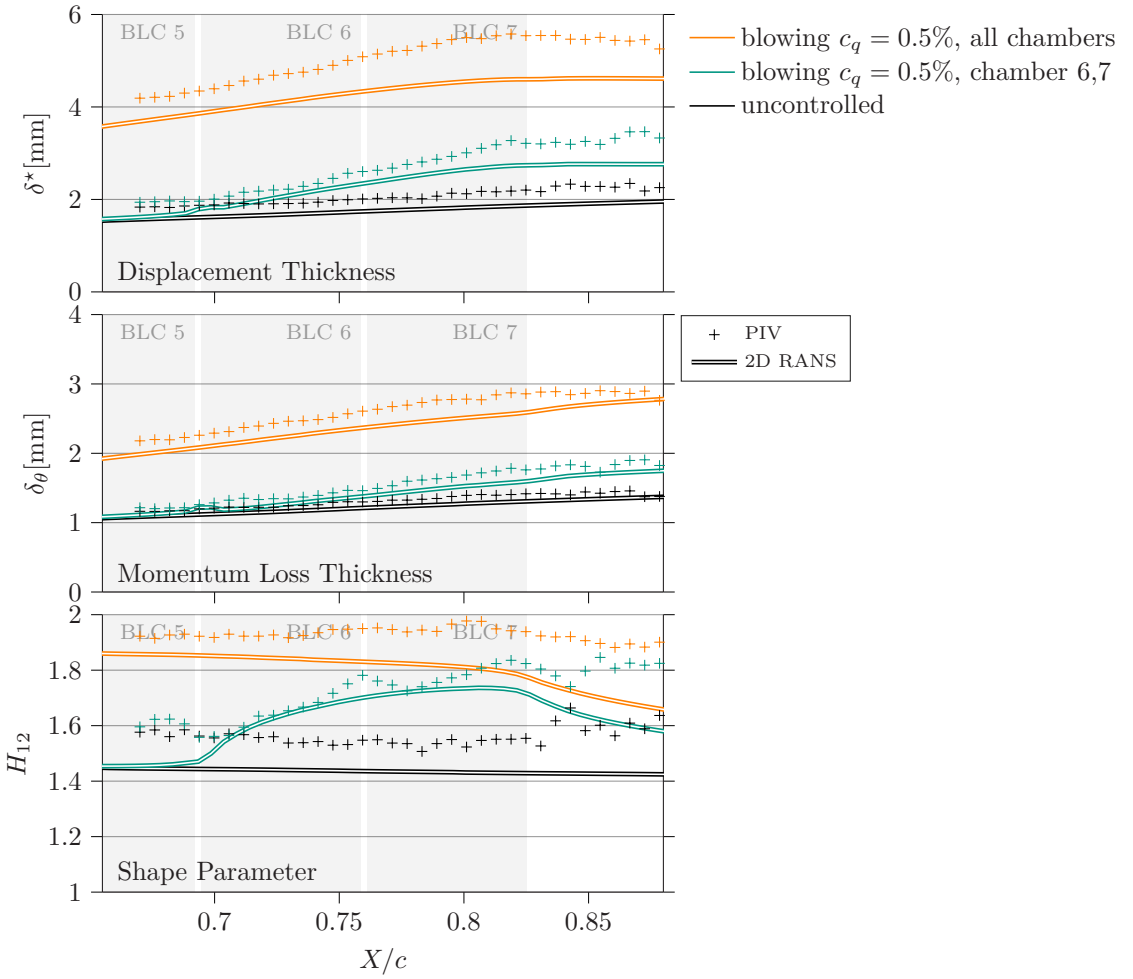

Figure 5.33: Development of boundary layer thicknesses and shape parameter H_{12}. AoA $\alpha_{\text{geom}} = 4°$, $\alpha_{\text{aero}} = 1.09°$, $Re_c = 1.5$Mio, absolute wall-normal blowing velocity $v_{\text{BLC}} = 15.9\frac{\text{cm}}{\text{s}}$, wind tunnel speed $U_\infty = 31.8\frac{\text{m}}{\text{s}}$

Figure 5.33 provides a comparison of the boundary layer thicknesses and the shape parameter of the same three cases displayed before: The uncontrolled cases show a monotonic increase in both displacement thickness and momentum loss thickness. The shape parameter equals $H_{12} = \delta^\star/\delta_\theta \approx 1.5$ which is close to the equilibrium value for a zero pressure gradient turbulent boundary layer of $H_{12} \approx 1.4$ [118, p. 420]. Naturally, the PIV result of the shape parameter is slightly above the RANS result due to the aforementioned overestimation of displacement thickness in PIV results. It has to be noted though, that the disagreement could also stem from true differences in the flow. However, the trends of the boundary layer thicknesses, especially the momentum loss thickness δ_θ agree very well comparing RANS and PIV. An active control hardly leaves any footprint upstream of its start position as the comparison of the black (uncontrolled) and green (controlled, chambers 6 & 7) shows. Within an active control region, the history of the boundary layer thickness is not noticeable in the slope. The thicknesses of controlled boundary layers are just offset to one another. It is also interesting to note, that the displacement thickness does not grow further downstream of the controlled region whereas the momentum loss thickness keeps increasing for the remaining FOV. This observation does not hold for the PIV measurements: The case with the longer control (orange, all chambers active) seems to stay at its level whereas the other control case mimics the

increasing slope of the RANS result. So far, the PIV results do not reveal new information apart from validating the RANS results for the loglayer of the turbulent boundary layer with blowing. A thicker boundary layer with a physically larger viscous sublayer would be needed to improve the wall-normal resolution close to the wall. The lower Reynolds number cases of the present thesis could deliver such conditions. However, they lack accuracy due to the (partial) phase separation of seeded freestream and unseeded boundary layer control stream. This effect was leveraged for figure 5.30 but other than that it obstructs accurate close-wall velocity results.

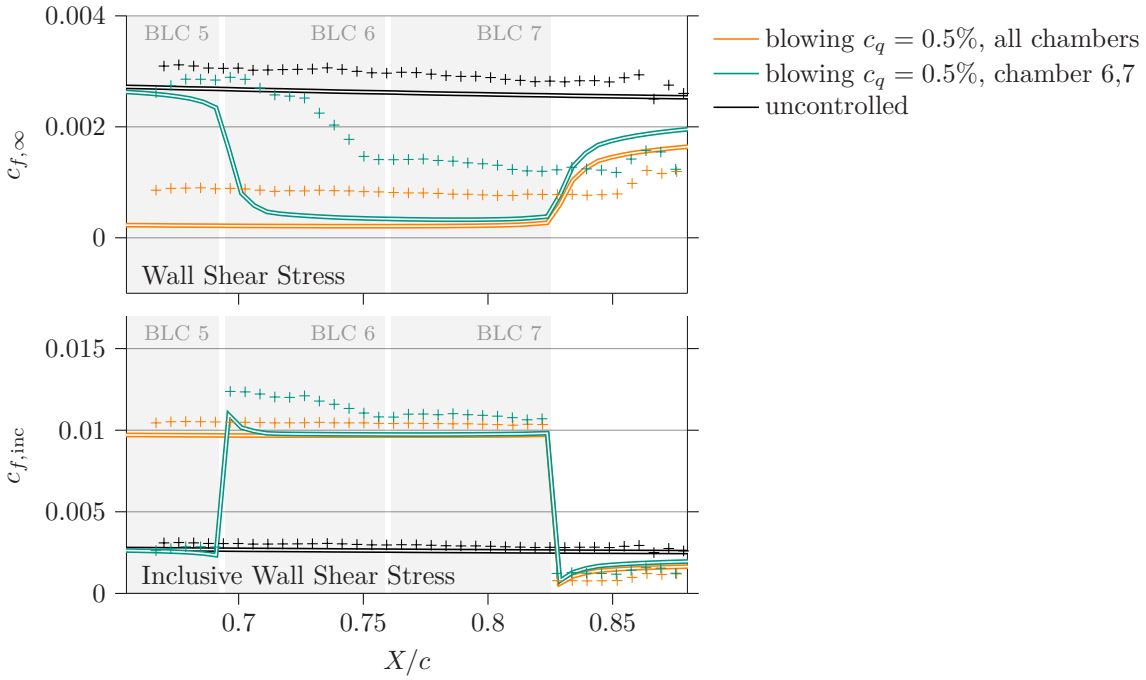

Figure 5.34: Dimensionless wall shear stress $c_{f,\infty}$ calculated from the Nickels fit function [85] and dimensionless inclusive wall shear stress $c_{f,\mathrm{inc}} = c_{f,\infty} + c_{f,\mathrm{BLC}}$ with $c_{f,\mathrm{BLC}}$ from equation 3.25. AoA $\alpha_{\mathrm{geom}} = 4°$, $\alpha_{\mathrm{aero}} = 1.09°$, $Re_c = 1.5$Mio, absolute wall-normal blowing velocity $v_{\mathrm{BLC}} = 15.9\frac{\mathrm{cm}}{\mathrm{s}}$, wind tunnel speed $U_\infty = 31.8\frac{\mathrm{m}}{\mathrm{s}}$

Figure 5.34 shows the friction coefficient c_f(dimensionless wall shear stress) over the same investigated area as the previous figures. It has to be noted that the wall shear stress cannot be estimated directly from the velocity gradient at the wall as it is defined in equation 2.36 due to the limited PIV resolution close to the wall (figures 5.31 & 5.32). Therefore, three different approaches were used to determine the wall shear stress indirectly:

1. A velocity defect law [25] is fitted onto the turbulent boundary layer velocity profile which scales with the wall shear stress. The fit function has no special treatment for the different boundary layer regions but is a polynomial calibrated for a zero pressure gradient boundary layer.

2. The fit function of Nickels [85] uses a composed modeling that consists of physically reasonable fit functions for the individual regions of a turbulent boundary layer. It also respects different equilibrium conditions such as mildly adverse and favorable pressure gradients. This method is superior to ① as it correctly resembles the viscous sublayer, buffer layer, log-layer, and the wake (outer part of the boundary layer) of a general turbulent boundary layer. The fit function is formulated in viscous units $(\cdot^+)$. This means, it directly includes the viscous velocity as a parameter from which the wall shear stress can be calculated.

3. The physically most accurate way to calculate the wall shear stress is the use of the von Karman equation (eq. 3.26). This is because no assumptions (fit function) about the shape of the boundary layer are used.

It turned out that only method ② proved to be viable. The use of a simple defect law approach ① is not suitable for the present boundary layer, not even in the uncontrolled case, due to a non-zero pressure gradient. The physically most appealing method is to use the von Karman equation (method ③). However, it relies on spatial derivatives of the boundary layer thicknesses δ_θ, $\delta^\star$. This proved to be challenging even in well-resolved LES simulations due to inaccuracies from interpolations and grid resolution [FAF+23]. In figure 5.33 mild noise in the boundary layer thickness data is visible. Consequently, the spatial derivatives oscillate strongly which means that the von Karman equation cannot be successfully employed to estimate the wall shear stress in the present measurements. Instead, the fit-formula by Nickels [85] is employed successfully in figure 5.34. Overall, the friction drag reduction by microblowing is visible and resembles the RANS result of truly uniform blowing. There is a clear sign that the experimental results do not show as strong of a friction drag reduction as the RANS results. However, this might be due to a systematic error that stems from the fact that the Nickels fit function is not calibrated for wall-normal blowing or any blowing as a matter of fact. Furthermore, the friction drag reduction in PIV data experiences a certain delay. In comparison to figure 5.32 this can also be explained by the nature of the fit: Clearly, it takes some development length for the outer part of the turbulent boundary layer to experience the influence of the blowing, eventually until a somewhat equilibrium of the boundary layer with blowing is reached. Only then does the PIV wall shear stress resume a horizontal slope again similar to the RANS data. Similar behavior is visible where the blowing region ends: The PIV wall shear stress sees some delay until it mimics the slope change of the RANS data.

Ultimately, RANS and PIV agree well in fact that the localized inclusive drag $c_{f,\mathrm{inc}}$ is increased significantly by uniform blowing despite the sizable reduction of the physical wall shear stress $c_{f,\infty}$. Similar to the integral considerations in the previous sections and the numerical section it can be stated that uniform blowing, or microblowing respectively, is successful in reducing the body drag (friction drag in localized formulation). The difference between uniform blowing and its physical resemblance — the microblowing technique — is small in comparison to the large penalty of the BLC penalty $c_{f,\mathrm{BLC}}$.

5.6 Conclusions of Experimental Results

The experimental investigations span a wide range of topics which all contribute to the main picture yet some of which are less important. Therefore, this section shall give a more detailed overview than the main conclusions (section 6) can do.

A moderate to sizable integral friction drag reduction could be achieved by uniform blowing at medium lift coefficients. It has to be noted that the integral friction drag (reduction) could not be measured directly but it was deduced from the pressure drag changes and the body drag changes measured with balance and wake rake. Friction drag reduction by blowing is also clearly observable for the local wall shear stress. The good agreement of RANS and experiments both in integral and local quantities means that the results of RANS simulations are validated from an experimental point of view. Moreover, the idealization of true uniformity of blowing in numerical simulations does not falsify general trends of integral body drag developments or the trends in the local boundary layer properties.

For integral quantities, the wake survey was the most accurate and repeatable measurement in terms of absolute drag values. Surprisingly, the best agreement of experimental and numerical drag reduction was achieved for the balance drag measurement despite the higher number of wind-tunnel corrections and sources of error during operation compared to the wake survey. Significant body drag reduction could be achieved by blowing on the pressure side of the airfoil at positive lift coefficients. This can be said up to the repeatability accuracy of the present experiments which ranges at about 10-30% of the drag change (depending on its magnitude). This results in a drag measurement repeatability accuracy of about 5% of the uncontrolled drag measurement value.

Similar to all numeric results, no integral inclusive drag reduction could be found. Even the systematic deviation of wake survey measurements and balance measurements cast no doubt: The present flow control at the present application location on the airfoil is far from achieving net drag reduction as a stand-alone boundary layer control scheme. The same can be said about the local inclusive wall shear stress with blowing which was always above that of the uncontrolled case.

A different picture arises in terms of possible combinations with other flow control schemes. The pressure drop measurements clearly showed, that only a small portion of the freestream dynamic pressure (roughly 10% to 30%, depending on exact configuration) is needed to force the fluid through the porous surface. This has several consequences:

1. The inclusive drag is the only relevant quantity to assess net drag reduction for stand-alone uniform blowing flow control schemes. It covers all efforts to operate the scheme up to excessive blowing rates $c_q > 1\%$ which could not be reached during the present study. Therefore, no additional pump effort is required for a wide range of conditions (much larger than the ones investigated in the present work).

2. For combined flow control, the inclusive drag of the blowing part can be taken as a baseline of what to exceed to improve on net drag reduction.

3. The present study provides the information that the pressure losses follow a linear pattern in a double-logarithmic plot over the hole Reynolds number, similar to laminar pipe flow. The resulting pressure loss compares well to the literature for identical hole-Reynolds number. Therefore, the present dimensionless values for pressure drop can serve as a baseline when estimating the required pump effort for combined suction/blowing flow control even if the implementation (surface thickness, hole diameter, Reynolds number, etc.) deviates from the current results.

It could also be demonstrated experimentally, that the control performance increases with increased static pressure at the control location. Moreover, this effect is consistent enough to consider an extrapolation to even higher static pressures at the control location. This opens the question for future studies if this correlation prevails when the static pressure at the control location reaches freestream stagnation pressure. Uniform blowing with the present parameters (blowing intensity, Reynolds number, incompressible flow, porous open area) can be operated at static pressures as high as $c_{p,\mathrm{BLC}} \lessapprox 0.8$ without additional pump effort thanks to the high margin of available control supply pressure.

6 Conclusions and Outlook

In this Dissertation, the turbulent boundary layer flow control scheme of uniform blowing or microblowing was investigated. The goal of such boundary layer control is to decrease the turbulent friction drag and therefore increase the efficiency of *e.g.* aircraft. Former studies have shown a significant viscous drag reduction capability of this active control scheme. These studies used numerical and experimental means to find sizeable friction drag reduction. Most studies so far focused on canonical flows like flat plate boundary layers and only few studies looked at more complex configurations to also investigate the effect of the control on other drag components such as the pressure drag. This and correct estimates of the operating effort of the control affect the overall performance of an active flow control scheme, hence its potential to achieve a total drag reduction, sometimes called net drag reduction.

The present study focused on closing the gap from the well-known friction drag reduction to the total drag reduction potential of uniform blowing. The results were obtained in three steps: An analytical study assessed the momentum and energy budget of a controlled flow. By this, the general quantity of inclusive drag was introduced to judge total drag reduction in a unified manner both valid in complex and canonical configurations. The inclusive drag is represented by the momentum deficit deduced from a wake survey behind the body (or at the end of an investigated boundary layer flow) for the control scheme of uniform blowing. It is important to note at this point, that for other control schemes, such as uniform suction, the wake survey does not resemble the inclusive drag as the wake survey momentum deficit does not include the theoretical effort to operate the control. Total energy budgets as shown by Drela [28] or Arnzt *et al.* [6] provide a general starting point for estimating the inclusive drag of a control scheme. Numerical Reynolds-Averaged Navier-Stokes simulations were used to investigate conditions in which uniform blowing in turbulent boundary layers would lead to the strongest drag reduction for airfoil flows. This also served as the basis for designing an airfoil-with-blowing experiment in which strong drag-reducing effects could be expected and measured accurately. These experimental investigations were carried out and lift and drag were measured utilizing balance, pressure, and wake flow measurements. Additionally, optical experiments were carried out to study the local velocity fields of the controlled turbulent boundary layer flows.

Both numerical as well as experimental results agree on the fact, that body drag reduction — consisting of friction and pressure drag reduction — is possible. The integral friction drag reduction is limited by the ratio of controlled area vs. uncontrolled airfoil surface. Thereby, integral friction drag reduction is difficult to detect in experiments yet it could be concluded from the clear difference in total body drag and pressure drag reduction. This is well in line with the measurement of the local wall shear stress reduction by microblowing which could be estimated from the boundary layer velocity profiles of controlled and uncontrolled flows. However, every numerical and experimental result showed a clear inclusive drag increase. This conclusion holds for both the numerical and experimental results of the present thesis without exception.

The analytical studies sparked the hypothesis, that drag reduction could be directly dependent on the static pressure level at the location of where the control is applied. In that sense static pressure level means the ratio of the local static pressure to stagnation pressure ($c_p = 1$) and static pressure

at infinity ($c_p = 0$). Indeed, both numerical and experimental results show a consistent correlation of drag reduction (or less drag increase) for cases in which the static pressure level was higher compared to those where it was lower with any other independent parameter kept constant. This is counter-intuitive at first because higher local static pressure means less velocity, less boundary layer shear, less friction stress, and hence less friction drag reduction potential. However, it was shown analytically that the total flow field losses are lower for higher static pressure at the location where the control fluid enters the flow domain.

An open area of $A_{\mathrm{hole}}/A_{\mathrm{BLC}} = 10\%$ is suitable for uniform blowing regarding the required pressure to force the control fluid through the control surface. Meanwhile, the uniformity of the blowing for this surface is good enough to still show local wall shear stress reduction close to the numerical results of truly uniform blowing. The present surface requires a supply pressure of roughly 10-30% of the freestream dynamic pressure to operate at a surface-average blowing rate of $c_q \in [0.1, 0.5]\%$. This means it can be operated passively without additional pump effort by stagnating fluid from the freestream. In consequence, the quantity of inclusive drag indeed includes every effort to operate the control scheme for reasonable control intensity by a good margin.

Based on the inclusive drag increase, it seems unlikely that a total net drag reduction by uniform blowing in turbulent boundary layers is possible as long as it is used as a stand-alone BLC scheme and the control fluid has to be drawn from the freestream around the body. Other authors have concluded that a net/total drag reduction — by their respective definitions — may be possible [70, 46, 88]. However, the present numerical study confirms the reoccurring experimental finding of increased wake survey drag which was shown to represent the inclusive drag in the present study. The discrepancy between the conclusion of the present and former studies in terms of net drag reduction potential is therefore rather a question of interpretation. Yet, this conclusion does not mean that a net drag reduction — in terms of a reduction of inclusive drag — by uniform blowing is impossible. It may be possible to find *e.g.* a staggered blowing scheme in which the wake size behind a body is decreased due to blowing. The present study also answered how to investigate such schemes with the objective of inclusive drag reduction. The von Karman equation provides a localized formulation of the inclusive drag therefore enabling fundamental flow research on inclusive drag reduction. Furthermore, the present study showed that placing the control in regions of higher static pressure (relative to stagnation pressure and static pressure at infinity) supposedly always increases control performance both in terms of body drag and inclusive drag. This means, that a scheme that is just short of inclusive drag reduction — net drag reduction — may likely be successful when placed at regions on a body, where the static pressure is higher.

It remains to be proven that a performance extrapolation towards stagnation pressure is accurate and under which circumstances and how it fails to predict BLC performance development accurately. The answer to such a question strongly impacts how to look for total drag / net drag / inclusive drag reduction and if such is feasible at all.

A different approach lies in investigating the combination of uniform blowing with other boundary layer control schemes, such as laminar flow control. The present study showed, that the pressure loss of the flow through a 10% open area laser-drilled surface is well below freestream dynamic pressure even for blowing ratios of one percent of the freestream velocity. This means that the combination of laminar flow control suction and uniform blowing in a turbulent boundary layer can significantly reduce pump effort for laminar flow control while simultaneously operating turbulent boundary layer uniform blowing. In that case, the high control penalty of collecting the blowing fluid is already covered by the laminar flow control. An example of such a combination was investigated briefly by Fahland [Fah21].

Yet another completely different approach is investigating the effectiveness of uniform blowing as a flow control scheme to control other effects than net drag reduction. The present study also showed effects on the lift and pitching moment of airfoils when operating uniform blowing. Bonfert extended such studies to demonstrate how to augment control of an aerobatic glider based on flow separation triggered by uniform blowing [Bon21].

7 References

Bibliography

[1] H. Altenbach. *Kontinuumsmechanik*. Springer Berlin Heidelberg, Berlin, Heidelberg, 2012. ISBN 978-3-642-24118-5 978-3-642-24119-2. DOI 10.1007/978-3-642-24119-2.

[2] D. Althaus. *Niedriggeschwindigkeitsprofile: Profilentwicklungen und Polarenmessungen im Laminarwindkanal des Instituts für Aerodynamik und Gasdynamik der Universität Stuttgart*. Vieweg, Braunschweig, 1996. ISBN 978-3-528-03820-5.

[3] D. Althaus and F. X. Wortmann. *Stuttgarter Profilkatalog*. F. Vieweg, Braunschweig, 1981. ISBN 978-3-528-08464-6.

[4] M. Amitay, D. R. Smith, V. Kibens, D. E. Parekh, and A. Glezer. Aerodynamic Flow Control over an Unconventional Airfoil Using Synthetic Jet Actuators. *AIAA Journal*, 39(3):361–370, 2001. ISSN 0001-1452, 1533-385X. DOI 10.2514/2.1323.

[5] B. Arnold and R. Groeneveld. Measuring Skewness with Respect to the Mode. *The American Statistician*, 49(1):34–38, Feb. 1995. ISSN 0003-1305, 1537-2731. DOI 10.1080/00031305.1995.10476109.

[6] A. Arntz, O. Atinault, and A. Merlen. Exergy-Based Formulation for Aircraft Aeropropulsive Performance Assessment: Theoretical Development. *AIAA Journal*, 53(6):1627–1639, June 2015. ISSN 0001-1452, 1533-385X. DOI 10.2514/1.J053467.

[7] M. Atzori. *Coherent structures and control in wall-bounded turbulent flows*. PhD Thesis, KTH Royal Institute of Technology, Stockholm, 2021. ISBN 978-91-7873-917-2.

[8] N. Beck, T. Landa, A. Seitz, L. Boermans, Y. Liu, and R. Radespiel. Drag Reduction by Laminar Flow Control. *Energies*, 11(1):252, 2018. ISSN 1996-1073. DOI 10.3390/en11010252.

[9] A. Betz. Ein Verfahren zur direkten Ermittlung des Profilwiderstandes. *Zeitschrift für Flugtechnik und Motorluftschiffahrt*, 16:42–44, 1925.

[10] D. Biermann and W. H. J. Hernnstein. The Interference Between Struts in Various Combinations. Technical Report NACA-TR-468, NACA, Washington, D.C., 1933. URL https://ntrs.nasa.gov/citations/19930091542.

[11] T. Black, A. Sarnecki, and W. Mair. The turbulent boundary layer with suction or injection. Reports and Memoranda 3387, Aeronautical Research Council, Cambridge, United Kingdom, 1958. URL https://reports.aerade.cranfield.ac.uk/handle/1826.2/3969.

[12] R. Blumrich, N. Widdecke, J. Wiedemann, A. Michelbach, F. Wittmeier, and O. Beland. New FKFS Technology at the Full-Scale Aeroacoustic Wind Tunnel of University of Stuttgart. *SAE International Journal of Passenger Cars - Mechanical Systems*, 8(1):294–305, 2015. ISSN 1946-4002. DOI 10.4271/2015-01-1557.

[13] P. Bradshaw and R. Pankhurst. The design of low-speed wind tunnels. *Progress in Aerospace Sciences*, 5:1–69, 1964. ISSN 03760421. DOI 10.1016/0376-0421(64)90003-X.

[14] M. B. Bragg and G. M. Gregorek. Experimental study of airfoil performance with vortex generators. *Journal of Aircraft*, 24(5):305–309, 1987. ISSN 0021-8669, 1533-3868. DOI 10.2514/3.45445.

[15] G. O. Brown. The History of the Darcy-Weisbach Equation for Pipe Flow Resistance. In *Environmental and Water Resources History*, pages 34–43, Washington, D.C., United States, Oct. 2002. American Society of Civil Engineers. ISBN 978-0-7844-0650-2. DOI 10.1061/40650(2003)4.

[16] G. W. Brune. Quantitative low-speed wake surveys. *Journal of Aircraft*, 31(2):249–255, 1994. ISSN 0021-8669, 1533-3868. DOI 10.2514/3.46481.

[17] A. L. Buck. New Equations for Computing Vapor Pressure and Enhancement Factor. *Journal of Applied Meteorology*, 20(12):1527–1532, 1981. ISSN 0021-8952. DOI 10.1175/1520-0450(1981)020<1527:NEFCVP>2.0.CO;2.

[18] R. Buckisch, B. Schwartekopp, and J. Pfisterer. Daimler Aeroacoustic Wind Tunnel: 5 Years of Operational Experience and Recent Improvements. In *Automotive Technical Papers*, pages 2018–01–5038, Sept. 2018. DOI 10.4271/2018-01-5038.

[19] D. E. Burns, Q. L. Williams, B. D. Phillips, S. A. Commo, and J. D. Ponder. Review Of Potential Wind Tunnel Balance Technologies. Conference Contribution NF1676L-23559, NASA, 2016. URL https://ntrs.nasa.gov/citations/20160009123. Presentation: International Symposium on Strain-Gage Balances, China.

[20] D. M. Bushnell. Aircraft drag reduction: a review. *Proceedings of the Institution of Mechanical Engineers, Part G: Journal of Aerospace Engineering*, 217(1):1–18, 2003. ISSN 0954-4100, 2041-3025. DOI 10.1243/095441003763031789.

[21] F. Chedevergne and Y. Marchenay. Transpired turbulent boundary layers: a general strategy for RANS turbulence models. *Journal of Turbulence*, 20(11-12):681–696, 2019. ISSN 1468-5248. DOI 10.1080/14685248.2019.1702198.

[22] X. Cheng, Z. Qiao, X. Zhang, M. Quadrio, and Y. Zhou. Skin-friction reduction using periodic blowing through streamwise slits. *Journal of Fluid Mechanics*, 920:A50, 2021. ISSN 0022-1120, 1469-7645. DOI 10.1017/jfm.2021.439.

[23] H. W. Coleman and W. G. Steele. *Experimentation, validation, and uncertainty analysis for engineers*. Wiley, Hoboken, NJ, USA, 4th edition, 2018. ISBN 978-1-119-41766-8.

[24] H. Dershin, C. A. Leonard, and W. H. Gallaher. Direct measurement of skin friction on a porous flat plate with massinjection. *AIAA Journal*, 5(11):1934–1939, 1967. ISSN 0001-1452, 1533-385X. DOI 10.2514/3.4343.

[25] L. Djenidi, K. M. Talluru, and R. A. Antonia. A velocity defect chart method for estimating the friction velocity in turbulent boundary layers. *Fluid Dynamics Research*, 51(4):045502, June 2019. ISSN 1873-7005. DOI 10.1088/1873-7005/ab225c.

[26] M. Drela. XFOIL: An Analysis and Design System for Low Reynolds Number Airfoils. In C. A. Brebbia, S. A. Orszag, J. H. Seinfeld, P. Spanos, A. S. Cakmak, P. Silvester, C. S. Desai, G. Pinder, R. McCrory, S. Yip, F. A. Leckie, A. R. S. Ponter, K.-P. Holz, K.-J. Bathe, J. Connor, W. Wunderlich, J. Argyris, and T. J. Mueller, editors, *Low Reynolds*

Number Aerodynamics, volume 54, pages 1–12. Springer, Berlin, Heidelberg, 1989. ISBN 978-3-540-51884-6 978-3-642-84010-4. DOI 10.1007/978-3-642-84010-4_1.

[27] M. Drela. Design and optimization method for multi-element airfoils. In *Aerospace Design Conference*, Irvine, CA, USA, 1993. American Institute of Aeronautics and Astronautics. DOI 10.2514/6.1993-969.

[28] M. Drela. Power Balance in Aerodynamic Flows. *AIAA Journal*, 47(7):1761–1771, July 2009. ISSN 0001-1452, 1533-385X. DOI 10.2514/1.42409.

[29] R. Eppler. *Airfoil Design and Data*. Springer Berlin, Heidelberg, 1st edition, 1990. ISBN 978-3-662-02646-5. DOI 10.1007/978-3-662-02646-5.

[30] K. Eto, Y. Kondo, K. Fukagata, and N. Tokugawa. Friction Drag Reduction on a Clark-Y Airfoil Using Uniform Blowing. In *2018 Flow Control Conference*, Atlanta, Georgia, 2018. American Institute of Aeronautics and Astronautics. ISBN 978-1-62410-554-8. DOI 10.2514/6.2018-3374.

[31] K. Eto, Y. Kondo, K. Fukagata, and N. Tokugawa. Assessment of Friction Drag Reduction on a Clark-Y Airfoil by Uniform Blowing. *AIAA Journal*, 57(7):2774–2782, 2019. ISSN 0001-1452, 1533-385X. DOI 10.2514/1.J057998.

[32] B. F. R. Ewald, editor. *Wind tunnel wall correction - La correction des effets de paroi en soufflerie*. Number 336 in AGARDOGRAPH. AGARD, Neuilly sur Seine, 1998. ISBN 978-92-836-1076-2. DOI.

[33] M. A. Feero, S. D. Goodfellow, P. Lavoie, and P. E. Sullivan. Flow Reattachment Using Synthetic Jet Actuation on a Low-Reynolds-Number Airfoil. *AIAA Journal*, 53(7):2005–2014, 2015. ISSN 0001-1452, 1533-385X. DOI 10.2514/1.J053605.

[34] M. A. Feero, P. Lavoie, and P. E. Sullivan. Influence of synthetic jet location on active control of an airfoil at low Reynolds number. *Experiments in Fluids*, 58(8):99, 2017. ISSN 0723-4864, 1432-1114. DOI 10.1007/s00348-017-2387-x.

[35] M. Ferro. *Experimental study on turbulent boundary-layer flows with wall transpiration*. PhD thesis, KTH Royal Institute of Technology, Stockholm, 2017. ISBN 9789177295563 ISSN 0348-467X.

[36] J. H. Ferziger and M. Peri. Compressible Flow. In *Computational Methods for Fluid Dynamics*, pages 309–328. Springer Berlin Heidelberg, Berlin, Heidelberg, 2002. ISBN 978-3-540-42074-3 978-3-642-56026-2. DOI 10.1007/978-3-642-56026-2_10.

[37] G. A. Flandro, H. M. McMahon, and R. L. Roach. *Basic Aerodynamics: Incompressible Flow*. Cambridge University Press, 1 edition, 2011. ISBN 978-0-521-80582-7.

[38] M. Gad-el Hak. *Flow Control: Passive, Active, and Reactive Flow Management*. Cambridge University Press, 1 edition, 2000. ISBN 978-0-511-52953-5. DOI 10.1017/CBO9780511529535.

[39] H. C. Garner, E. W. E. Rogers, W. E. A. Acum, and E. C. Maskell. *Subsonic Wind Tunnel Wall Corrections*. Number 109 in AGARDOGRAPH. AGARD, Neuilly sur Seine, France, 1966.

[40] K. Gersten and J. Wiedemann. *Widerstandsverminderung umströmter Körper durch kombiniertes Ausblasen und Absaugen an der Wand*. VS Verlag für Sozialwissenschaften, Wiesbaden, 1982. ISBN 978-3-531-03103-3 978-3-322-87701-7. DOI 10.1007/978-3-322-87701-7.

[41] F. R. Goldschmied. Skin friction of incompressible turbulent boundary layer under adverse pressure gradients. Technical Note NACA-TN-2431, NACA, Cleveland, Ohio, 1951. URL https://ntrs.nasa.gov/citations/19930083044.

[42] B. Gregory, W. Walker, and A. Devereux. Wind-Tunnel Tests on the 30 per cent Symmetrical Griffith Aerofoil with Distributed Suction over the Nose. Reports and Memoranda 2647, Ministry of Supply, Aeronatical Research Council, London, United Kingdom, 1953. URL https://reports.aerade.cranfield.ac.uk/handle/1826.2/3187.

[43] G. Hasanuzzaman, S. Merbold, C. Cuvier, V. Motuz, J.-M. Foucaut, and C. Egbers. Experimental investigation of turbulent boundary layers at high Reynolds number with uniform blowing, part I: statistics. *Journal of Turbulence*, 21(3):129–165, 2020. ISSN 1468-5248. DOI 10.1080/14685248.2020.1740239.

[44] A. Hellsten. Some improvements in Menter's k-omega SST turbulence model. In *29th AIAA, Fluid Dynamics Conference*, Albuquerque, NM, USA, 1998. American Institute of Aeronautics and Astronautics. DOI 10.2514/6.1998-2554.

[45] R. Hink. Validation of the komega turbulence model for the thermal boundary layer profile of effusive cooled walls. *CEAS Space Journal*, 7(3):389–398, 2015. ISSN 1868-2502, 1868-2510. DOI 10.1007/s12567-015-0089-x.

[46] S. Hirokawa, M. Ohashi, K. Eto, K. Fukagata, and N. Tokugawa. Turbulent Friction Drag Reduction on Clark-Y Airfoil by Passive Uniform Blowing. *AIAA Journal*, pages 1–3, 2020. ISSN 0001-1452, 1533-385X. DOI 10.2514/1.J059627.

[47] D. Hwang. Review of research into the concept of the microblowing technique for turbulent skin friction reduction. *Progress in Aerospace Sciences*, 40(8):559–575, 2004. ISSN 03760421. DOI 10.1016/j.paerosci.2005.01.002.

[48] A. S. Iberall. Attenuation of Oscillatory Pressures in Instrument Lines. *Journal of Research*, 45:85–108, 1950. DOI 10.21236/ADA800533. Report Number RP2115, National Bureau of Standards, Washington D.C., USA.

[49] E. N. Jackobs, K. E. Ward, and R. M. Pinkerton. The characteristics of 78 related airfoil sections from tests in the variable-density wind tunnel. Technical Report 460, NACA, Washington D.C., USA, 1935. URL https://ntrs.nasa.gov/citations/19930091108.

[50] B. M. Jones. The measurement of profile drag by the pitot traverse method. Technical Report 1688, Air Ministry, Aeronautical Research Committee, Cambridge, Great Britain, 1937.

[51] Y. Kametani and K. Fukagata. Direct numerical simulation of spatially developing turbulent boundary layers with uniform blowing or suction. *Journal of Fluid Mechanics*, 681:154–172, 2011. ISSN 0022-1120, 1469-7645. DOI 10.1017/jfm.2011.219.

[52] Y. Kametani, K. Fukagata, R. Örlü, and P. Schlatter. Effect of uniform blowing/suction in a turbulent boundary layer at moderate Reynolds number. *International Journal of Heat and Fluid Flow*, 55:132–142, 2015. ISSN 0142727X. DOI 10.1016/j.ijheatfluidflow.2015.05.019.

[53] Y. Kametani, K. Fukagata, R. Örlü, and P. Schlatter. Drag reduction in spatially developing turbulent boundary layers by spatially intermittent blowing at constant mass-flux. *Journal of Turbulence*, 17(10):913–929, 2016. ISSN 1468-5248. DOI 10.1080/14685248.2016.1192285.

[54] S. H. Kim and C. Kim. Separation control on NACA23012 using synthetic jet. *Aerospace Science and Technology*, 13(4-5):172–182, 2009. ISSN 12709638. DOI 10.1016/j.ast.2008.11.001.

[55] R. B. Kinney. Skin-friction drag of a constant-property turbulent boundary layer with uniform injection. *AIAA Journal*, 5(4):624–630, 1967. ISSN 0001-1452, 1533-385X. DOI 10.2514/3.4039.

[56] V. Kornilov. Current state and prospects of researches on the control of turbulent boundary layer by air blowing. *Progress in Aerospace Sciences*, 76:1–23, 2015. ISSN 03760421. DOI 10.1016/j.paerosci.2015.05.001.

[57] V. Kornilov. Combined Blowing/Suction Flow Control on Low-Speed Airfoils. *Flow, Turbulence and Combustion*, 106(1):81–108, 2020. ISSN 1386-6184, 1573-1987. DOI 10.1007/s10494-020-00157-7.

[58] V. I. Kornilov and A. V. Boiko. Efficiency of Air Microblowing Through Microperforated Wall for Flat Plate Drag Reduction. *AIAA Journal*, 50(3):724–732, 2012. ISSN 0001-1452, 1533-385X. DOI 10.2514/1.J051426.

[59] V. I. Kornilov, I. N. Kavun, and A. N. Popkov. Modification of turbulent airfoil section flow using a combined control action. *Thermophysics and Aeromechanics*, 26(2):14, 2019. DOI 10.1134/S0869864319020021.

[60] K. Krishnan, O. Bertram, and O. Seibel. Review of hybrid laminar flow control systems. *Progress in Aerospace Sciences*, 93:24–52, 2017. ISSN 03760421. DOI 10.1016/j.paerosci.2017.05.005.

[61] F. Kronthaler. *Statistik angewandt mit dem R Commander: Datenanalyse ist (k)eine Kunst*. Springer Berlin Heidelberg, Berlin, Heidelberg, Germany, 2021. ISBN 978-3-662-63603-9 978-3-662-63604-6. DOI 10.1007/978-3-662-63604-6.

[62] K. K. Kuo and R. Acharya. *Applications of Turbulent and Multiphase Combustion*. Wiley, 1 edition, Apr. 2012. ISBN 978-1-118-12756-8 978-1-118-12757-5. DOI 10.1002/9781118127575.

[63] C. J. Kähler and J. Kompenhans. Near Wall Turbulent Boundary Layer. In *Particle Image Velocimetry*. Springer International Publishing, Cham, 3rd edition, 2018. ISBN 978-3-319-68851-0 978-3-319-68852-7. DOI 10.1007/978-3-319-68852-7.

[64] B. Lambert. *Bestimmung des instationären Druckfeldes einer freifahrenden Luftschraube*. PhD Thesis, TU Karlsruhe, Karlsruhe, Germany, 1967.

[65] J. J. Lee, S. P. Lukachko, I. A. Waitz, and A. Schafer. Historical and Future Trends in Aircraft Performance, Cost, and Emissions. *Annual Review of Energy and the Environment*, 26(1):167–200, 2001. ISSN 1056-3466. DOI 10.1146/annurev.energy.26.1.167.

[66] Y.-L. Lin, M. Chyu, T. Shih, B. Willis, and D. Hwang. Skin-friction reduction through micro blowing. In *36th AIAA Aerospace Sciences Meeting and Exhibit*, Reno, NV, USA, Jan. 1998. American Institute of Aeronautics and Astronautics. DOI 10.2514/6.1998-359.

[67] B. Lu and M. Bragg. Experimental investigation of airfoil drag measurement with simulated leading-edge ice using the wake survey method. In *18th Applied Aerodynamics Conference*, Denver, CO, USA, 2000. American Institute of Aeronautics and Astronautics. DOI 10.2514/6.2000-3919.

[68] B. Lu and M. Bragg. Experimental Investigation of the Wake-Survey Method for a Bluff Body with a Highly Turbulent Wake. In *20th AIAA Applied Aerodynamics Conference*, St. Louis, Missouri, USA, 2002. American Institute of Aeronautics and Astronautics. ISBN 978-1-62410-110-6. DOI 10.2514/6.2002-3060.

[69] C. Lyon, M. Selig, A. Broeren, C. Lyon, M. Selig, and A. Broeren. Boundary layer trips on airfoils at low Reynolds numbers. In *35th Aerospace Sciences Meeting and Exhibit*, Reno, NV, USA, 1997. American Institute of Aeronautics and Astronautics. DOI 10.2514/6.1997-511.

[70] O. A. Mahfoze, A. Moody, A. Wynn, R. D. Whalley, and S. Laizet. Reducing the skin-friction drag of a turbulent boundary-layer flow with low-amplitude wall-normal blowing within a Bayesian optimization framework. *Physical Review Fluids*, 4(9):094601, 2019. ISSN 2469-990X. DOI 10.1103/PhysRevFluids.4.094601.

[71] C. R. Maliska. *Fundamentals of computational fluid dynamics: the finite volume method*. Number Volume 135 in Fluid mechanics and its applications. Springer, Cham, 2023. ISBN 978-3-031-18234-1.

[72] F. Mallor, G. Semprini-Cesari, T. Mukha, S. Rezaeiravesh, and P. Schlatter. Bayesian optimization of wall-normal blowing and suction-based flow control of a NACA 4412 wing profile. *Flow, Turbulence and Combustion*, (Progress in Flow Control and Drag Reduction), 2023. DOI 10.1007/s10494-023-00475-6.

[73] H. Marcinowski, K. von Sanden, and J. Zierep. *Einrichtungen und Arbeiten des Strömungslaboratoriums*. Number 1 in Mitteilungen des Instituts für Strömungslehre und Strömungsmaschinen und des Lehrstuhls für theoretische Strömungslehre der TH Karlsruhe. Zierep, J., Karlsruhe, 1962.

[74] L. Mathelin, F. Bataille, and A. Lallemand. The Effect of Uniform Blowing on the Flow Past a Circular Cylinder. *Journal of Fluids Engineering*, 124(2):452–464, June 2002. ISSN 0098-2202, 1528-901X. DOI 10.1115/1.1467919.

[75] M. Mendez, M. Raiola, A. Masullo, S. Discetti, A. Ianiro, R. Theunissen, and J.-M. Buchlin. POD-based background removal for particle image velocimetry. *Experimental Thermal and Fluid Science*, 80:181–192, Jan. 2017. ISSN 08941777. DOI 10.1016/j.expthermflusci.2016.08.021.

[76] F. Menter. Zonal Two Equation k-w Turbulence Models For Aerodynamic Flows. In *23rd Fluid Dynamics, Plasmadynamics, and Lasers Conference*, Orlando, FL, USA, July 1993. American Institute of Aeronautics and Astronautics. DOI 10.2514/6.1993-2906.

[77] F. R. Menter. Performance of popular turbulence model for attached and separated adverse pressure gradient flows. *AIAA Journal*, 30(8):2066–2072, Aug. 1992. ISSN 0001-1452, 1533-385X. DOI 10.2514/3.11180.

[78] F. R. Menter, R. Langtry, and S. Völker. Transition Modelling for General Purpose CFD Codes. *Flow, Turbulence and Combustion*, 77(1-4):277–303, Oct. 2006. ISSN 1386-6184, 1573-1987. DOI 10.1007/s10494-006-9047-1.

[79] F. R. Menter, P. E. Smirnov, T. Liu, and R. Avancha. A One-Equation Local Correlation-Based Transition Model. *Flow, Turbulence and Combustion*, 95(4):583–619, Dec. 2015. ISSN 1386-6184, 1573-1987. DOI 10.1007/s10494-015-9622-4.

[80] E. Mercker, K. R. Cooper, O. Fischer, and J. Wiedemann. The Influence of a Horizontal Pressure Distribution on Aerodynamic Drag in Open and Closed Wind Tunnels. In *SAE International*, pages 2005–01–0867. SAE International, Apr. 2005. DOI 10.4271/2005-01-0867.

[81] H. S. Mickley, R. C. Ross, A. L. Squyers, and W. E. Stewart. Heat, mass, and momentum transfer for flow over a flat plate with blowing or suction. Technical Note NACA TN 3208, NACA, Washington, D.C., 1954. URL https://ntrs.nasa.gov/citations/19930084056.

[82] S. Miura, M. Ohashi, K. Fukagata, and N. Tokugawa. Drag Reduction by Uniform Blowing on the Pressure Surface of an Airfoil. *AIAA Journal*, 60(4):2241–2250, Apr. 2022. ISSN 0001-1452, 1533-385X. DOI 10.2514/1.J060831.

[83] R. J. Moffat and W. M. Kays. The turbulent boundary layer on a porous plate: Experimental heat transfer with uniform blowing and suction. *International Journal of Heat and Mass Transfer*, 11(10):1547–1566, Oct. 1968. ISSN 00179310. DOI 10.1016/0017-9310(68)90116-6.

[84] T. Moller, J. Ortmanns, M. El Khalfaoui, and R. Radespiel. The new low speed wind tunnel of the TU Braunschweig. In *20th International Congress on Instrumentation in Aerospace Simulation Facilities, 2003. ICIASF '03.*, pages 399–402, Gottingen, Germany, 2003. IEEE. ISBN 978-0-7803-8149-0. DOI 10.1109/ICIASF.2003.1274892.

[85] T. B. Nickels. Inner scaling for wall-bounded flows subject to large pressure gradients. *Journal of Fluid Mechanics*, 521:217–239, Dec. 2004. ISSN 0022-1120, 1469-7645. DOI 10.1017/S0022112004001788.

[86] W. Nitsche and A. Brunn. *Strömungsmesstechnik*. VDI-Buch. Springer, Berlin Heidelberg, 2., aktualisierte und bearbeitete edition, 2006. ISBN 978-3-540-20990-4.

[87] B. Norton. *STOL progenitors: the technology path to a large STOL transport and the C-17A*. American Institute of Aeronautics and Astronautics, Inc, Reston, Va, 2002. ISBN 978-1-56347-576-4. DOI 10.2514/4.868160.

[88] M. Ohashi, Y. Morita, S. Hirokawa, K. Fukagata, and N. Tokugawa. Parametric study toward optimization of blowing and suction locations for improving lift-to-drag ratio on a Clark-Y airfoil. *Journal of Fluid Science and Technology*, 15(2):JFST0008–JFST0008, 2020. ISSN 1880-5558. DOI 10.1299/jfst.2020jfst0008.

[89] M. Ohashi, K. Fukagata, and N. Tokugawa. Adjoint-Based Sensitivity Analysis for Airfoil Flow Control Aiming at Lift-to-Drag Ratio Improvement. *AIAA Journal*, 59(11):4437–4448, Nov. 2021. ISSN 0001-1452, 1533-385X. DOI 10.2514/1.J060415.

[90] P. M. Ostafichuk and S. I. Green. A low interaction two-axis wind tunnel force balance designed for large off-axis loads. *Measurement Science and Technology*, 13(10):N73–N76, Oct. 2002. ISSN 0957-0233. DOI 10.1088/0957-0233/13/10/401.

[91] T. Oyama, T. Ichige, A. Inoue, and J. Bredenbeck. Electrical wind tunnel external balance system. In M. Bargende, H.-C. Reuss, and J. Wiedemann, editors, *14. Internationales Stuttgarter Symposium*, pages 1177–1191. Springer Fachmedien Wiesbaden, Wiesbaden, 2014. ISBN 978-3-658-05129-7 978-3-658-05130-3. DOI 10.1007/978-3-658-05130-3_84.

[92] J. Park and H. Choi. Effects of uniform blowing or suction from a spanwise slot on a turbulent boundary layer flow. *Physics of Fluids*, 11(10):3095–3105, Oct. 1999. ISSN 1070-6631, 1089-7666. DOI 10.1063/1.870167.

[93] S. V. Patankar. *Numerical heat transfer and fluid flow*. Series in computational methods in mechanics and thermal sciences. Hemisphere Publ. Co, New York, 1980. ISBN 978-0-89116-522-4. OCLC: 31743097.

[94] C. J. Pennycuick, C. E. Heine, S. J. Kirkpatrick, and M. R. Fuller. The Profile Drag of a Hawk'S Wing, Measured by Wake Sampling in a Wind Tunnel. *Journal of Experimental Biology*, 165(1):1–19, Apr. 1992. ISSN 1477-9145, 0022-0949. DOI 10.1242/jeb.165.1.1.

[95] U. Piomelli and J. R. Chasnov. Large-Eddy Simulations: Theory and Applications. In P. Hutchinson, W. Rodi, M. Hallbäck, D. S. Henningson, A. V. Johansson, and P. H. Alfredsson, editors, *Turbulence and Transition Modelling*, volume 2, pages 269–336. Springer Netherlands, Dordrecht, 1996. ISBN 978-90-481-4707-6. DOI 10.1007/978-94-015-8666-5_7. Series Title: ERCOFTAC Series.

[96] U. Piomelli, P. Moin, and J. Ferziger. Large eddy simulation of the flow in a transpired channel. *Journal of Thermophysics and Heat Transfer*, 5(1):124–128, Jan. 1991. ISSN 0887-8722, 1533-6808. DOI 10.2514/3.238.

[97] J. Piquet. *Turbulent Flows*. Springer Berlin Heidelberg, Berlin, Heidelberg, 2001. ISBN 978-3-642-08475-1 978-3-662-03559-7. DOI 10.1007/978-3-662-03559-7.

[98] S. B. Pope. *Turbulent Flows*. Cambridge University Press, 1 edition, Aug. 2000. ISBN 978-0-521-59125-6 978-0-521-59886-6 978-0-511-84053-1. DOI 10.1017/CBO9780511840531.

[99] L. Prandtl. Über Flüssigkeitsbewegungen bei sehr kleiner Reibung. In *Verhandlung des III. Internationalen Mathematiker-Konrgresses Heidelberg*, pages 484 – 494, Heidelberg, Germany, 1904. Teubner.

[100] L. Prandtl and A. Betz, editors. *Ergebnisse der Aerodynamischen Versuchsanstalt zu Göttingen - IV. Lieferung*, volume 7 of *Göttinger Klassiker der Strömungmechanik*. Göttingen University Press, Göttingen, 1932. ISBN 978-3-941875-42-5. DOI 10.17875/gup2009-104.

[101] A. Prasannakumar, J. Wolff, R. Radespiel, L. Boermans, C. Hühne, and C. Badrya. Design and power calculation of HLFC suction system for a subsonic short-range aircraft. *CEAS Aeronautical Journal*, 13(4):1003–1026, Oct. 2022. ISSN 1869-5582, 1869-5590. DOI 10.1007/s13272-022-00614-1.

[102] M. Raffel, C. E. Willert, F. Scarano, C. J. Kähler, S. T. Wereley, and J. Kompenhans. *Particle Image Velocimetry: A Practical Guide*. Springer International Publishing, Cham, 3rd edition, 2018. ISBN 978-3-319-68851-0 978-3-319-68852-7. DOI 10.1007/978-3-319-68852-7.

[103] D. Raymer. *Aircraft Design: A Conceptual Approach, Sixth Edition and RDSwin Student SET*. American Institute of Aeronautics and Astronautics, Inc., Washington, DC, Jan. 2019. ISBN 978-1-62410-574-6. DOI 10.2514/4.105746.

[104] M. Reder. Modellierung der Reibungsminderung bei Flügelprofilen mittels homogenem Ausblasen. Master's thesis, Karlsruhe Institute of Technology, Karlsruhe, Germany, 2018.

[105] M. Rennie, M.-S. Kim, J.-H. Lee, and J.-D. Kee. Suppression of Open-Jet Pressure Fluctuations in the Hyundai Aeroacoustic Wind Tunnel. In *SAE International*, pages 2004–01–0803. SAE International, Mar. 2004. DOI 10.4271/2004-01-0803.

[106] O. Reynolds. IV. On the dynamical theory of incompressible viscous fluids and the determination of the criterion. *Philosophical Transactions of the Royal Society of London. (A.)*, 186:123–164, Dec. 1895. ISSN 0264-3820, 2053-9231. DOI 10.1098/rsta.1895.0004.

[107] J. A. Rice. *Mathematical statistics and data analysis*. Brooks/Cole, Cengage Learning, Belmont, CA, 3rd edition, 2007. ISBN 978-0-495-11868-8. OCLC: 71364578.

[108] J.-L. Rioual, P. A. Nelson, P. Hackenberg, and O. R. Tutty. Optimum drag balance for boundary-layer suction. *Journal of Aircraft*, 33(2):435–438, Mar. 1996. ISSN 0021-8669, 1533-3868. DOI 10.2514/3.46956.

[109] I. Roehle, R. Schodl, P. Voigt, and C. Willert. Recent developments and applications of quantitative laser light sheet measuring techniques in turbomachinery components. *Measurement Science and Technology*, 11(7):1023–1035, July 2000. ISSN 0957-0233, 1361-6501. DOI 10.1088/0957-0233/11/7/317.

[110] P. N. Romanenko and V. N. Kharchenko. The effect of transverse mass flow on heat transfer and friction drag in a turbulent flow of compressible gas along an arbitrarily shaped surface. *International Journal of Heat and Mass Transfer*, 6(8):727–738, Aug. 1963. ISSN 00179310. DOI 10.1016/0017-9310(63)90043-7.

[111] M. W. Rubesin. An analytical Estimation of the Effect of Transpiration Cooling on the Heat-Transfer and Skin-Friction Characteristics of a compressible, turbulent Boundary Layer. Technical Note NACA TN 3341, NACA, Washington, D. C., 1954. URL https://ntrs.nasa.gov/citations/19930084158.

[112] C. L. Rumsey and T. Nishino. Numerical study comparing RANS and LES approaches on a circulation control airfoil. *International Journal of Heat and Fluid Flow*, 32(5):847–864, Oct. 2011. ISSN 0142727X. DOI 10.1016/j.ijheatfluidflow.2011.06.011.

[113] G. P. Russo. *Aerodynamic measurements: from physical principles to turnkey instrumentation*. Woodhead publishing in mechanical engineering. Woodhead Publishing, Cambridge ; Philadelphia, PA, 2011. ISBN 978-1-84569-992-5. OCLC: ocn698329550.

[114] M. Samimy and S. K. Lele. Motion of particles with inertia in a compressible free shear layer. *Physics of Fluids A: Fluid Dynamics*, 3(8):1915–1923, Aug. 1991. ISSN 0899-8213. DOI 10.1063/1.857921.

[115] A. M. Savill. A Synthesis of T3 Test Cases Predictions. In *Numerical Simulation of Unsteady Flows and Transition to Turbulence*, pages 404–442. Cambridge University Press, Cambridge, United Kingdom, 1 edition, 1992. ISBN 978-0-521-41618-4.

[116] H. Schlichting. *Grenzschicht-Theorie*. Springer, Berlin, Heidelberg, 5., völlig neubearbeitete und erweiterte edition, 1964.

[117] H. Schlichting and K. Gersten. *Boundary-layer theory*. Springer, Berlin; New York, 8th revised and enlarged edition, 2000. ISBN 978-3-540-66270-9.

[118] H. Schlichting and K. Gersten. *Grenzschicht-Theorie mit 22 Tabellen*. Springer, Berlin, 10., überarbeitete edition, 2006. ISBN 978-3-540-23004-5. OCLC: 636610285.

[119] P. Scholz. Simulation of Pressure Losses for the Design of Tailored Suction Distributions for Laminar Flow Control, Mar. 2015. URL http://edrfcm-2015.eng.cam.ac.uk/pub/EDRFCM2015/MeetingProgram/56_Scholz.pdf. Presented at EDRFCM 2015, Cambridge, United Kingdom.

[120] G. H. Schrauf and H. von Geyr. Simplified Hybrid Laminar Flow Control for the A320 Fin - Aerodynamic and System Design, First Results. In *AIAA Scitech 2020 Forum*, Orlando, FL, Jan. 2020. American Institute of Aeronautics and Astronautics. ISBN 978-1-62410-595-1. DOI 10.2514/6.2020-1536.

[121] O. Schrenk. Profileigenschaften eines Absaugeflügels. volume 2 of *Ergebnisse der Aerodynamischen Versuchsanstalt zu Göttingen*, pages 49–62. Verlag von R. Oldenbourg, München und Berlin, 1 edition, 1932.

[122] R. L. Simpson, R. Moffat, and W. Kays. The turbulent boundary layer on a porous plate: Experimental skin friction with variable injection and suction. *International Journal of Heat and Mass Transfer*, 12(7):771–789, July 1969. ISSN 00179310. DOI 10.1016/0017-9310(69)90181-1.

[123] D. Sonntag. Fortschritte in der Hygrometrie. *Meteorologische Zeitschrift*, 3(2):51–66, May 1994. ISSN 0941-2948. DOI 10.1127/metz/3/1994/51.

[124] P. Spalart and S. Allmaras. A one-equation turbulence model for aerodynamic flows. In *30th Aerospace Sciences Meeting and Exhibit*, Reno, NV, USA, Jan. 1992. American Institute of Aeronautics and Astronautics. DOI 10.2514/6.1992-439.

[125] P. R. Spalart and J. D. McLean. Drag reduction: enticing turbulence, and then an industry. *Philosophical Transactions of the Royal Society A: Mathematical, Physical and Engineering Sciences*, 369(1940):1556–1569, Apr. 2011. ISSN 1364-503X, 1471-2962. DOI 10.1098/rsta.2010.0369.

[126] J. H. Spurk and N. Aksel. *Fluid Mechanics*. Springer International Publishing, Cham, 2020. ISBN 978-3-030-30259-7. DOI 10.1007/978-3-030-30259-7.

[127] A. Stroh, Y. Hasegawa, P. Schlatter, and B. Frohnapfel. Global effect of local skin friction drag reduction in spatially developing turbulent boundary layer. *Journal of Fluid Mechanics*, 805:303–321, Oct. 2016. ISSN 0022-1120, 1469-7645. DOI 10.1017/jfm.2016.545.

[128] Y. Sumitani and N. Kasagi. Direct numerical simulation of turbulent transport with uniform wall injection and suction. *AIAA Journal*, 33(7):1220–1228, July 1995. ISSN 0001-1452, 1533-385X. DOI 10.2514/3.12363.

[129] W. Sutherland. The viscosity of gases and molecular force. *The London, Edinburgh, and Dublin Philosophical Magazine and Journal of Science*, 36(223):507–531, Dec. 1893. ISSN 1941-5982, 1941-5990. DOI 10.1080/14786449308620508.

[130] U. Teubner and H. J. Brückner. *Optical imaging and photography: introduction to science and technology of optics, sensors and systems*. De Gruyter STEM. De Gruyter, Berlin Boston, 2019. ISBN 978-3-11-047294-3 978-3-11-047293-6. DOI 10.1515/9783110472943.

[131] A. A. Townsend. *The structure of turbulent shear flow*. Cambridge monographs on mechanics and applied mathematics. Cambridge University Press, Cambridge [Eng.] ; New York, 2d ed edition, 1976. ISBN 978-0-521-20710-2.

[132] C. Tropea, A. Yarin, and J. Foss, editors. *Springer handbook of experimental fluid mechanics*. Springer, Berlin, 2007. ISBN 978-3-540-25141-5.

[133] C. P. van Dam. Natural Laminar Flow Airfoil Design Considerations for Winglets on Low-Speed Airplanes. Contractor Report 3853, NASA, 1984. URL https://ntrs.nasa.gov/citations/19850004555.

[134] R. Vinuesa, P. Negi, M. Atzori, A. Hanifi, D. Henningson, and P. Schlatter. Turbulent boundary layers around wing sections up to $Re_c = 1$Mio. *International Journal of Heat and Fluid Flow*, 72:86–99, Aug. 2018. ISSN 0142727X. DOI 10.1016/j.ijheatfluidflow.2018.04.017.

[135] U. von Glahn. Use of the Coanda Effect for obtaining Jet Deflection and Lift with a single Flat-Plate Deflection Surface. Technical Note 4272, NACA, Cleveland, Ohio, 1958. URL https://ntrs.nasa.gov/citations/19930085044.

[136] M. J. Walsh. Riblets for aircraft skin-friction reduction. In *Langley Symposium on Aerodynamics*, volume 1, pages 557–571, Langley, VA, USA, Dec. 1986. NASA. URL https://ntrs.nasa.gov/citations/19880005573. NASA-CP-2397.

[137] J. Walter, E. Duell, B. Martindale, S. Arnette, R. Geierman, M. Gleason, and G. Romberg. The DaimlerChrysler Full-Scale Aeroacoustic Wind Tunnel. pages 2003–01–0426. SAE International, Mar. 2003. DOI 10.4271/2003-01-0426.

[138] C. Warsop and W. Crowther. NATO AVT-239 Task Group: Flight Demonstration of Fluidic Flight Controls on the MAGMA Subscale Demonstrator Aircraft. In *AIAA Scitech 2019 Forum*, San Diego, California, Jan. 2019. American Institute of Aeronautics and Astronautics. ISBN 978-1-62410-578-4. DOI 10.2514/6.2019-0282.

[139] J. Weiss. A Tutorial on the Proper Orthogonal Decomposition. In *AIAA Aviation 2019 Forum*, Dallas, Texas, June 2019. American Institute of Aeronautics and Astronautics. ISBN 978-1-62410-589-0. DOI 10.2514/6.2019-3333.

[140] H. Weller and H. Jasak. OpenFOAM Documentation, 2011. URL https://openfoam.org. Open Source Software.

[141] G. Wickern, W. Von Heesen, and S. Wallmann. Wind Tunnel Pulsations and their Active Suppression. pages 2000–01–0869. SAE International, Mar. 2000. DOI 10.4271/2000-01-0869.

[142] D. C. Wilcox. Reassessment of the scale-determining equation for advanced turbulence models. *AIAA Journal*, 26(11):1299–1310, 1988. ISSN 0001-1452, 1533-385X. DOI 10.2514/3.10041.

[143] D. C. Wilcox. *Turbulence modeling for CFD*. DCW Industries, La Cãnada, Calif, 3rd ed edition, 2006. ISBN 978-1-928729-08-2.

[144] S. Wilkinson, J. Anders, B. Lazos, and D. Bushnell. Turbulent drag reduction research at NASA langley: progress and plans. *International Journal of Heat and Fluid Flow*, 9(3): 266–277, Sept. 1988. ISSN 0142727X. DOI 10.1016/0142-727X(88)90037-9.

[145] R. Wokoeck, A. Grote, N. Krimmelbein, J. Ortmanns, R. Radespiel, and A. Krumbein. RANS Simulation and Experiments on the Stall Behaviour of a Tailplane Airfoil. In E. H. Hirschel, W. Schröder, K. Fujii, W. Haase, B. Leer, M. A. Leschziner, M. Pandolfi, J. Periaux, A. Rizzi, B. Roux, H.-J. Rath, C. Holze, H.-J. Heinemann, R. Henke, and H. Hönlinger, editors, *New Results in Numerical and Experimental Fluid Mechanics V*, volume 92, pages 208–216. Springer Berlin Heidelberg, Berlin, Heidelberg, 2006. ISBN 978-3-540-33286-2 978-3-540-33287-9. DOI 10.1007/978-3-540-33287-9_26. Series Title: Notes on Numerical Fluid Mechanics and Multidisciplinary Design (NNFM).

[146] S. Yarusevych, P. E. Sullivan, and J. G. Kawall. Airfoil boundary layer separation and control at low Reynolds numbers. *Experiments in Fluids*, 38(4):545–547, Apr. 2005. ISSN 0723-4864, 1432-1114. DOI 10.1007/s00348-005-0943-2.

[147] C. Yorke and G. Coleman. Assessment of common turbulence models for an idealised adverse pressure gradient flow. *European Journal of Mechanics - B/Fluids*, 23(2):319–337, Mar. 2004. ISSN 09977546. DOI 10.1016/j.euromechflu.2003.07.002.

[148] T. Young, B. Humphreys, and J. Fielding. Investigation of hybrid laminar flow control (HLFC) surfaces. *Aircraft Design*, 4(2-3):127–146, June 2001. ISSN 13698869. DOI 10.1016/S1369-8869(01)00010-6.

[149] W. Zhang and R. Samtaney. A direct numerical simulation investigation of the synthetic jet frequency effects on separation control of low-Re flow past an airfoil. *Physics of Fluids*, 27 (5):055101, May 2015. ISSN 1070-6631, 1089-7666. DOI 10.1063/1.4919599.

[150] J. Zierep and K. Bühler. *Grundzüge der Strömungslehre: Grundlagen, Statik und Dynamik der Fluide*. Teubner, Wiesbaden, 7., verbesserte edition, 2008. ISBN 978-3-8351-0231-6.

[151] R. Örlü and R. Vinuesa. Thermal anemometry. In *Experimental Aerodynamics*, pages 393–428. CRC Press Taylor & Francis Group, Boca Raton, 1 edition, 2017. ISBN 978-1-315-37173-3.

List of Conference Contributions

[EMF+22] A. Eberhard, H. Metni, G. Fahland, A. Stroh, and P. Friederich. Actively Learning Costly Reward Functions for Reinforcement Learning. In *6th Conference on Neural Information Processing Systems*, 2022. Publisher: arXiv Version Number: 1.

[Fah20] G. Fahland. RANS Untersuchungen zur Strömungskontrolle in turbulenter Grenzschicht von Flügelprofilen, 2020. presented at Deutscher Luft- und Raumfahrtkongress (DLRK 2020), Publisher of Slides: KITopen. DOI 10.5445/IR/1000123966.

[Fah21] G. Fahland. Kombination Turbulenter und Laminarer Strömungskontrolle an Flügelprofilen. In *70. Deutscher Luft- und Raumfahrtkongress (DLRK 2021)*, Bremen, Germany, 2021. DGLR. Publisher: KITopen. DOI 10.5445/IR/1000136912.

[FEW+23] G. Fahland, F. Elsner, K. Weber, F. Kauffmann, M. Wickberg, D. Achzehnter, and J. Kriegseis. Modal Decomposition of Wind-Tunnel Fluctuations. In *AIAA AVIATION 2023 Forum*, San Diego, CA and Online, June 2023. American Institute of Aeronautics and Astronautics. DOI 10.2514/6.2023-4368.

[FGF+19] G. Fahland, D. Gatti, B. Frohnapfel, A. Stroh, M. Atzori, R. Vinuesa, and P. Schlatter. RANS Investigation of Blowing and Suction for Turbulent Flow Control on a Wing Section, 2019. Publisher: KITopen. DOI 10.5445/IR/1000097975.

[FGSF22] G. Fahland, D. Gatti, A. Stroh, and B. Frohnapfel. Implementation Aspects of Uniform Blowing in Turbulent Boundary Layers. In *9th European Conference for Aeronautics and Space Science (Eucass 3AF 2022)*, page 10, Lille, France, 2022. EDP Sciences. DOI 10.13009/EUCASS2022-6123.

[FSG+21] G. Fahland, A. Stroh, D. Gatti, M. Atzori, R. Vinuesa, P. Schlatter, and B. Frohnapfel. Energy Budgets and Performance Development of Turbulent Boundary-Layer Control on Airfoils. In *ETMM13 Conference Proceedings*, pages 123–127, Rhodes, Greece, September 2021. ERCOFTAC. Publisher: KITopen. DOI 10.5445/IR/1000136911.

[FSGF19] G. Fahland, A. Stroh, D. Gatti, and B. Frohnapfel. RANS Untersuchungen zur Strömungskontrolle in turbulenter Grenzschicht von Flügelprofilen, June 2019. Publisher of Slides: KITopen. DOI 10.5445/IR/1000099698.

List of Journal Publications

[AVF+20] M. Atzori, R. Vinuesa, G. Fahland, A. Stroh, D. Gatti, B. Frohnapfel, and P. Schlatter. Aerodynamic Effects of Uniform Blowing and Suction on a NACA4412 Airfoil. *Flow,*

Turbulence and Combustion, 105:735–759, April 2020. DOI 10.1007/s10494-020-00135-z.

[FAF+23] G. Fahland, M. Atzori, A. Frede, A. Stroh, B. Frohnapfel, and D. Gatti. Drag Assessment for Boundary Layer Control Schemes with Mass Injection. *Flow, Turbulence and Combustion*, (Progress in Flow Control and Drag Reduction), 2023. DOI 10.1007/s10494-023-00462-x.

[FSF+21] G. Fahland, A. Stroh, B. Frohnapfel, M. Atzori, R. Vinuesa, P. Schlatter, and D. Gatti. Investigation of Blowing and Suction for Turbulent Flow Control on Airfoils. *AIAA Journal*, 59(11):4422–4436, July 2021. DOI 10.2514/1.J060211.

Author Contributions of Journal Papers

Karlsruhe Institute of Technology

Institute of Fluid Mechanics
Building 10.23, 6th floor, Kaiserstraße 10, D-76131 Karlsruhe, Germany
http://www.istm.kit.edu

Author Contributions

Marco Atzori, Ricardo Vinuesa, Georg Fahland, Alexander Stroh, Davide Gatti, Bettina Frohnapfel and Philipp Schlatter
Aerodynamic Effects of Uniform Blowing and Suction on a NACA4412 Airfoil
Flow, Turbulence and Combustion, 105:735–759, 2020
DOI: 10.1007/s10494-020-00135-z

The LESs have been performed by MA, with input from RV and PS. The RANS simulations have been performed by GF with help from AS and DG. The post-processing has been carried out by MA, with input from RV (LESs), and by GF (RANS simulations). The paper has been written by MA with input from GF, RV, and PS. RV, PS, AS, DG and BF revised the manuscript and provided feedback.

All co-authors agree to this description of their contribution:

Marco Atzori	MA	Date, Signature:	Firmato digitalmente da:MARCO ATZORI Organizzazione: POLITECNICO DI MILANO/80057930150 Note:Marco Atzori
Ricardo Vinuesa	RV	Date, Signature:	
Georg Fahland	GF	Date, Signature:	26.02.2024
Alexander Stroh	AS	Date, Signature:	13.2.2024
Davide Gatti	DG	Date, Signature:	12.2.2024
Bettina Frohnapfel	BF	Date, Signature:	13.12.2024
Philipp Schlatter	PS	Date, Signature:	12.2.2024

Karlsruhe Institute of Technology

Institute of Fluid Mechanics
Building 10.23, 6th floor, Kaiserstraße 10, D-76131 Karlsruhe, Germany
http://www.istm.kit.edu

Author Contributions

Georg Fahland, Alexander Stroh, Bettina Frohnapfel, Marco Atzori, Ricardo Vinuesa, Philipp Schlatter, Davide Gatti
Investigation of Blowing and Suction for Turbulent Flow Control on Airfoils
AIAA Journal, 59(11):4422–4436, 2021
DOI: 10.2514/1.J060211

The design of the study was conducted by GF, AS and DG. The RANS simulations have been performed by GF with the help from AS and DG. The post-processing has been carried out by GF, with input from AS, DG and BF. Validation data (LES) was provided, processed and interpreted for the purpose of this study by MA with input from RV and PS. The paper has been written by GF with input from DG, AS, and BF. AS, BF, MA, RV, PS and DG revised the manuscript and provided feedback.

All co-authors agree to this description of their contribution:

Georg Fahland	GF	Date, Signature:	26.02.2024
Alexander Stroh	AS	Date, Signature:	13.2.2024
Bettina Frohnapfel	BF	Date, Signature:	13.2.2024
Marco Atzori	MA	Date, Signature:	Firmato digitalmente da:MARCO ATZORI Organizzazione: POLITECNICO DI MILANO/80057930150 Note:Marco Atzori
Ricardo Vinuesa	RV	Date, Signature:	
Philipp Schlatter	PS	Date, Signature:	12.2.2024
Davide Gatti	DG	Date, Signature:	12.2.2024

Karlsruhe Institute of Technology

Institute of Fluid Mechanics
Building 10.23, 6th floor, Kaiserstraße 10, D-76131 Karlsruhe, Germany
http://www.istm.kit.edu

Author Contributions

Georg Fahland, Marco Atzori, Annika Frede, Alexander Stroh, Bettina Frohnapfel, Davide Gatti
Drag Assessment for Boundary Layer Control Schemes with Mass Injection
Flow, Turbulence and Combustion, 2023
DOI: 10.1007/s10494-023-00462-x

GF: design of the study, incompressible RANS data, manuscript draft. MA: LES data, its evaluation and discussion. AF: compressible RANS data, its evaluation and discussion. AS: discussion of boundary layer formulation, final text. BF: supervision and final text. DG: design of the study, supervision and final text.

This description of author contributions was published alongside the paper with agreement of all authors.

Acronyms and symbols

Acronyms

AoA	angle of attack
APG	adverse pressure gradient
BLC	boundary layer control
CTA	constant temperature anemometry
DAQ	data acquisition
DNS	direct numerical simulations
DOF	degrees of freedom
FIR	finite impulse response (filter)
FS	sensor full scale — the range of a sensor from minimum to maximum reading
FS2D	flow domain: freestream, two dimensional
IIR	infinite impulse response (filter)
ISTM	Institute of Fluid Mechanics at KIT
KIT	Karlsruhe Institute of Technology (KIT)
LES	large eddy simulations
MPG	mixed pressure gradient
PIV	particle image velocimetry
POD	proper orthogonal decomposition
PS	airfoil pressure side (lower side)
PTPv2	precision time protocol version 2 (IEEE 1588)
RANS	Reynolds-averaged Navier-Stokes equations
SR	(current) sensor reading — the output value of a sensor
SS	airfoil suction side (upper side)
TBL	turbulent boundary layer
TKE	turbulent kinetic energy
WT2D	flow domain: wind tunnel, two dimensional (on jet symmetry plane)
WT3D	flow domain: wind tunnel, three dimensional (whole model)

ZPG zero pressure gradient

Latin Letter - Upper Case

A time coefficient function matrix in POD

A_{BLC} area of BLC surface

A_f frontal area the airfoil model poses to wind tunnel flow

A_{hole} total open area of holes in BLC surface

A_{ref} reference area

A_t total cross-section area of wind tunnel jet

$\mathcal{A}$ parameterized area, *e.g.* $\oiint(...)\mathrm{d}\mathcal{A}$

$\mathbf{C}_{xx}$ covariance matrix of x

$\mathcal{C}$ parameterized line, *e.g.* $\oint(...)\mathrm{d}\mathcal{C}$

E efficiency $= c_l/c_d$

$\mathcal{E}$ absolute error/uncertainty (unit identical to quantity unit)

F force

F_D integral drag force

F_L integral lift force

H distance of model images (potential theory of wind tunnel lift correction)

K snapshot matrix of POD

P power

P_{aux} power consumption of auxiliary devices

$P_{\mathrm{jet},\infty}$ freestream reference power

Re Reynolds number

Re_c Reynolds number based on freestream velocity U_∞ and airfoil chord length c

U_e velocity in inviscid flow field outside boundary layer (edge): “edge velocity”

U_∞ freestream velocity at infinity distance from a test object

Stk Stokes number

V volume

$\mathcal{V}$ parameterized volume, *e.g.* $\iiint(...)\mathrm{d}\mathcal{V}$

$\dot{V}$ volume flux

$\{X, Y, Z\}$ body conform coordinate system

$\{\overline{X}, \overline{Y}, \overline{Z}\}$ aerodynamic coordinate system (freestream aligned)

Latin Letter - Lower Case

a_{wk}	experimental wake fit parameter: curve height
b_{wk}	experimental wake fit parameter: curve shift
c	airfoil chord length
c_{BLC}	boundary layer control penalty
c_d	drag coefficient
$c_{d,\mathrm{aux}}$	equivalent drag of power consumption of auxiliary devices
$c_{d,B}$	body drag coefficient
$c_{d,\mathrm{inc}}$	inclusive drag coefficient
$c_{d,W}$	wake survey drag coefficient
$c_{d,f}$	friction drag coefficient
$c_{d,p}$	pressure drag coefficient
$c_{f,\mathrm{BLC}}$	BLC penalty in localized boundary layer formulation
$c_{f,\mathrm{inc}}$	inclusive dimensionless wall shear stress
$c_{f,l}$	dimensionless wall shear stress referenced by "edge" velocity U_e
$c_{f,\infty}$	dimensionless wall shear stress referenced by freestream velocity U_∞
$c_{f,\mathrm{EP}}$	dimensionless wall shear stress on test rig end plate
c_l	lift coefficient
$c_{l,p}$	lift coefficient from pressure integral
c_m	pitching moment coefficient
c_p	dimensionless local pressure
$\overline{c_{p,\mathrm{BLC}}}$	average of dimensionless local pressure within active boundary layer control region
c_q	dimensionless blowing velocity $v_{\mathrm{BLC}}/U_\infty$
c_{wk}	experimental wake fit parameter: curve width
d_p	particle diameter
d_{pTap}	pressure tap hole diameter
d_{FF}	general distance of far-field boundary
d_O	distance of far-field outflow boundary in meshes
d_{TE}	distance of a point (*e.g.* wake probe) to airfoil trailing edge
$x\mathrm{e}y$	$x \cdot 10^y$
e	specific energy
f	airfoil camber

f_f	filter frequency
f_s	sample frequency
g or $\mathbf{g}$	force per mass $\equiv$ acceleration
i, j, k, m, n	indices
k	turbulent kinetic energy
l_{BLC}	boundary layer control region length along wall
m	mass
$\dot{m}$	mass flux
n_{crit}	critical amplification ration of disturbances
$\mathbf{n}$	unity normal vector
p	static pressure
p_t	total pressure
$p_{<\mathrm{index}>,\mathrm{SR}}$	sensor reading of a pressure sensor
p_∞	static pressure at infinite distance from the test object
q	dynamic pressure
q_∞	dynamic pressure in freestream streamline for $p = p_\infty$
$\mathbf{r}$	position vector
r_C	radius of far-field boundary in meshes
s	wing section span
t	time
t_p	particle response time
$\mathbf{t}$	viscous stress vector on a surface
t_a	airfoil thickness
u and $\mathbf{u}$	velocity
v_{BLC}	boundary layer control velocity (wall-normal)
w_i	weight (of a parameter/quantity)
$\{x, y, z\}$	wall coordinate system
y_{min}	mesh cell height at the wall

Greek Letters - upper Case

Γ	circulation
Φ	potential
Ψ	porosity of BLC surface

$\mathbf{\Psi} \in \mathbb{R}^{n \times m}$	spatial mode matrix of POD with spatial dimension n and temporal dimension m
Ω	power associated with viscous losses within the control volume

Greek Letters - lower Case

α	angle of attack
β	boundary layer equilibrium parameter / Clauser parameter
β_{Ma}	compressibility parameter $\sqrt{1 - Ma^2}$
β_{y^+}	cell size factor for maintaining $y^+ \lessapprox 1$ mesh requirement for off-design operating points
γ_m	skewness
δ_{ij}	Kronecker delta
δ_{99}	boundary layer thickness
$\delta^\star$	boundary layer displacement thickness
δ_θ	boundary layer momentum loss thickness
δ_0	upwash parameter
δ_1	curvature parameter
ϵ	relative error/uncertainty (non-dimensional)
ζ_{BLC}	dimensionless flow resistance of BLC surface
ζ_{avail}	dimensionless available BLC supply pressure difference from freestream total pressure to static pressure at the surface of an active control region
μ	dynamic viscosity
ν	kinematic viscosity
ν_T	eddy viscosity
ρ	density
$\boldsymbol{\tau}$	shear stress tensor
τ_w	wall shear stress
$\{\xi, \zeta\}$	dimensionless aerodynamic coordinate system
χ	coordinate along streamline
ω	turbulence specific dissipation rate

Mathematical Operators

$\partial\,(...)$	partial derivative
$\dot{(...)}$	temporal derivative $= \frac{\partial(...)}{\partial t}$

$\overline{(...)}$	temporal average
$(...)'$	instantaneous difference from the mean quantity $= (...) - \overline{(...)}$
$\widetilde{(...)}$	standard deviation of a set
Δ	difference
Exp()	expectation operator
$\|\mathbf{a}\|$	Euclidean norm of $\mathbf{a}$
∇	Laplace operator
$\mathbf{a}$	bold print: tensor of first (vector) or second rank
$\mathbf{A}$	bold print without serifs: matrix
$\mathbf{a} \cdot \mathbf{a}$	vector dot product $= a_i b_i$
$(...)^+$	quantity denoted by (...) is expressed in inner scaling of the turbulent boundary layer

List of Figures

2.1 Principle of the images for closed and open 2D wind-tunnel sections [32, p. 2-11]. . . 18
2.2 Relevant Vectors for Pressure Distribution Integration 23
2.3 Experimental arrangement for planar 2C-2D PIV of a boundary layer flow. Inspired by [102, Fig. 1.9] 24
2.4 The shift and deformation of interrogation areas (squares) when using multipass and image deformation for multigrid algorithms. Inspired by [102, Fig. 5.22, 5.26] . . 25

3.1 Control Volume (CV) for the airfoil momentum budget in which $\mathbf{n}$ is the normal vector pointing out of the CV. Adapted from [FAF+23] 29
3.2 Law of Bernoulli for an isentropic flow at varying velocities. 32
3.3 Energy Budget for a moving body in fluid at rest. 32
3.4 Energy Budget for a moving fluid and a body at rest. 34

4.1 Computational domain with definition of boundaries and coordinate axes: the global rigid body coordinate system $\{X, Y, Z\}$ and the local wall coordinate system $\{x, y, z\}$. Adapted from [FSF+21, figure 1] 40
4.2 Control schemes and their location. Modified from [FSF+21, figure 2]. 41
4.3 Comparison of LES (dashed) and RANS (solid) predictions of the BLC effect on aerodynamic coefficients at $Re_c = 2 \cdot 10^5$ and $\alpha = 5°$. Adapted from [FSF+21, figure 5] 43
4.4 Comparison of boundary-layer properties of LES and RANS. The shaded area indicates the region where BLC is active. $Re_c = 4 \cdot 10^5$, $\alpha = 5°$. Adapted from [FSF+21, figure 6] 44
4.5 Pressure coefficent c_p for $Re_c = 4 \cdot 10^5$, NACA 4412, $\alpha = 5°$,$v_{\mathrm{BLC}} = 0.1\%U_\infty$. Adapted from [FSF+21, figure 7] 45
4.6 Polar plot of three example cases ($Re_c = 4 \cdot 10^5$) with a blowing rate of $v_{\mathrm{BLC}} = 0.5\%U_\infty$. Straight lines show the polar of the body drag coefficient $c_{d,B}$. The dotted lines show the polar of the inclusive drag coefficient $c_{d,\mathrm{inc}}$. Updated from [FSF+21, figure 8] to show inclusive drag 47
4.7 Skin-friction coefficient c_f at $\alpha = 5°$ (left) and $\alpha = 9°$ (right). The shaded area represents the BLC location. Adapted from [FSF+21, figure 9] 48
4.8 Wake profile f_{WS} (eq. 3.4) and Re-Stresses f_{ReStress} ([FAF+23, eq. 4]) for blowing on the SS and blowing on the PS at $d_{\mathrm{TE}}/c = 0.2$ behind the trailing edge. NACA 4412, angle of attack $\alpha = 5°$, $Re = 4 \cdot 10^5$, $v_{\mathrm{BLC}} = 0.1\%U_\infty$. Adapted from [FAF+23, figure 2] 49
4.9 Comparison of *wake survey* drag, *body drag* and *BLC penalty*. NACA 4412, $Re = 4 \cdot 10^5$, $v_{\mathrm{BLC}} = 0.5\%U_\infty$, $d_{\mathrm{TE}}/c = 0.8$, $h/c = 1.1$, $\alpha = 5°$. $\Delta c_d = c_{d,\mathrm{controlled}} - c_{d,\mathrm{uncontrolled}}$. Modified from [FAF+23, figure 3] 49
4.10 Development of drag components with Reynolds number. $\alpha = 5°$, $v_{\mathrm{BLC}} = 0.5\%u_\infty$. Friction drag $c_{d,f}$ (a), pressure drag $c_{d,p}$ (b), and ratio of friction drag to total body drag $c_{d,f}/c_{d,B}$ (c). Modified from [FSF+21, figure 10] 50
4.11 Development of aerodynamic coefficients and efficiency improvement relative to the uncontrolled polar. Operating point: NACA4412, $\alpha = 5°$, $v_{\mathrm{BLC}} = 0.5\%U_\infty$. Modified from [FSF+21, figure 11] to add inclusive drag evolution (dotted) 50
4.12 Drag portion development for increasing intensity of uniform blowing on SS (left) and PS (right) for NACA 4412, $Re = 4 \cdot 10^5$, $\alpha = 5°$. Adapted from [FAF+23, figure 4] 52

4.13 Polar plot for varying thickness in case of blowing on PS with $v_{\mathrm{BLC}} = 0.5\%$,$Re_c = 4 \cdot 10^5$. Dashed lines are uncontrolled cases. Modified from [FSF+21, figure 12] to show inclusive drag (dotted) . . . 53
4.14 Drag reduction ($\Delta c_d < 0$: drag reduction; $\Delta c_d > 0$: drag increase) as function of airfoil thickness t_a and Reynolds number Re_c (a) respectively blowing intensity v_{BLC} (b). Plain aerodynamic comparison $\Delta c_{d,B}$ is plotted in black, and inclusive drag difference $\Delta c_{d,\mathrm{inc}}$ is plotted in red. $\alpha = 5°$ Modified from [FSF+21, figure 13] to show inclusive drag. . . . 54
4.15 Pressure coefficient c_p on PS for $\alpha = 0°$ (left) and $\alpha = 5°$ (right). $Re = 4 \cdot 10^6$. The shaded area represents the BLC location. . . . 54
4.16 Airfoil GFAPG006 with 7 different blowing regions on airfoil PS at approximately similar pressure gradient but different mean pressure level. AoA $\alpha = 1°$, $Re_c = 1$Mio, $c_q = 1\%U_\infty$. Airfoil coordinates in table C.1 . . . 55
4.17 Airfoil MPG with 3 different blowing regions on airfoil PS at similar adverse and favorable pressure gradients but three different mean pressure levels. AoA $\alpha = 7°$, $Re_c = 1$Mio,$c_q = 1\%U_\infty$. Airfoil coordinates in table C.1 . . . 56
4.18 Comparison of drag reduction due to uniform blowing for different pressure levels in application region. Left: Adverse Pressure Gradient test case; right: mixed pressure gradient test case. $Re_c = 1$Mio, $c_q = 1\%U_\infty$ . . . 57

5.1 Calculation of Wind-Tunnel reference quantities . . . 60
5.2 Turbulence Spectra prior and after the measurement campaign of VACA4412s019, bandpass filtered $[2, 5000]$Hz (left), bin size $f_{\mathrm{bin}} = 0.5$Hz, integral turbulence intensity over wind-tunnel velocity (right) . . . 61
5.3 Porosity with circular and conical holes of experimental studies from literature on uniform blowing in turbulent boundary layers . . . 62
5.4 RANS data: Boundary layer equilibrium parameter / Clauser Parameter β for different freestream AoA, $Re_c = 10^6$, NACA4412 and VACA4412s019. The final location of the control area is given in grey. . . . 63
5.5 General test rig schematic and part nomenclature. Final test rig design in figure D.1 . 64
5.6 DOF decoupling for the balance for the installation with the VACA4412s019 airfoil model. The forces measured by the balance directly do not represent the actual lift and drag forces but have to be corrected by the angle of attack error (see section 5.3) 67
5.7 Errors of the balance readings based on sensor error (table 5.2) and linear error propagation through the coupling equations 5.2 - 5.4. . . . 68
5.8 Distribution of pressure taps of the VACA4412s019 airfoil model (development of the model described in section 5.2.1) . . . 70
5.9 PIV calibration target and positions of Field of Views (FOV). The quad-pattern has an edge length of 1% airfoil chord length ($c/100 = 7.5$mm) . . . 74
5.10 Data processing chain for 2D-2C PIV measurements at the wing test stand . . . 75
5.11 Overview of the wind-tunnel corrections to mitigate the errors (violet boxes) and the location of measurement methods (wake rake, balance, pressure taps) in terms of necessary corrections steps . . . 81
5.12 Geometric properties of the turntables contributing to the balance drag measurement due to turbulent boundary layer friction drag . . . 82
5.13 Repetition and Fluctuation Deviation Definition and Error Bar Representation. . . . 84
5.14 Wind tunnel correction steps applied to the balance measurement results including the linear error propagation fields and the repetition error. Uncontrolled cases, tripping at $X_{\mathrm{tr}}/c = 10\%$, $Re_c = 1.5$Mio, VACA4412s019 airfoil model. . . . 86
5.15 Comparison of digital twin results [Kai22] for lift-correction consequences in terms of effective AoA (α_{aero}) vs. geometrical AoA during experiments (α_{geom}) for pressure taps and balance. Uncontrolled Cases, $Re_c = 1.5$Mio, tripped cases: $X_{\mathrm{tr}}/c = 10\%$, VACA4412s019 airfoil model. . . . 87

5.16 Comparison polar plot of measurement techniques balance, pressure taps, and wake rake. All wind-tunnel corrections applied (FS2D). Uncontrolled cases, tripping at $X_{\mathrm{tr}}/c = 10\%$, $Re_c = 1.5$Mio, VACA4412s019 airfoil model. 89
5.17 Comparison of tripped and untripped polar plots. Uncontrolled cases, $Re_c = 1.5$Mio, VACA4412s019 airfoil model. 90
5.18 Comparison of tripped and non-tripped: Pressure Distribution (left) and wake survey (right). Uncontrolled cases, $Re_c = 1.5$Mio, AoA $\alpha_{\mathrm{geom}} = 4°$, VACA4412s019 airfoil model. 91
5.19 Pressure Distribution (left) and fitted wake survey results (right) for controlled (solid lines) and uncontrolled cases (dashed). $Re_c = 1.5$Mio, control rate $c_q = 0.5\%$ chambers 1 through 7, VACA4412s019 airfoil model. Grey areas show the X location of the BLC chambers. 92
5.20 Drag change $\Delta c_d = c_{d,\mathrm{controlled}} - c_{d,\mathrm{uncontrolled}}$ for body drag (left) and inclusive drag (right) over airfoil lift. $Re_c = 1.5$Mio, tripping at $X_{\mathrm{tr}}/c = 10\%$, $c_q = 0.5\%$, AoA $\alpha_{\mathrm{geom}} = [-9°, 12°]$ 93
5.21 Pressure Distribution (left) and wake survey fit (right) for increasing control intensity $c_q = [0, 0.9]\%$. $Re_c = 650000$, tripping at $X_{\mathrm{tr}}/c = 10\%$, $\alpha_{\mathrm{geom}} = 4° \equiv \alpha_{\mathrm{aero}} \approx 1.1°$ 94
5.22 Comparison of drag change $\Delta c_d = c_{d,\mathrm{controlled}} - c_{d,\mathrm{uncontrolled}}$ for different airfoil chord Reynolds numbers Re_c and increasing control intensity. Tripping at $X_{\mathrm{tr}}/c = 10\%$, AoA $\alpha_{\mathrm{geom}} = 4°$ 95
5.23 Convergence Plot AoA -3 oder -9, balance and wake rake results for uncontrolled cases and cases with different individual control chambers (1 and 7) turned on separately. $Re_c = 1.5$Mio, tripping at $X_{\mathrm{tr}}/c = 10\%$, $c_q = 0.5\%$, AoA $\alpha_{\mathrm{geom}} = -9°$. . . 96
5.24 Comparison of drag change $\Delta c_d = c_{d,\mathrm{controlled}} - c_{d,\mathrm{uncontrolled}}$ for changing of which control area of the model is operated. This involves operating the same control schemes in different static pressures $\overline{c_{p,\mathrm{BLC}}}$. Red curve for zero overall lift ($\alpha_{\mathrm{geom}} = -3° \equiv c_l \approx 0$), blue curve for negative lift ($\alpha_{\mathrm{geom}} = -9° \equiv c_l < 0$). $Re_c = 1.5$Mio, tripping at $X_{\mathrm{tr}}/c = 10\%$, $c_q = 0.5\%$ 97
5.25 Drag change $\Delta c_d = c_{d,\mathrm{controlled}} - c_{d,\mathrm{uncontrolled}}$ for body drag and inclusive drag (right) over the average static pressure $\overline{c_{p,\mathrm{BLC}}}$ within the active control region (chamber 1 through 7). Individual datapoints are created by varying AoA $\alpha_{\mathrm{geom}} = [-9°, 12°]$. $Re_c = 1.5$Mio, tripping at $X_{\mathrm{tr}}/c = 10\%$, $c_q = 0.5\%$. 97
5.26 Hypothetical comparison of exhausting the BLC fluid at collection pressure ($c_p = 1$) through a nozzle (identity, momentum, and energy balance remain unaltered to the uncontrolled case: Option B) vs. using the BLC fluid to operate blowing control (Option A). 98
5.27 Drag change $\Delta c_d = c_{d,\mathrm{controlled}} - c_{d,\mathrm{uncontrolled}}$ for body drag (solid lines) and inclusive drag (dotted lines). Trendlines extrapolated for $\overline{c_{p,\mathrm{BLC}}} \to 1$. Data from previous figures is indicated in the respective title. $c_q = 0.5\%$ 99
5.28 Dimensionless pressure loss plotted over the Reynolds number formed with the hole bulk velocity (left) and over the dimensionless blowing ratio (right). Based on data with $Re_c = 6.5 \cdot 10^5$, AoA $\alpha_{\mathrm{geom}} = 4°$. 102
5.29 Development of flow resistance over measurement campaign for $Re_{\mathrm{hole}} \in [6, 7]$ which is equivalent to the most common investigated blowing rate $c_q = 0.5\%$ at $Re_c = 1.5$Mio. 103
5.30 Quantitative Light Sheet (QLS) result (410 A-Frames in red, 410 B-Frames in green) with unseeded blowing. Logarithmic brightness scaling: plotted brightness is calculated $g_{\mathrm{plot}} = 255 \cdot \ln(g_{\mathrm{rec}}) / \ln(g_{\max})$ with recorded grey value g_{rec} and a maximum displayed grey value of $g_{\max} = 600$. AoA $\alpha_{\mathrm{geom}} = 10°$, $\alpha_{\mathrm{aero}} = 4.7°$, pressure gradient within the controlled region $\frac{\partial c_p}{\partial x} \approx -0.15 \frac{1}{\mathrm{m}}$, $Re_c = 650000$, $c_q = 1\%$ (chamber 6 and 7 only), absolute wall-normal blowing velocity $v_{\mathrm{BLC}} = 13.8 \frac{\mathrm{cm}}{\mathrm{s}}$, wind tunnel speed $U_\infty = 13.8 \frac{\mathrm{m}}{\mathrm{s}}$ 104

5.31 Boundary layer velocity profile and boundary layer layer thickness development of an uncontrolled boundary layer flow. AoA $\alpha_{\text{geom}} = 4°$, $\alpha_{\text{aero}} = 1.09°$, $Re_c = 1.5$Mio, wind tunnel speed $U_\infty = 31.8\frac{\text{m}}{\text{s}}$ 105
5.32 Time-averaged wall-parallel velocity u normalized by wind tunnel velocity U_∞ displayed by lines and markers. Opaque fields show the uncertainty indicator $1 - n_{\text{avg.}}/n_{\text{tot}}$ of the average as a function of wall distance as described in section 5.2.7. The colors of the opaque fields correspond to the case colors. The greyish areas are made up of overlapping opaque fields. AoA $\alpha_{\text{geom}} = 4°$, $\alpha_{\text{aero}} = 1.09°$, $Re_c = 1.5$Mio, absolute wall-normal blowing velocity $v_{\text{BLC}} = 15.9\frac{\text{cm}}{\text{s}}$, wind tunnel speed $U_\infty = 31.8\frac{\text{m}}{\text{s}}$ 106
5.33 Development of boundary layer thicknesses and shape parameter H_{12}. AoA $\alpha_{\text{geom}} = 4°$, $\alpha_{\text{aero}} = 1.09°$, $Re_c = 1.5$Mio, absolute wall-normal blowing velocity $v_{\text{BLC}} = 15.9\frac{\text{cm}}{\text{s}}$, wind tunnel speed $U_\infty = 31.8\frac{\text{m}}{\text{s}}$ 107
5.34 Dimensionless wall shear stress $c_{f,\infty}$ calculated from the Nickels fit function [85] and dimensionless inclusive wall shear stress $c_{f,\text{inc}} = c_{f,\infty} + c_{f,\text{BLC}}$ with $c_{f,\text{BLC}}$ from equation 3.25. AoA $\alpha_{\text{geom}} = 4°$, $\alpha_{\text{aero}} = 1.09°$, $Re_c = 1.5$Mio, absolute wall-normal blowing velocity $v_{\text{BLC}} = 15.9\frac{\text{cm}}{\text{s}}$, wind tunnel speed $U_\infty = 31.8\frac{\text{m}}{\text{s}}$ 108

C.1 Model Drawing VACA4412s019 Page 1, Revision A 160
C.2 Model Drawing VACA4412s019 Page 2, Revision A 161
C.3 Model Drawing VACA4412s019 BLC Positions 162
C.4 Model Drawing VACA4412s019 BLC Surface Sheet, Revision C 163

D.1 Final airfoil test rig configuration for VACA4412s019 BLC experiments with PIV, pressure taps, balance, and wake measurements depicted. 173
D.2 Relevant distances of test rig during VACA4412s019 experimental campaign 174
D.3 Wake Rake Final Drawing with 3 probing rows. From top to bottom: 2 angled tubes for yaw measurement (not connected in the present campaign), 81 total pressure pitot tubes, and 7 static probes 175
D.4 Wake Rake in its final setup at the wing test stand inside the test section 175
D.5 Polar plot of the HGR-01 airfoil model, 2D freestream corrected form (FS2D). Date of recording: Aug. 16, 2022. No tripping, $Re_c \in [4.6 \cdot 10^5, 5 \cdot 10^5]$, about nominal zero flap deflection position. 176

List of Tables

2.1 Elementary solutions for 2D potential flow cases within the x_1, x_2-plane 9
2.2 Boundary conditions of closed jet and open jet and corresponding representations for the potential theory "approach of the images". 19
2.3 Upwash δ_0 and curvature parameter δ_1 of closed jet and open jet and corresponding representations for the potential theory "approach of the images". . . . 20

4.1 OpenFOAM boundary conditions in their incompressible form including applicable Dirichlet values. All values are given relative to the freestream velocity U_∞ and chord length c. Adapted from [FSF+21, Table 1], note that all quantities are given as kinematic quantities (meaning *e.g.* pressure quantities are expressed as pressure divided by the density). 41
4.2 Parameter variations for numerical investigations 46

5.1 Re_c and blockage ratio for different combinations of angle of attack α and chord length c. Brown entries mark the operating point of the HGR-01 validation campaign. Blue entries mark possible operating points of the VACA4412s019 campaign. 65
5.2 Absolute random sensor error ($\mathcal{E}_{r,s}$) and random sensor error relative to the respective sensor range ($\epsilon_{r,s,\mathrm{FS}}$) for the assignment of KDs40 sensors as it was used for the VACA4412s019 campaign 68
5.3 Sensor Accuracy of pressure taps as applied on the VACA4412s019 model for the present measurement campaign using the MPS 4264 Sensors from Scanicalve [201] . . 69
5.4 Devices for 2D-2C PIV measurements in wall-normal plane of the turbulent boundary layer at the wing profile 74
5.5 Data Acquisition (DAQ) properties of all recorded quantities 79
5.6 Parameter variations for experimental investigations 80

C.1 Coordinates of the airfoils conceived in the present study 156
C.2 Pressure Taps VACA4412s019 airfoil model 158
C.3 BLC chamber pressure taps and BLC chamber positions of VACA4412s019 airfoil model 159

A Appendix: Facility Manuals

Several devices and facilities were developed alongside the studies for the present PhD Thesis. In part, this supported the goals of the present thesis. However, the improvements, renovation and additions are also supposed to ensure continued operations of the "Göttinger Windkanal am ISTM" in the future. The following documents contain relevant data for maintenance, scientific reference, lessons learned and best practices as well as documentation of newly added features and devices.

A.1 G-Tunnel Manual

This document [Fah24b] contains information about the wind-tunnel as a complete system:

- Operating instructions
- Safety information
- Reference measurements of wind-tunnel characteristics
- Information on Data Acquisition Systems
- Sensor wiring information
- Properties of existing test stands
- Collection of technical drawings and circuit diagrams of the following subs-systems. This shall enable remodeling or reproducing parts for maintenance and future development. Also, it may be helpful for trouble shooting.
  - Tunnel Layout and test section enclosure
  - Air-bearing Loadcell
  - Wake Rake
  - Airfoil Test Rig

A.2 Technische Dokumentation des Traversen Systems am Göttinger Windkanal am ISTM

This document [Fah24a] contains information about the largest subsystem of the Göttinger Windtunnel: The probe positioning system, also called "Traverse Sysystem"

- Operating instructions
- Safety information

- Licensing information (CE-certificate) and corresponding documentation
- Technical drawings
- Electric circuit diagrams

Reference to Manuals

[Fah24a] G. Fahland. Technische Dokumentation des Traversen Systems am Göttinger Windkanal am ISTM. User Manual V1.2.0, Institute of Fluid Mechanics (ISTM), Karlsruhe Institute of Technology, Karlsruhe, Germany, 2024.

[Fah24b] G. Fahland. User Manual for the Göttinger Windtunnel at ISTM. User Manual V1.3.0.eng, Institute of Fluid Mechanics (ISTM), Karlsruhe Institute of Technology, Karlsruhe, Germany, 2024. doi.org/10.5445/IR/1000162981.

B Appendix: Student Contributions

In total, 14 students contributed to either the facility improvement or certain parts of the airfoil investigations. This chapter covers an acknowledgement of how the respective contribution impacted the present manuscript.

B.1 Investigation of requirements for a traverse system for the Göttinger wind tunnel of the ISTM and the resulting influence on flow measurements

Bachelor Thesis by Edward Volz [Vol20]

This thesis provided the necessary information to design a traverse system for the present Göttinger Wind Tunnel at ISTM. This included the influence structural elements have on the flow within the test section (see also [Fah24b]) as well as ideas on general design aspects such as mounting locations and their respective drawbacks and benefits.

B.2 Development and commissioning of a scale model of the ISTM closed circuit wind tunnel

Bachelor Thesis by David Achzehnter [Ach21]

This thesis paved the way for investigations of wind tunnel fluctuations and subsequent success of both methodical aspects as well as flow quality improvement. Furthermore, it showcased the possibility of fast iterations of improvement measures by filament deposit 3D printing. The structural basis of this scale model tunnel allowed for all subsequent work ([Els22, Wic22, Kau22, Ruf23]) to rely on the interfaces defined by it and the accordance of the scale model tunnel with the full scale tunnel proved to be accurate.

B.3 Development and validation of a simulation of the flow in the scale model of the Göttinger wind tunnel

Bachelor Thesis by Michael Willmann [Wil21]

This work allowed for visualization of the flow within the wind tunnel. It helped in understanding the flow topology yet it also proved that it is impractical to investigate the complex problem of wind-tunnel fluctuations with numerical methods with nowadays computing power.

B.4 Testing of optimisation measures on the scale model of the closed return wind tunnel at ISTM

Bachelor Thesis by Ferdinand Elsner [Els22]

In this thesis the methodology of analyzing wind-tunnel fluctuations by means of Spectral Proper Orthogonal Decomposition (SPOD) was employed the first time. It showed that the phase distribution along the tunnel axis allowed for clear identification of both acoustic resonance and convective modes. Also, the separation of the fluctuation energy in modes allowed to find regions of spectra where single modes dominated the fluctuation patterns which proved to be a method to treat data with much random noise.

B.5 Testing of improvement measures at the nozzle outlet of the Göttinger wind tunnel at ISTM

Bachelor Thesis by Frederic Kauffmann [Kau22]

This study tested different improvement measures which confirmed the understanding of the edgetone feedback mechanism as well as the cases in which to employ certain features at the nozzle in order to reduce fluctuations. The 3D elements developed in this thesis are deemed to work for the full scale tunnel as well but are yet to be tested in a suitable measurement task at the full scale tunnel.

B.6 Investigation of collector improvement measures at the scale model of the Göttinger Wind Tunnel at ISTM

Bachelor Thesis by Michael Wickberg [Wic22]

In this thesis the influence of the length of the test section was investigated. It could be shown that for the present wind-tunnel it is beneficial to aim for a shorter-than-current test section. Also, the option of a teeth-collector design was tested. No superior collector design was found. However, the trends of which measures have prospect of success became clear: Test section length should be around 3 to 3.5 hydraulic nozzle diameters and the collector inlet plane should be broken apart to show swept leading edges to the incoming flow.

B.7 Testing of two new collectors with breather gap to improve the flow at the closed-circuit wind tunnel at ISTM

Bachelor Thesis by Johannes Rufer [Ruf23]

Based on the conclusions of Wickberg [Wic22], in this thesis a collector design far superior to the current collector was tested and found. Also, a very thorough analysis showcased opportunities how to reduce the streamwise pressure gradient inside the test section simultaneously. This collector design should be implemented in the full scale tunnel if no further improvements are developed.

B.8 Development and Validation of a distributed Measurement System for a Modal Analysis of the Göttinger Windkanal

Master Thesis by Kai Weber [Web22]

This work showed the accordance of full scale tunnel and scale model tunnel. It enabled this by conceiving a simple yet powerful measurement system. It could also be shown that the mode identification by SPOD was even better than for the small scale tunnel. Additionally, a formal criterion for edge tone feedback identification was first tested in this thesis. Building on this thesis an enhanced variant of this criterion was developed which became part of the mutual presentation at AIAA Aviation in San Diego 2023 [FEW+23].

B.9 Design and measurement of a Helmholtz resonator for the Göttingen wind tunnel at ISTM

Master Thesis by Paul Gueib [Gue23]

This work built on the hardware and understanding of [Web22]. In the course of this work the first improvement measure was installed at the full scale wind-tunnel and proved to be extremely effective. This also influenced the measurements of the present PhD Thesis as the tunnel fluctuations after the installation of one of the Helmholtz Resonators were more than cut in half.

B.10 Aufbau und Verifikation von RANS-Simulationen für Flügelprofile mit turbulenter Grenzschichtkontrolle in kompressibler Strömung

Bachelor Thesis by Lucas C.V. Alencar [Ale20]

In this thesis it was tried to simulate compressible airfoil flows with OpenFOAM.

B.11 Effects of active flow controls on different airfoils with focus on laminar airfoils

Bachelor Thesis by Erik Techen [Tec21]

Based on the conclusions of this thesis a study was conducted to investigate possible combinations of laminar and turbulent flow control. No definitely beneficial configuration was found in the subsequent study of which the results were presented in [Fah21] despite the insight from this Bachelor's Thesis during design of the presented study. Nevertheless, further studies in this direction are of interest due to the conclusions that uniform blowing is very likely not an advantageous stand-alone drag reduction scheme (section 6).

B.12 Numerical parametric analysis for flow separation on aerofoils induced by active flow control

Bachelor Thesis by Philipp Bonfert [Bon21]

This work gave a broad overview and detailed results on how to implement a control augmentation of an aircraft based on uniform blowing on airfoils. It can therefore be regarded as an example of what future research should focus on given the fact that uniform blowing as a stand-alone control scheme does not provide net drag reduction potential as concluded in section 6.

B.13 Numerical Research of Wind Tunnel Wall Corrections for Boundary Layer Control Experiments

Master Thesis by David Kaiser [Kai22]

In this contribution a multitude of wind-tunnel corrections and their effectiveness was investigated numerically for the present test rig and model design. This provided valuable insight in which correction methods to focus on for the processing of the actual experimental data. This enabled a thorough treatment of the tunnel corrections shown in this PhD thesis, namely: Lift correction, end-plate friction correction and horizontal buoyancy correction (section 5.3). Other corrections, *e.g.* due to influence by the boundary layer control and non-uniform lift distribution were neglected for the treatment of experimental data because this master thesis provided the information that this is negligible.

B.14 Measurement of Turbulent Boundary Layers via PIV

Master Thesis by Dominik Wöllstein [Wö23]

The experiments of this master's thesis were conducted jointly with the author of the present PhD thesis. In this master thesis the focus was put on the technical aspect of the measurements: How is the data to be processed and what accuracy of boundary layer velocity measurements is to be reached? Based on these information, the PIV results shown in the present PhD thesis were generated and interpreted by the author of the PhD thesis.

Reference to Student Contributions

[Ach21] D. Achzehnter. *Development and commissioning of a scale model of the ISTM closed circuit wind tunnel.* Bachelor Thesis, Karlsruhe Institute of Technology, Karlsruhe, Germany, 2021.

[Ale20] L. C. V. Alencar. *Aufbau und Verifikation von RANS-Simulationen für Flügelprofile mit turbulenter Grenzschichtkontrolle in kompressibler Strömung.* Bachelor Thesis, Karlsruhe Institute of Technology, Karlsruhe, Germany, 2020.

[Bon21] P. Bonfert. *Numerical parametric analysis for flow separation on aerofoils induced by active flow control.* Bachelor Thesis, Karlsruhe Institute of Technology, Karlsruhe, Germany, 2021.

[Els22] F. Elsner. *Testing of optimisation measures on the scale model of the closed return wind tunnel at ISTM.* Bachelor Thesis, Karlsruhe Institute of Technology, Karlsruhe, Germany, 2022.

[Fah19] G. Fahland. Flow Control for Turbulent Skin-friction drag reduction on airfoils. Master's thesis, Karlsruhe Institute of Technology, Karlsruhe, Germany, 2019.

[Gue23] P. Gueib. *Design and measurement of a Helmholtz resonator for the Göttingen wind tunnel at ISTM.* {Master Thesis}, Karlsruhe Institute of Technology, Karlsruhe, Germany, 2023.

[Kai22] D. Kaiser. Numerical Research of Wind Tunnel Wall Corrections for Boundary Layer Control Experiments. Master's thesis, Karlsruhe Institute of Technology, Karlsruhe, Germany, 2022.

[Kau22] F. J. Kauffmann. *Testing of improvement measures at the nozzle outlet of the Göttinger wind tunnel at ISTM.* Bachelor Thesis, Karlsruhe Institute of Technology, Karlsruhe, Germany, 2022.

[Ruf23] J. Rufer. *Testing of two new collectors with breather gap to improve the flow at the closed-circuit wind tunnel at ISTM.* Bachelor Thesis, Karlsruhe Institute of Technology, Karlsruhe, Germany, 2023.

[Sch20] F. Schmitt. Simulationsergebnisse der Schallabsorption zur Sicherung besprochener Entwurfskonzepte für den Windkanalausbau. Internal Report 1, Karlsruhe Institute of Technology, Karlsruhe, Germany, 2020.

[Tec21] E. Techen. *Effects of active flow controls on different airfoils with focus on laminar airfoils.* Bachelor Thesis, Karlsruhe Institute of Technology, Karlsruhe, Germany, 2021.

[Vol20] E. Volz. *Investigation of requirements for a traverse system for the Göttinger wind tunnel of the ISTM and the resulting influence on flow measurements.* Bachelor Thesis, Karlsruhe Institute of Technology, Karlsruhe, Germany, 2020.

[Web22] K. Weber. *Development and Validation of a distributed Measurement System for a Modal Analysis of the Göttinger Windkanal.* {Master Thesis}, Karlsruhe Institute of Technology, Karlsruhe, Germany, 2022.

[Wic22] M Wickberg. *Investigation of collector improvement measures at the scale model of the Göttinger wind tunnel at ISTM.* Bachelor Thesis, Karlsruhe Institute of Technology, Karlsruhe, Germany, 2022.

[Wil21] M. Willmann. *Development and validation of a simulation of the flow in the scale model of the Göttinger wind tunnel.* Bachelor Thesis, Karlsruhe Institute of Technology, Karlsruhe, Germany, 2021.

[Wö23] D. Wöllstein. *Measurement of Turbulent Boundary Layers via PIV.* {Master Thesis}, Karlsruhe Institute of Technology, Karlsruhe, Germany, 2023.

C Appendix: Airfoil Specifications

GFMPG002		GFAPG006		VACA4412s019	
$X'[X/c]$	$Y'[Y/c]$	$X'[X/c]$	$Y'[Y/c]$	$X'[X/c]$	$Y'[Y/c]$
1.000000	0.001260	1.000000	0.001260	1.000000	0.000685
0.991107	0.003678	0.991177	0.003659	0.993933	0.002341
0.979599	0.006761	0.979339	0.006830	0.983352	0.005196
0.966713	0.010152	0.965925	0.010357	0.971014	0.008469
0.952507	0.013816	0.951326	0.014117	0.957216	0.012059
0.937146	0.017692	0.935970	0.017985	0.942407	0.015832
0.920854	0.021705	0.920178	0.021870	0.927000	0.019670
0.903868	0.025785	0.904149	0.025719	0.911266	0.023498
0.886390	0.029872	0.887988	0.029503	0.895355	0.027275
0.868579	0.033923	0.871752	0.033210	0.879348	0.030982
0.850544	0.037907	0.855469	0.036831	0.863287	0.034608
0.832359	0.041807	0.839152	0.040364	0.847186	0.038150
0.814069	0.045609	0.822809	0.043807	0.831061	0.041603
0.795701	0.049308	0.806443	0.047160	0.814909	0.044969
0.777269	0.052900	0.790056	0.050421	0.798742	0.048246
0.758772	0.056382	0.773647	0.053592	0.782552	0.051432
0.740207	0.059757	0.757210	0.056671	0.766351	0.054530
0.721526	0.063023	0.740743	0.059662	0.750136	0.057536
0.702703	0.066237	0.724209	0.062561	0.733909	0.060451
0.683937	0.069383	0.707549	0.065413	0.717669	0.063273
0.665253	0.072411	0.690903	0.068227	0.701420	0.066002
0.646659	0.075313	0.674313	0.070956	0.685161	0.068638
0.628148	0.078081	0.657761	0.073595	0.668900	0.071178
0.609719	0.080709	0.641242	0.076136	0.652632	0.073621
0.591373	0.083192	0.624750	0.078575	0.636362	0.075966
0.573113	0.085524	0.608282	0.080908	0.620088	0.078212
0.554946	0.087700	0.591836	0.083131	0.603815	0.080356
0.536883	0.089714	0.575413	0.085238	0.587542	0.082398
0.518941	0.091556	0.559014	0.087226	0.571273	0.084335
0.501138	0.093221	0.542642	0.089088	0.555009	0.086166
0.483499	0.094681	0.526303	0.090820	0.538753	0.087887
0.465953	0.095925	0.510002	0.092413	0.522506	0.089498
0.448482	0.096959	0.493741	0.093859	0.506271	0.090995
0.431065	0.097781	0.477513	0.095128	0.490052	0.092374
0.413686	0.098389	0.461314	0.096220	0.473849	0.093635
0.396329	0.098783	0.445144	0.097133	0.457672	0.094774
0.378984	0.098966	0.429002	0.097865	0.441530	0.095787
0.361650	0.098938	0.412890	0.098412	0.425446	0.096669
0.344333	0.098703	0.396810	0.098775	0.409446	0.097419
0.327048	0.098264	0.380766	0.098957	0.393618	0.098025
0.309820	0.097622	0.364761	0.098958	0.377967	0.098435

GFMPG002		GFAPG006		VACA4412s019	
$X'[X/c]$	$Y'[Y/c]$	$X'[X/c]$	$Y'[Y/c]$	$X'[X/c]$	$Y'[Y/c]$
0.292678	0.096778	0.348801	0.098784	0.362418	0.098643
0.275665	0.095735	0.332890	0.098435	0.346941	0.098644
0.258830	0.094494	0.317036	0.097916	0.331525	0.098437
0.242228	0.093057	0.301246	0.097225	0.316163	0.098019
0.225927	0.091425	0.285527	0.096365	0.300862	0.097387
0.209999	0.089602	0.269887	0.095333	0.285624	0.096536
0.194521	0.087594	0.254335	0.094127	0.270457	0.095463
0.179573	0.085407	0.238881	0.092740	0.255368	0.094164
0.165236	0.083053	0.223535	0.091166	0.240368	0.092634
0.151583	0.080549	0.208311	0.089395	0.225466	0.090870
0.138677	0.077913	0.193225	0.087414	0.210675	0.088868
0.126565	0.075166	0.178294	0.085207	0.196015	0.086624
0.115274	0.072334	0.163569	0.082762	0.181499	0.084135
0.104812	0.069439	0.149077	0.080059	0.167153	0.081399
0.095167	0.066504	0.134824	0.077070	0.153012	0.078415
0.086309	0.063549	0.120902	0.073781	0.139113	0.075184
0.078198	0.060589	0.107411	0.070184	0.125515	0.071714
0.070784	0.057635	0.094482	0.066285	0.112290	0.068017
0.064013	0.054692	0.082267	0.062107	0.099536	0.064122
0.057833	0.051762	0.070937	0.057699	0.087389	0.060073
0.052189	0.048847	0.060655	0.053131	0.075995	0.055929
0.047032	0.045953	0.051542	0.048497	0.065508	0.051774
0.042315	0.043085	0.043636	0.043911	0.056050	0.047696
0.037998	0.040251	0.036884	0.039483	0.047683	0.043774
0.034048	0.037455	0.031178	0.035283	0.040389	0.040062
0.030432	0.034697	0.026385	0.031338	0.034092	0.036584
0.027125	0.031977	0.022375	0.027651	0.028675	0.033341
0.024105	0.029292	0.019024	0.024211	0.024017	0.030317
0.021351	0.026640	0.016228	0.021004	0.020003	0.027488
0.018846	0.024017	0.013900	0.018016	0.016532	0.024827
0.016576	0.021423	0.011967	0.015234	0.013525	0.022308
0.014528	0.018855	0.010370	0.012648	0.010916	0.019908
0.012690	0.016312	0.009060	0.010251	0.008652	0.017607
0.011054	0.013794	0.008000	0.008044	0.006696	0.015385
0.009614	0.011300	0.007160	0.006039	0.005017	0.013229
0.008362	0.008832	0.006508	0.004239	0.003598	0.011125
0.007298	0.006388	0.006012	0.002640	0.002423	0.009067
0.006419	0.003971	0.005639	0.001225	0.001485	0.007047
0.005728	0.001582	0.005363	-0.000030	0.000778	0.005068
0.005222	-0.000773	0.005158	-0.001143	0.000301	0.003131
0.004887	-0.003087	0.004993	-0.002235	0.000049	0.001247
0.004667	-0.005348	0.004868	-0.003255	0.000011	-0.000583
0.004531	-0.007550	0.004743	-0.004490	0.000193	-0.002423
0.004531	-0.009707	0.004545	-0.007214	0.000626	-0.004286
0.004701	-0.011856	0.004535	-0.009810	0.001335	-0.006139
0.005072	-0.014008	0.004702	-0.011866	0.002328	-0.007953
0.005708	-0.016131	0.005096	-0.014118	0.003607	-0.009702
0.006806	-0.018093	0.005877	-0.016518	0.005163	-0.011375
0.008321	-0.019855	0.007304	-0.018785	0.006992	-0.012966
0.010089	-0.021416	0.009084	-0.020955	0.009093	-0.014478

GFMPG002		GFAPG006		VACA4412s019	
$X'[X/c]$	$Y'[Y/c]$	$X'[X/c]$	$Y'[Y/c]$	$X'[X/c]$	$Y'[Y/c]$
0.012075	-0.022795	0.011361	-0.023003	0.011476	-0.015919
0.014240	-0.023991	0.014103	-0.024833	0.014159	-0.017296
0.016595	-0.025028	0.017255	-0.026462	0.017176	-0.018616
0.019188	-0.025938	0.020818	-0.027976	0.020570	-0.019886
0.021978	-0.026727	0.024807	-0.029427	0.024402	-0.021114
0.024977	-0.027432	0.029287	-0.030842	0.028751	-0.022302
0.028203	-0.028089	0.034348	-0.032233	0.033717	-0.023449
0.031676	-0.028725	0.040101	-0.033598	0.039427	-0.024555
0.035410	-0.029353	0.046691	-0.034929	0.046035	-0.025607
0.039415	-0.029983	0.054298	-0.036207	0.053711	-0.026590
0.043713	-0.030623	0.063120	-0.037401	0.062611	-0.027477
0.048342	-0.031283	0.073321	-0.038474	0.072839	-0.028233
0.053353	-0.031972	0.084956	-0.039389	0.084415	-0.028822
0.058808	-0.032700	0.097933	-0.040128	0.097245	-0.029215
0.064785	-0.033478	0.112032	-0.040680	0.111145	-0.029406
0.071377	-0.034318	0.126974	-0.041045	0.125892	-0.029399
0.078696	-0.035233	0.142499	-0.041232	0.141287	-0.029217
0.086867	-0.036239	0.158407	-0.041261	0.157161	-0.028890
0.096021	-0.037348	0.174559	-0.041149	0.173376	-0.028445
0.106277	-0.038575	0.190867	-0.040916	0.189838	-0.027904
0.117735	-0.039928	0.207278	-0.040579	0.206477	-0.027286
0.130453	-0.041417	0.223760	-0.040149	0.223260	-0.026605
0.144428	-0.043042	0.240300	-0.039640	0.240153	-0.025877
0.159583	-0.044801	0.256892	-0.039060	0.257131	-0.025114
0.175783	-0.046691	0.273534	-0.038417	0.274179	-0.024324
0.192863	-0.048707	0.290221	-0.037719	0.291278	-0.023513
0.210657	-0.050848	0.306946	-0.036971	0.308418	-0.022692
0.229014	-0.053112	0.323697	-0.036179	0.325585	-0.021862
0.247811	-0.055493	0.340457	-0.035348	0.342769	-0.021029
0.266947	-0.057975	0.357202	-0.034484	0.359960	-0.020196
0.286348	-0.060537	0.373899	-0.033593	0.377149	-0.019364
0.305955	-0.063151	0.390495	-0.032680	0.394325	-0.018539
0.325727	-0.065790	0.406949	-0.031752	0.411492	-0.017720
0.345634	-0.068421	0.423136	-0.030818	0.428652	-0.016910
0.365655	-0.071011	0.439579	-0.029852	0.445802	-0.016109
0.385773	-0.073525	0.456402	-0.028847	0.462943	-0.015319
0.405977	-0.075926	0.473380	-0.027818	0.480080	-0.014541
0.426255	-0.078175	0.490470	-0.026768	0.497208	-0.013775
0.446599	-0.080230	0.507615	-0.025704	0.514332	-0.013023
0.466997	-0.082049	0.524797	-0.024629	0.531448	-0.012285
0.487439	-0.083586	0.542005	-0.023545	0.548558	-0.011562
0.507910	-0.084793	0.559234	-0.022454	0.565663	-0.010855
0.528387	-0.085619	0.576481	-0.021358	0.582764	-0.010165
0.548849	-0.086008	0.593745	-0.020260	0.599856	-0.009492
0.569284	-0.085891	0.611023	-0.019161	0.616944	-0.008838
0.589692	-0.085162	0.628313	-0.018063	0.634028	-0.008202
0.610066	-0.083643	0.645611	-0.016970	0.651105	-0.007585
0.630391	-0.081286	0.662909	-0.015883	0.668175	-0.006990
0.650684	-0.078286	0.680198	-0.014806	0.685238	-0.006416
0.670950	-0.074772	0.697472	-0.013741	0.702296	-0.005864

GFMPG002		GFAPG006		VACA4412s019	
$X'[X/c]$	$Y'[Y/c]$	$X'[X/c]$	$Y'[Y/c]$	$X'[X/c]$	$Y'[Y/c]$
0.691168	-0.070828	0.714729	-0.012692	0.719344	-0.005336
0.711301	-0.066526	0.731966	-0.011661	0.736387	-0.004833
0.731323	-0.061930	0.749178	-0.010652	0.753416	-0.004355
0.751220	-0.057095	0.766363	-0.009668	0.770441	-0.003904
0.770982	-0.052077	0.783517	-0.008713	0.787453	-0.003481
0.790593	-0.046934	0.800633	-0.007792	0.804455	-0.003088
0.810030	-0.041723	0.817707	-0.006910	0.821447	-0.002726
0.829251	-0.036511	0.834729	-0.006071	0.838430	-0.002397
0.848182	-0.031376	0.851689	-0.005281	0.855400	-0.002101
0.866725	-0.026402	0.868570	-0.004548	0.872358	-0.001839
0.884798	-0.021669	0.885349	-0.003877	0.889297	-0.001611
0.902348	-0.017244	0.901987	-0.003277	0.906179	-0.001413
0.919331	-0.013183	0.918421	-0.002754	0.922922	-0.001243
0.935672	-0.009554	0.934539	-0.002313	0.939341	-0.001096
0.951226	-0.006448	0.950168	-0.001955	0.955105	-0.000969
0.965731	-0.003984	0.965003	-0.001686	0.969702	-0.000866
0.978982	-0.002274	0.978716	-0.001504	0.982658	-0.000803
0.990816	-0.001364	0.990886	-0.001328	0.993700	-0.000734
1.000000	-0.001260	1.000000	-0.001260	1.000000	-0.000685

Table C.1: Coordinates of the airfoils conceived in the present study

Pressure Line Name	$X[mm]$	$Y[mm]$	$X'[X/c]$	$Y'[Y/c]$
0.1	750	0.5	1.00000	0.00067
0.2	750	-0.5	1.00000	-0.00067
1	737.41	3.93	0.98321	0.00524
2	712.01	10.56	0.94935	0.01408
3	682.53	17.84	0.91004	0.02379
4	652.04	24.93	0.86939	0.03324
5	621.29	31.62	0.82839	0.04216
6	590.44	37.89	0.78725	0.05052
7	559.51	43.71	0.74601	0.05828
8	528.52	49.1	0.70469	0.06547
9 (defect)	497.49	54.02	0.66332	0.07203
10	466.44	58.47	0.62192	0.07796
11	435.38	62.44	0.58051	0.08325
12	404.35	65.89	0.53913	0.08785
13	373.36	68.8	0.49781	0.09173
14	342.46	71.13	0.45661	0.09484
15	311.76	72.86	0.41568	0.09715
16	281.68	73.86	0.37557	0.09848
17	252.14	73.89	0.33619	0.09852
18	222.89	72.9	0.29719	0.09720
19	193.96	70.85	0.25861	0.09447
20	165.45	67.68	0.22060	0.09024
21	137.52	63.35	0.18336	0.08447
22	110.42	57.83	0.14723	0.07711
23	84.65	51.14	0.11287	0.06819
24	61.23	43.52	0.08164	0.05803

Pressure Line Name	$X[mm]$	$Y[mm]$	$X'[X/c]$	$Y'[Y/c]$
25	41.84	35.68	0.05579	0.04757
26	27.55	28.56	0.03673	0.03808
27	17.71	22.53	0.02361	0.03004
28	10.94	17.42	0.01459	0.02323
29	6.23	12.93	0.00831	0.01724
30	3	8.81	0.00400	0.01175
31	0.97	4.93	0.00129	0.00657
32 (defect)	0.07	1.25	0.00009	0.00167
33	0	0	0.00000	0.00000
34	0.23	-2.26	0.00031	-0.00301
35	1.62	-5.77	0.00216	-0.00769
36	4.38	-9	0.00584	-0.01200
37	8.46	-11.86	0.01128	-0.01581
38	14.02	-14.41	0.01869	-0.01921
39	21.55	-16.72	0.02873	-0.02229
40	32.1	-18.84	0.04280	-0.02512
41	47.39	-20.65	0.06319	-0.02753
42	68.89	-21.81	0.09185	-0.02908
43	95.87	-22.04	0.12783	-0.02939
44	125.98	-21.45	0.16797	-0.02860
45	157.52	-20.36	0.21003	-0.02715
46	170.99	-19.8	0.22799	-0.02640
47	187.98	-19.06	0.25064	-0.02541
48	205.08	-18.27	0.27344	-0.02436
49	222.25	-17.45	0.29633	-0.02327
50	239.46	-16.63	0.31928	-0.02217
51 (defect)	256.71	-15.79	0.34228	-0.02105
52	273.96	-14.95	0.36528	-0.01993
53	291.21	-14.12	0.38828	-0.01883
54	308.44	-13.3	0.41125	-0.01773
55	325.66	-12.49	0.43421	-0.01665
56	342.87	-11.69	0.45716	-0.01559
57	360.07	-10.91	0.48009	-0.01455
58	377.26	-10.14	0.50301	-0.01352
59	394.45	-9.39	0.52593	-0.01252
60	411.62	-8.66	0.54883	-0.01155
61	428.79	-7.96	0.57172	-0.01061
62	445.95	-7.27	0.59460	-0.00969
63	463.1	-6.61	0.61747	-0.00881
64	480.25	-5.98	0.64033	-0.00797
65	497.38	-5.37	0.66317	-0.00716
66	514.51	-4.79	0.68601	-0.00639
67	531.63	-4.24	0.70884	-0.00565
68	548.74	-3.73	0.73165	-0.00497
69	565.83	-3.25	0.75444	-0.00433
70	582.91	-2.8	0.77721	-0.00373
71	599.98	-2.39	0.79997	-0.00319
72	617.04	-2.03	0.82272	-0.00271
73 (defect)	634.08	-1.7	0.84544	-0.00227
74	651.11	-1.43	0.86815	-0.00191
75	668.11	-1.19	0.89081	-0.00159

Pressure Line Name	$X[mm]$	$Y[mm]$	$X'[X/c]$	$Y'[Y/c]$
76	685.02	-1	0.91336	-0.00133
77	701.65	-0.85	0.93553	-0.00113
78	717.5	-0.72	0.95667	-0.00096
79	731.72	-0.63	0.97563	-0.00084
80	743.55	-0.56	0.99140	-0.00075

Table C.2: Pressure Taps VACA4412s019 airfoil model

pressure line, BLC chamber	$X_{\text{start}}[mm]$	$X_{\text{end}}[mm]$	$X'_{\text{start}}[X/c]$	$X'_{\text{end}}[X/c]$
81, BLC 1	270	319	0.3600	0.4253
82, BLC 2	321	369	0.4280	0.4920
83, BLC 3	371	419	0.4947	0.5587
84, BLC 4	421	469	0.5613	0.6253
85, BLC 5	471	519	0.6280	0.6920
86, BLC 6	521	569	0.6947	0.7587
87, BLC 7	571	619	0.7613	0.8253

Table C.3: BLC chamber pressure taps and BLC chamber positions of VACA4412s019 airfoil model

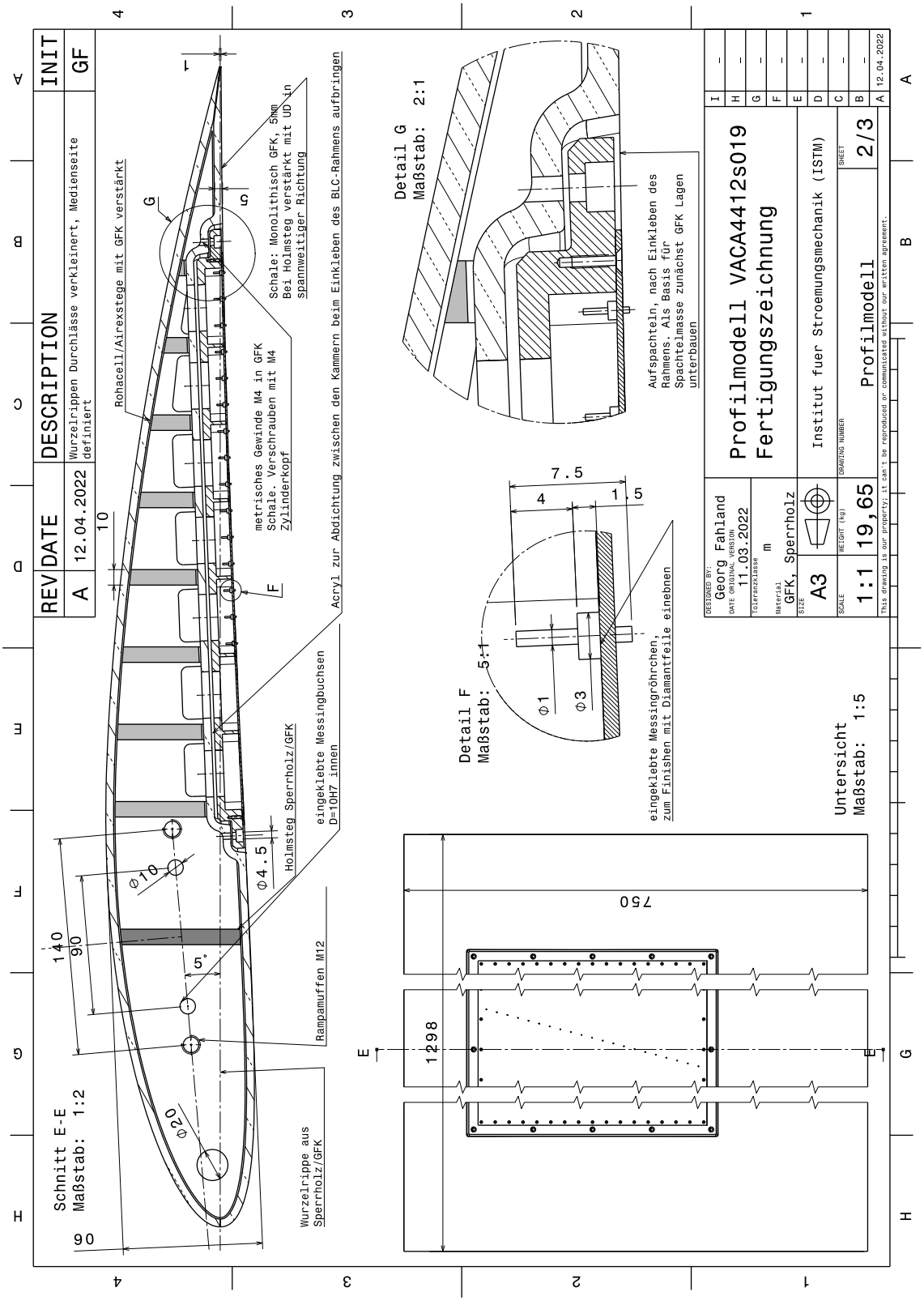

Figure C.1: Model Drawing VACA4412s019 Page 1, Revision A

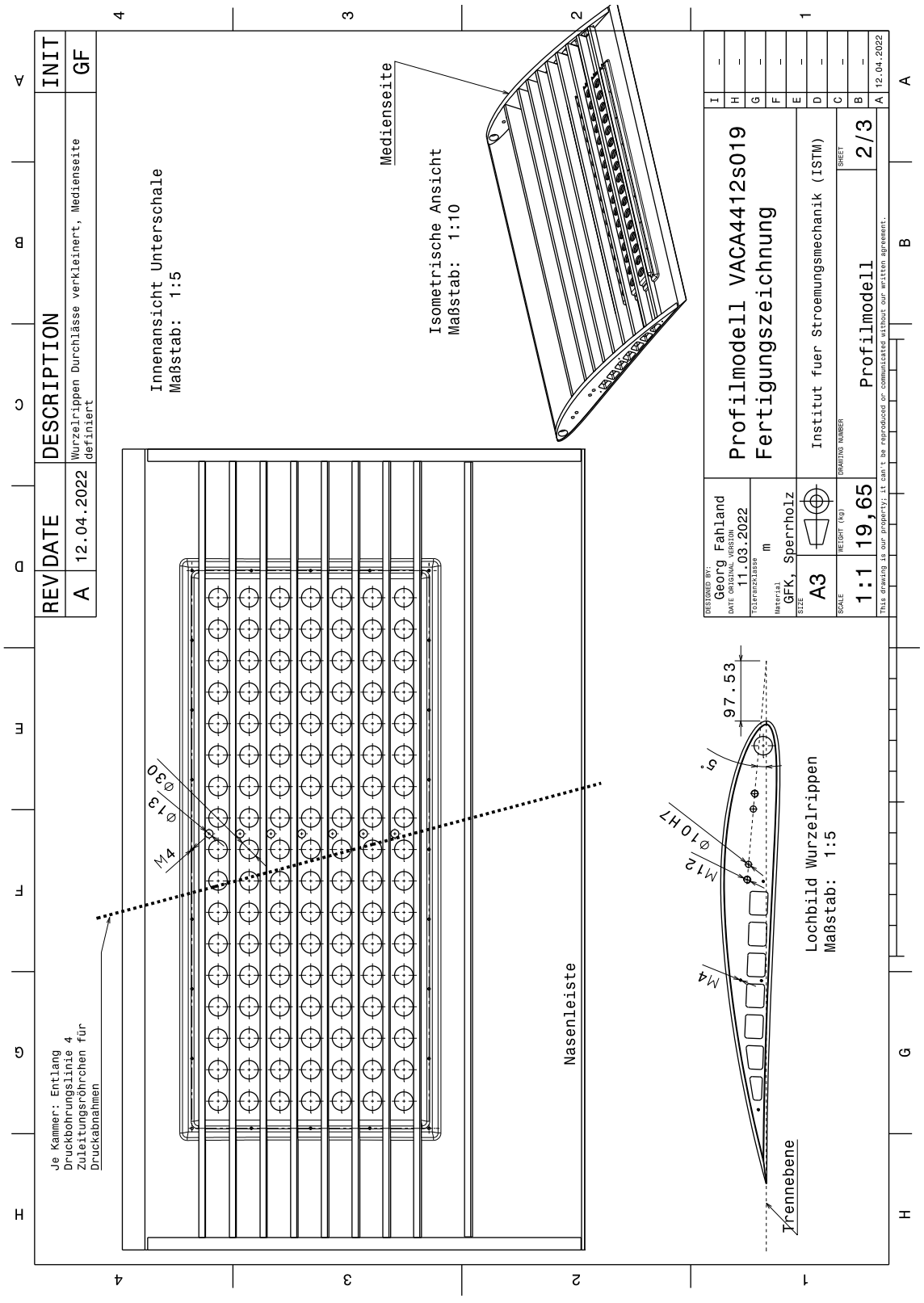

Figure C.2: Model Drawing VACA4412s019 Page 2, Revision A

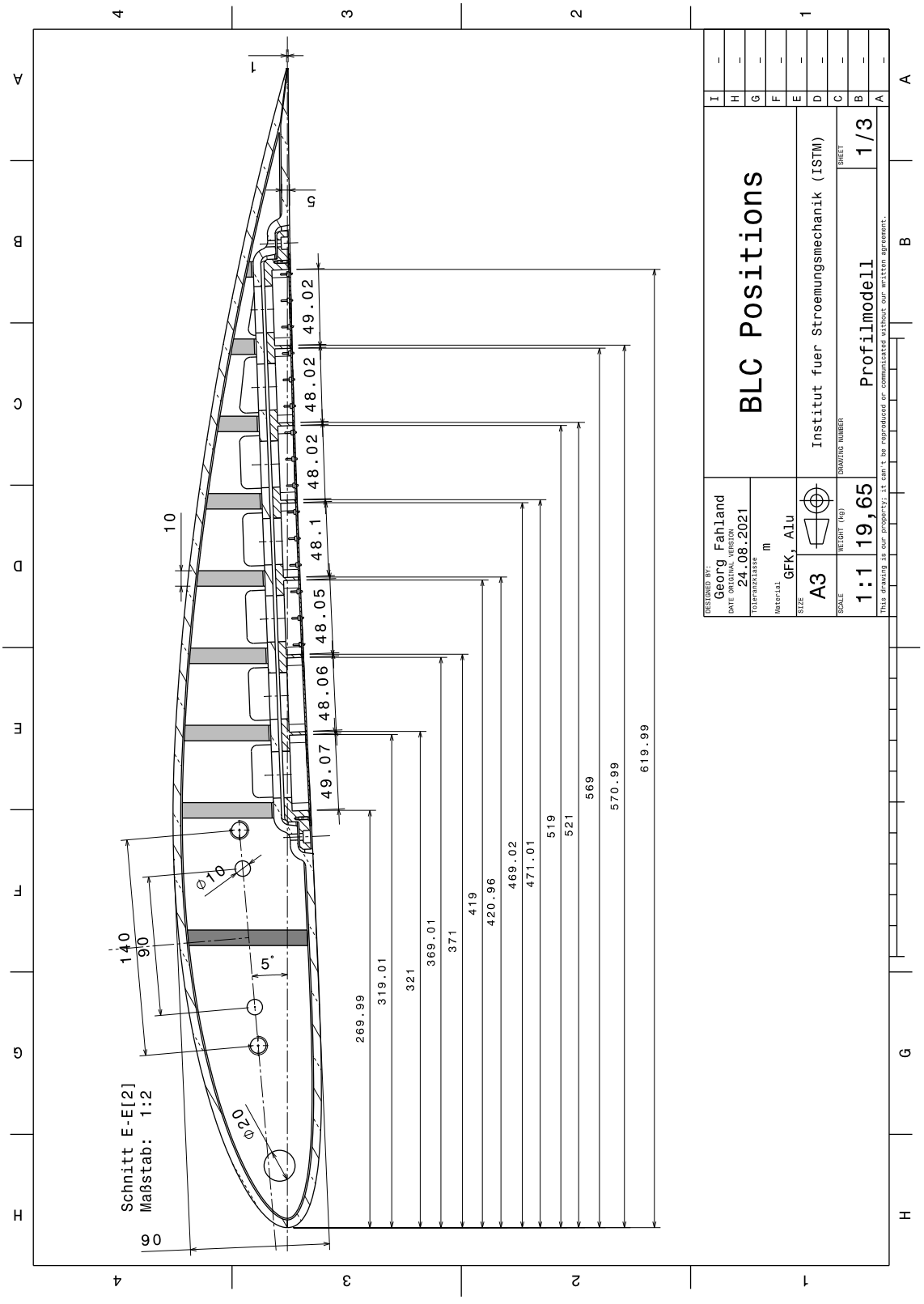

Figure C.3: Model Drawing VACA4412s019 BLC Positions

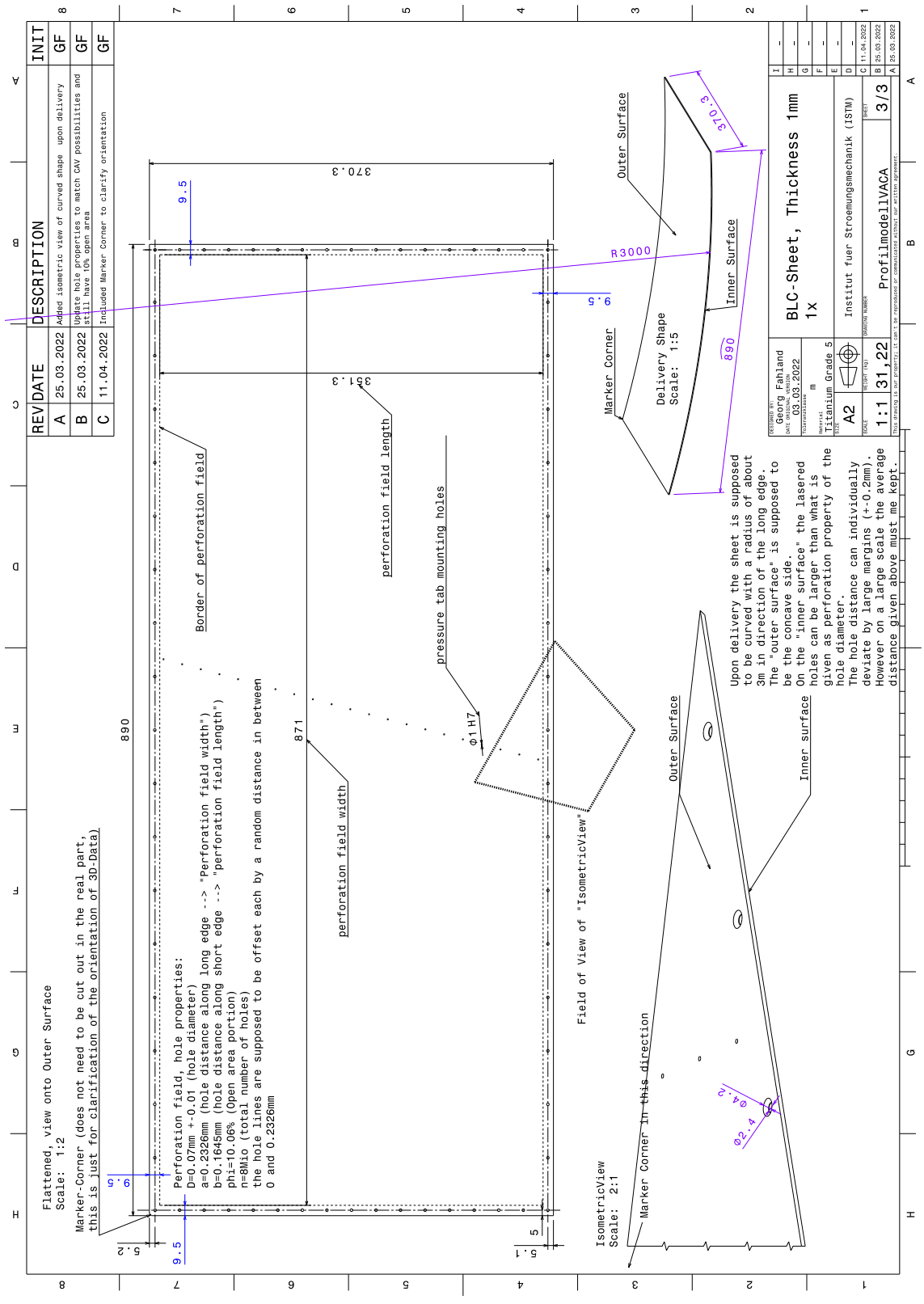

Figure C.4: Model Drawing VACA4412s019 BLC Surface Sheet, Revision C

Inspection Report: AT-ER-0525 KIT Inspection Report
Part: Kralsruher Institut für Technologie (KIT) Wind Tunnel Model
Specification/Drawing: ProfilemodellVACA Rev C
Inspector: Steven Carr.

Revision	Comments	Date
1	First issue	09 June 2022

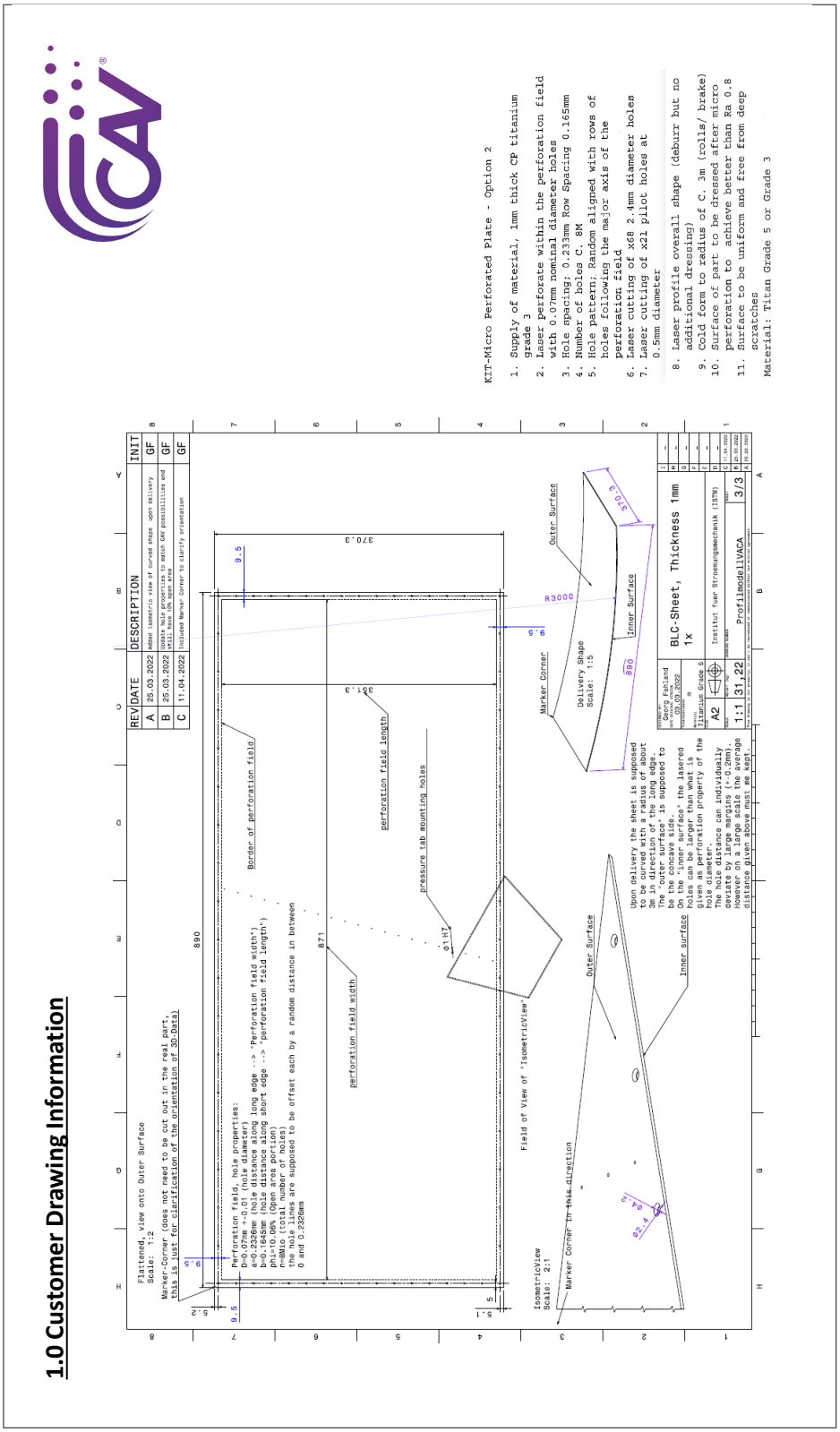
1.0 Customer Drawing Information
KIT-Micro Perforated Plate - Option 2
1. Supply of material, 1mm thick CP titanium grade 3
2. Laser perforate within the perforation field with 0.07mm nominal diameter holes
3. Hole spacing: 0.233mm Row Spacing 0.165mm
4. Number of holes C. 8M
5. Hole pattern; Random aligned with rows of holes following the major axis of the perforation field
6. Laser cutting of x68 2.4mm diameter holes
7. Laser cutting of x21 pilot holes at 0.5mm diameter
8. Laser profile overall shape (deburr but no additional dressing)
9. Cold form to radius of C. 3m (rolls/ brake)
10. Surface of part to be dressed after micro perforation to achieve better than Ra 0.8
11. Surface to be uniform and free from deep scratches
Material: Titan Grade 5 or Grade 3
REV DATE DESCRIPTION INIT
A 25.03.2022 Added isometric view of curved shape - upon delivery GF
B 25.03.2022 Update hole properties to match CAV possibilities and still have 10% open area GF
C 11.04.2022 Included Marker Corner to clarify orientation GF
Flatmodel, view onto Outer Surface
Scale: 1:2
Marker Corner does not need to be cut in the real part, this is just for clarification of the orientation of 3D-Data)
Perforation field, hole properties:
D=0.07mm +-0.01 (hole diameter)
a=0.2326mm (hole distance along long edge --> 'Perforation field width')
b=0.1656mm (hole distance along short edge --> 'perforation field length')
phi=10.00% (Open area portion)
n=8Mio (total number of holes)
the hole lines are supposed to be offset each by a random distance in between 0 and 0.2326mm
Border of perforation field
perforation field width
perforation field length
pressure tab mounting holes
Field of view of "IsometricView"
IsometricView
Scale: 2:1
Marker Corner in this direction
Outer Surface
Inner surface
Upon delivery the sheet is supposed to be curved with a radius of about 3m in direction of the long edge. The "outer surface" is supposed to be the concave side.
On the "inner surface" the lasered holes can be larger than what is given as perforation property of the hole diameter.
The hole distance can individually deviate by a few percent (+-10%). However on a large scale the average distance given above must me kept.
Delivery Shape
Scale: 1:5
R3000
Outer Surface
Inner Surface
BLC-Sheet, Thickness 1mm
1x
Titanium Grade 5
A2
1:1
31.22
3/3
Institut fuer Stroemungsmechanik (ISTM)
ProfilmodellVACA

3.2.1 Perforation area image

3.2.3 Outer Surface Hole Inspection Results: *(Twenty microscope images in total – hole diameter , hole pitch and row spacing determined).*

Image	Outer Surface Hole diameter µm					Hole pitch (x) µm	Row spacing (y) µm
1	55	61	44	38	57	223	171
2	63	49	63	66	50	229	171
3	64	61	66	61	61	235	167
4	72	61	50	74	66	226	159
5	50	55	69	52	58	229	176
6	61	80	63	50	63	223	165
7	61	22	46	44	68	230	152
8	66	50	52	89	61	229	165
9	55	69	88	61	58	224	171
10	80	50	85	55	69	237	150
11	69	52	69	63	61	264	155
12	57	72	69	58	69	206	162
13	58	72	72	72	52	234	173
14	66	77	63	66	88	234	162
15	52	61	72	69	72	234	145
16	52	66	80	61	66	237	169
17	61	66	74	74	61	231	163
18	61	52	67	58	61	229	156
19	58	63	75	74	69	237	167
20	61	69	64	52	75	232	159

Average (mean): hole diameter 63µm
hole pitch(x) 231µm
Row spacing (y) 163µm

3.2.5 Inner Surface Hole Inspection Results: *(Twenty microscope images in total –hole diameter , hole pitch and row spacing determined).*

Inner Surface							
Image	Hole diameter µm					Hole pitch (x)	Row spacing (y)
						µm	µm
1	110	102	129	113	113	270	175
2	110	116	97	96	83	240	158
3	91	96	107	113	116	234	190
4	110	116	102	99	121	220	162
5	113	105	110	110	110	259	165
6	85	91	80	85	102	242	177
7	99	118	102	91	94	237	165
8	110	72	105	102	102	237	180
9	104	85	77	110	105	214	138
10	91	94	99	94	85	234	162
11	102	102	107	72	66	248	160
12	77	77	106	102	114	240	162
13	116	103	102	88	99	226	173
14	102	95	107	95	127	223	150
15	101	111	115	103	115	240	147
16	78	76	92	100	109	228	154
17	109	78	123	110	102	226	164
18	89	124	106	112	109	251	153
19	84	95	73	128	89	234	169
20	111	95	84	103	100	254	168

Average (mean): hole diameter 101µm
hole pitch(x) 238µm
Row spacing (y) 164µm

3.2.8 Surface Roughness Profile

OUTER	Roughness - Profile			
	Test 1	Test 2	Test 3	Test 4
EVA-L	4.0mm	4.0mm	4.0mm	4.0mm
λc	0.8mmX5	0.8mmX5	0.8mmX5	0.8mmX5
Ra	1.86µm	0.86µm	1.14µm	1.22µm
Rz	15.92µm	6.30µm	13.49µm	15.71µm
Rq	2.78µm	1.27µm	2.05µm	2.07µm

INNER	Roughness - Profile			
	Test 1	Test 2	Test 3	Test 4
EVA-L	4.0mm	4.0mm	4.0mm	4.0mm
λc	0.8mmX5	0.8mmX5	0.8mmX5	0.8mmX5
Ra	18.59µm	16.48µm	17.71µm	16.35µm
Rz	86.33µm	80.50µm	85.46µm	75.92µm
Rq	21.98µm	20.15µm	20.96µm	20.15µm

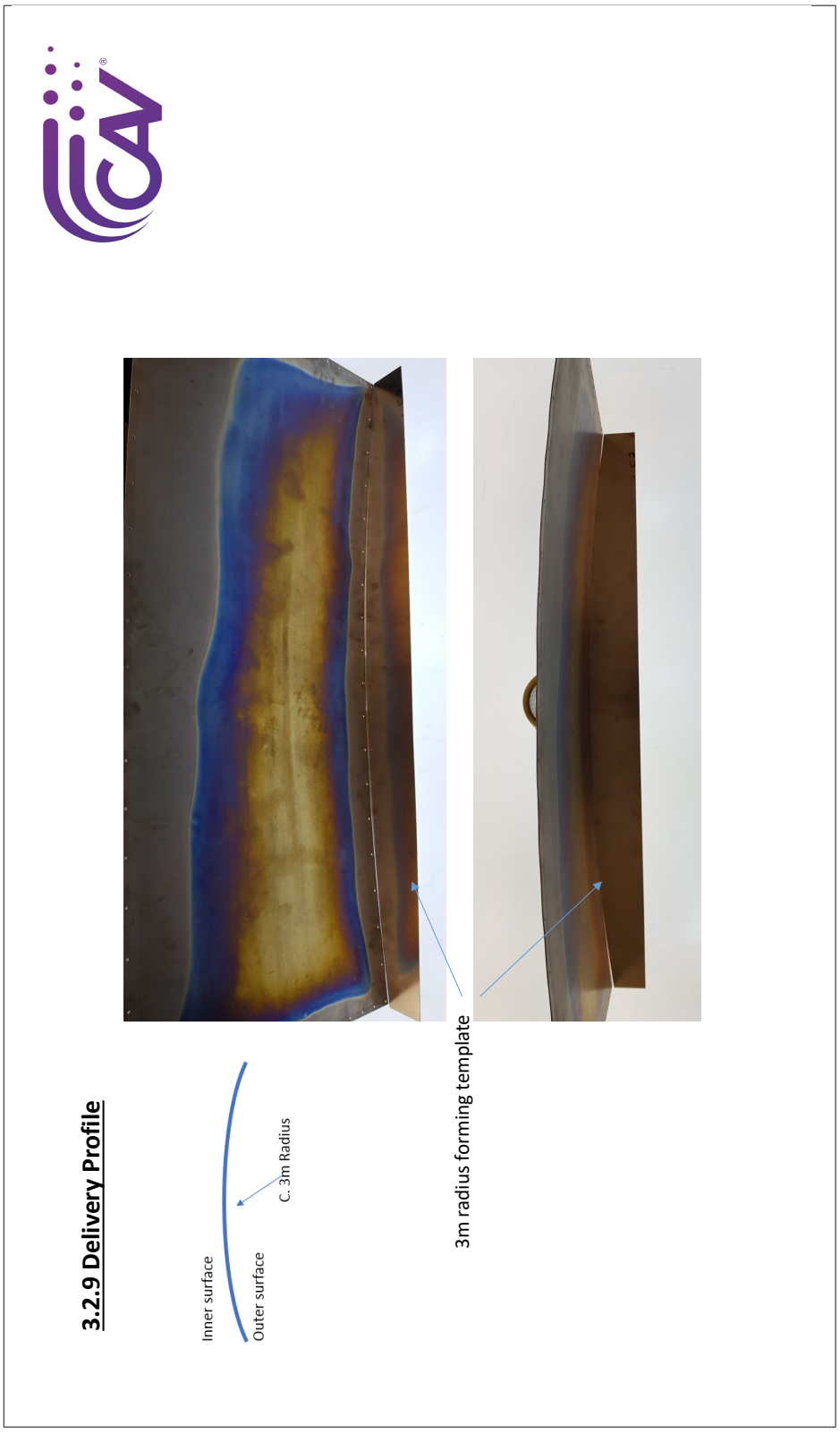
3.2.9 Delivery Profile
Inner surface
Outer surface
C. 3m Radius
3m radius forming template

4.0 Inspection Summary

Feature	Actual	Comments
length of part	886-887mm	
width of part	369.5-370mm	
length of perforation field	867-870mm	
width of perforation field	351mm	
perforation field hole diameter (outer surface)	63µm	average (mean) of 100 randomly selected holes measured
perforation field hole diameter (inner surface)	101µm	average (mean) of 100 randomly selected holes measured
hole pitch (long edge)	231µm	
row spacing (short edge)	163µm	
perimeter 2.4mm holes	2.45-2.48mm	
perimeter 2.4mm holes (long edge offset distance)	878mm	
perimeter 2.4mm holes (short edge offset distance)	359.5mm	
pressure tab mounting holes	0.96mm	
surface finish (Ra) outer	1.27µm	
surface finish (Ra) inner	17.28µm	

D Appendix: Airfoil Test Rig Properties

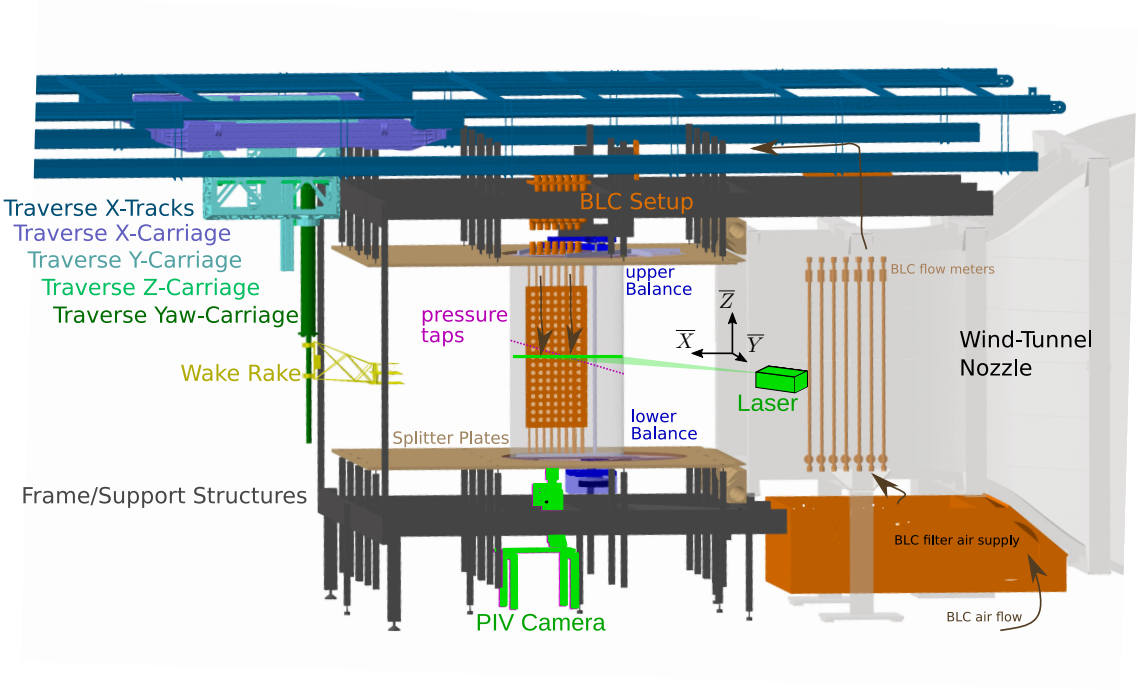

Figure D.1: Final airfoil test rig configuration for VACA4412s019 BLC experiments with PIV, pressure taps, balance, and wake measurements depicted.

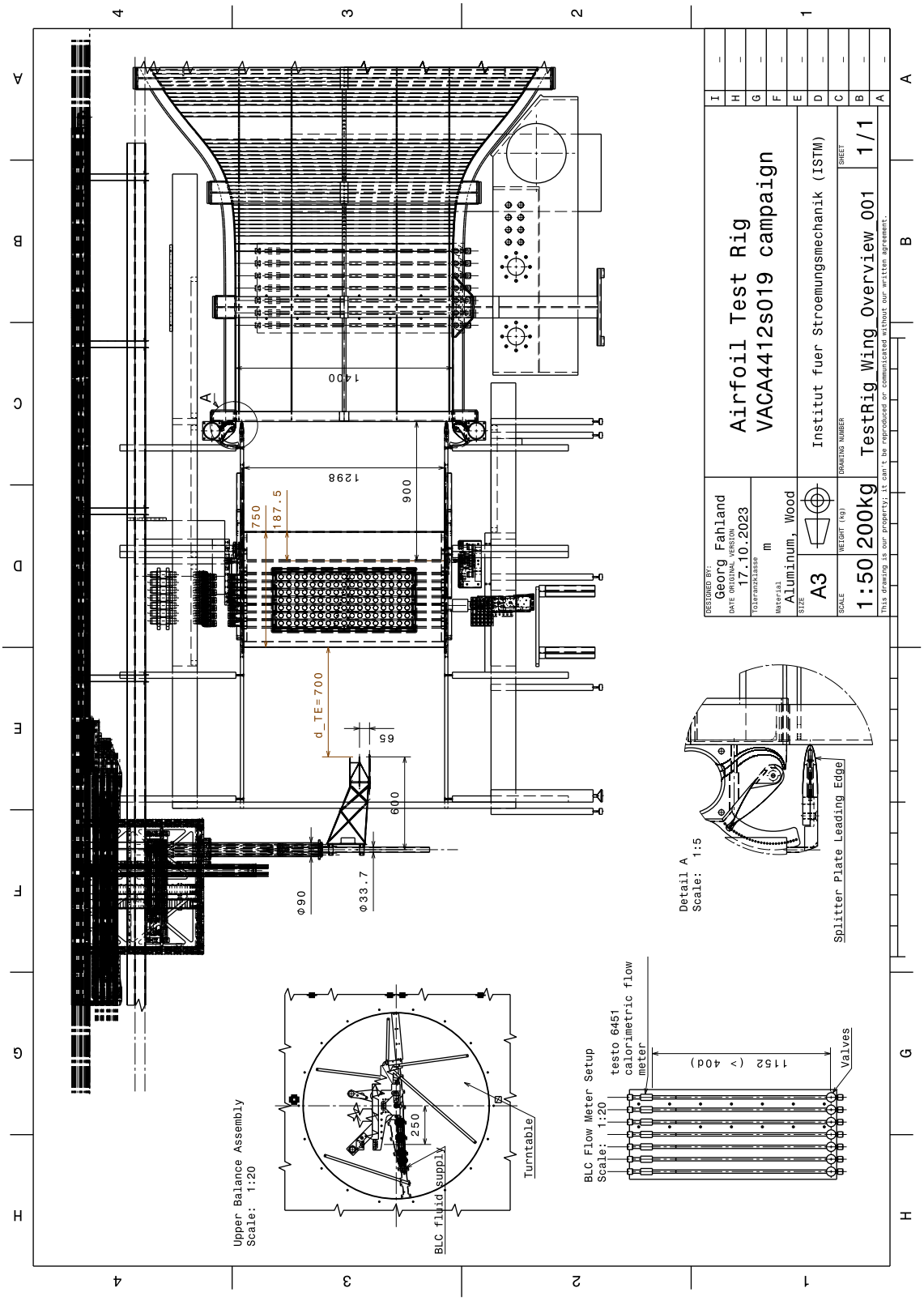

Figure D.2: Relevant distances of test rig during VACA4412s019 experimental campaign

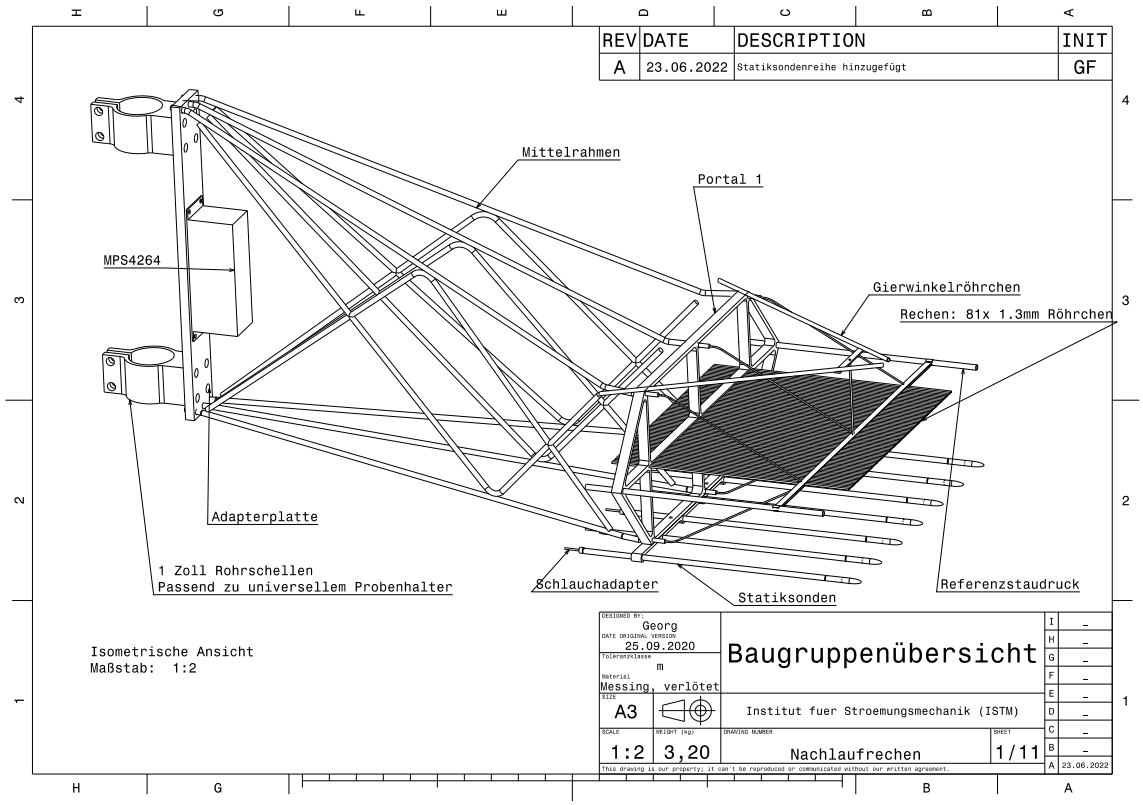

Figure D.3: Wake Rake Final Drawing with 3 probing rows. From top to bottom: 2 angled tubes for yaw measurement (not connected in the present campaign), 81 total pressure pitot tubes, and 7 static probes

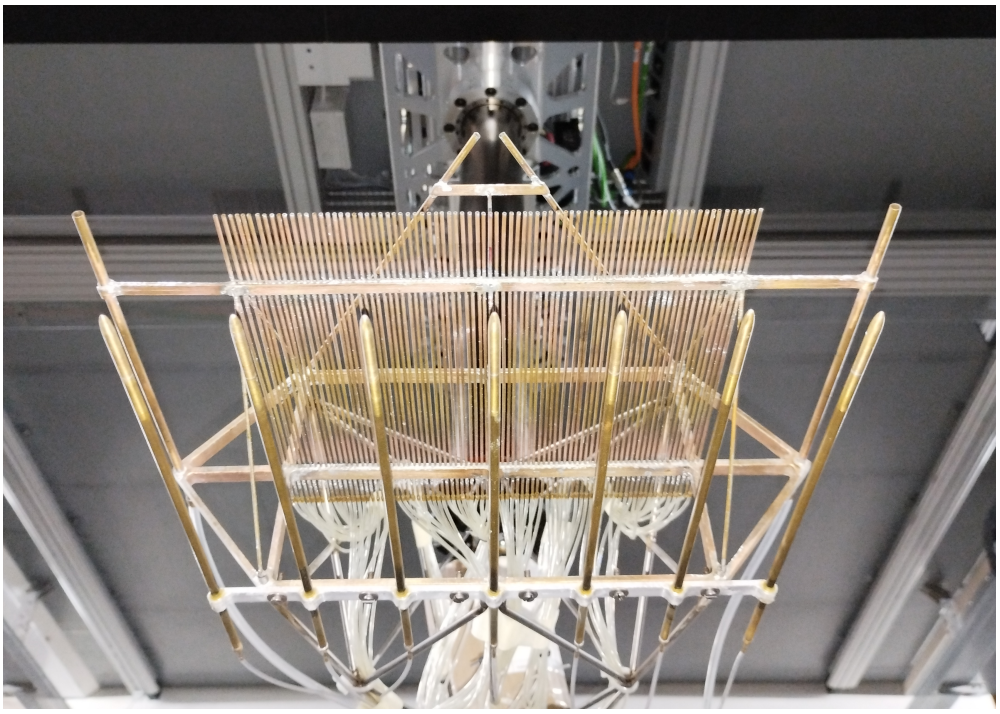

Figure D.4: Wake Rake in its final setup at the wing test stand inside the test section

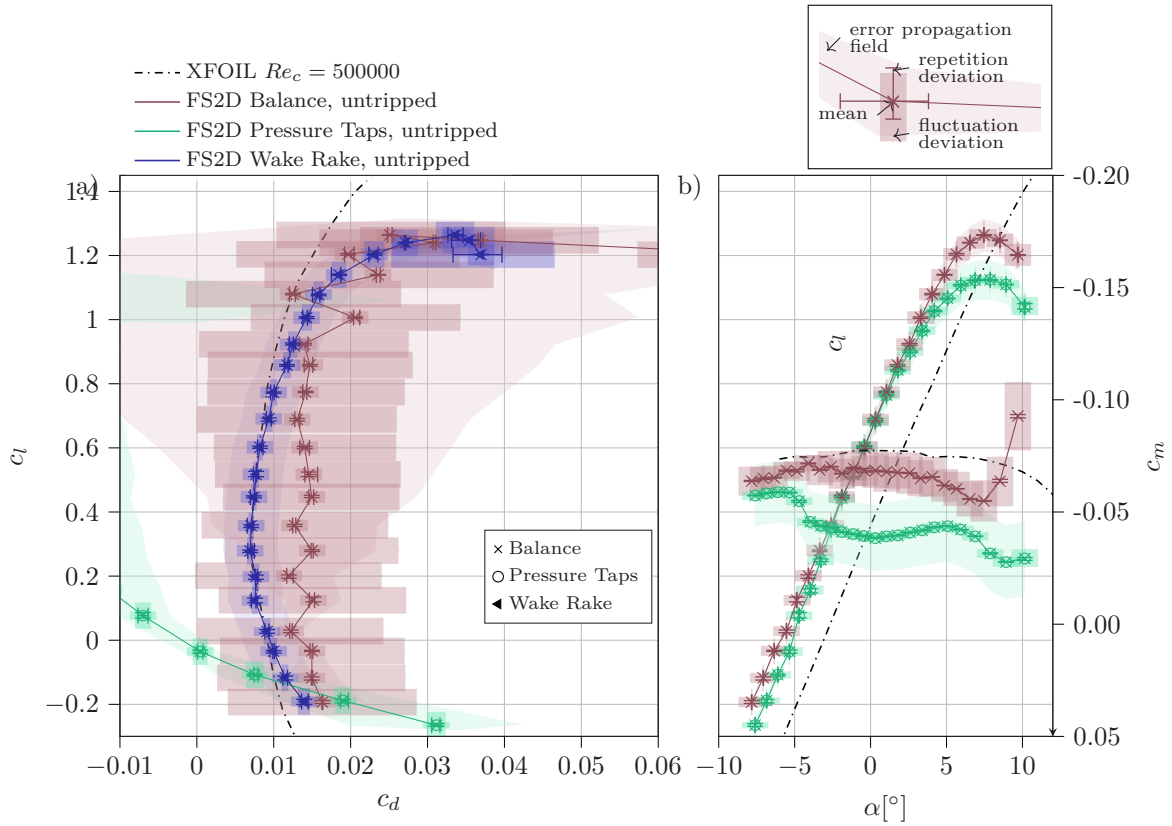

Figure D.5: Polar plot of the HGR-01 airfoil model, 2D freestream corrected form (FS2D). Date of recording: Aug. 16, 2022. No tripping, $Re_c \in [4.6 \cdot 10^5, 5 \cdot 10^5]$, about nominal zero flap deflection position.

Reference to Datasheets

[181] Industrial platinum resistance thermometers and platinum temperature sensors (IEC 60751:2008), 2009.

[182] Eitzenberger Luftlagertechnik GmbH. Elementar Luftlager. Datasheet, Wessobrunn, Germany, 2016. https://eitzenberger.com/de/produkte/elementarluftlager-pad/standardlager Retrieved 2023.

[183] Eitzenberger Luftlagertechnik GmbH. EZ-4000 Planarführung. Datasheet, Wessobrunn, Germany, 2020. https://eitzenberger.com/de/produkte/koplanare-passive-systeme-hubzylinder/passives-3-achssystem?tx_indexedsearch_pi2%5Baction%5D=form&tx_indexedsearch_pi2%5Bcontroller%5D=Search&tx_indexedsearch_pi2%5Bsearch%5D%5BextendedSearch%5D=0&cHash=c7bf7b60f40e1b8d67403bcc31b78844 Retrieved 2023.

[184] Hottinger Baldwin Messtechnik GmbH. HBM Common API. User Manual, Darmstadt, Germany. https://www.hbm.com/fileadmin/mediapool/hbmdoc/technical/A04174.pdf Retrieved 2023.

[185] Hottinger Baldwin Messtechnik GmbH. QuantumX Outputs Activation. Technical Note, Darmstadt, Germany, 2015.

[186] Hottinger Baldwin Messtechnik GmbH. QuantumX. User Manual, Darmstadt, Germany, 2019.

[187] Hottinger Baldwin Messtechnik GmbH. HBM LabVIEW Driver. User Manual, Darmstadt, Germany, 2020. https://www.hbm.com/fileadmin/mediapool/hbmdoc/technical/A04175.pdf Retrieved 2023.

[188] ME-MeSSsysteme GmbH. KD40s. Datasheet, Hennigsdorf, Germany. https://www.me-systeme.de/product-pdf?product_id=1735&lang=de Retrieved 2023.

[189] ME-MeSSsysteme GmbH. Sensoren und Messverstärker. User Manual, Hennigsdorf, Germany. https://www.me-systeme.de/de/support/grundlagen Retrieved 2023.

[190] SKF GmbH. SIKB 6 F. Datasheet, Schweinfurt, Germany. https://www.skf.com/de/products/plain-bearings/spherical-plain-bearings-rod-ends/rod-ends/productid-SIKB%206%20F Retrieved 2022.

[191] SKF GmbH. Table 6 - Radial Gap and Friction Moment for maintenance-free spherical-plain-bearings-rod-ends. Datasheet, Schweinfurt, Germany. https://www.skf.com/de/products/plain-bearings/spherical-plain-bearings-rod-ends/rod-ends/general-rod-end-specifications Retrieved 2023.

[192] Honeywell. ABP2. Technical report, Richardson, USA, 2021. https://prod-edam.honeywell.com/content/dam/honeywell-edam/sps/siot/de-de/products/sensors/pressure-sensors/board-mount-pressure-sensors/basic-abp2-series/documents/sps-siot-abp2-series-datasheet-32350268-en.pdf?download=false Retrieved 2023.

[193] MKS Instruments. High Accuracy Systems: AA06A and AD06A Sensors, 670C Signal Conditioner. Datasheet, Andover, USA. https://www.mks.com/mam/celum/celum_assets/resources/AA06A-AD06A-670C-DS.pdf?6 Retrieved 2023.

[194] BVS Akustik GmbH Co. KG. Caruso-Iso-Bond. Datasheet, Verl, Germany. http://akustik-shop.com/web/assets/Uploads/akustipur/bvsdaemmungcaruso.pdf Retrieved 2023.

[195] A.A. Lab Systems LTD. AN-1003. Datasheet, Ramat-Gan, Israel, 2006. https://www.lab-systems.com/products/flow-mea/an1003/AN-1003%20Brochure.pdf Retrieved 2023.

[196] measurements Specialties. HM1500LF Relative Humidity Module. Datasheet, Toulouse, France. https://www.te.com/commerce/DocumentDelivery/DDEController?Action=showdoc&DocId=Data+Sheet%7FHPC062_F%7FA%7Fpdf%7FEnglish%7FENG_DS_HPC062_F_A.pdf%7FCAT-HSA0002 Retrieved 2023.

[197] pco. PCO-edge5.5. Datasheet v2.02, Kelheim, Germany.

[198] PIVTEC. Pivlight seeding with pivlight30 seeder. Seeding, Göttingen, Germany. http://www.pivtec.com Retrieved 2024.

[199] PIVTEC. Pivview2c, version 3.9.8. Software, Göttingen, Germany. http://www.pivtec.com Retrieved 2024.

[200] Rockwool. Sonoroll 040. Datasheet, Gladbeck, Germany. https://www.baustoffshop.de/pub/media/pdf/rockwool/db-sonoroll-040-rockwool.pdf Retrieved 2023.

[201] Scanivalve. MPS4264. User Manual, Liberty Lake, USA. https://scanivalve.com/wp-content/uploads/2023/05/MPS4264_V304.pdf Retrieved 2023.

[202] Inc. Setra Systems. AccuSense(TM) Model ASL. Datasheet, Boxborough, USA. https://www.setra.com/hubfs/Product_Data_Sheets/Setra_Model_ASL_Data_Sheet.pdf?hsLang=en Retrieved: 2023.

[203] Inc. Setra Systems. Model 278. User Manual, Boxborough, USA. https://www.setra.com/products/pressure/model-278-barometric-pressure-transducer Retrieved: 2023.

[204] testo. Testo 6451. Datasheet, Titisee-Neustadt, Germany. https://static-int.testo.com/media/e5/30/46066b136f39/testo-6451-6454-Datasheet-DE.pdf Retrieved 2023.